A low-temperature ageing and irradiation study on 14YWT Nanostructured Ferritic Alloys for nuclear fusion applications



Kris Bhojwani

Oriel College
University of Oxford

A thesis submitted for the degree of Doctor of Philosophy

Trinity 2017

Abstract

14YWT Nanostructured Ferritic Alloys (NFAs) are candidate alloys for tokamak blanket applications. They differ from conventional steels as they contain dispersoids that are distributed across its matrix. These dispersoids pin dislocations and grain boundaries, and are responsible for the superior high temperature properties associated with these alloys. However, at $\leq 475°C$, Fe-Cr based alloys are susceptible to the formation of α' precipitates. Their presence induces increases in hardness and embrittlement. In irradiation environments the kinetics of α' formation are enhanced. At these low-temperatures and under irradiation it is unknown whether 14YWT also forms α' precipitates, other secondary phases and tertiary intermetallics. It is also unknown whether segregation of alloying elements occurs too.

This thesis describes an isothermal ageing study which sought to determine whether 14YWT NFAs are susceptible to the formation of α' precipitates, other secondary phases and tertiary intermetallics. This study aged samples of 14YWT NFA and 14WT non-NFA at $475°C$ for 1, 3 and 8 months. 14WT non-NFA is a control variant of 14YWT containing no dispersoids. A second study was also completed that sought to study phase stability within 14YWT NFA ion-irradiated and neutron irradiated at low-temperatures separately. Ion-irradiation was conducted using $^{56}Fe^{8+}$ to a peak dose of 0.74-1.49dpa, at $3.24-6.53\times10^{-5} dpa\, s^{-1}$ at $288°C$. Neutron irradiation was conducted to 1.82dpa at $3.85\times10^{-7} dpa\, s^{-1}$ (E>0.1MeV) at $288°C$. Three variants of 14YWT were used in this thesis. They differed primarily in terms of their nominal concentrations of Ti and Y_2O_3, and are referred to as 14YWT1, 14YWT2, and 14YWT3. 14YWT1 was utilised in the isothermal ageing study, 14YWT2 was ion-irradiated and 14YWT3 was neutron irradiated. Post-experimental analysis for both studies primarily comprised of

Atom Probe Tomography (APT), which provides nm-scale chemical resolution of alloying element distributions within the alloys. Microhardness indentation tests were also conducted on the isothermally aged alloys only, to determine whether any hardening occurred.

Before APT experiments on the treated alloys could be conducted, an APT calibration experiment on 14YWT1 was completed. This sought to determine a combination of analysis parameters that produced datasets which were of a high quality. A dataset was deemed to be of a high quality if all of the following criteria was maximised: compositional measurement accuracy, signal-to-noise ratio and mass resolution. It was found that all three were satisfied when experiments were conducted at: a temperature of $55K$, laser pulse energies of $0.4nJ$, laser pulse repetition rate of $200kHz$ and an evaporation rate of $0.005\,ions\,pulse^{-1}$.

APT characterisation of the aged 14WT showed α' precipitates had formed within the sample aged for 3 months and 8 months. This suggests an incubation period between 1 and 3 months. α' precipitate characteristics varied significantly between three experimental repeats in terms of: number density, radius, and precipitate Cr concentration. Average α' precipitate characteristics across three experimental repeats within the 14WT aged for 8 months are: $36 \pm 32 \times 10^{22} m^{-3}$, $1.38 \pm 0.26nm$ and $52.17 \pm 3.39wt.\%$ respectively. 14YWT1 did not form any α' precipitates. No other secondary phases or intermetallics were observed to form in the aged 14WT and 14YWT1. Therefore 14YWT1 has a stable α phase and Cr is soluble in Fe under these conditions. Aged 14YWT1 grain boundaries (GBs) were seen to be enriched in Cr, W, Si and Mn. However, due to significant variation in the data, no trends as a function of ageing duration could be determined. NFA dispersoids were deemed to be stable after residing at $475°C$ for 8 months as no significant change in their radius and Y-Ti-O concentrations were observed. Microindentation tests revealed that after 8 months of ageing, 14WT had

hardened by $32 \pm 4 kg\, mm^{-2}$. However, 14YWT1 had softened by $26 \pm 10 kg\, mm^{-2}$. APT characterisation of both the ion-irradiated 14YWT2 and neutron irradiated 14YWT3 showed that the matrix α phase did not contain any α' precipitates, other secondary phases or intermetallics. Therefore 14YWT2 and 14YWT3 are deemed to be stable under these irradiation conditions. Since little differences in the microstructures of the ion-irradiated and neutron irradiated occurred, ion-irradiation is thought to be a good analogue to fission neutron irradiation at these irradiation conditions.

Preface

The work presented in this doctoral thesis has been carried out at the Department of Materials, University of Oxford from October 2012 to October 2017, under the supervision of Dr Steven P. Fitzgerald, Dr Philip D. Edmondson and Professor Steve G. Roberts. All of the research carried out for this thesis is original, and where the work of others has been included it has been referenced and acknowledged. No part of this thesis has been submitted for a degree at this, or any other university.

Acknowledgements

I am grateful for the advice, support and encouragement my suprvisors Dr S. Fitzgerald, Dr P. Edmondson and Professor S. Roberts have given me. This opportunity they afforded me has been life changing.

My thanks also go to Dr. M. Auger, Dr D. Haley, Dr P. Bagot, Dr T. Martin, Dr S. Pedrazzini, Professor M. Moody and the wider atom probe research group at the University of Oxford. This work would not be possible without their technical advice.

I am incredibly grateful to Dr A. London for the numerous occasions I have sought his advice, and the various matlab subroutines he has allowed me to utilise in this thesis.

I am grateful for the financial support from the department of Materials at the University of Oxford and the York Plasma institute, at the University of York. Thanks also go to my former and present colleagues within the department for their friendship, humour and the numerous materials science related discussions: Dr C. Hardie, Dr C. Burrows, Dr M. Gorley, Dr S. Yardley, Dr. A. Xu, Dr F. Ferroni, Dr. Y. Zayachuk, Dr. E Tarleton, Dr. C. Jones, K. Plummer, J. Jiang, B. Li, L. Hewitt and T. Tanaka.

Thank you to Professor G.R Odette and Dr P. Wells for supplying the neutron irradiated 14YWT, and their support when applying for FIB and atom probe time at CAES. I am also grateful for NSUF funding and the staff at CAES who enabled me to study the neutron irradiated samples. Thank you to the MRF at CCFE for access to their FIB.

Common symbols and abbreviations

AFM Antiferromagnetic

APT Atom Probe Tomography

ATR Advanced Test Reactor

BCC Body Centred Cubic

CALPHAD Calculation of Phase Diagrams

CAES Centre of Advanced Energy Studies

dpa displacements per atom

DLD Delay Line Detector

DLM Disordered Local Magnetic Moment

DSA Dispersoid Strengthened Alloy

EBSD Electron BackScatter Diffraction

ED Edge Dislocation

EDS Energy Dispersive Spectroscopy

EELS Electron Energy Loss Spectroscopy

EMG Exponentially Modified Gaussian

EPMA Electron Probe Micro-Analyser

FCC Face Centred Cubic

FIB Focussed Ion Beam

FM FerroMagnetic

FWHM Full Width Half Maximum

GB Grain Boundary

GIE Gibbsian Interfacial Excess

HCLL Helium Cooled Lithium Lead

HDR High Dose Rate

IKE Inverse Kirkendall Effect

JANNuS Joint Accelerators for Nanosciences and NUclear Simulation

KS Kolli and Seidman

LDR Low Dose Rate

MCP Micro Channnel Plate

MD Molecular Dynamics

NFA Nanostructured Ferritic Alloy

NN Nearest Neighbours

NPE Nano-Patterning Engine

ODS Oxide Dispersion Strengthened

PM ParaMagnetic

PKA Primary Knock on Atom

PWR Pressure Water Reactor

RAF Reduced Activation Ferritic

RED Radiation Enhanced Diffusion

REP Radiation Enhanced Precipitation

RIP Radiation Induced Precipitation

RIS Radiation Induced Segregation

ROI Region Of Interest

SANS Small Angle Neutron Scattering

SCC Stress Corrosion Cracking

SEM Scanning Electron Microscopy

SGTE Scientific Group Thermodata Europe

SIA Self Interstitial Atom

SNR Signal to Noise Ratio

TBM Test Blanket Module

TEM Transmission Electron Microscope

ToF Time of Flight

UCSB University of California Santa Barbara

Contents

1 Introduction **1**

2 Literature review **8**

2.1 Introduction 8

2.2 Overview of 14YWT NFAs 8

2.2.1 14YWT composition 9

2.2.2 14YWT microstructure 11

2.2.3 14YWT mechanical properties 13

2.2.4 Principles of dispersion strengthening mechanisms 14

2.2.4.1 Dispersoid composition and coherency 15

2.2.5 Irradiation management 18

2.3 NFAs at low-temperature 19

2.3.1 Phase stability of 14YWT NFAs 19

2.3.1.1 Magnetic frustration 20

2.3.1.2 Cr solubility limit in Fe 21

2.3.1.3 $\alpha + \alpha'$ phase formation mechanisms 23

2.3.1.4 α' precipitate equilibrium physical characteristics post-ageing 27

2.3.1.5 α' precipitate influenced mechanical changes 28
2.3.1.6 α' precipitate interactions with dislocations 31
2.3.1.7 α' formation within higher order dispersion strengthened Fe-Cr based alloys 32
2.3.2 Segregation of alloying elements at low-temperatures 38
2.3.3 NFA dispersoid thermal stability 40
2.4 Irradiation damage 43
2.4.1 Quantifying irradiation dose 45
2.4.2 Ionised particle energy loss mechanisms 46
2.4.3 Simulation of fusion radiation 48
2.4.3.1 Variations in the Primary Knock on Atom (PKA) spectrum 50
2.4.3.2 Dose rate effect 52
2.5 Low temp. irrad. effects 55
2.5.1 Low-temperature radiation induced mechanical property change 55
2.5.1.1 Potential sources of low-temperature irradiation induced hardening and embrittlement in 14YWT 56
2.5.2 Radiation Induced Segregation (RIS) 57
2.5.2.1 RIS within 14YWT NFAs 59
2.5.2.2 Neutron and ion irradiation comparative studies on RIS and RIP 62
2.5.3 Irradiation altered phase stability 64
2.5.3.1 Recoil dissolution 64
2.5.3.2 Irradiation disordering 65
2.6 Conclusion 66
2.6.1 14YWT NFAs at low-temperature 67

2.6.2 14YWT NFAs exposed to low-temperature irradiation 67

3 Materials and experimental methods 69

3.1 Materials 70

3.1.1 Fabrication 70

3.1.1.1 14YWT1 and 14WT Oxford alloys 70

3.1.1.2 14YWT2 and 14YWT3 UCSB alloys 70

3.1.2 Microstructure characterisation 71

3.1.2.1 14YWT1 and 14WT Oxford alloys 71

3.1.2.2 14YWT2 and 14YWT3 UCSB alloy 76

3.2 Isothermal ageing 78

3.2.1 Furnace calibration 79

3.2.2 Isothermal ageing experiment 81

3.3 Irradiation experiments 82

3.3.1 Ion irradiation 82

3.3.2 Neutron irradiation 88

3.4 Atom probe tomography 91

3.4.1 A brief introduction to atom probe tomography 91

3.4.2 Field evaporation 94

3.4.3 LEAP 3000X-HR and LEAP 4000X-HR 95

3.4.4 Parameter determination 95

3.4.5 NFA dispersoid cluster analysis 97

3.4.5.1 Determining the core clustering solute ions 97

3.4.5.2 Defining D_{max} and N_{min} 99

3.4.5.3 Defining L, E and η 104

3.4.5.4 Cluster analysis output 105

3.4.6 α' and Ti cluster analysis 108
3.4.7 Trajectory aberrations around clusters 108
3.4.7.1 Trajectory abberations in 14YWT NFAs 110
3.4.7.2 Trajectory abberations in 14WT 111
3.4.8 The shadow effect 112
3.5 Microhardness tests 113

4 LEAP 3000X-HR calibration for 14YWT 116

4.1 Introduction 118
4.2 Background 119
4.2.1 Materials and samples 119
4.2.2 Calibration tests 119
4.2.3 Calibration study objectives 121
4.2.3.1 Exponentially Modified Gaussian (EMG) function . . . 124
4.3 Results & discussion 125
4.3.1 Objective 1: minimising the difference between APT measured concentrations and that measured by EPMA 125
4.3.1.1 Assessing the extent of peak overlaps in the spectrum . 125
4.3.1.2 Comparing Fe, Cr and W concentrations measured from APT experiments with that from EPMA 129
4.3.2 Objective 2: maximise the SNR and minimise background count rate 135
4.3.3 Objective 3: maximising the mass and spatial resolutions 138
4.3.3.1 Maximising the mass resolution 138
4.3.3.2 Maximising the spatial resolution 141
4.4 Conclusion 145

5 Isothermal ageing of 14WT and 14YWT at 475℃ 147

5.1 Introduction 149

5.2 Materials and methods 149

5.3 Results 151

5.3.1 APT characterisation of isothermally aged 14WT 160

5.3.1.1 Cr rich α' precipitates within 14WT alloys aged for 3 and 8 months at $475°C$ 160

5.3.1.2 No segregation of minor elements towards α' precipitates 170

5.3.1.3 14WT Ti rich precipitates 170

5.3.1.4 Concentrations of Ti and W within 14WT aged for 8 months 173

5.3.1.5 14WT grain boundary segregation 175

5.3.2 APT characterisation of isothermally aged 14YWT1 176

5.3.2.1 Fe and Cr distributions within the as-received and aged 14YWT1 179

5.3.2.2 Mn, Si and Al distributions within the as-received and aged 14YWT1 184

5.3.2.3 14YWT1 grain boundary segregation 187

5.3.2.4 NFA particles within the as-received and aged 14YWT1 190

5.3.3 14WT and 14YWT1 microhardness measurements 197

5.4 Discussion 199

5.4.1 α' precipitate characteristics in the aged 14WT 199

5.4.1.1 Inhomogeneity in the α' precipitate distribution 200

5.4.2 14YWT1 NFA resistance to α' precipitate formation 203

5.4.3 14YWT1 grain boundary enrichment 205

5.4.4 14YWT1 NFA cluster thermal stability at low-temperatures . . . 206
5.4.5 Establishing the origins of the hardening in 14WT and softening in 14YWT1 . . . 207
5.4.5.1 Estimating the dislocation breakway angle in 14WT alloys aged for 3 and 8 months . . . 209
5.5 Conclusion . . . 211

6 Phase stability of ion and neutron irradiated 14YWT 213

6.1 Introduction . . . 214
6.2 Materials and methods . . . 214
6.3 Results . . . 216
6.3.1 14YWT2 as-received and ion-irradiated . . . 217
6.3.1.1 Fe and Cr solvent distributions . . . 219
6.3.1.2 Grain boundary segregation of alloying elements . . . 224
6.3.1.3 14YWT2 minor solute distributions . . . 225
6.3.2 14YWT3 as-received and neutron irradiated . . . 226
6.3.2.1 Distribution of dispersoids in the as-received 14YWT3 . 228
6.3.2.2 Fe and Cr solvent distributions within 14YWT3 . . . 229
6.3.2.3 Grain boundary segregation of alloying elements within 14YWT3 . . . 235
6.3.2.4 14YWT3 Minor solute distributions . . . 235
6.4 Discussion . . . 236
6.4.1 Phase stability of irradiated 14YWT2 and 14YWT3 . . . 236
6.4.2 Comparison of ion and neutron irradiated 14YWT microstructures 238
6.5 Conclusion . . . 238

7 Conclusion **240**

7.1 Previous work 240

7.2 Work completed in this thesis 241

7.2.1 Atom probe tomographic parameter determination experiment . 241

7.2.2 Isothermal ageing experiment 242

7.2.3 Ion and neutron irradiation comparative study 243

7.3 Limitations 244

7.4 Future work 245

A Atom probe tomographic procedures **280**

A.1 Sample fabrication 280

A.1.0.1 Fabricating APT samples via the FIB lift out technique 281

A.2 Post-experimental analysis 283

A.2.1 Reconstructing datasets 283

A.2.2 Peak identification 286

A.2.3 Peak overlap 287

A.2.4 Grain boundary analysis 287

B Isothermal ageing experiment: 14YWT1 experimental repeats **290**

C Aged 14WT grain boundary Gibbsian excess data **295**

D Irradiated 14YWT2 and 14YWT3 experimental repeats **297**

E Gibbsian excess data from GBs in 14YWT2 and 14YWT3 **302**

Chapter 1

Introduction

By the year 2035, the global population is likely to be close to nine billion people while the global gross domestic product is set to double [1]. In this period energy demand has been predicted to increase by 34% [1]. Due to an increasing awareness of climate change, governments around the world are re-evaluating their energy policies to ensure a larger proportion of their energy is from low carbon energy sources [2]. Nuclear fusion technology has the potential to fulfil this requirement and is likely to form a significant proportion of a state's energy portfolio.

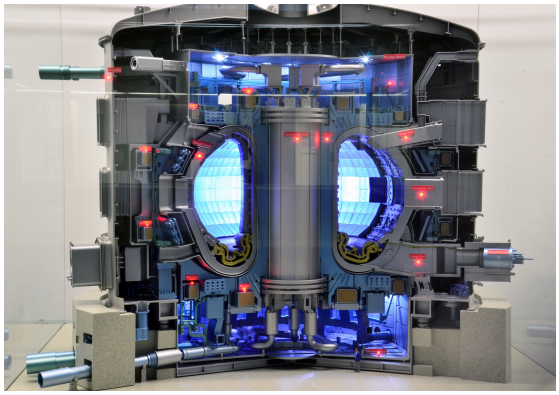


Figure 1.1: Model of ITER - the tokamak device under construction in Cadarache in France [3].

Fusion is a type of nuclear reaction in which two light nuclei are brought together to form a single heavier nucleus and occurs naturally in stars such as the Sun. One leading method to implement this reaction artificially is within a magnetically confined fusion tokamak reactor, similar to that shown in figure 1.1. In effect, this replicates the method stars use as the reactants ionise and form a plasma via various heating mechanisms. External magnetic fields generated by large superconducting magnets are also utilised to control the plasma.

$$ {}^{2}_{1}H + {}^{3}_{1}H \rightarrow {}^{4}_{2}He + {}^{1}_{0}n \tag{1.1} $$

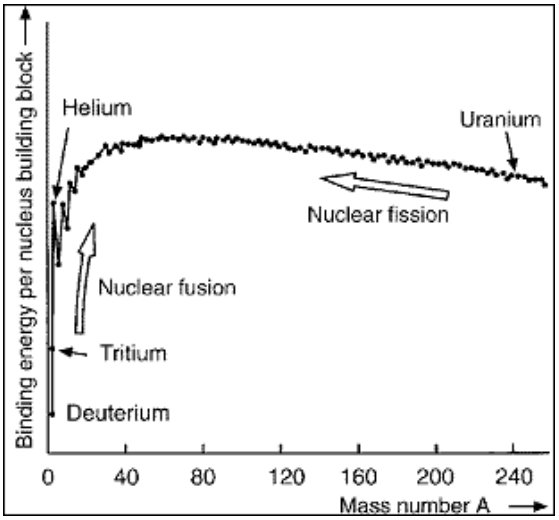


Figure 1.2: Binding energy per nucleon [4]. The fusion of Deuterium and Tritium are placed on the side of the plot that will yield an exothermic reaction.

Deuterium and tritium (D-T) are the preferred reactants and produces helium and a neutron as shown in equation 1.1. This fuel mixture fuses at lower temperatures relative to other reactants and provides a significant energy yield. Energy is released from this reaction because He has a lower mass relative to the sum of its nucleons. This is due to a higher binding energy per nucleon within He as illustrated in figure 1.2.

17.6MeV of energy is released from a single D-T fusion reaction. The distribution of this energy is unequal amongst the reaction products as the neutron and He obtains 14.1MeV and 3.5MeV of energy respectively. Advantageously, D-T fusion reactions have a considerable gross energy density of $576 \times 10^{12} J\,kg^{-1}$, relative to crude oil, which has $46.3 \times 10^{3} J\,kg^{-1}$ [5].

Unfortunately, commercial fusion is several decades away as tokamak technology is still in its infancy [6]. Tokamak devices contain an array of technologies that must be harmonised and work consistently. This includes understanding the plasma physics, plasma diagnostics, superconducting magnet technology and advanced materials science [7]. Of the four listed, materials challenges are the most significant because of the extreme environments fusion reactions take place within [8]. The temperature range enclosed within a tokamak range from $-269°C$ where the superconducting magnets are located [9, 10, 11] to several millions of $℃$ in the plasma [11]. To add to this harsh environment, materials will also have to withstand neutron induced damage to levels as high as 200 displacements per atom (dpa) [12, 13]. Fundamentally, it is vital that fusion technology demonstrates it can produce energy reliably; therefore tokamak components must be able to function for 3-5 year operation cycles.

A central tokamak component is the blanket as it provides structure to the tokamak, facilitates tritium breeding reactions and contains the coolant system [14]. Many blanket designs have been proposed for use in future commercial tokamaks [15, 16]. Six short-listed prototype designs will be installed onto ITER - the precursor to a demonstrator tokamak [17]. Each of the six prototypes known as Test Blanket Modules (TBMs) will be studied while being used during ITER campaigns. One of the six TBM designs is the Helium Cooled Lithium Lead (HCLL) module, whose schematic is shown in figure 1.3 [18]. Designs specify a structural wall to be constructed out of an Fe-Cr based alloy [19] as well as a coolant system with inlet and outlet temperatures at $300°C$ and

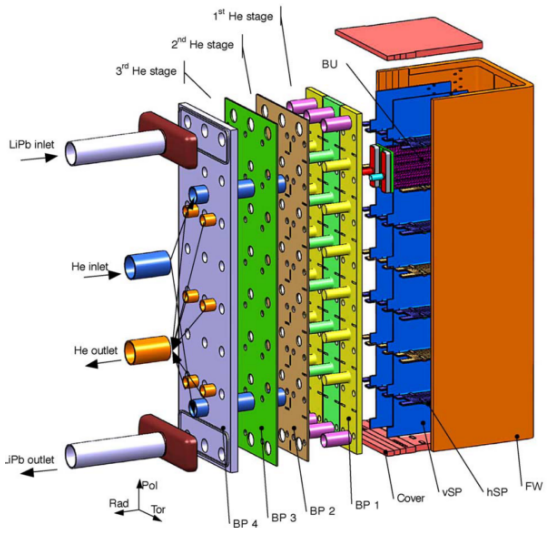


Figure 1.3: HCLL proposed blanket for use in ITER [18]. Where: BU=Breeder unit, BP=Back Plate, vSP=vertical Stiffened Plate, hSP=horizontal Stiffened Plate, FW=First Wall.

$500°C$ respectively [18].

Conventional steels such as type 316 are unsuitable for constructing the first structural wall of the HCLL [18]. This is primarily due to its inability to withstand neutron irradiation stemming from the plasma. For example, irradiation would produce a large population of point defects that could cause swelling [20]. Volumetric changes to this steel would be detrimental to its mechanical properties e.g. high-temperature creep [21, 22]. Thus a material that can manage the generation of point defects appropriately under irradiation conditions is required. 14YWT NFAs are candidate materials for structural first wall applications [23] and are designed to manage defect populations within their microstructure. The name 14YWT is based on the nominal composition of the alloy: $Fe-14Cr-3W-0.2Ti-0.25Y_2O_3(wt.\%)$. They are low activation alloys since they do not contain large quantities of elements that are highly susceptible to activation e.g. Mo and Ni [19]. 14YWT NFAs contain a high density of ultrafine

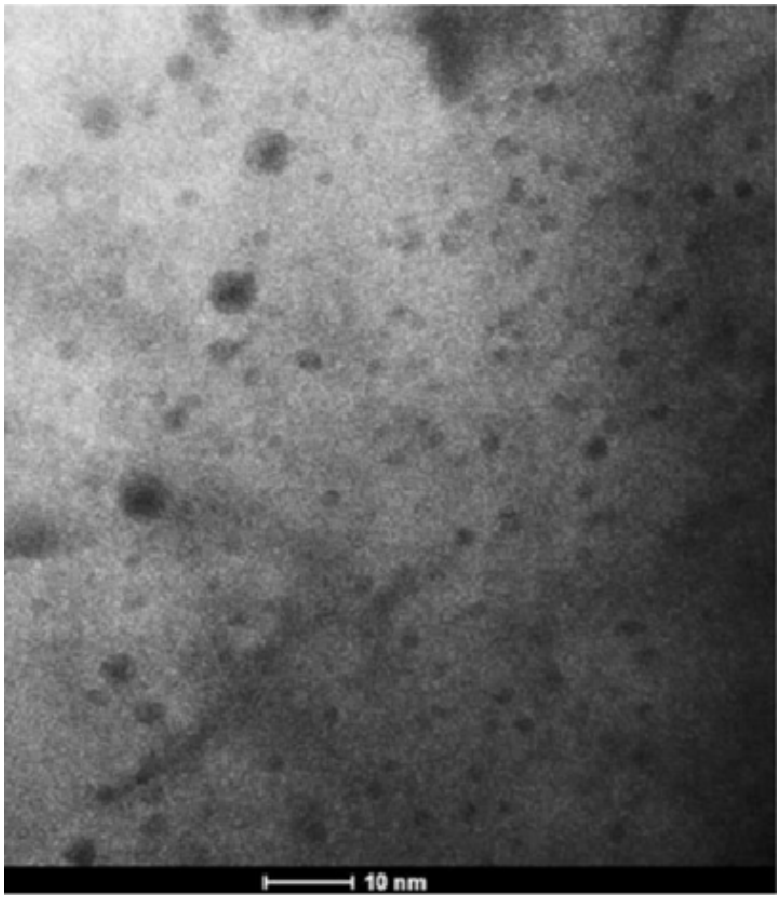


Figure 1.4: TEM image of 14YWT NFA steel at high magnification. Black spots represent dispersoids distributed across the α ferrite matrix [31].

2^{nd} phase oxide dispersoids, as shown in figure 1.4, which are distributed throughout their matrix. The presence of these dispersoids enhance the alloy's high-temperature strength properties [24, 25, 26]. This is likely to be due to the dispersoids impeding dislocation motion [27, 28]. Under irradiation conditions, the dispersoids are thought to promote the recombination of point defects by trapping them at the dispersoid-matrix interface [29, 30].

Fe-Cr based alloys that have resided at the range of temperatures the HCLL TBM coolants are pumped in and out at ($300℃$ and $500℃$), have formed α' precipitates [32].

These are spherical isolated structures that are composed predominantly of Cr [33]. The presence of α' precipitates, will impede dislocation motion [34, 35] and therefore influence the mechanical properties of the alloy they form within. As a result, an increase in hardness and embrittlement is often observed [36, 37].

Isothermal ageing experiments at $475°C$ on complex ODS alloy systems such as PM2000 have reported the presence of both α' and β' phases [38]. Rich in Ti and Al, these β' phases also influence the mechanical properties of the aged alloys [39]. The addition of elements such as Ti and Al can perturb the Fe-Cr binary phase diagram dramatically by introducing new phases, which is the case for PM2000 [40]. Additionally, existing phase boundaries could be removed or changed as the free energy of the alloy system is modified [41]. As 14YWT is also a complex alloy containing W and Ti as well as many other minor solutes, it is possible for other phases, in addition to α', to form and modify the kinetics of precipitate formation.

In the presence of irradiation, α' precipitate formation is enhanced [42]. A recent study comparing the elemental distributions within ion irradiated and neutron irradiated Fe-Cr binary alloys at similar conditions reported a distinct difference [43]. While the neutron irradiated sample had formed α' precipitates, the ion irradiated sample had not. As ion irradiation is often used within the nuclear materials research community to simulate neutron irradiation, this observation is striking. Whether this difference in elemental distributions, within ion and neutron irradiated 14YWT NFAs occurs, remains to be answered.

This thesis will seek to study samples of 14YWT NFA after a series of low temperature: isothermal ageing, ion irradiation and neutron irradiation treatments. Microstructural characterisation will be conducted using APT, which provides the investigator 3D atom-by-atom reconstructions with nm resolution and chemical identification. Analysis of the results acquired from this technique will give insight to whether α', or indeed any other

additional phases form after each of the three treatments. It will also be possible to determine whether there is preferential segregation of solutes to specific microstructural features e.g. NFA dispersoids or Grain Boundary (GB). Vickers hardness tests will also be conducted on the aged samples to observe how the mechanical properties of the alloys evolve as ageing duration increases. This will provide insight into how the microstructure and mechanical properties relate to each other.

The outline of this thesis begins with: an overview of 14YWT NFAs, low temperature effects on Fe-Cr based alloys, an overview of irradiation physics and the effects of low temperature irradiation on Fe-Cr based alloys (chapter 2). Chapter 3 will present the various experimental methods employed to carry out this research. As APT is a key piece of experimental equipment in this thesis, the rationale behind the choice of analysis parameters will be presented in chapter 4. Following this, observations from the isothermal ageing study in will be described in chapter 5. Chapter 6 will detail the study into phase stability within 14YWT NFAs under ion and neutron irradiation. Finally, a summary, concluding remarks and a recommendations for future work to be carried out will be outlined in chapter 7.

Chapter 2

Literature review

2.1 Introduction

Firstly an overview of 14YWT NFAs is given. Secondly, microstructural and mechanical changes that occur within Fe-Cr based alloys after long-term exposure to low-temperature are described. This is followed by an overview of irradiation physics and the utilisation of ion implantation to simulate neutron irradiation. Finally, theory and literature related to low-temperature irradiation effects on 14YWT NFAs is presented.

2.2 Overview of 14YWT Nanostructured Ferritic Alloys (NFAs)

This overview will cover the following areas: 14YWT composition, microstructure, mechanical properties, principles of dispersion strengthening mechanisms and finally irradiation management.

2.2.1 14YWT composition

The nominal composition is $Fe{-}14Cr{-}3W{-}0.2Ti{-}0.25Y_2O_3(wt.\%)$; the culmination of systematic optimisation studies e.g. [27, 44, 45, 46]. Each alloying element contributes towards 14YWT's superior mechanical properties.

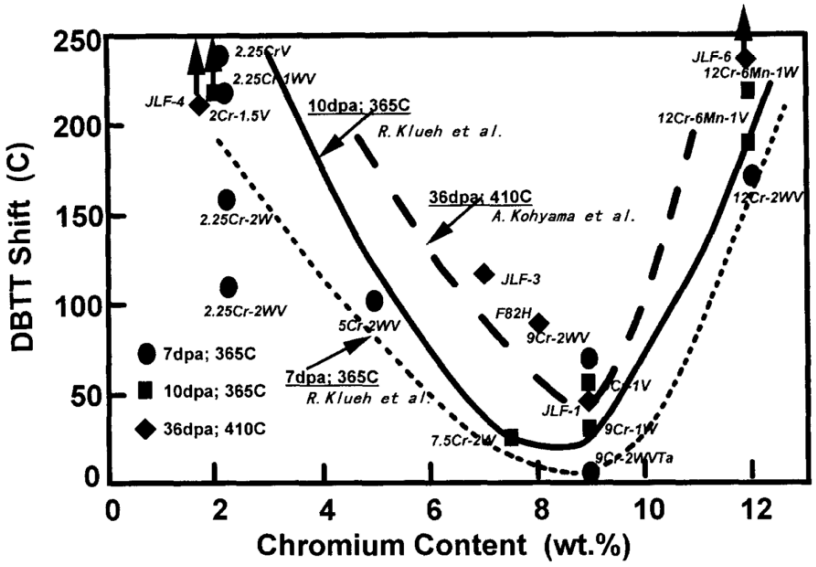


Figure 2.1: $\Delta DBTT$ (change in the Ductile to Brittle Transistion Temeperature) as a function of alloy Cr concentration [47]. A minima is observed for alloys with a Cr content of 9wt.%. Data points from various experiments: available in the original text.

As the second most abundant element in 14YWT, Cr has a significant influence on its properties. Figure 2.1 shows $\Delta DBTT$ (ΔDuctile to Brittle Transition Temperature) as a function of the Cr concentration within various irradiated alloys. Above and below the minimum, which occurs at $[Cr] \sim 9wt.\%$, $\Delta DBTT$ increases significantly [47]. Extrapolating the black solid line in figure 2.1, indicates an Fe-14Cr based alloy irradiated to 10dpa at $365°C$ will result in $\Delta DBTT \sim +190°C$. Creep rupture strength increases with decreasing Cr content as shown in figure 2.2 to a plateau of $[Cr] \sim 9.5wt.\%$ [48, 49, 50, 51]. Yield strength is seen to increase with increasing Cr

content as shown in figure 2.3 [52].

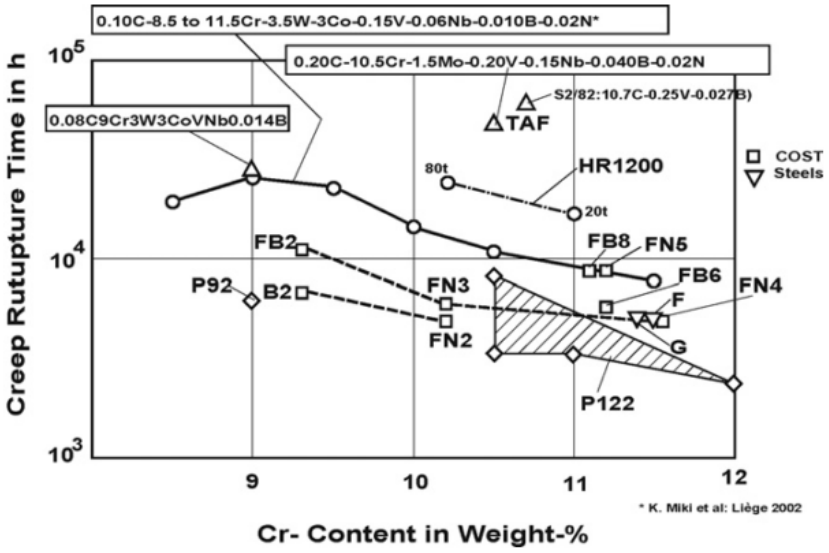


Figure 2.2: Creep rupture time as a function of alloy Cr content for a test stress of 100MPa at 650°C [50, 51]

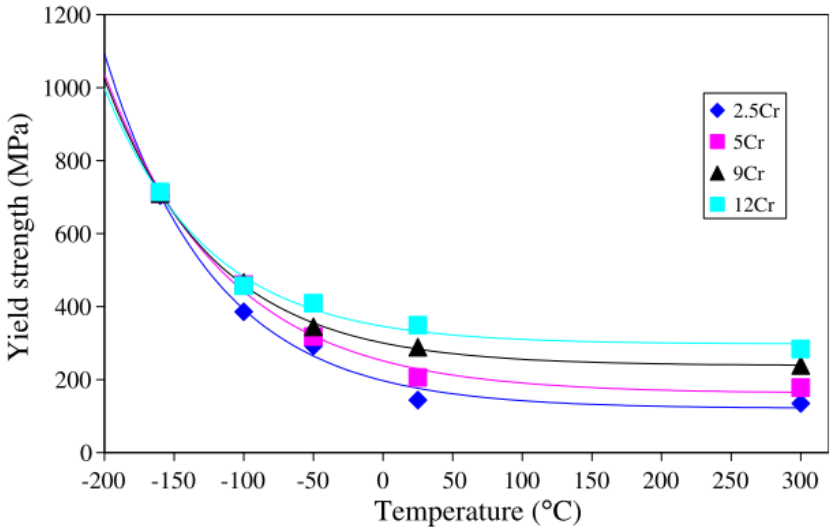


Figure 2.3: Yield strength as a function of temperature for four alloys with differing Cr contents. Cr concentrations are in wt.% [52]

Corrosion resistance increases with increasing Cr concentration and is optimised within Dispersoid Strengthened Alloys (DSAs) that have $[Cr] \geqslant 14wt.\%$ [53].

Therefore 14YWT nominally contains $[Cr] = 14wt.\%$ as it is optimised for corrosion resistance and yield strength, but compromises on its $\Delta DBTT$ and creep resistance properties. Further, by containing $[Cr] = 14wt.\%$, 14YWT has a fully ferritic Body Centred Cubic (BCC) structure. Under irradiation conditions, this structure is expected to have a swelling rate of $0.2\%\, dpa^{-1}$ [54, 55]. This is significantly lower than Face Centred Cubic (FCC) systems, which have a swelling rate typically of $1.4\%\, dpa^{-1}$ [54, 55].

The third most abundant element in 14YWT is W (nominally $3wt.\%$). W is primarily a solid solution strengthener [56] in Reduced Activation Ferritic (RAF) alloys as it is less prone to activation than conventional solid solution strengtheners such as Mo [57]. It is also a ferrite stabiliser [56], reducing the size of the γ loop and the likelihood of an FCC structure forming at higher temperatures.

Y is the principal dispersoid-forming element in 14YWT because of it's low Gibbs free energy and low diffusion coefficient in an Fe-Cr matrix [58]. Residual Y not contained in the dispersoid also contributes to solid solution strengthening [56]. The optimal quantity of Y for creep resistance and ductility was observed to be ($[Y_2O_3]_{14YWT} = 0.25wt.\% \;\; \therefore Y = 0.20wt.\%$) [24].

Ti, the second principle dispersoid-forming element, refines the nanoclusters, increases their volume fraction and enhances their resistance to coarsening [24, 59]. Residual Ti contributes to further solid solution strengthening.

2.2.2 14YWT microstructure

The literature refers to 14YWT as either an NFA or Oxide Dispersion Strengthened (ODS) alloy. The latter is erroneous as the dispersoids within 14YWT are finer than

those in ODS alloys. Table 2.1 shows dispersoids within 14YWT are finer, have a higher number density and a reduced average spacing between dispersoids than PM2000 and MA957 ODS.

Alloy	Average dispersoid radius [nm]	Average dispersoid density $[m^{-3}]$	Interparticle spacing $[nm]$	Source
PM2000	16.2	3.6×10^{21}	65	[60]
MA957	$2.8 - 3.4$	$(1.3 - 1.8) \times 10^{23}$	$14 - 20$	[61]
14YWT	1.79	3.36×10^{23}	14	This work

Table 2.1: Physical characteristics of dispersoids within PM2000, MA957 and 14YWT. Interparticle spacing is estimated by: $(< r > \sim n^{-1/3})$

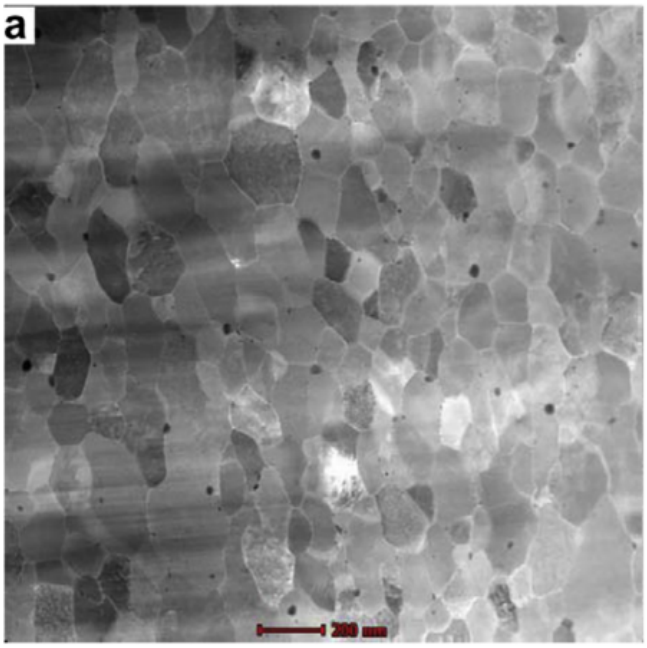


Figure 2.4: Grain structure within 14YWT NFAs [62]. The scalebar is labelled as 200nm.

A typical dispersoid distribution within 14YWT is shown in figures 1.4 and 2.4. The dispersoids, seen as black spots, are distributed randomly [27, 44].

Grain distributions within 14YWT, shown in figure 2.4, are bimodal and are finer than conventional steels [44]. Small and large grains typically range between $50nm - 1\mu m$ and $1\mu m - 10\mu m$ respectively. 14YWT's superior high-temperature mechanical properties are due to the dispersoids pinning these fine grains [63].

2.2.3 14YWT mechanical properties

Mechanical properties of 14YWT NFAs and 14WT non-NFAs are shown in table 2.2. 14WT is a control alloy that doesn't contain any dispersoids and therefore provides insight into the effects dispersoids have on the mechanical properties of 14YWT. Overall the data shows that 14YWT is a significantly stronger material than 14WT but is less ductile.

	14WT	14YWT	Source
Impact energy [J]	~ 3.5	~ 0.4	
Uniform elongation [%]	~ 14.8	~ 4.25	[44]
Yield strength [MPa]	~ 340	~ 1240	

Table 2.2: 14YWT NFA and 14WT non-NFA (control alloy with no dispersoids) mechanical property data at room temperature [44].

Figures 2.5 shows 14YWT's yield strength decreases with increasing test temperature. The plot also demonstrates 14YWT's superiority regarding yield strength at test temperatures as high as $700°C$.

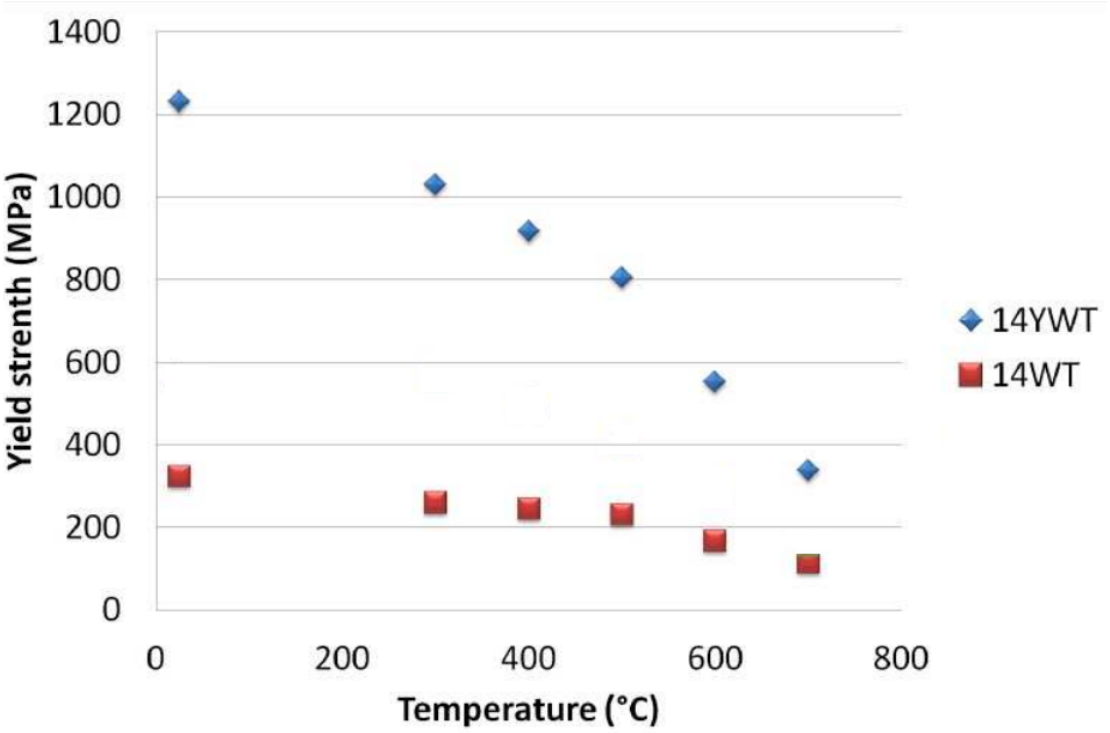


Figure 2.5: Yield strength measurements as a function of test temperature for 14WT and 14YWT [44]

2.2.4 Principles of dispersion strengthening mechanisms

There are five primary alloy strengthening mechanisms: work hardening, grain size refinement, solid solution strengthening, precipitation strengthening and dispersion strengthening.

Each strengthening mechanism works within a range of temperatures defined in figure 2.6. Apart from precipitation and dispersion strengthening, each of the strengthening mechanisms are inadequate to provide high-temperature strength. Work hardening from the mechanical alloying of the powders is ineffective due to annealing; strengthening from ultra fine grains and solid solution mechanisms are unlikely to deter creep at the

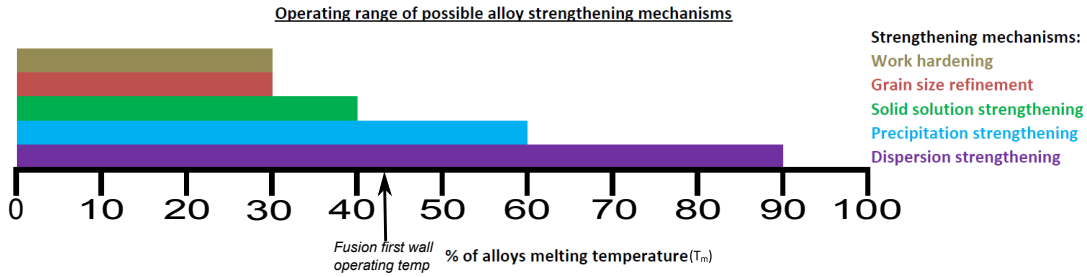


Figure 2.6: An overview, based on the summary within [27], of all the strengthening mechanisms that can be employed within an alloy. Each mechanism depends on the temperature (T_m is the melting temperature of the material) of the environment it is to be applied within. Assuming a melting temperature of $1500°C$ and a tokamak first wall temperature of $650°C$ [64, 46], the operating conditions have been overlaid ($\sim 43\% T_m$).

expected high temperatures [27, 65, 66, 67].

Precipitation and dispersion strengthening involves the introduction of 2nd phase particles into the alloy matrix to impede dislocation motion [28, 68] and pin grains [69, 70]. Precipitates tend to be carbides or nitrides in steels whereas dispersoids are Y, Ti and O-rich in 14YWT. At high-temperatures, second phase precipitates either dissolve into the matrix or undergo Ostwald ripening [28, 71] and therefore high-temperature strength properties are not sustained for long durations. Dispersoids, however, are insoluble within the parent matrix and are stable while at high-temperatures for long durations [72].

2.2.4.1 Dispersoid composition and coherency

The coherency of the dispersoid relative to the matrix largely determines if it is shearable or impenetrable to dislocations. However, coherency is dependent on dispersoid size, composition and structure; all of which vary in 14YWT [73]. Two classes of dispersoids within NFAs have been reported in the literature to date. The first is referred to as "nanoclusters" and the second is referred to as the "non-stoichiometric oxides".

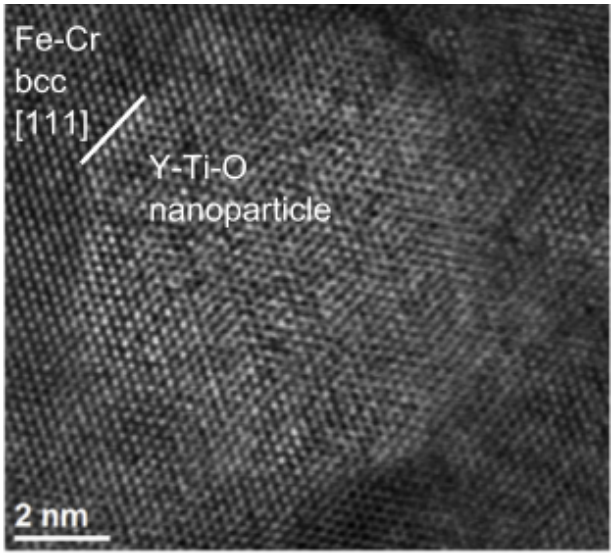


Figure 2.7: Bright field image of a typical of coherent nanocluster rich in Y, Ti and O [77]

Nanoclusters range from 1-3nm in diameter and are Y-Ti-O-enriched metastable compounds [74]. They are coherent with the BCC matrix [72], as shown in figure 2.7, and possess a structure similar to that of NaCl [75]. They are highly defective as they contain a large population of vacancies which have a positive binding energy with all the solute atoms within the nanocluster (Y, Ti and O) [76].

The non-stoichiometric oxides have diameters greater than 3nm, and structural analysis has shown that they can be one of two structures: orthorhombic Y_2TiO_5 [73, 78] or pyrochlore $Y_2Ti_2O_7$ [73, 79]. $Y_2Ti_2O_7$ is largest and tends to be observed and reported more frequently in the literature [72, 74, 78, 80, 81, 82]. $Y_2Ti_2O_7$ has a pyrochlore structure [77], as shown in figure 2.8a, and has a Cr shell [83] which is thought to be 0.6-1.6nm thick [77]. This Cr shell thickness decreases as the dispersoid size decreases [84] and is hypothesised to lower the interfacial free energy [85], and moderate the lattice mismatch between the matrix and dispersoid [75]. Experimental characterisations of the pyrochlore have confirmed that they are indeed coherent dispersoids as seen in figures

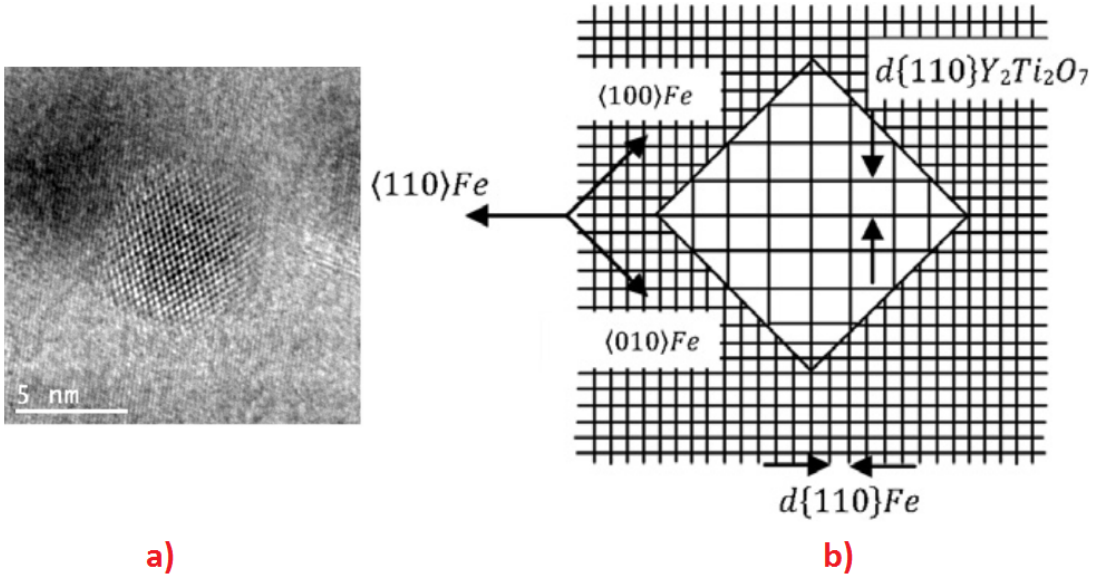


Figure 2.8: a) High resolution TEM image of a pyrochlore. b) A schematic inferred from TEM analysis showing the pyrochlore embedded into the matrix [72]. Lattice planes in the pyrochlore match those within the matrix and therefore these particles are coherent/semi-coherent with the matrix.

2.8a and 2.8b.

There are also precipitates within 14YWT NFA which tend to be much larger. Their diameters range from $50-300nm$. They can be $CrTiO_3$ rhombohedral structures [74], carbides in the form of $M_{23}C_6$ (where M is a mixture of Cr, Fe and W) [86, 87] and nitrides (e.g. Ti-nitrides or Cr-nitrides) [87, 88].

Generally, it is this class of larger precipitates that are impenetrable, whereas the Y-rich dispersoids (the nanoclusters and the non-stoichiometric oxides) tend to be shearable [89]. Accordingly, dislocation-dispersoid interactions are not uniform and will vary between the dispersoid and larger precipitates in the 14YWT matrix.

2.2.5 Irradiation management

Irradiation creates an excess of two types of point defects: Self Interstitial Atom (SIA) and a vacancy. They can annihilate with each other or remain in the alloy's matrix and induce microstructural change (see section 2.5). 14YWT dispersoids act as point defect traps, as shown in figure 2.9 [90]. This increases the probability of annihilation which reduces the alloy's defect population and is why 14YWT is described as a 'self-healing' alloy [91, 92].

The dispersoids also attract and trap transmutation products such as He, which are generated during irradiation [30, 93], also shown in figure 2.9. When a critical number of He atoms have been trapped at the dispersoid interface, He bubbles can nucleate heterogeneously [94, 95]. This reduces the concentration of He in the matrix as well as the effects of irradiation-induced embrittlement [96, 97]. Increasing the density of dispersoids has been shown to increase the number density of He bubbles and therefore improves He bubble formation management [98].

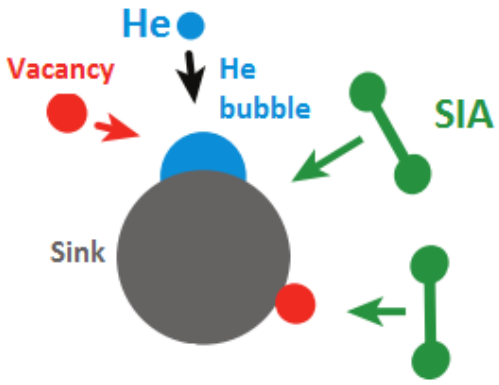


Figure 2.9: **Dispersoids** are distributed within 14YWT and act as sink points for **vacancies**, **SIAs** (in a dumbbell configuration) and **helium** [29].

2.3 NFAs at low-temperature

2.3.1 Phase stability of 14YWT NFAs

The Fe-Cr binary phase diagram shows the phases that can form within Fe-Cr binary alloys at a particular temperature.

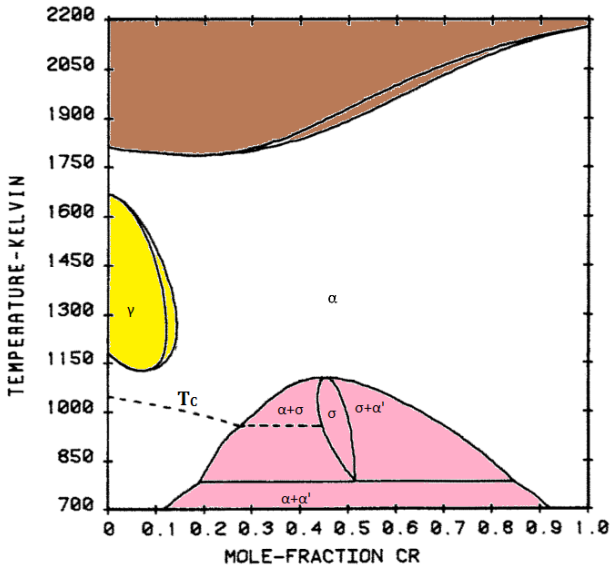


Figure 2.10: The Fe-Cr system as originally calculated using the CALPHAD approach [99]. Colouring and labels have been added to assist in the identification of each region. The brown, Yellow and Pink regions are known as the liquid state, gamma loop, and miscibility gap respectively.

The CALPHAD thermodynamic model of the Fe-Cr system is the industry standard and is shown in figure 2.10 [100]. It is based on thermodynamic data that has been experimentally measured above 700K and for alloys with Cr concentrations above 10at.% [99]. Mixing enthalpies are assumed to be positive regardless of Cr quantities and temperature [101]. Therefore thermodynamic data for other sections of the diagram, such as the low-temperature and low Cr concentration region, are deduced via extrapolation. Figure 2.10 shows the existence of 4 different phases: γ, σ, α and α'. The γ phase is

enclosed in the so-called gamma loop as shown in figure 2.10. This is principally an FCC cubic crystal structure that may occur in low Cr alloys at temperatures approximately 1150-1650K. The miscibility gap is the region that contains the α, α' and σ phases. First identified by Williams et al. in 1957 [34], this is the large pink area in figure 2.10 where Fe and Cr do not form a homogenous mixture [102]. The σ phase is an intermetallic and can occur with Fe-rich $\alpha + \sigma$, as well as Cr-rich $\sigma + \alpha'$ phases. The $\alpha + \alpha'$ region is the phase in which a secondary Cr-rich phase may form.

2.3.1.1 Magnetic frustration

For Cr-rich α' phases to form, Cr atoms need to segregate away from the Fe-Cr matrix and the mixing enthalpy has to become endothermic (positive). The physical similarities of Fe and Cr, in terms of its atomic size and lattice parameters, means that contributions to the mixing enthalpy from strain and elastic terms are small. However electronic sources, such as the magnetic moments of the Fe and Cr atoms have a much greater influence on the mixing enthalpy [103, 104, 105, 106, 107, 108, 109].

For a system comprising of only Fe atoms, the individual magnetic moments are unidirectional i.e. FerroMagnetic (FM) [110]. Conversely, a pure Cr system has magnetic moments that are in a regular pattern with atoms having an opposite spin to their neighbouring atom i.e. Antiferromagnetic (AFM). When a critical number of Cr atoms are added to a majority Fe system at a given temperature, the Cr atoms are unable to reside within a definite FM or AFM state relative to their Nearest Neighbours (NN). Consequently, a phenomenon known as magnetic moment quenching, or magnetic frustration arises which results in the ejection of Cr atoms out of the Fe-Cr solution [111, 112].

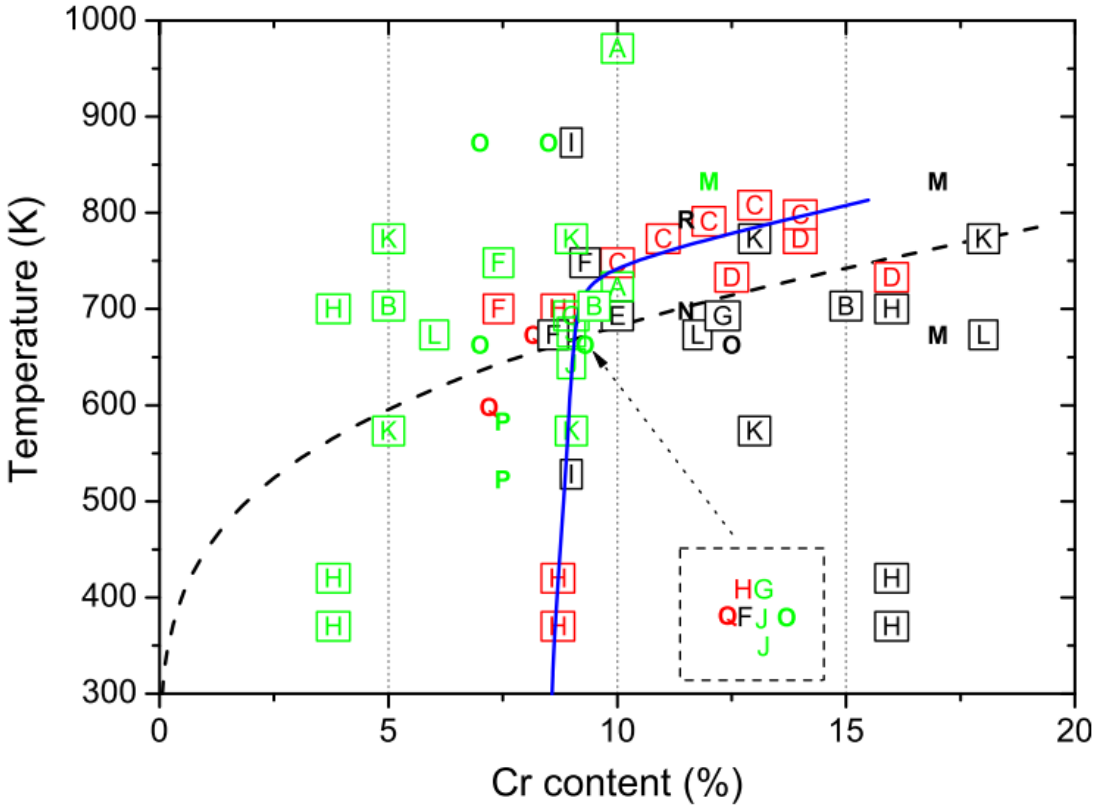


Figure 2.11: The CALPHAD predicted position of the boundary between the miscible and imiscible regions shown by the dashed black line. Green squares represent experimental data observations from short range ordering studies and are not considered here. Red squares are suggested miscibility gap boundary positions from the sources considered. Black squares illustrate various alloys and experimental temperature in which precipitates are observed. Finally, the blue line denotes the position of the miscibility gap boundary which is congruent with the suggested boundary positions (red squares). A variety of experimental conditions, analysis methods and subject alloys are considered. For further details on sources A-H, the reader is referred to the original text [32].

2.3.1.2 Cr solubility limit in Fe

Though the CALPHAD model does predict the existence of these stable states in the Fe-Cr system well, the solubility limits it predicts are not consistent with experimental results, as shown in figure 2.11.

This CALPHAD-experiment discrepancy is probably due to assumptions associated with fundamental parameters within the model e.g. the mixing enthalpy [113, 114, 115] and the solubility limit [32, 116].

Ultimately, the formulation of the Fe-Cr phase diagram is the subject of ongoing research and as such many in the Fe-Cr nuclear materials community, e.g. [117], who require knowledge of the α and $\alpha + \alpha'$ boundary (blue line) rely on the experimentally-determined boundary given in figure 2.11.

2.3.1.3 $\alpha + \alpha'$ phase formation mechanisms

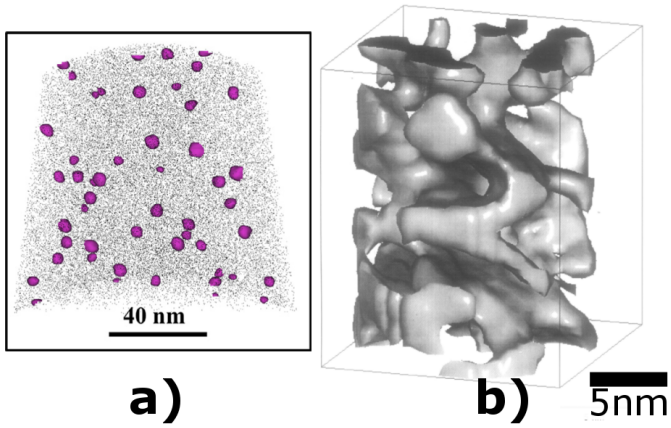


Figure 2.12: a) α' precipitates (purple) within a neutron irradiated Fe-9Cr alloy [43]. b) α' spinodal phase within isothermally aged Fe-45Cr binary alloy [118].

α' phases may take either a spherical [33] or spinodal structure [120], as shown in figure 2.12. The different mechanism arises due to changes in the curvature of the Gibbs free energy with respect to the concentration of Cr, $\frac{d^2G}{d\chi^2}$.

Figure 2.13 shows the section of the Fe-Cr binary miscibility gap belonging to the $\alpha+\alpha'$ region. The areas marked "NG" are metastable and are where α' precipitates form via the nucleation and growth mechanism. Region "S" is enclosed by the spinodal curve and is where α' precipitates form via spinodal decomposition. These are unstable regions.

The spinodal boundaries shown in figure 2.13 are calculated by CALPHAD [100] and are inconsistent with the experimental datapoints overalaid in the Fe rich region. Anomalous datapoints in figure 2.13 are marked and show either spinodal mechaisms occuring in region "NG" or nucleation and growth mechanisms occuring in region "S". Nearly all of the experiments (bar "Lagneborg 1967", "Vintaikin et al.1969" Miyazaki et al. 1974", "Katano and Lizumi 1982", "Furusaka et al. 1986" and "Kuwano 1985") which contribute to figure 2.13 utilise high purity Fe-Cr binary alloys. Unfortunately only

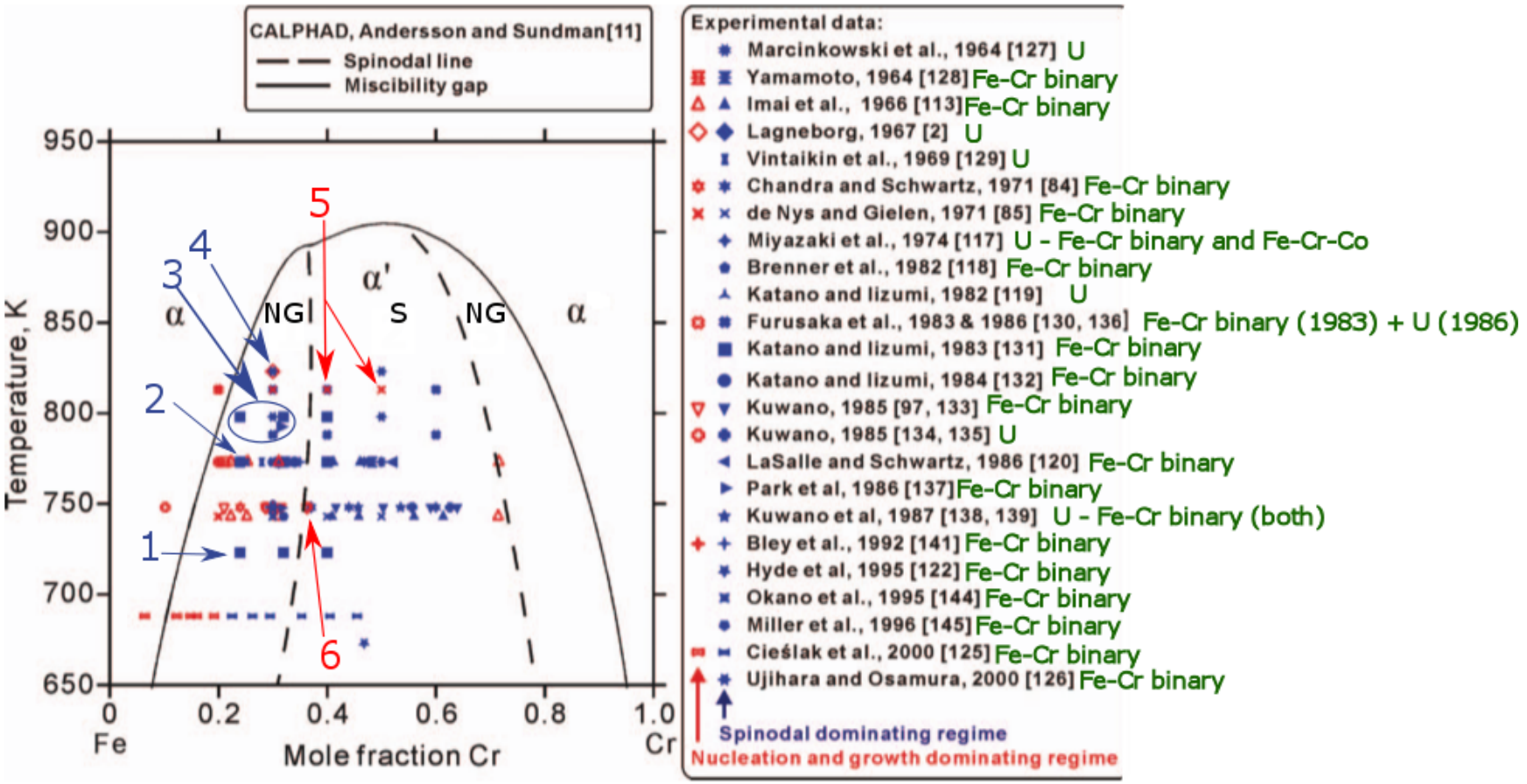


Figure 2.13: The Fe-Cr CALPHAD miscibility gap and spinodal regions in black solid and black dashed lines respectively [119]. "NG" and "S" refer to the nucleation and growth and spinodal regions respectively. Overlaid are experimental observations of α' phases formed via nucleation and growth (in red) and spinodal decomposition (in blue). The reader is referred to the original text for a complete list of the citations in the box on the right side of the figure. Adjacent to the citations are the alloy systems studied in the original publications. "U" means the alloy system studied in the original publication is unknown because the publication was unobtainable. For the case of some publications such as Miyazaki et al. the alloy system was stated in the title. Arrows 1-6 highlight the positions of anomalous data points.

"de Nys and Gielen 1971" presented a full composition of their alloys (Fe-20.10Cr-0.002C-0.021S-0.02Mn-0.030N, Fe-29.75Cr-0.015C-0.019S-0.02Mn-0.025N, Fe-39.45Cr-0.010C-0.013S-0.02Mn-0.02N, Fe-49.60-0.007C-0.010S-0.02Mn-0.02N wt.%). The remaining publications merely state their nominal bulk compositions. Since the anomalous datapoints which are marked from 1-6, are from experiments that utilise high purity Fe-Cr binary alloys, it is unlikely that alloy chemistry is the reason for their divergence from the CALPHAD model. Further investigation into the reason for their divergence is beyond the scope of this review. More generally, the experimental datapoints indicate the nucleation and growth - spinodal boundary in the Fe-rich side should be moved to lower Cr concentrations.

Given the nominal Cr concentration within 14YWT NFA (14wt.%Cr), it is clear that it would reside within region "NG" in figure 2.13. Therefore if the α' phase were to form, it is likely that they would do so via the nucleation and growth mechanism. However the effect the additional alloying elements such as W, Ti and Y within 14YWT have on the phase transformation mechanism is yet to be determined.

Figure 2.14a shows two R_c (the critical radius) profiles for α' precipitates as a function of matrix Cr concentration for an Fe-Cr binary alloy [121]. The two profiles are calculated from two different interface systems modelled. The $\alpha - \alpha'$ interface is one that separates FM/PM magnetic moments, however the model assumes a PM/PM interface for the DLM model and an FM/FM interface for the FM model. The authors, Lu et al. state that the FM model is more representative of the FM/PM interface because Cr atoms inside the α' phase which are near the $\alpha - \alpha'$ interface maintain a FM order [107, 122]. Figure 2.14a shows that R_c quickly falls with increasing Cr content until it reaches a minimum in the spinodal region. Therefore the probability of α' nuclei forming increases with Cr content. Using the same model as that in figure 2.14b and assuming a FM/FM interface R_c is evaluated as a function of temperature for two binary alloys: $Fe_{80}{-}Cr_{20}$

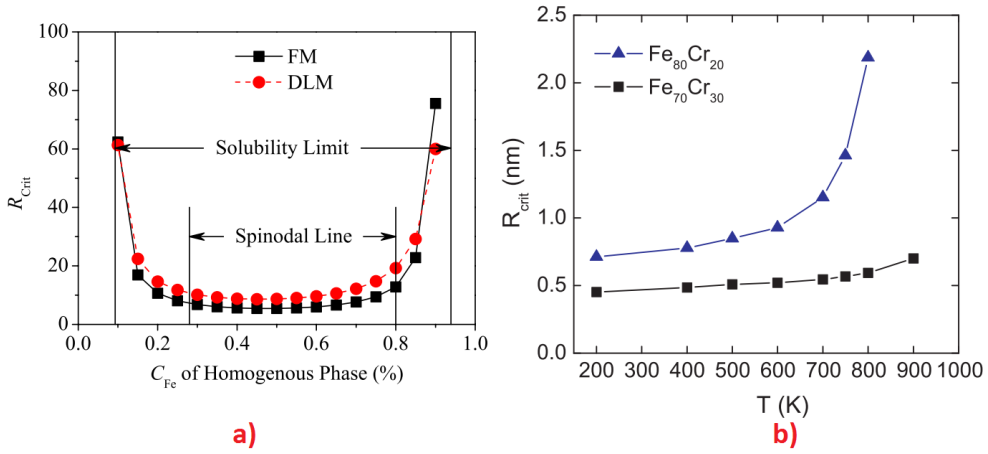


Figure 2.14: a) Critical radius, $R_c\,[\mathring{A}]$ as a function of a homogenous α phase comprised of at $Fe_c - Cr_{1-c}$ at $T = 673K$ [121]. DLM and FM lines are from the models of the PM/PM and the FM/FM α and α' interfaces respectively. Lu et al. state that the FM model is more representative of the actual $\alpha - \alpha'$ interface which is FM/PM. b) Using the same model as a), R_c is evaluated as a function of temperature for $Fe_{80} - Cr_{20}$ and $Fe_{70} - Cr_{30}$ [122].

and $Fe_{70} - Cr_{30}$. It is consistent with figure 2.14a at $T \sim 700K$ and shows that R_c increases exponentially with temperature for the $Fe_{80} - Cr_{20}$ alloy which is metastable at this temperature range i.e. decomposes non-spinodally.

Once nucleated, the precipitate evolves with time and proceeds through intermediate stages before achieving thermodynamic stability [123]. This is exhibited in figure 2.15 which shows the α' precipitate Cr concentration as a function of ageing duration for an Fe-20Cr binary alloy aged at $500°C$. The Cr concentration increases with time and does not achieve equilibrium concentrations of $\sim 80\%$ immediately after nucleation.

The nucleation of precipitates may occur heterogeneously [124] or homogeneously [125]. The former happens when precipitates nucleate on the surface of microstructural features such as grain boundaries, impurities, dislocations, other defect clusters and precipitates [41, 126]. By nucleating on these sinks, the surface energy contribution to the free energy is reduced thus increasing the probability of nucleation [41]. Conversely,

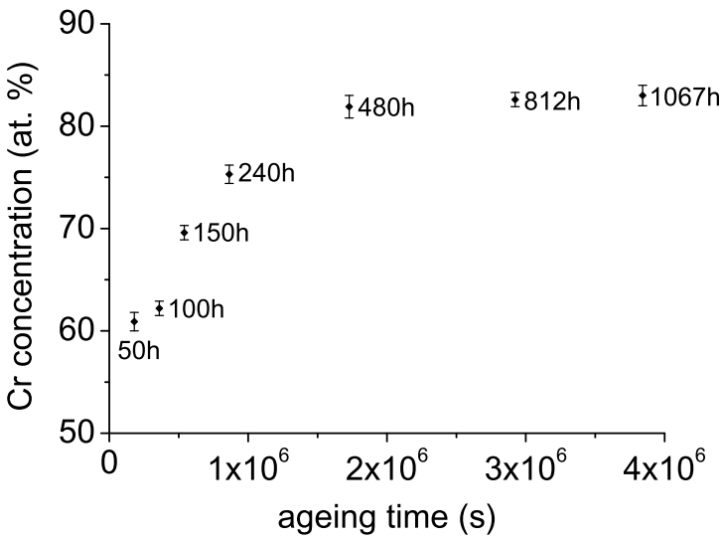


Figure 2.15: α' precipitate Cr concentration as a function of ageing duration for an Fe-20Cr binary alloy aged at 500℃ [33]

homogeneous nucleation occurs away from any surfaces.

2.3.1.4 α' precipitate equilibrium physical characteristics post-ageing

α' precipitates formed within isothermally aged dilute Fe-Cr based alloys are spherical isolated structures, as shown in figure 2.16. They are coherent and have a higher shear modulus ($\Delta G \sim 33GPa$ between pure Fe and Cr crystals [127]) relative to the parent matrix [127].

Table 2.3 presents α' precipitate characteristics from two isothermally aged Fe-Cr binary and two higher order Dispersoid Strengthened Alloys (DSAs). The measured α' precipitate Cr concentration and the matrix Cr concentrations can be seen to vary slightly between the Fe-Cr binary alloys. These variations are attributed to differences in the kinetics of phase separation between the two alloy systems due to varying ageing times and temperatures [33]. The differences in the precipitate and matrix Cr concentrations are much larger in the higher order DSAs. MA956 ODS contains a higher Cr con-

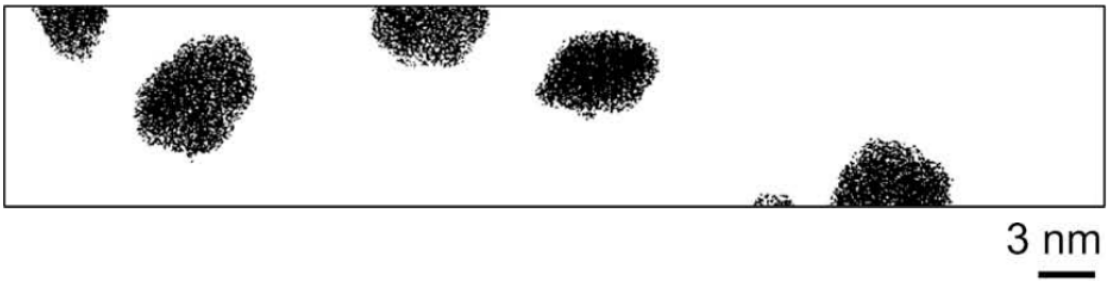


Figure 2.16: APT Cr atom map from an Fe-20Cr binary alloy thermally aged for 1067 hours at 773K [33]. Cr-rich precipitates can be seen to have formed within the alloy's microstructure.

tent which should provide a greater driving force for phase separation to occur, which would translate into faster kinetics [41]. Theories to why phase separation may occur differently are discussed in section 2.3.1.7.

2.3.1.5 α' precipitate influenced mechanical changes

α' precipitates harden and embrittle the alloy they form within [36]. The changes in both of these properties increase with Cr concentration [130, 131], ageing duration [132] and ageing temperature [133].

Table 2.4 shows ΔH_v measurements on DSAs and non-DSAs aged at either $450°C$ or $475°C$. Their grouping is based on their Cr content primarily. After 1000 hours of ageing, at approximately similar temperatures, the DSAs exhibit a lower increase in hardness than their non-DSA counterparts. This difference in ΔH_v between the DSAs and non-DSAs, at durations up to 5000 hours ($\sim$ 208 days), increases significantly, as shown in figure 2.17.

Table 2.5 presents $\Delta DBTT$ data from three separate studies. The SUS340 non-ODS alloy has a similar Cr content to the 15Cr ODS alloy and therefore is considered here as its quasi-non-dispersoid variant. The comparison between the two measurements suggests that DSAs incur a reduced $\Delta DBTT$ relative to non-DSAs. The $\Delta DBTT$

Alloy	Ageing temperature [$^{\circ}C$]	Ageing duration [Days]	α' radius [nm]	α' Cr concentration [at.%]	α' number density [m^{-3}]	Matrix Cr concentration [at.%]	Source
			Fe-Cr binary alloys				
Fe-20at.%Cr binary	500	45	2.53	$83 \pm 1\%$	$\sim 10^{24}$	14	[33]
Fe-21at.%Cr binary	475	125	-	85	-	10	[128]
			Higher order DSAs				
PM2000 ODS (18.5at.%Cr)	475	2.5	9	86	$\gg 10^{22}$	17.0 ± 0.11	[40]
MA956 ODS (20.2at.%Cr)	475	121	-	51.5 ± 0.78	-	13.1 ± 0.43	[129]

Table 2.3: Characteristics of α' precipitates formed in isothermally aged Fe-Cr binary and higher order multiphase alloys. A hyphen is shown to represent unreported data.

Comparison	Alloy	DSA?	Ageing temp. [$°C$]	Ageing duration [hours]	ΔH_v $[kg\,mm^{-2}]$	Source
1	SUS430 (16Cr)	No	475	1000	72	[134]
	15Cr ODS	Yes	475	1000	28	[134]
2	Fe-20Cr model	No	450	1000	125	[132]
	K4 ODS (19Cr)	Yes	475	1000	87	[130]

Table 2.4: Change in Vickers hardness (ΔH_v) within two groups of dispersoid and non-dispersoid strengthened alloys isothermally aged for 1000 hours

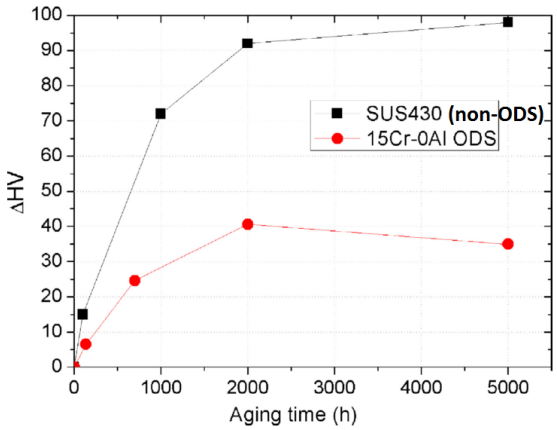


Figure 2.17: Change in Vickers hardness as a function of ageing time for SUS430 (16Cr) and 15Cr-0Al ODS alloys aged at 475$°C$ [134]

measured from the aged PM2000 and MA956 is much higher than that of the 15Cr ODS and the SUS430 despite the reduced ageing duration. This is probably due to it's

Alloy	$\Delta DBTT$ [$^{\circ}C$]	Ageing temp. [$^{\circ}C$]	Ageing duration [Hours]	Source
15Cr ODS	+40	475	2000	[135]
SUS340 non-ODS (16Cr)	+62	475	2000	[135]
PM2000 ODS (20Cr)	+110	475	500	[136]
MA956 ODS (19Cr)	∼+200	475	1000	[137]

Table 2.5: $\Delta DBTT$ data from isothermally aged alloys

higher Cr content which would increase the driving force for separation in the alloy. Studies that do report microhardness and $\Delta DBTT$ data are purely mechanical property studies and fail to verify whether the α' phase has formed in the microstructure e.g. [137]. Such studies tend to assume that the low-temperature ageing will inevitably form α' and the increase in hardness they measure, for example, is due to the formation of this phase. However, it is possible that other phases or precipitates form in these conditions e.g. $M_{23}C_6$ or σ phases [138].

In addition, it is difficult to deconvolute hardening contributions from solid solution strengtheners within each of the subject alloys from the publications e.g. [132]. This is especially important given that Al additions within an aged Fe-Cr based alloy increases the strain within its crystal structure [139]. This often results in an increase in hardness.

2.3.1.6 α' precipitate interactions with dislocations

α' precipitate-dislocation interactions are linked to hardness and embrittlement properties [140] and are influenced by: α' characteristics such as Cr concentration, radius and number density; dislocation properties and the temperature of the system [141].

α' precipitates are characterised as repulsive, oversized and coherent obstacles ($a_{Fe} = 0.28553nm$, $a_{Cr} = 0.2878nm$ [127]) [142]. They are repulsive because the shear modulus within the precipitate is higher than the alloy matrix (shear modulus misfit, $\Delta G \sim 33GPa$) [127, 143, 144]. Therefore, as the dislocation moves closer to the precipitate, the resolved shear stress, τ, required by the dislocation to glide increases.

The literature contains results from Molecular Dynamics (MD) simulations of pure edge and pure screw dislocations interacting with pure (100at.%) Cr precipitates [127, 145]. These simulations are qualitatively consistent with the particle shearing model [146, 147]. Two general trends emerge from these works [127, 145]: 1) the largest contribution to phase separation induced hardening and embrittlement come from the Edge Dislocation (ED)-α' precipitate interactions; 2) Cr precipitates of size below 2-3 nm are weak shearable obstacles. These general trends have been confirmed by studies that have applied both the dispersed barrier hardening [140, 148] and single crystal models [149], to experimental data.

However, the simulations utilise pure 100% Cr precipitates. Therefore mechanical data from these studies e.g. τ_c (critical stress) are likely to be inconsistent with experiments, because obstacle strength decreases with precipitate Cr concentration [145]. τ_c is also highly dependent on the potential used in the MD simulations and varies significantly [144, 150]. No studies on mixed type dislocation-α' precipitate interactions have been conducted and reported.

2.3.1.7 α' formation within higher order dispersion strengthened Fe-Cr based alloys

The free energies of higher order DSAs, such as those in table 2.6, may differ from that of an Fe-Cr binary alloy [154]. If this difference in the free energy is significant, then the conditions required for secondary phases to form, e.g. α', may also alter [155]. As

	Cr	Al	Ti	W	Y	O	Mo	C	
PM2000	18.60	5.20	0.54	-	0.39	0.09	-	-	[40]
K2	13.64	4.12	0.28	1.65	0.30	0.08	-	-	[151]
MA956	19.93	4.75	0.39	-	0.40	0.11	-	0.02	[152]
MA957	14.20	-	1.07	-	0.20	0.05	0.31	-	[153]
14YWT	13.86	-	0.19	2.59	0.21	0.19	-	-	Table 3.3

Table 2.6: Bulk concentrations of the main alloying elements within PM2000, K2, MA956 and MA957 in wt.%. The concentrations for 14YWT from table 3.3 is copied here for convenience. Impurity elements are present in PM2000, K2 and MA957, and 14YWT, but are not shown here.

such, the phase diagrams belonging to these higher order DSAs may also differ from that of the Fe-Cr binary system [41].

The change observed in the free energy and the phase diagram is highly dependent on the element that has been introduced and its concentration within the alloy. There are works in the literature which were originally published in the 1950-1980s that attributed varying low-temperature phase separation behaviour within non-DSAs, to elements such as: C [156], Ni [157], Mo [36, 158, 159], Ti [36, 159], Nb [159], Si [156] and Co [160]. However, no follow-up investigations were conducted to investigate the effects these elements had on the α' phase formation energies, α'-matrix interfacial energies or free energies of the alloy systems.

More recently, the influence Al has on the phase diagram of a PM2000 ODS alloy has been investigated [38]. Figure 2.18 shows three miscibility gaps for three different alloy systems. Table 2.6 shows that the three main matrix elements in PM2000 are Fe, Cr, Al and Ti. The thermodynamic effect these elements have on PM2000's miscibility gap has been modelled in three different alloy systems: Fe–Cr, Fe–Cr–$11at.\%Al$ and

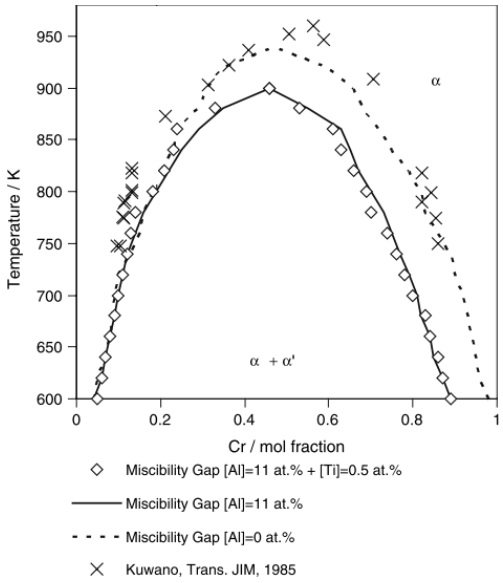


Figure 2.18: The miscibility gap for $Fe{-}Cr$, $Fe{-}Cr{-}11at.\%Al$ and $Fe{-}Cr{-}11at.\%Al{-}0.5at.\%Ti$ systems modelled using the SGTE database adapted from [38]. The experimentally observed miscibility gap for an Fe-Cr binary alloy system obtained from [161] is represented by the crosses.

Fe–Cr–$11at.\%Al$–$0.5at.\%Ti$ [38]. Overlaid on figure 2.18 is the experimentally observed miscibility gap for Fe-Cr binary alloy taken from the experiments conducted by [161]. The model predicts that the addition of $11at.\%Al$ to an Fe-Cr system will reduce the critical temperature of the spinodal region (the height of the miscibility gap), and moves the higher Cr concentration miscibility gap boundary to a lower Cr concentration, i.e. from close to $\sim 100\%Cr$ to $\sim 90\%Cr$. This reduces the area of the thermodynamically unstable region and increases the area of the α phase region. Therefore $11at.\%Al$ can be regarded as an α phase stabiliser. Conversely adding Ti to the $Fe{-}Cr{-}11at.\%$ system had no considerable influence on the miscibility gap. This is probably because the concentrations of Ti are significantly lower.

Experiments have shown that Al within an Fe-Cr binary system generally: retards the onset of α' precipitate formation [162], slows down precipitate coarsening [134], and

contrary to the model in figure 2.18, shifts the miscibility gap to higher Cr concentrations [163]. This is because Al increases the α' precipitate formation energy and its interfacial energy [122]. In 2010, Kobayashi et al. [163] reported experimental results that indicated that alloys containing $<2at.\%Al$ promoted phase separation whereas those containing $>2at.\%Al$ suppressed phase separation. More recently, Han et al. have reported that the Cr/Al ratio, and not the absolute concentration of Al present in the alloy like Kobayashi suggested, influences phase separation [134]. This claim is supported by

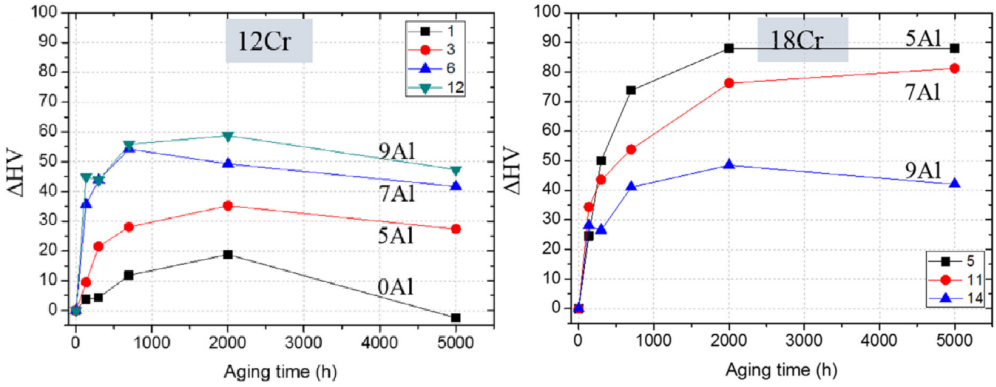


Figure 2.19: Vickers hardness tests on a) 12Cr ODS and b) 18Cr ODS alloys aged at $475°C$ [134].

figure 2.19, which shows data from Vickers hardness tests on isothermally aged 12Cr and 18Cr (wt.%) ODS alloys at $475℃$, with three different concentrations of Al: 5, 7 and 9 wt%. The 12Cr ODS alloy with 9wt.% Al hardens the most whereas the 12Cr ODS alloy with 5wt.% hardens the least. The 18Cr ODS alloy shows the opposite trends as the 5wt.% Al hardened the most while the 18Cr ODS alloy with 9wt.% Al hardened the least. TEM studies were only conducted on the aged 18Cr ODS alloy with $5wt.\%$ and $9wt.\%$ Al and not on the 12Cr ODS alloy. The aged 18Cr ODS alloy with 5wt.% Al was observed to contain α' precipitates, as shown in figure 2.20, while the aged 18Cr ODS alloy with 9wt.% Al did not form any. No TEM data on the isothermally aged 18Cr ODS alloy with 9wt.% Al was published.

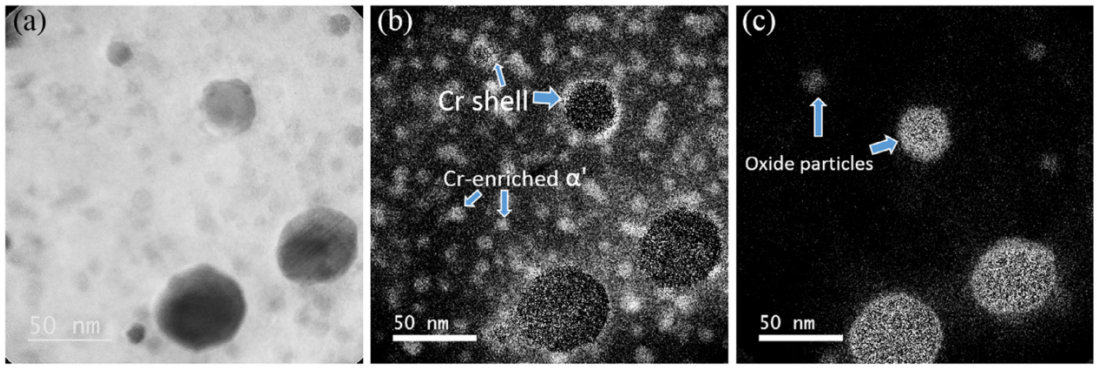


Figure 2.20: TEM images of isothermally aged 18Cr-5Al for 500hours at 475℃ [134]. a) is a bright field image b) is an EELS map of Cr and c) is an EELS map of O. The sample can be seen to contain a high number of α' precipitates.

Han et al. remain to be the only group that have suggested that the Cr/Al ratio influences the formation of α' precipitates in ODS alloys. Despite this, it demonstrates that various combinations of elements can affect the free energy differently. Ergo, there is no simple criterion, such as that initially suggested by Kobayashi et al. [163], to predict if a particular element can impede or enhance α' precipitation in Fe-Cr based alloys.

The free energy of higher order alloy systems, such as those in table 2.6, may allow for tertiary metastable phases to form in parallel to the α' phase. Observations of tertiary phases formed within non-DSAs exposed to low-temperature environments are ubiquitous in the literature, e.g. Ni and Si-rich intermetallic G phase [164], Carbides [165] and Laves phases [131]. The literature also suggests that tertiary phases can influence secondary phases e.g. the G phase can retard the onset of spinodal decomposition [157] and that carbides may promote the formation of the σ phase [166] e.g. in [138].

In contrast, only one publication has reported the presence of tertiary phases within a DSA in the literature. The β' intermetallic has been observed to form within PM2000 ODS aged at 475℃, and is shown in figure 2.21 [39]. Rich in Al and Ti, this intermetallic

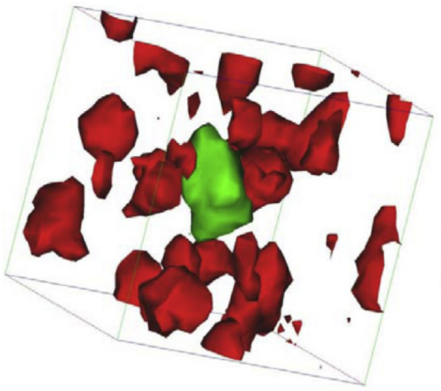


Figure 2.21: APT isoconcentration surface map of Cr (red) and Ti+Al (green) [167]. The concentration thresholds used are 30at.% for Cr and 25at.% for Al+Ti. The β' phase is the green object in the sampled volume.

is not shown in the miscibility gap in figure 2.18, which was produced using the SGTE thermodynamic database, and is not predicted.

During the growth phase of the α' precipitates, partitioning of particular elements away from the Cr-rich α' zone and towards the α matrix can occur in higher order alloys. This phenomenon has been observed within two dispersion strengthened alloy systems, which were both aged at 475℃ for varying durations: MA956 [168] and PM2000 [39]. In both of the aged alloys, Al was seen to partition away from the α' precipitate and into the matrix. Interestingly, Al partitioning was much slower in the MA956 than that seen in the PM2000 alloy. After 2900 hours of ageing, κ_{Al}, the Al partition coefficient, in MA956 was measured to be $\kappa_{Al} = 1.70 \pm 0.19$, whereas the PM2000 had a partition coefficient $\kappa_{Al} = 3.6$ after 2040 hours of ageing [40]. Ti was also seen to partition away from the α' precipitate zone in the PM2000 and $\kappa_{Ti} = 4.0$ after the 2040 hours of ageing. No partitioning of Ti was reported in the MA956 even though it contains similar concentrations of this element.

Partitioning is highly dependent on solute-solute interactions, initial bulk concentrations within the alloys of interest and the temperature of the environment [169]. This is why

the partitioning behaviour observed in MA956 [168], PM2000 ODS alloys [39] and higher order DSAs listed in table 2.6, are likely to differ.

Interactions between different elemental species in a higher order alloy are important to consider [169]. Therefore observations from a low-temperature study of a particular higher order DSAs are unlikely to be the same for another. There are no experimental observations in the literature that state whether 14YWT NFAs succumb to α' precipitate formation, tertiary phase formation and solute partitioning. There has been an acknowledgement that matrix elements other than Fe-Cr such as Ti and residual Y can affect the formation of α', including the interfacial energies, in a similar way Al has done [134]. Despite this, no theoretical calculations on the effects of W, Ti, Y and other impurity elements will have on the formation of the α' phase, have been conducted. Nor is there data from models to predict the partitioning behaviour of these elements within 14YWT. As such, it is challenging to predict whether Ti and W will partition in the same way as Ti and Al have done in the aged PM2000 ODS [40].

2.3.2 Segregation of alloying elements at low-temperatures

Between $300-500°C$ in non-irradiation environments, alloying elements can segregate to sinks such as GBs [170], dislocations [171] and phase boundaries [172], via vacancy mediated diffusion [41, 173]. The degree of segregation is dictated by the diffusion coefficient, D and at $500°C$ within Fe-20Cr alloys, Cr has a $D_{Cr} = 3.2 \times 10^{-19} cm^2\, s^{-1}$ [174].

Segregation within DSAs has only been reported to occur after consolidation via extrusion and not as a result of long-term low-temperature or high-temperature ageing treatments [170, 171]. Figure 2.22a shows that W, Cr, C and N have segregated at a GB within an as-received 14YWT sample. Figure 2.22b shows segregation of Cr, W, B and C at a dislocation within as-received 12YWT NFA. 14YWT and 12YWT were

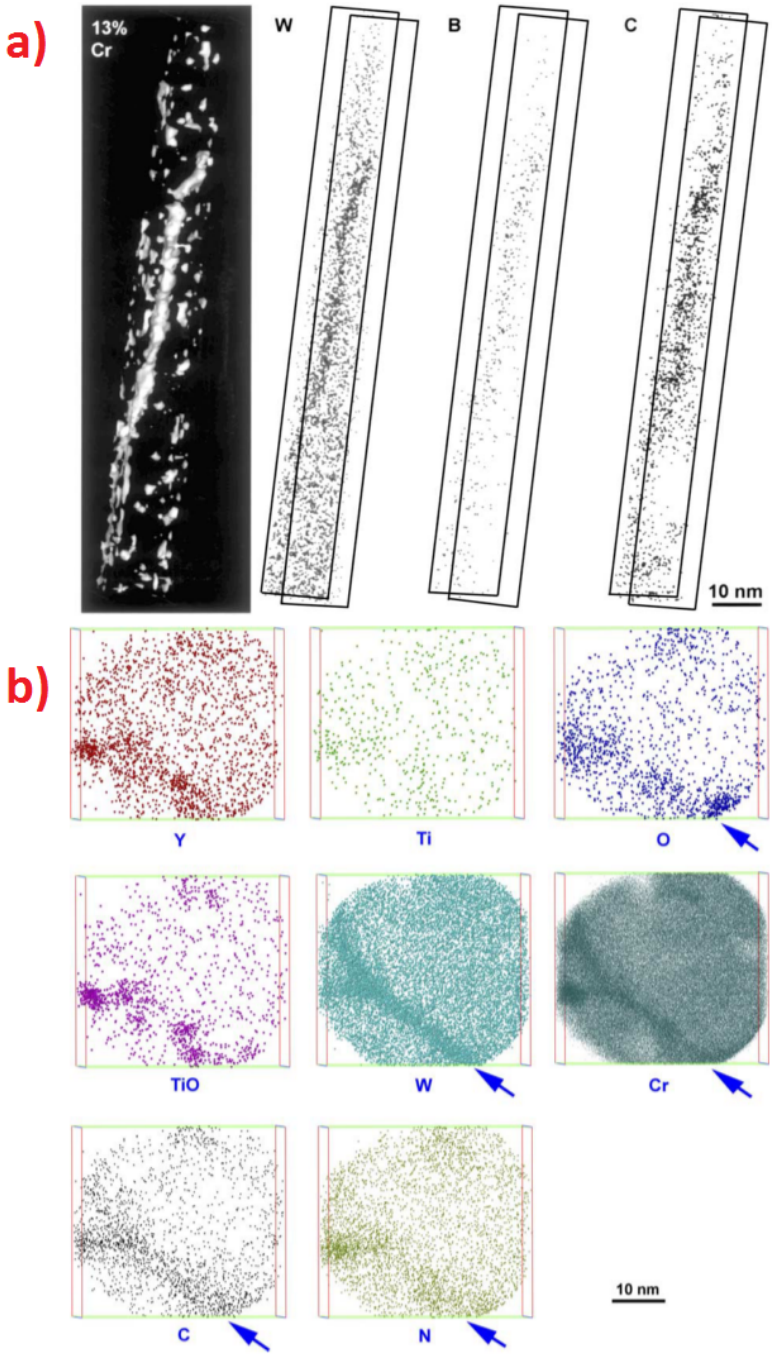


Figure 2.22: Atom probe maps of as-received a) 14YWT NFA [170] and b) 12YWT NFA [171]. a) depicts segregation of W, Cr, C and N at a GB within as-received 14YWT . b) depicts segregation of Cr, W, B and C at a dislocation captured in the sample volume.

consolidated via extrusion at $850°C$ and $1150°C$ respectively. No Gibbsian Interfacial Excess (GIE) data were reported in these publications and there was no mention of whether solutes had segregated to dispersoid surfaces.

2.3.3 NFA dispersoid thermal stability

14YWT's dispersoids are metastable and have high activation barrier energies to coarsening [175, 176] due to their highly defective structures [75]. Dispersoids within $Fe-14Cr-1W-0.3Ti-0.3Y_2O_3$ exposed to $600°C$ for 5000 hours changed from an "unknown" FCC form to an FCC $Y_2Ti_2O_7$ with Cr outer shells [175]. The Cr shells form because of the strong repulsive interaction between Cr and Ti atoms [76] which makes Cr insoluble within a Y-Ti-O system [176, 177]. Ageing this alloy at $1300°C$ however, did not bring about the same changes. No Cr shells were observed to have formed as a result of this higher temperature. This is probably because the Cr shell dissolves into the surrounding matrix [175].

Dispersoids have a high coarsening activation energy [72, 178] because Y and Ti atoms are significantly larger than Fe atoms and therefore, diffuse slowly through the predominantly Fe matrix [94, 179]. At high-temperatures dispersoids coarsen via the Ostwald ripening mechanism.

Coarsening rates for dispersoids containing Al, such as those in the Japanese K-series alloys are higher [180, 181] than dispersoids that do not e.g. 14YWT [170]. This is because Al can diffuse through the alloy matrix more quickly [182].

W within the matrix is thought to reduce the dispersoid coarsening rate [170]. W binds to O atoms in the ferrite matrix and this bond would have to break for O to deposit onto the surface of the dispersoid. However, this is not energetically favourable as the energy barrier is very large [170].

There are no publications that seek to directly compare the coarsening rates between

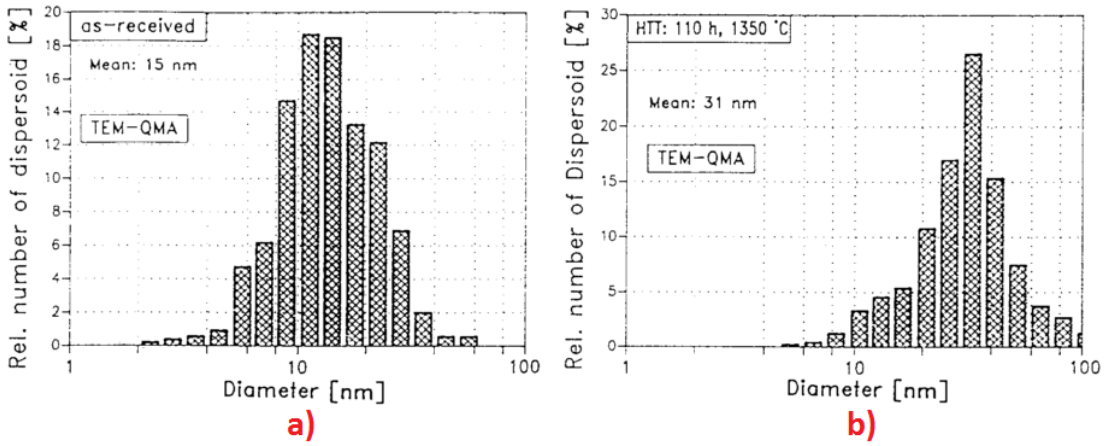


Figure 2.23: Dispersoid radius distributions within PM2010 ($20Cr-5.5Al-0.5Ti-1.0Y_2O_3$) a) as recieved and b) isothermally aged at 1350°C for 110 hours [182]

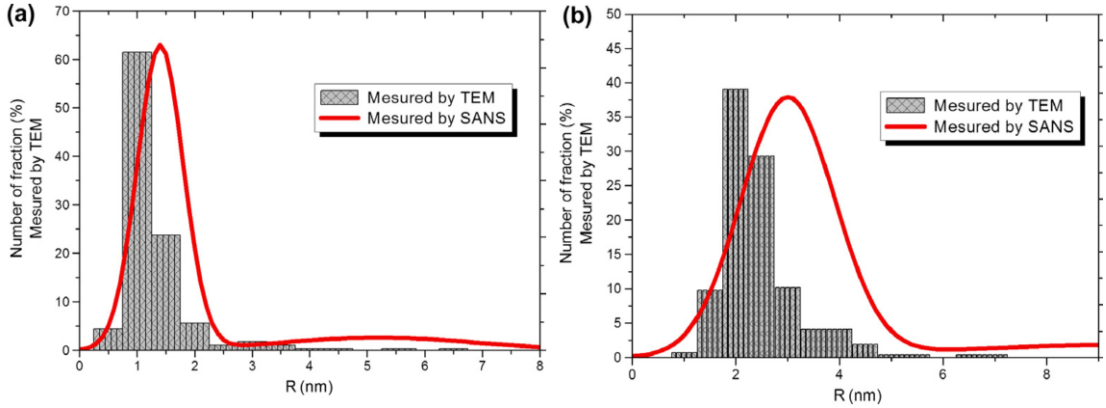


Figure 2.24: Dispersoid radius distributions within J27M2 ($14Cr-1W-0.3Ti-0.3Y_2O_3$) a) as received and b)isothermally aged at 1400°C for 1 hour [183]

alloys containing dispersoids composed of Al and those without. However data from two separate studies that determine dispersoid radius distribution within isothermally aged PM2010 ($20Cr-5.5Al-0.5Ti-1.0Y_2O_3$) and J27M2 ($14Cr-1W-0.3Ti-0.3Y_2O_3$) at 1350°$C$ and 1400°C respectively are presented in figures 2.23 and 2.24. The dispersoids in the as-received PM2010 are coarser than those in J27M2. As the ageing

durations are not equivalent, a growth rate has been estimated by taking the difference in the modal values from each measurement for each alloy and dividing it by the total ageing duration. The rates for PM2010 and J27M2 are roughly $0.16\,nm\,hour^{-1}$ and $1\,nm\,hour^{-1}$ respectively. While the J27M2 alloy has been aged at a temperature that is higher by $50°C$, it is clear that its dispersoids coarsens more quickly than that of PM2010. Ribis et al. report a coarsening rate of 2.2nm/hour in a 14YWT variant ($Fe-14Cr-1W-0.3Ti-0.3Y_2O_3$) aged at $1300°C$ [175].

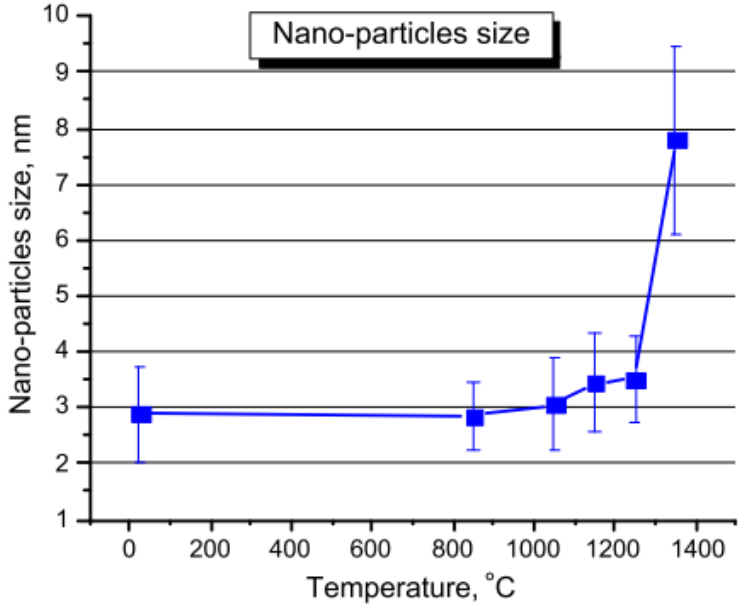


Figure 2.25: Dispersoid average size as a function of annealing temperature from an isochronal ageing experiment [178]. The subject alloy was an RAF alloy with the following composition: $14Cr-2W-0.3Ti-0.3Y_2O_3$. Annealing durations were for 1 hour.

This data indicates the theories proposed in [170, 182], that W inhibits coarsening, may be incorrect. However, J27M2 and the 14YWT variant used by Ribis et al. contain 1 wt.% nominal quantity of W suggesting a larger quantity of W is needed.

Studies on dispersoid low-temperature coarsening are even fewer in number relative to

their high-temperature studies. Lee et al. reported no change in terms of dispersoid number density or their size within K-series alloys (contains 4 wt.% Al) isothermally aged at $475°C$ for 1000 hours [130]. This is congruent with figure 2.25, which shows dispersoid diameters within an isochronally aged RAF alloy (composition is $14Cr$–$2W$–$0.3Ti$–$0.3Y_2O_3$). As can be seen, no coarsening occurs below $800°C$. Dispersoids at low-temperatures are expected to be stable given the high activation energy for coarsening that is required.

2.4 An overview of irradiation damage

Ballistic collisions between incident energetic particles and lattice atoms causes radiation damage. If the incident particle transfers a quantity of energy equal or greater than the displacement energy (E_d), lattice atoms are displaced and a Primary Knock on Atom (PKA) is created [126]. E_d is dependent on the crystallographic direction and lower indices have a lower E_d and vice versa. $\bar{E_d}$ for Fe is 38.9eV and that for Cr is 46.2eV [184, 142]. The incident particle continues to create PKAs until its kinetic energy, $(T) < E_d$ [126]. This all occurs within the the displacement cascade zone. Meanwhile, the PKAs also travel through the lattice displacing other atoms until $T_{PKA} < E_d$. T_{PKA} for fusion environments can be as high as 1MeV [185] and $\bar{T_{PKA}} = 487keV$ [186, 187]. T_{PKA} for fission environments can be as high as 200keV [188] and $\bar{T_{PKA}} = 10keV$ [189]. This concludes the 1st phase known as the ballistic phase which lasts $\sim 0.2ps$ [190].

Lattice atom displacements creates two types of point defects: an SIA and a vacancy [191]. A thermal spike occurs in the cascade zone as the PKAs comes to rest, which increases temperatures close to the melting point. As depicted in figure 2.26a and 2.26b, vacancies form a dense core while the SIAs gather around them. These events are referred to as the relaxation phase, which lasts for roughly 0.5ps [190].

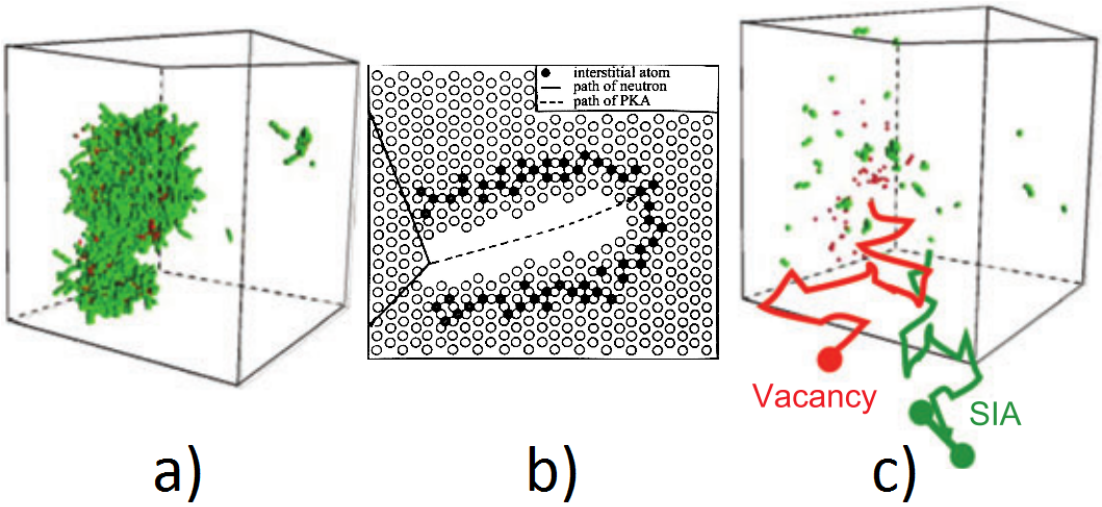


Figure 2.26: a) Schematic depicting a displacement cascade consiting of point defects: SIAs, and Vacancies [29]. b) Schematic showing a cross section of a cascade zone during the thermal spike. It consists of a vacancy dense core surrounded by SIAs [192]. c) After the cascade zone has cooled, the vacancy core collapses and a population of cascade surviving defects remain [29].

During the cooling phase, which lasts a few ps, the vacancy core collapses, and $\sim$90% of the SIAs recombine with vacancies [29]. The cascade zone reaches thermal equilibrium with the matrix and a fraction of defects remain as seen in figure 2.26c. These are the cascade surviving defects and they are responsible for the radiation induced changes to the microstructure.

Nuclear reactions can also occur within fission and fusion environments and generate transmutation products and α, β or γ radiation [193, 194]. Examples of these nuclear reactions in the format $target(projectile,light\,products)heavy\,products$ are shown in equations 2.1, 2.2, 2.3 and 2.4 [195]. In an ITER-like device, Fe-Cr alloys are expected to produce He and H at a rate of 11.4 appm dpa^{-1} and 44.5 appm dpa^{-1} respectively [13]. He is insoluble in Fe and may form bubbles [196, 197, 198] that cause embrittlement [96, 97]. Dispersoids within DSAs trap He at the matrix-dispersoid inter-

face [199] and create finer and more distributed He bubbles, and reduce He concentrations at GBs [45]. H can bind to point defects and He bubbles, causing embrittlement and reductions to the alloy's toughness [200, 201].

$$^{56}\mathrm{Fe}\,(n,p)^{56}\,\mathrm{Mn} \tag{2.1}$$
$$^{56}\mathrm{Fe}\,(n,\alpha)^{53}\,\mathrm{Cr} \tag{2.2}$$
$$^{50}Cr\,(n,\gamma)^{51}\,\mathrm{Cr} \tag{2.3}$$
$$^{58}Ti\,(\alpha,\gamma)^{52}\,\mathrm{Cr} \tag{2.4}$$

2.4.1 Quantifying irradiation dose

The average number of dpa quantifies irradiation dose [126, 202]. It is not a measure of damage, as it does not account for the recombination of initially-produced defects, and hence the fraction of these surviving defects that form visible and effective damage. 1 dpa means every atom within a given volume has been displaced on average once and the Kinchin and Pease (KP) model is used to calculate this metric [203]. A mathematical representation of this model is given by equation 2.5 and is shown pictorially in figure 2.27. This model is implemented in the SRIM software written by Zeigler [204] and is utilised ubiquitously in the literature. The software only models the ballistic phase and assumes: collisions are elastic, the target material is amorphous and resides at 0K, and ignores channelling.

$$\nu(T) = \begin{cases} 0 \; for \; T < E_d \\ 1 \; for \; E_d < T < 2E_d \\ \frac{T}{2E_d} \; for \; 2E_d < T < E_c \\ \frac{E_c}{2E_d} \; for \; T \geqslant E_c \end{cases} \tag{2.5}$$

$\nu(T)$ is the number of displacements as a function of kinetic energy, E_c is the critical energy for ionisation which is 7.1keV for Fe [205].

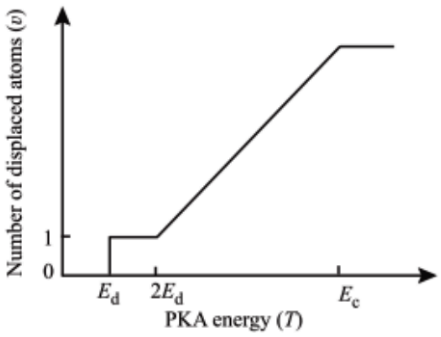


Figure 2.27: The number of displaced atoms as a function of incident particle energy [126]

The displacement rate can be determined by equation 2.6.

$$R_d = N \int_{E_1}^{E_2} \phi(E)\sigma_D(E)dE \tag{2.6}$$

N is the number density of atoms, $\phi(E)$ is the particle flux as a function of energy E, $\sigma_D(E)$ is the displacement cross section which is calculated by equation 2.7.

$$\sigma_D(E) = \int_{T_1}^{T_2} \sigma(E,T)\nu(T)dT \tag{2.7}$$

$\sigma(E,T)$ is the differential energy transfer cross section, $\nu(T)$ is defined in equation 2.5. The total number of displacements occurred can be calculated by substituting for N and t (irradiation duration), into equation 2.8.

$$dpa = \frac{R_d t}{N} \tag{2.8}$$

2.4.2 Ionised particle energy loss mechanisms

Energy transfer from an irradiating particle to lattice atoms is dependent on its net charge. Neutrons are charge neutral and therefore transfer energy by direct elastic

ballistic collisions only. Ions have a non-zero net charge and transfer energy via three processes: 1) Bremsstrahlung ("braking energy") (r), 2) electron excitation (often referred to as electron stopping) (e) and 3) elastic collisions (n). The total loss of energy per unit length from charged particles is defined by the contributions from each of these three processes, shown in equation 2.9.

$$\left(-\frac{dE}{dx}\right)_{total} = \left(-\frac{dE}{dx}\right)_{r} + \left(-\frac{dE}{dx}\right)_{e} + \left(-\frac{dE}{dx}\right)_{n} \tag{2.9}$$

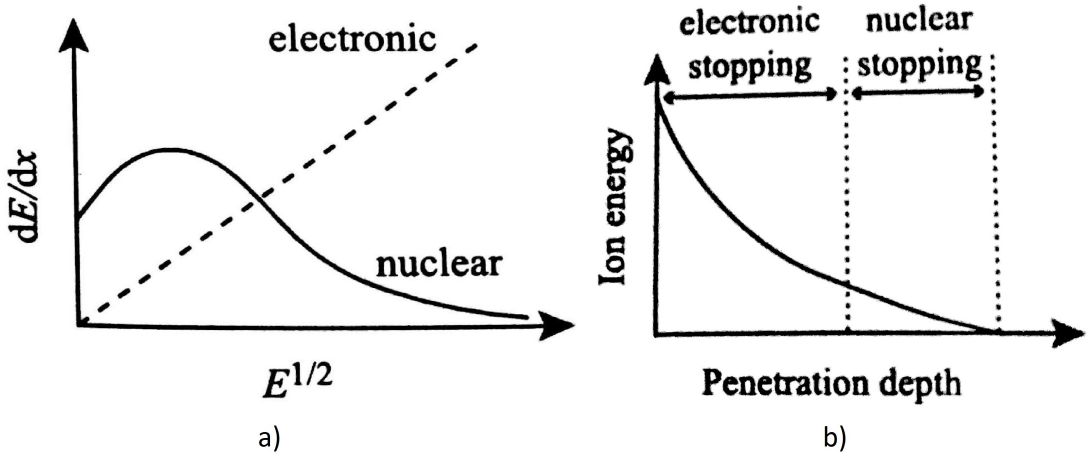


Figure 2.28: a) Nuclear and electronic stopping powers over an energy range that is relevant to ion-solid interactions [126]. b) Energy range of an energetic ion incident to a target material and the dominance of the electronic and nuclear stopping regimes [126]

Energy loss from Bremsstrahlung is negligible. Electron stopping refers to inelastic interactions between the incident irradiating particle and valence or free electrons within the lattice atom. This can excite the bound electrons or the electron cloud of the irradiating ion. Nuclear stopping refers to elastic collision interactions between incoming ions and the target nuclei.

Figure 2.28a, shows energy loss from electron stopping dominates at higher energies, whereas nuclear stopping dominates at lower energies. Therefore, incoming energetic ions will incur energy loss from electron stopping at low penetration depths as shown in figure 2.28b. At higher penetration depths, ions incur energy losses that ensure nuclear stopping dominates. For example SRIM predicts a 10keV Fe^+ in Fe loses 7% of its energy mainly via nuclear stopping, whereas a 500keV Fe^+ loses 69% mainly via electron stopping [206].

2.4.3 Simulation of fusion radiation

A fusion neutron source is not available, therefore surrogate irradiation sources are required [207]. Irradiation can be simulated by using fission-spectrum neutrons [208], heavy ions [195], protons [196] and electrons [209].

Charged particle irradiation is advantageous over fission neutron irradiation [210]: charged particle implantations achieve high dose rates, samples are not radioactive and are cheap. However, this technique produces a thin, spatially non-uniform damage layer; and transmutation products are not generated either. Interstitials are introduced which alter the microchemistry and can inhibit irradiation induced phenomena e.g. swelling [211].

Fission neutron irradiated samples can generate transmutation products and create a deep, mm-scale, spatially uniform damage layer. They are very expensive to conduct, and specialised equipment is required to handle the radioactive samples. Irradiation occurs at low dose rates, and therefore experiments can take years.

Neutrons generated from fission reactors have a broad energy spectrum as shown in figure 2.29. Ions are produced in accelerators and are monoenergetic beams with narrow energy widths.

Ion irradiation parameters such as beam energy, fluence and number of overlapping

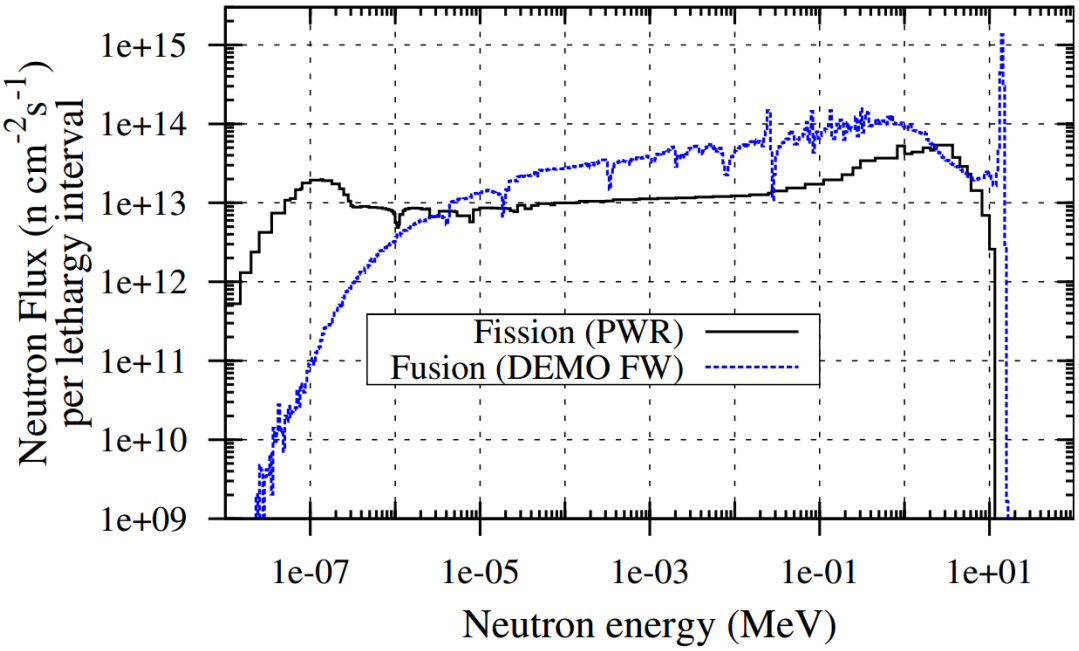


Figure 2.29: The energy spectrum of neutrons produced within a fission PWR reactor and a fusion DEMO tokamak [194]

beams can be adjusted to provide an equivalent maximum irradiation dose in terms of dpa.

Ion and neutron irradiation comparative studies have observed differences. Irradiation induced hardening within a neutron irradiated Fe-6Cr was +5GPa whereas the ion irradiated material was $\sim +3GPa$ [212]. Neutron irradiated Ni had a peak swelling temperature of $400^{\circ}C$ whereas Ni^{+} irradiated specimen had a peak swelling temperature of$\sim 600^{\circ}C$ [213]. Microchemical related phenomena cannot be simulated straightforwardly with ion implantation experiments either [214].

The different responses to ion and neutron irradiation arise because the fraction of surviving defects vary as a result of the: different PKA recoil spectrums, cascade morphologies and defect densities [215]. Dose rate effects occur too [195].

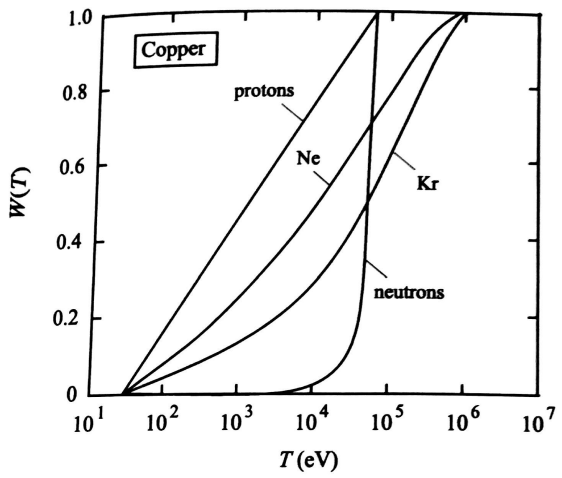


Figure 2.30: The weighted recoil spectra for 1 MeV particles in pure Cu [126]

2.4.3.1 Variations in the PKA spectrum

The mass and T of the incident irradiating particle influences the number of PKAs created and their T_{PKA}. T_{PKA} influences the creation of point defects and their mobilities. A weighted primary recoil spectra shows the fraction of defects produced from the primary recoils that have a particular energy as shown in figure 2.30 [126]. Ions tend to create PKAs with lower energies while neutrons create a larger proportion of PKAs with higher energies [216]. Heavy ions seem to replicate the energy distribution of recoils created by neutrons. But at the extremes of the range of T, neither the light or the heavy ions produce the fraction of recoil energies adequately.

Cascade zone volumes are directly related to T_{PKA} [217]. Figure 2.31 shows that higher T_{PKA} produce larger cascade volumes. For $E_d < T_{PKA} < 2.5E_d$, isolated Frenkel pairs are produced [216]. As T_{PKA} is increased, multiple SIAs and vacancies are distributed in the form shown in figure 2.26b. When $T_{PKA} > 20keV$ in Fe, sub-cascades form [187, 218] and the total energy is distributed between sub-cascades as exhibited in figure 2.31b. Experiments show that Au irradiated with 14MeV neutrons [217] produces subcascades

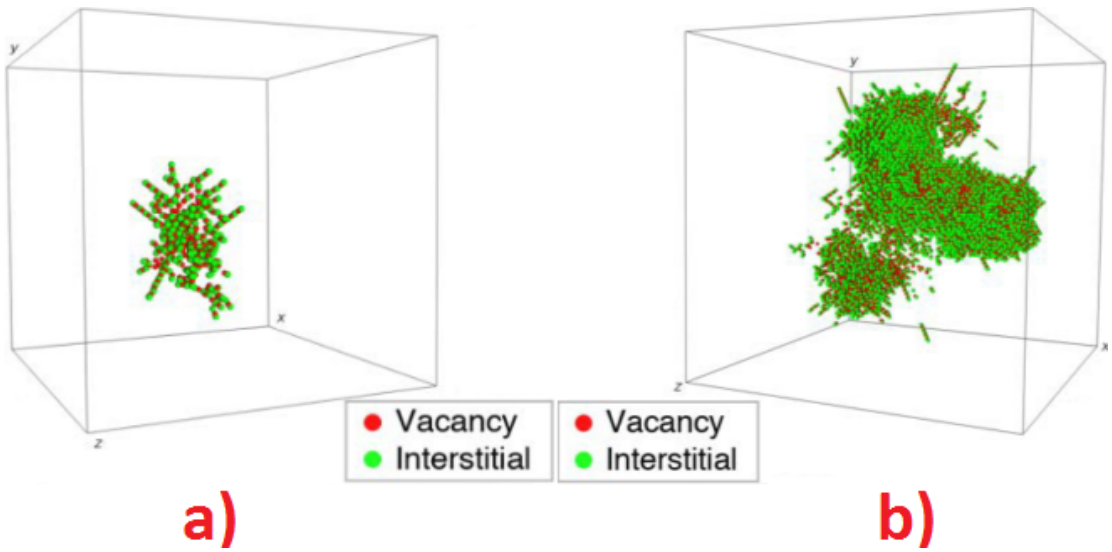


Figure 2.31: MD simulation of a cascade initiated by a a) 1keV and b) 20keV PKA in pure Fe at the height of the thermal spike [219, 220]

with average energies of 17keV [217].

As the cascade volume increases, so does the defect population [184, 187, 221, 222, 223] and density [224, 225]. In-cascade recombination rate increases within larger cascades and reduces ϵ, the number of surviving defects [216]. ϵ is a function of T_{PKA} and decreases with increasing T_{PKA} [226]. For the case of Au irradiated with 14MeV neutrons, given above, $\epsilon \sim 0.13 - 0.25$ [217].

Higher irradiation temperatures increase the intracascade recombination rate and reduces ϵ. $\epsilon \sim 0.33$ for a cascade initiated $T_{PKA} = 10keV$ at 100K in Fe, whereas at 900K, $\epsilon \sim 0.26$ [219]. For $E_{PKA} \geqslant 20keV$ in pure Fe and Fe-10Cr, ϵ tends to plateau around 0.2-0.3, as seen in figure 2.32 [220, 221] because of subcascade formation [184, 221, 223, 227].

During the cooling phase, like-defects cluster within high energy displacement cascades. As irradiation temperature and cascade energies increase, there is a greater tendency for interstitial clustering [228]. In pure Fe, 40% of interstitials produced within cascades with energies of 10keV at 100K were clustered. At 900K this increased to nearly

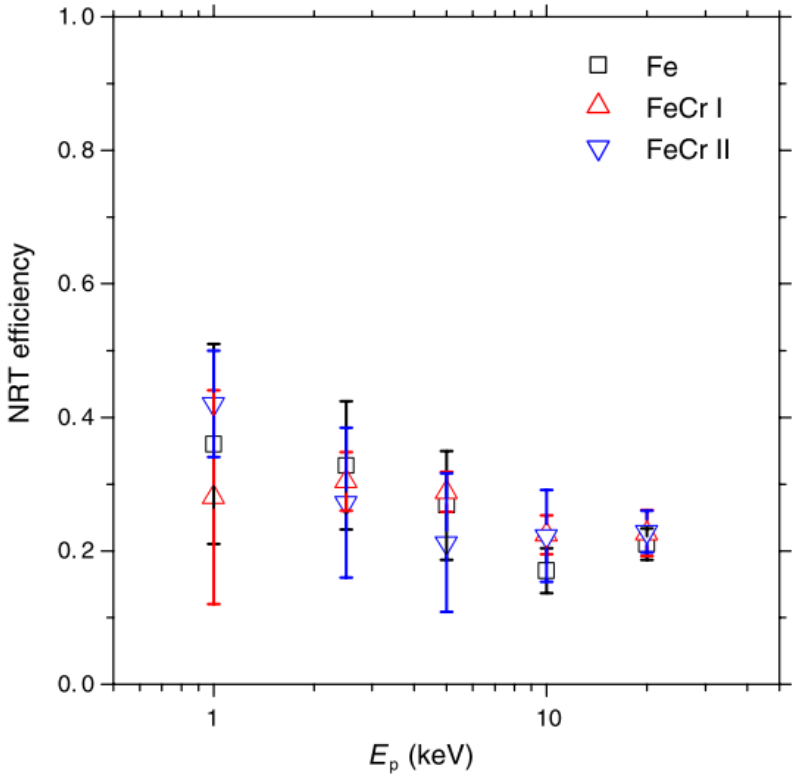


Figure 2.32: MD calculations of ϵ as a function of E_{PKA} (E_p in this figure) within Fe and Fe-10Cr. FeCrI and FeCrII are two different Fe-Cr potentials used in the simulations [222].

70%. In-cascade vacancy clustering within Fe does not occur as frequently [229]. For a cascade with an energy of 10keV at 100K, only a maximum of 15% of the vacancies were clustered. However, at higher temperatures, this drops to approximately 13% [220] because vacancy clusters are thermally unstable [230].

2.4.3.2 Dose rate effect

Dose rates for fusion and fission irradiation in Fe-Cr based alloys are $\sim 10^{-6} dpa\, s^{-1}$ [13] and $\sim 10^{-7} dpa\, s^{-1}$ [213] respectively; ion implantations are significantly higher at $\sim 10^{-5} - 10^{-3} dpa\, s^{-1}$ [195, 213].

Once created, defects can take one of three reaction paths [195, 211]: a) recombination events, b) growth or shrinkage of defect clusters via the capture of defects c) loss of defects at extended sinks.

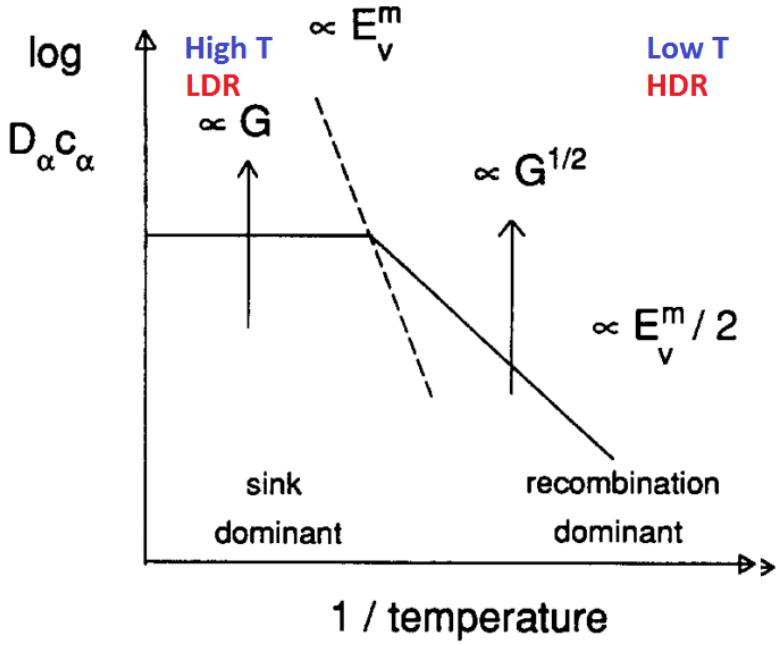


Figure 2.33: Irradiation enhanced diffusion, $D_\alpha C_\alpha$, as a function of the inverse of temperature, T [211]. G is the production rate of point vacancies or interstitials ($G_i = G_v = G$), E_v^m is the vacancy migration energy.

Reaction pathway a) is dominant at high dose rates and/or low-temperature i.e. when defect concentrations are high, and defect mobility is reduced [195, 211]. Irradiation enhanced diffusion is proportional to $\sqrt{G}$ and is dependent on temperature as shown in figure 2.33. Reaction pathway c) is dominant at high temperatures and/or low dose rates. $D_\alpha C_\alpha$ is independent of temperature and is directly proportional to G.

Low dose rates tend to favour vacancy driven processes e.g. void nucleation and growth [231]. High dose rates favour SIA driven processes e.g. amorphisation of crystalline materials or growth of interstitial clusters [232].

The varying temperature dependencies for pathway a) and c) are due to the defect

migration energies in Fe: $E_v^m = 0.68eV$ and $E_{SIA}^m = 0.33eV$ [233]. The difference in migration energies lead to production bias which causes a difference in SIA and vacancy fluxes to sinks. Therefore pathway a) is dominant at higher temperatures because both defects are mobile [234].

To account for the dose rate effect Mansur proposed the temperature shift model [235, 236]. It states that an increase in the irradiation temperature is required for a high dose rate and vice versa. Equation 14 in [235] calculates the temperature shift required.

Hardie has shown that differences in irradiation induced hardening between irradiation at a Low Dose Rate (LDR) ($3 \times 10^{-5} dpa\, s^{-1}$) and a High Dose Rate (HDR) ($6 \times 10^{-4} dpa\, s^{-1}$), can be reduced by increasing the irradiation temperature. This is shown in figure 2.34.

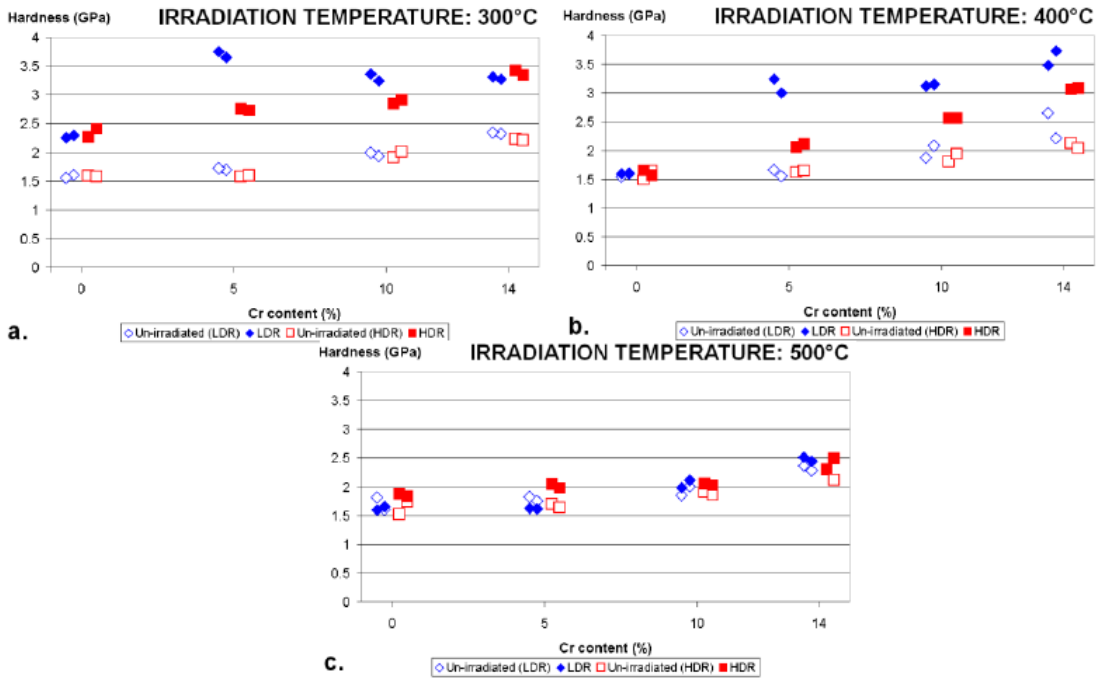


Figure 2.34: Average hardness as a function of alloy Cr content ($wt.\%$) and irradiation dose rate at three different irradiation temperatures [195]. Alloys were irradiated with Fe^+ to 0.06dpa at two dose rates $3 \times 10^{-5} dpa\, s^{-1}$ (LDR) and $6 \times 10^{-4} dpa\, s^{-1}$ (HDR).

2.5 Low-temperature irradiation effects on 14YWT

2.5.1 Low-temperature radiation induced mechanical property change

Fe-Cr based alloys exposed to low-temperature irradiation undergo mechanical property changes. Figure 2.35 shows yield stress and elongation test data from 14WT and 14YWT neutron irradiated to 1.5dpa at $300 - 670°C$. Relative to the 14WT, 14YWT has not hardened as severely. At low test temperatures, the hardening effect is negligible.

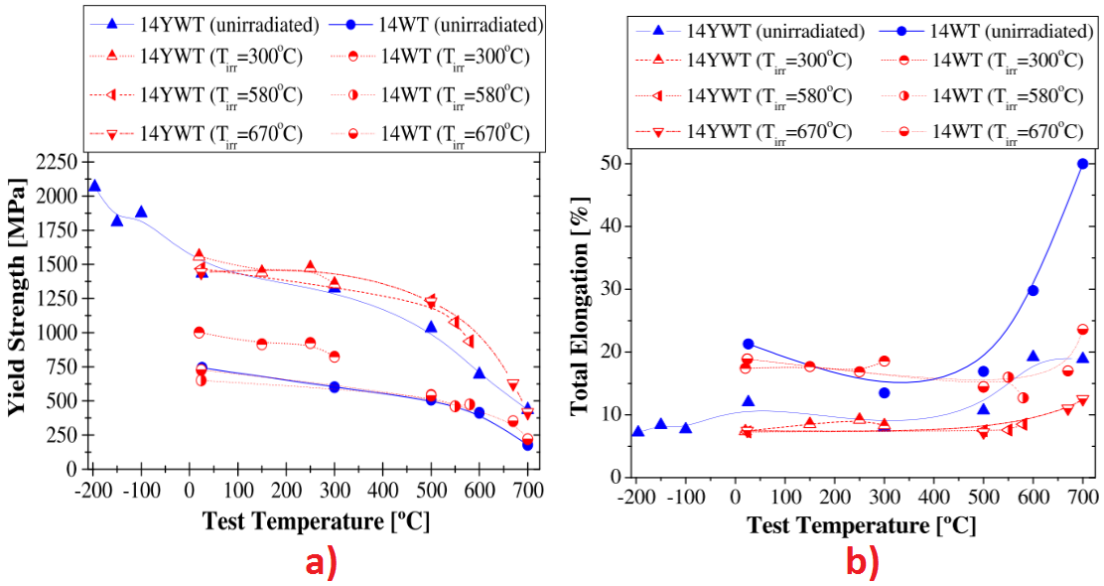


Figure 2.35: a) Yield stress and b) elongation data from mechanical tests performed on 14WT non-NFA and 14YWT NFA neutron irradiated to 1.5dpa at $300 - 670°C$ [237]

Figure 2.35b shows irradiation effects on ductility at low-temperatures is insignificant for both alloys, but at higher temperatures embrittlement occurs. The change in ductility is less pronounced in the 14YWT relative to 14WT.

$\Delta DBTT$ data on irradiated 14YWT is not available in the literature at the time of

writing. However, $\Delta DBTT$ for Fe-14Cr-4Al ODS neutron irradiated to approximately 0.79dpa at $300°C$, $420°C$ and $550°C$ are $+73K, +70K$ and $+35K$ respectively [151].

2.5.1.1 Potential sources of low-temperature irradiation induced hardening and embrittlement in 14YWT

Cascade surviving defects can migrate and form voids, dislocation loops and enhance precipitate formation. Each structure contributes towards irradiation-induced hardening and embrittlement as they effect dislocation motion [147]. Their characteristics e.g. number densities are dependent on irradiation conditions and the material they form within [238].

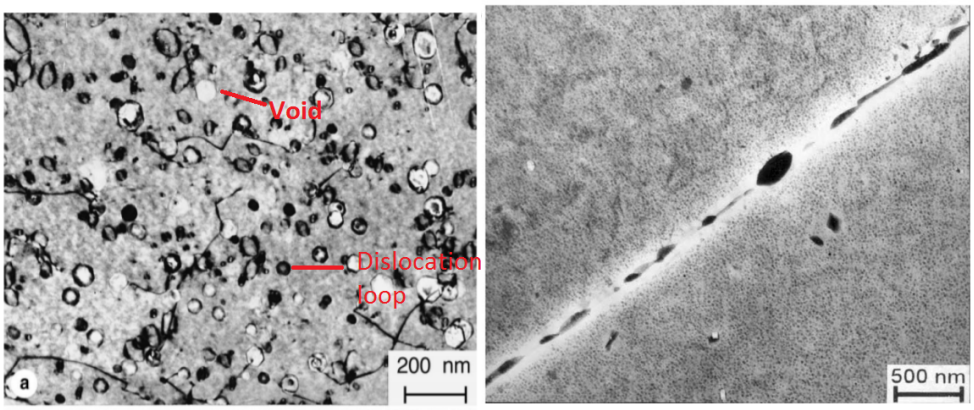


Figure 2.36: a) TEM image of pure Fe neutron irradiated to 5.5-6.5dpa at $400°C$, showing dislocation loops and voids [239] b)TEM image of Fe-8Cr neutron irradiated to 25.8dpa at $400°C$, showing a M_7C_3 precipitate [240]

Voids are vacancies clustered together, as shown in figure 2.36a, and form when concentration of vacancies are supersaturated. Large voids can induce swelling which is detrimental to the structural integrity of components. In Fe neutron irradiated to 25.8dpa at $400°C$, voids are $\sim 120nm$ and have populations of $0.32 \times 10^{20} m^{-3}$ [240]. Voids have not been reported to form in 14YWT.

Dislocation loops, also shown in figure 2.36a, are the strongest obstacles to dislocation

motion [148, 241]. Irradiated, Fe-Cr based alloys are populated with two dislocation loop types: sessile (immobile) $b = a\langle 100\rangle$ and glissile (mobile) $b = \frac{a}{2}\langle 111\rangle$ [52]. Their relative fractions depend on radiation dose, temperature and alloy Cr concentration [241], and are challenging to determine accurately due to the relatively small sample volumes analysed in the TEM [52]. For Fe-12Cr neutron irradiated to 0.6dpa at $300°C$, loops are $\sim 6nm$ in diameter and have populations of $1.6 \times 10^{21} m^{-3}$. K3 (16Cr–4Al) ODS neutron irradiated to 0.01dpa at $290°C$, loops were 12nm in diameter and had populations of $6.1 \times 10^{21} m^{-3}$ [242]. It is unclear whether the loops were correlated with the dispersoids within K3.

α' and M_7C_3 precipitates, shown in figure 2.36b, may form in irradiated Fe-Cr based DSAs such as 14YWT. These are generally the weakest obstacles to dislocation motion in Fe-Cr binary alloys [148]. Fe-15Cr alloys neutron irradiated to 1.82dpa at $290°C$ has been reported to form α' precipitates that are 2.4nm in radius and have populations of $3.2 \times 10^{24} m^{-3}$ [125]. Radiation Enhanced Diffusion (RED) [243] and RIS [244] enhances their formation [42].

2.5.2 RIS

RIS is a non-equilibrium phenomenon. Under irradiation conditions, mobile point defects can migrate to defect sinks such as GBs and dislocations [243]. Solutes can couple to these fluxes and undergo redistribution [246]. RIS can occur via the Inverse Kirkendall Effect (IKE) or interstitial binding mechanisms [247]. The redistribution of solutes can lead to Stress Corrosion Cracking (SCC) [248] and Radiation Induced Precipitation (RIP) [249]. Both can contribute to hardening and embrittlement [250]. Irradiation conditions such as irradiation temperature impacts defect mobility and therefore RIS behaviour. RIS occurs at $300 - 700℃$ in Fe-Cr based alloys as shown in figure 2.37 [245]. At the lower end of this temperature range, vacancies are not as

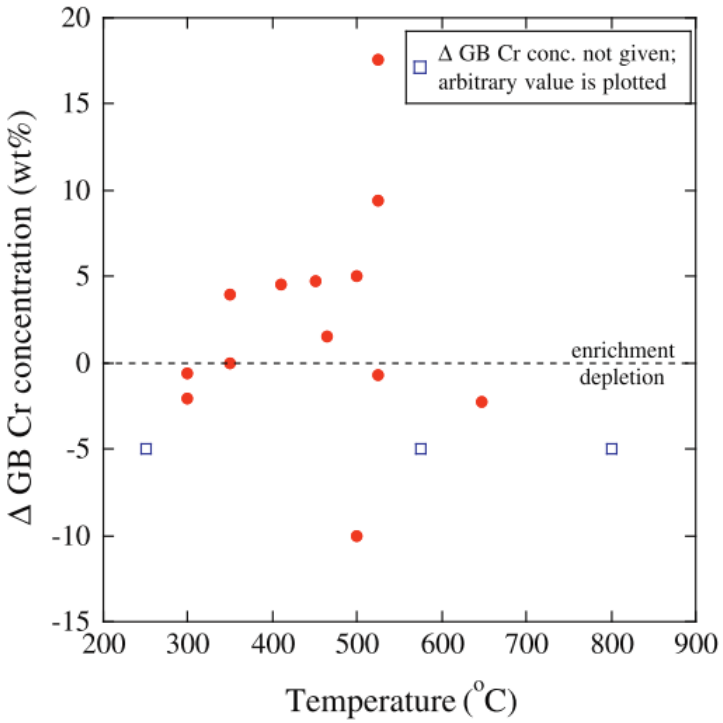


Figure 2.37: Change in Cr GB concentration as a function of irradiation temperature for a range of experiments reported in the literature compiled by [245]. Open squares are from studies that do not report the change in concentration, and therefore an arbitrary value has been used to indicate the direction RIS occurs at.

mobile as SIAs as they have a high migration energy. Therefore interstitial binding dominates [251]. At temperatures above 700℃ , recombination dominates [252].

Irradiation dose and dose rate are also influential RIS parameters. A high dose increases the sink density e.g. by creating more dislocation loops. Concentrations of segregated solutes have been experimentally seen to increase with increasing dose [253] and eventually plateaus as seen in figure 2.38 for Fe-9Cr alloys. At ultra high doses self-ion irradiated T91 to 150dpa at 450℃ did not seem to undergo any RIS of Cr or depletion [254]. Consistent with Mansur's temperature-shift model, high dose rates enhance the recombination rate, therefore, defect populations reduce, and RIS reduces [235].

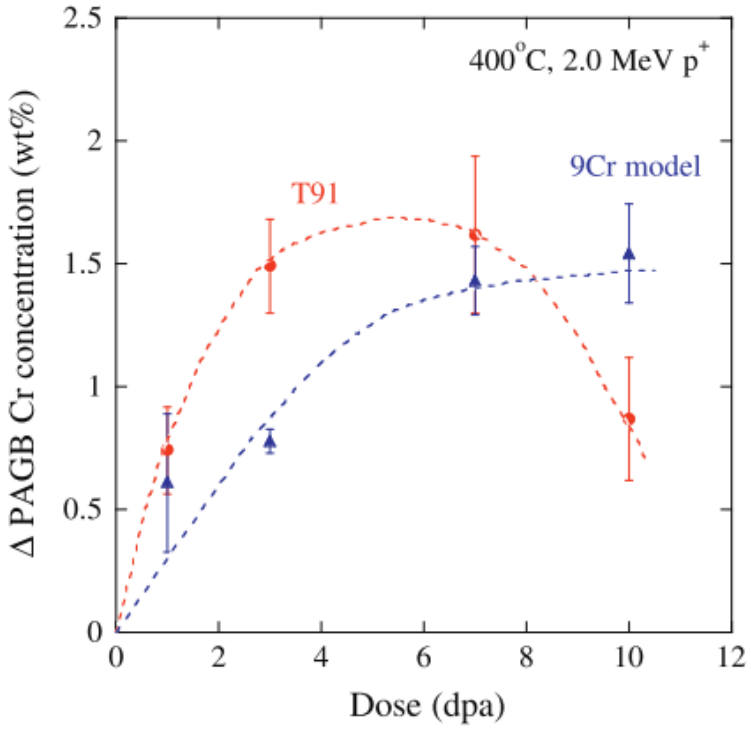


Figure 2.38: Change in the Cr concentration within PAGBs (Prior Austenite GBs) as a function of dose for proton irradiated T91 (8.37Cr wt.%) and model Fe-9Cr binary alloys at 400°C [245]. The alloys exhibit different dose dependancies when the dose exceeds 7dpa

There is no experimental data in the literature to exhibit this at the time of writing.

2.5.2.1 RIS within 14YWT NFAs

RIS within ferritic DSAs is not understood well because they have not been studied in great detail. The lattice parameter influences RIS tendencies. Higher order alloys containing various solid solution strengtheners will have varying lattice parameters. Therefore RIS observed in ferritic non-DSAs could be different to that within ferritic DSAs [255].

Cr is always depleted at GBs in austenitic steels as interstitial binding is less dominant

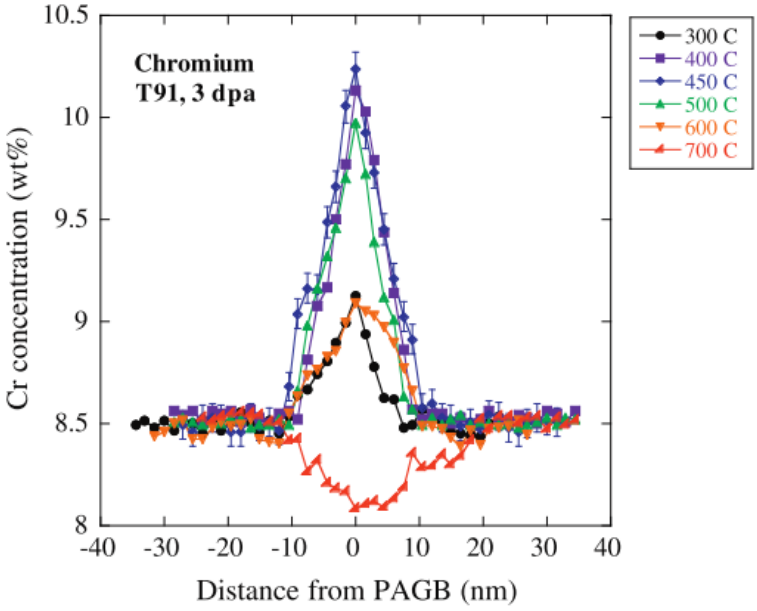


Figure 2.39: Cr concentration profiles across GBs within T91 (8.37Cr wt.%) proton irradiated to 3dpa at various irradiation temperatures [245]. The crossover from an enriched GB to a depleted GB can be seen to occur at a temperature between $600°C - 700°C$.

and Cr is oversized [256]. However, in BCC Fe-Cr alloys, Cr is undersized and binds to interstitials resulting in Cr enrichment at the interstitial sinks. At higher temperatures, it is energetically favourable for vacancy-Cr exchanges to occur [257], and this results in the reduction of Cr and the enrichment of Fe at the GBs [245, 258]. The cross-over between the enrichment of a GB with Cr to that, that is depleted, occurs when $\frac{d_{Fe\,V}}{d_{Cr\,V}} = \frac{d_{Fe\,I}}{d_{Cr\,I}}$ (where d is the diffusivity coefficient). Within T91 (8.37Cr wt.%) proton irradiated to 3dpa, this crossover occurred between $600℃$ and $700℃$ as seen in figure 2.39 [245]. With increasing Cr content this cross-over temperature decreases [259] and so for Fe-14Cr based alloys the cross-over should be in the region of $300 - 400℃$ [260, 261]. It has been hypothesised that the presence of oversized solutes such as W, as is the case for 14YWT, increases the lattice parameter. Therefore the tendency of Cr to deplete,

decreases as it becomes more undersized [255]. A 9Cr ODS alloy proton irradiated 3.7dpa at 400℃ containing 1.96at.% W had GBs that were enriched with Cr by 1.3at.% [245]. A model Fe-9Cr binary alloy also proton irradiated at 400℃ to 3dpa had an average increase in Cr at its GBs by around 0.8w.t% or $\sim 0.8at.\%$ [245]. The results from these studies suggest that a larger quantity of W is required to reduce RIS of Cr or this hypothesis is incorrect.

Grain orientation influences RIS of Cr to GBs in ferritic and austenitic alloys [262] and GBs do not all act as homogenous ideal sinks. Field et al. reported greater RIS of Cr within GBs that had high misorientation angles because they had higher dislocation densities near their GB relative to the lower angle GBs [263]. A higher dislocation density increases the sink strength within the vicinity of a GB and vice versa [264]. A GB with a misorientation angle, $\theta = 3.7°$ within Fe-9Cr proton irradiated to 2pa at 400℃ had a peak Cr concentration of around 10wt.%. Whereas a GB with $\theta = 49.1°$ had a peak Cr concentration of around 12.2wt.% [265]. 80% of GBs within 14YWT have a misorientation angle $> 15°$ [266], so RIS may be enhanced relative to binary alloys.

W is oversized in an Fe-based alloy by about 32.99% [267]. Therefore it should be depleted at GBs. In non-DSAs, W has not been detected at GBs within proton irradiated T91 or HT9 to doses as high as 10dpa [245] and HCM12A irradiated with Fe^{2+} to 100dpa at 500°C [268]. However in 9Cr ODS steel proton irradiated to a dose of 3.7dpa at 400°C, GBs were observed to be enriched with W by 0.8at.% [269]. No other studies that have irradiated DSAs containing W, e.g. [270], have reported RIS of W at GBs and therefore this could be an anomalous result.

Williams et al reported that Mn had segregated to dislocation networks within EUROFER 97 ODS irradiated with Fe^{2+} to 2pa at 400℃, as shown in figure 2.40 [270]. Up to 2.7at.% was detected within 1nm of the dislocation core, which is significantly higher than the bulk composition (0.33at.%). Segregated solutes to dislocations can



Figure 2.40: Mn atom map from Eurofer ODS (8.9wt.%Cr) Fe^{2+} irradiated to 2dpa 400°C [270]. Mn appears to preferentially segregate to dislocations in the sample volume

pin them, and therefore contributes to radiation-induced hardening. Mn is oversized by 4.9% in BCC Fe [267] and therefore is inclined to segregate to sinks to minimise strain energy [126].

No direct observation of RIS at the matrix-dispersoid interface has been reported. However Williams et al. also stated in [270] that there was a clear reduction in the enrichment of Mn in areas containing dispersoids relative those without [270]. They suggested that this was due to dispersoid enhanced recombination.

Ti is oversized in Fe by 14.44% [267] and therefore may behave in the same way W does. The literature does not contain any reports of RIS of Ti to any defect sinks.

2.5.2.2 Neutron and ion irradiation comparative studies on RIS and RIP

Pareige et al. have studied Fe-12Cr alloys self-ion irradiated to 0.5dpa and neutron irradiated to 0.6dpa at 300℃ [43]. For the ion irradiation, three beams with different energies (0.5MeV, 2MeV and 5MeV) were used to create a fairly uniform damage profile. Clusters, rich in Si, P, Ni and Cr, shown in figure 2.41, were observed to form via RIS and RIP in both samples.

Clusters in the neutron irradiated specimen contained significantly more Cr, Si and Ni than the ion irradiated sample as shown in table 2.7. The neutron irradiated sample had a lower number of clusters which were larger. The differences in their physical

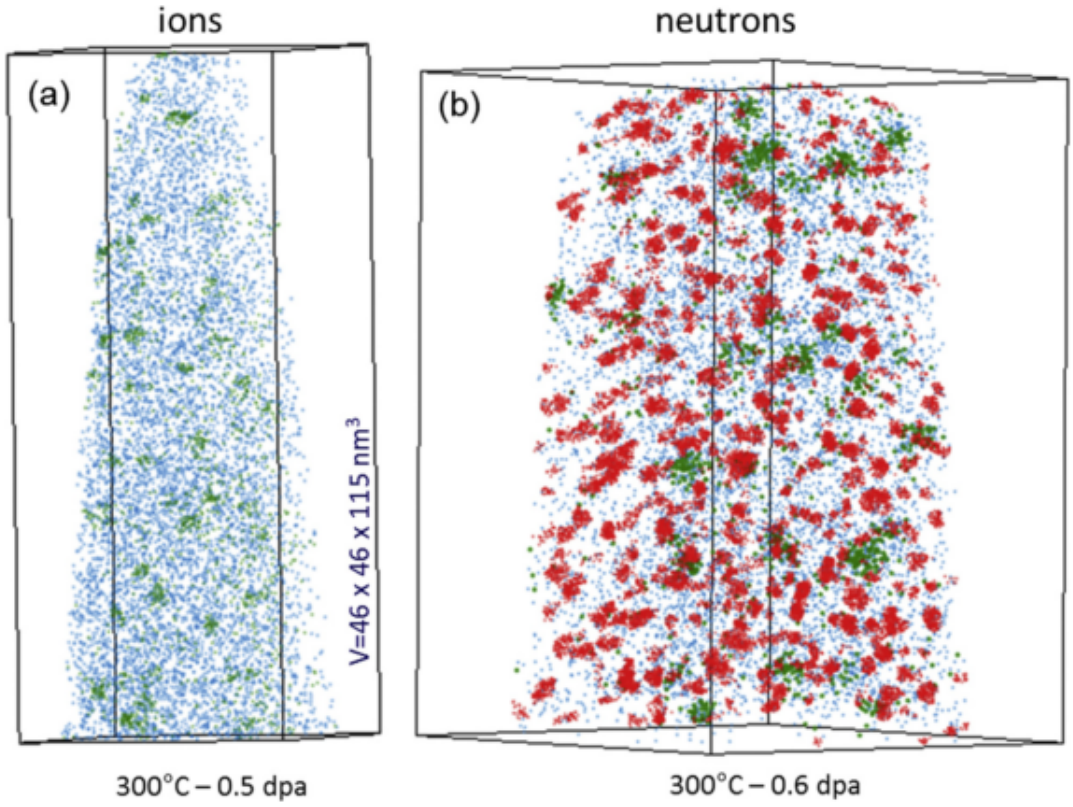


Figure 2.41: APT data of Fe-12Cr alloys a) ion irradiated to 0.5dpa and b) neutron irradiated to 0.6dpa at 300℃. Si and P atoms are blue and green respectively. Red zones are isoconcentration surfaces of 28at.%Cr [43].

characteristics are thought to arise because of the difference in dose rates. The neutron irradiated sample incurred a lower dose rate. Therefore RIS of Si, P, Ni and Cr is enhanced, by shifting the maximum concentration of these segregated elements at the defect sinks towards lower temperatures. The ion irradiation occurred at a faster dose rate and therefore translates this maximum towards higher temperatures. Since the irradiation experiments were conducted at 300℃, RIS within the ion irradiated samples would be lower in concentration.

Figure 2.41 also shows a high density ($2 \times 10^{24} m^{-3}$) of α' precipitates in the neutron irradiated specimen, with average internal Cr concentrations of $58.5 at.\%$ [249, 271].

	Cr	Si	P	Ni	Density	Radius
Neutron irradiated	16	7.8	3.3	1.2	$1.1 \pm 0.7 \times 10^{23} m^{-3}$	$1.6 \pm 0.2 nm$
Ion irradiated	2.7	1.3	3.5	0.3	$3.3 \pm 0.6 \times 10^{23} m^{-3}$	$1.3 \pm 0.3 nm$

Table 2.7: Enrichment of Cr, Si, P and Ni within the clusters rich in Cr, Si and Ni shown in figure 2.41 relative to the matrix (i.e. cluster concentration - matrix concentration). Their densities and radius are also shown [43]

However, none had formed in the ion irradiated [43]. This is because the multiple energetic ion beams introduce an excess number of interstitials, which enhance the recombination rate and also creates defect sinks such as SIA clusters or dislocation loops [272]. Both of these effects reduce the population of vacancies which reduces the diffusion of Cr in the microstructure. This, in turn, reduces the kinetics of α' precipitate formation.

2.5.3 Irradiation altered phase stability

2.5.3.1 Recoil dissolution

Atoms within precipitates can be ballistically driven out and into the surrounding matrix by atomic displacements induced by irradiation. The ejected solute can then either undergo back-diffusion, where it will diffuse back into the precipitate, or remain within the matrix. Nelson et al. state that the rate of precipitate dissolution is directly proportional to the displacement rate [273]. A high dose rate will likely result in the precipitate shrinking, provided the temperature is low enough to reduce the back-diffusion rate. Soisson et al. have modelled irradiation at $290℃$ occurring at dose rates as high as $10^{-4} dpa\, s^{-1}$ [261]. It was observed that irradiation only accelerates α' precipitation and does not dissolve or prevent them from coarsening further. Though, it is possible irradiation at high dose rates occurring at even lower temperatures could provide

an environment in which ballistic mixing processes could dominate [274]. Fe^{2+} implantation experiments within Fe-15Cr binary alloys at dose rates up to $10^{-5} dpa\, s^{-1}$ and at irradiation temperatures of $300℃$ formed α' precipitates; thus proving that the ballistic dissolution of α' precipitates is not possible within these range of irradiation conditions [272].

2.5.3.2 Irradiation disordering

Irradiation disorders lattice atoms, which can affect the Gibbs free energy [41]. Hence, certain Cr concentration and temperature combinations that are stable at equilibrium may be unstable or metastable [126]. As such, non-equilibrium phase diagram boundaries will differ from that at equilibrium [275].

Kuwano et al. have seen this occur as α' precipitates formed within Fe-4.7Cr alloys irradiated to 0.4dpa [276]. Another example, is from Wakai et al., where α' precipitates were observed in high purity Fe-9Cr binary alloys neutron irradiated to 0.3dpa at $\sim 600℃$ [277]. According to figure 2.11, these alloys should reside outside the miscibility gap.

As shown in figure 2.42, no investigations to determine the non-equilibrium free energies and corresponding phase diagrams for the Fe-Cr system under specific irradiation conditions have been conducted, despite the experimental observations by Kuwano et al. from the 1980s and Wakai in 2000.

Irradiation altered phase stability of Fe-Cr alloys is a topic of ongoing debate. Bonny et al. believe irradiation doesn't alter Fe-Cr phase stability and only enhances the kinetics of α' precipitate formation via RED [32, 42]. This hypothesis is based on: 1) irradiation induced defects such as dislocation loops do not act as nucleation points, and 2) a review of experimental data. However this review mixes the results from higher order alloys as well as binary alloys. He also doesn't consider observations from Kuwano, in his

discussion [119]. Therefore it is questionable whether Bonny's hypothesis is correct.

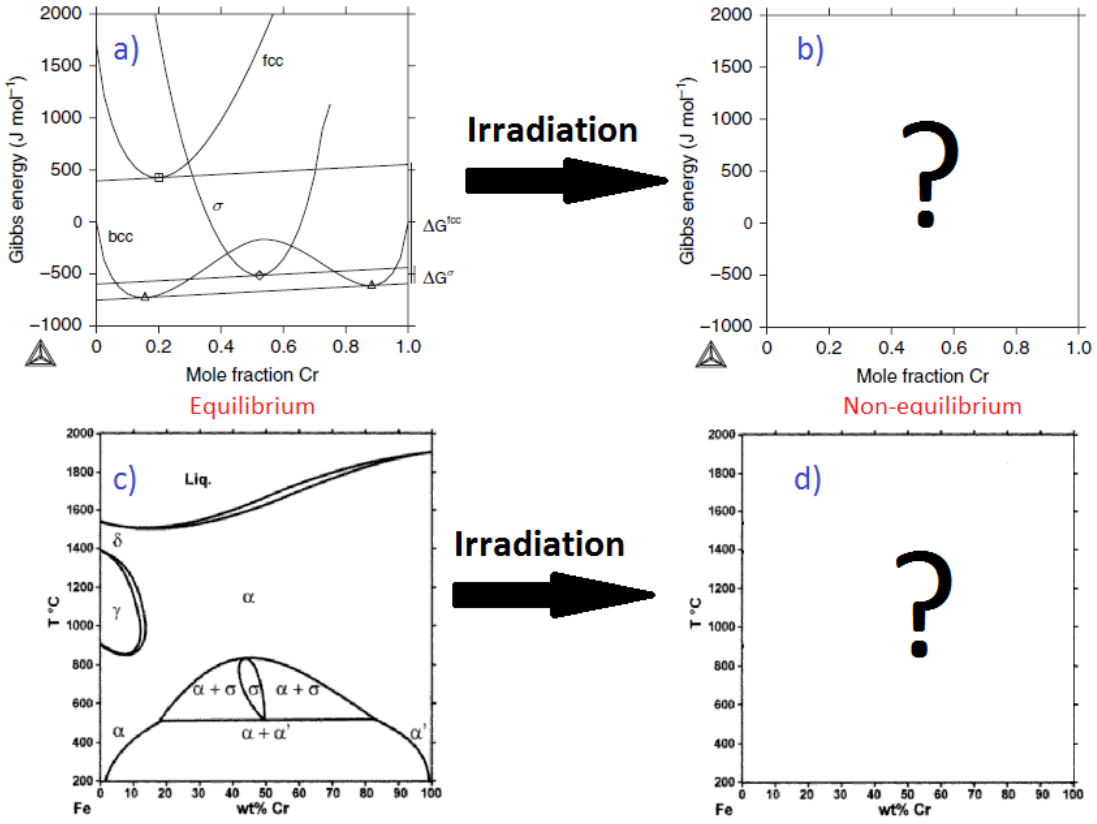


Figure 2.42: a) and c) are the equilibrium Fe-Cr free energy and phase diagram as a function of Cr concentration calculated using CALPHAD [99, 278]. b) and d) are the unknown non-equilibrium Fe-Cr free energy and phase diagrams as a function of Cr under irradiation at a constant dose rate.

2.6 Conclusion and proposed work

This chapter has presented the works that have led to the production of 14YWT and the current state of knowledge regarding their response to low-temperatures and irradiation environments.

Fe-Cr binary alloys and some DSAs are susceptible to the formation of α' precipitates

and tertiary intermetallics e.g. β' in PM2000 [167]. Both features can induce mechanical properties changes such as increases in hardness and embrittlement [36].

In the presence of irradiation the formation of these phases can be enhanced (Radiation Enhanced Precipitation (REP)) [42, 125, 261]. However, the effects of ion implantation and neutron irradiation have not always been coherent. Neutron irradiation has been seen to enhance α' precipitate formation, while self-ion-multi-energy irradiated samples do not form any [43].

Though, this review of works in the literature has shown that knowledge of this field has expanded, gaps still do occur. Especially when it concerns the response of 14YWT exposed to low-temperatures only, and low-temperature ion or neutron irradiation.

2.6.1 14YWT NFAs at low-temperature

The literature studied in section 2.3, has failed to explain:

1. How the 14YWT microstructure responds to low-temperatures:
   (a) Do secondary phases or tertiary intermetallic form within 14YWT?
      i. Since 14YWT contains many alloying elements, does partitioning at low-temperatures occur?
      ii. If α' and a tertiary phase do form, do the ultrafine dispersoids effect this process?
   (b) Do these alloying elements segregate to the dispersoid-matrix interface or other extended sinks?

2.6.2 14YWT NFAs exposed to low-temperature irradiation

The literature studied in section 2.5, has failed to explain:

1. How the 14YWT NFA microstructure responds to a low-temperature irradiation environment:

   (a) If α' precipitates or tertiary intermetallics do form within 14YWT NFAs, does irradiation effect their characteristics e.g. density, composition and distribution?

      i. Do these features form via RIP or REP?

   (b) When irradiated with self-ions or neutrons, do the 14YWT NFAs respond differently?

To investigate the queries outlined in sections 2.6.1 and 2.6.2, further experimentation is required. It is proposed that samples of 14YWT NFA and 14WT non-NFA are to be isothermally aged at $475℃$. Proposed secondly, 14YWT NFAs are to be irradiated with self-ions and neutrons to the same peak dose and irradiation temperature.
Samples of 14YWT and 14WT used for the isothermal ageing study have been obtained from Gorley, who successfully produced batches of both materials [44]. As-received and neutron irradiated 14YWT NFA have been obtained from University of California Santa Barbara (UCSB). Self-ion irradiation experiments on the as-received 14YWT produced at UCSB, have been conducted at the Joint Accelerators for Nanosciences and NUclear Simulation (JANNuS) facility as beam time has been awarded to this author.
APT was utilised to study the distributions of alloying elements within the matrices of the treated alloys. It offers near atomic resolution and can be used to determine microstructural chemistry.

Chapter 3

Materials and experimental methods

Chapter summary

This chapter describes the various materials, experimental protocols and instrumentation utilised in this thesis. Details regarding the fabrication of the 14WT non-NFAs and 14YWT NFAs are described first, followed by the methodology used for the thermal ageing and separate ion and neutron irradiation campaigns. APT methodologies as well as microhardness theory and measurement protocols are also included.

3.1 Materials

This thesis utilised three variants of 14YWT NFAs and one 14WT non-NFA. The first 14YWT variant referred to as 14YWT1 hereafter, as well as the 14WT non-NFA, was produced at the University of Oxford. Whereas the second and third 14YWT variants, referred to as 14YWT2 and 14YWT3 respectively hereafter, were produced at the University of Santa Barbara California in the United States.

3.1.1 Fabrication

3.1.1.1 14YWT1 and 14WT Oxford alloys

14YWT1 and 14WT were fabricated and provided by Gorley [44]. The fabrication of 14YWT1 involved the mechanical alloying of $Fe-14Cr-3W-0.2Ti$ $(wt.\%)$ pre-alloyed powders with $0.25Y_2O_3$ $(wt.\%)$. For the case of 14WT, yttria was not added to the pre-alloyed powders. Mechanical alloying was performed in a P5 ball mill at 250rpm for 60hrs with a 10:1 ball to powder weight ratio. Both variations of the mechanically alloyed powders were stored in stainless steel cans which were transferred to the University of Birmingham for HIP (Hot isostatic Press) consolidation. Cans were first degassed at $500°C$ for 24 hours to a pressure of $1 \times 10^{-3} mBar$ and then HIPed at $1150°C$ and $150MPa$ for 4 hours. Nominal compositions for 14WT and 14YWT1 are given in table 3.1.

3.1.1.2 14YWT2 and 14YWT3 UCSB alloys

The fabrication route of 14YWT2 and 14YWT3 also consists of a powder metallurgical route followed by HIP consolidation. For 14YWT2, pre-alloyed powders consisted of $Fe-14Cr-3W-0.4Ti$ with additions of $0.30Y_2O_3$ [279]. 14YWT3 consisted of $Fe-14Cr-3W-0.5Ti$ pre-alloyed powders and $0.25Y_2O_3$ additions. HIP consolidation

occured at $1150°C$ and $200MPa$ for 4 hours. Nominal compositions for both 14YWT2 and 14YWT3 are given in table 3.1.

	Fe	Cr	W	Ti	Y_2O_3
14WT	Bal	14	3	0.2	
14YWT1	Bal	14	3	0.2	0.25
14YWT2	Bal	14	3	0.4	0.3
14YWT3	Bal	14	3	0.5	0.25

Table 3.1: Summary of the nominal compositions of all alloys used in this thesis. Units of concentration are in wt.%.

3.1.2 Microstructure characterisation

3.1.2.1 14YWT1 and 14WT Oxford alloys

Post consolidation characterisation of both 14YWT1 and 14WT alloys were conducted by Gorley [44], and include Electron Probe Micro-Analyser (EPMA), Electron BackScatter Diffraction (EBSD) and TEM analytical techniques. APT characterisation of both alloys was conducted by this author.

EPMA compositional measurements of consolidated 14YWT1 and 14WT are given in table 3.2 and were evaluated by London Scandinavian Metals UK. Concentrations of O and C were determined by LECO (Laboratory Equipment COrportation) and the remaining elements by X-ray fluorescence. Concentrations of Y within the consolidated 14YWT1 are not shown in table 3.2 as these analytical techniques are unable to detect this element.

Bulk concentrations from APT experiments for both 14YWT1 and 14WT are given in table 3.3. Unlike the EPMA measurements, these also include the Y content. Aside

from Ti and Y, elements within the 14YWT1 and 14WT APT sample volumes were seen to be distributed homogeneously. Ti and Y in 14YWT1 were seen to be concentrated in discrete zones. These zones were identified as the ultrafine dispersoids. Ti in 14WT was concentrated in discrete zones which were identified to be Ti-rich precipitates. This is why the Ti concentration in 14WT in table 3.3 is significantly higher than that quoted in table 3.2. These observations are consistent with other APT characterisation studies conducted by Burrows [45] and Gorley [44].

Consolidated alloy	Fe	Cr	W	Ti	Al	Si	V	Mn	Co
14WT	Bal	13.06	2.65	0.21	0.17	0.15	<0.05	0.35	<0.05
14YWT1	Bal	13.34	2.66	0.21	0.11	0.18	<0.05	0.33	<0.05

Consolidated alloy	Ni	Cu	Nb	Mo	Sn	C	N	O
14WT	0.05	0.07	<0.05	<0.05	<0.05	0.112	0.031	0.092
14YWT1	0.05	0.09	<0.05	<0.05	<0.05	0.091	0.2	0.281

Table 3.2: Post consolidated composition of 14WT and 14YWT1 used in this thesis [44]. Concentrations are quoted in $[wt.\%]$. Y is absent as it is not detected using this analysis technique.

Grain characterisation was conducted using a combination of EBSD and TEM. Grain size distributions were observed to vary significantly between both alloys [44]. This is seen clearly by comparing figure 3.1a and 3.1c, which show EBSD images of 14WT and 14YWT1 respectively. For the case of the 14WT, grains had a mean average diameter of $9.5\mu m$ and ranged from $700nm$ to $25\mu m$. 14YWT1 has a bi-modal grain size distribution of small and large grains. 14YWT1 possessed small grains as shown in figure 3.2. These had a mean grain diameter of $300nm$ and range from $50nm$ to $1\mu m$. 14YWT1 large

grains have a mean grain diameter of $4.3\mu m$ and range from $1\mu m$ to $10\mu m$.

Consolidated alloy	Fe	Cr	W	Ti	Y	O	Si	V	Mn
14WT	Bal	12.51 ± 0.46	2.77 ± 0.34	0.60 ± 0.12	-	0.03 ± 0.02	0.16 ± 0.02	0.02 ± <0.01	0.56 ± 0.20
14YWT1	Bal	13.86 ± 0.51	2.59 ± 0.08	0.19 ± 0.01	0.21 ± 0.01	0.19 ± 0.07	0.19 ± 0.05	-	0.22 ± <0.01

Consolidated alloy	Ni	Cu	Mo	C	N	Al	Co
14WT	0.06 ± 0.04	<0.01 ± <0.01	-	0.07 ± 0.02	0.08 ± 0.02	0.01 ± <0.01	0.07 ± 0.07
14YWT1	0.02 ± <0.01	0.02 ± <0.01	0.01 ± <0.01	0.06 ± 0.03	0.23 ± 0.11	-	0.03 ± 0.01

Table 3.3: 14WT and 14YWT1 average bulk composition measurements in [wt.%] from APT characterisation studies conducted by this author. The errors quoted are the standard errors calculated from three APT datasets. Hyphens represents elements that were not detected within the sample volumes.

Intragranular distributions of NFA particles were also seen to be random in both Gorley's TEM and this author's APT datasets. More detailed high-resolution TEM also indicated the NFA particles in 14YWT1 were spherical and largely coherent with the matrix [44], as shown in figure 3.3. As measured by APT, NFA particles had an average density and radius of $3.36 \pm 0.71 \times 10^{23} m^{-3}$ and $1.79 \pm 0.02 nm$ respectively. This data

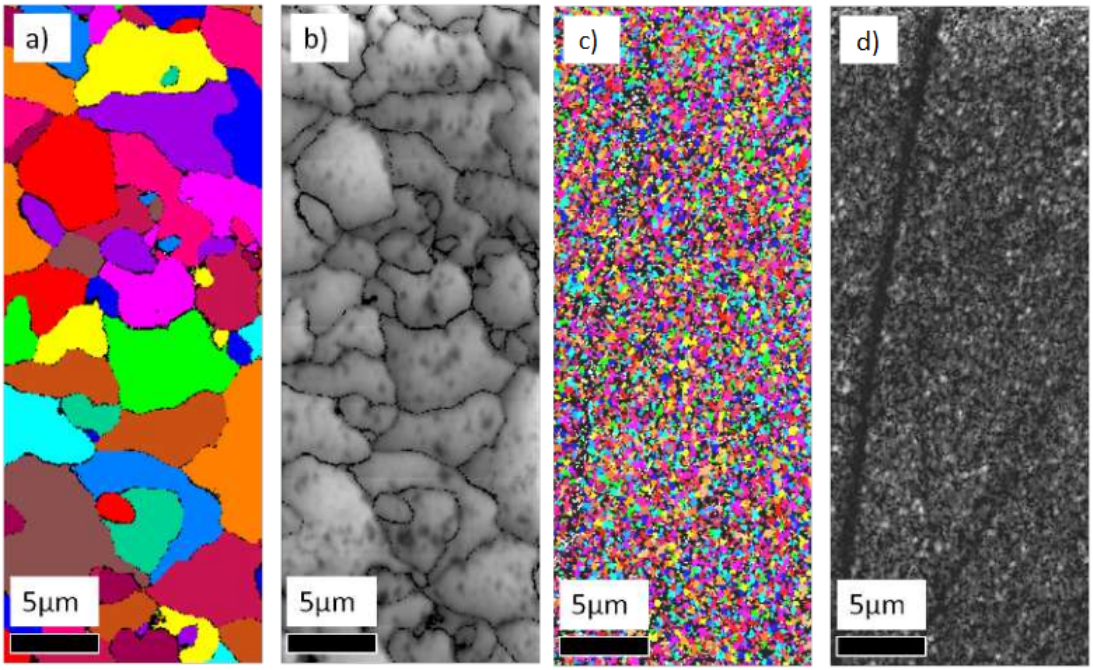


Figure 3.1: EBSD maps showing the grain orientation within 14WT and 14YWT1 [44]. a) Unique colour map and b) image quality map of 14WT over $600\mu m^2$ using a $100nm$ step size. c) Unique colour map and d) image quality map of 14YWT1 over $600\mu m^2$ using a $100nm$ step size.

is consistent with the APT study conducted by Burrows on the NFA particles within 14YWT1 [45].

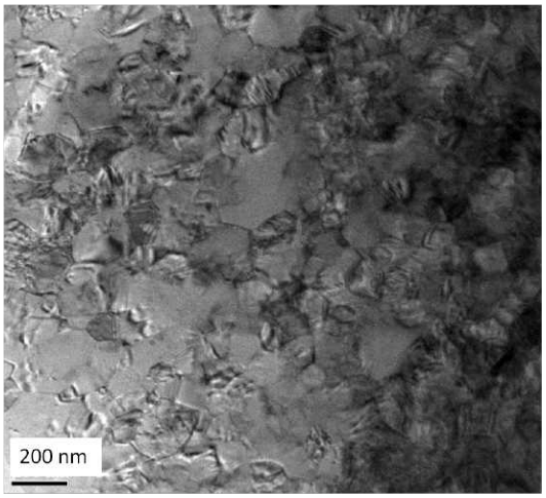


Figure 3.2: Bright field TEM image of 14YWT1 originally produced by Dr Karl Dawson from the University of Liverpool, exhibiting the smaller population of grains [44].

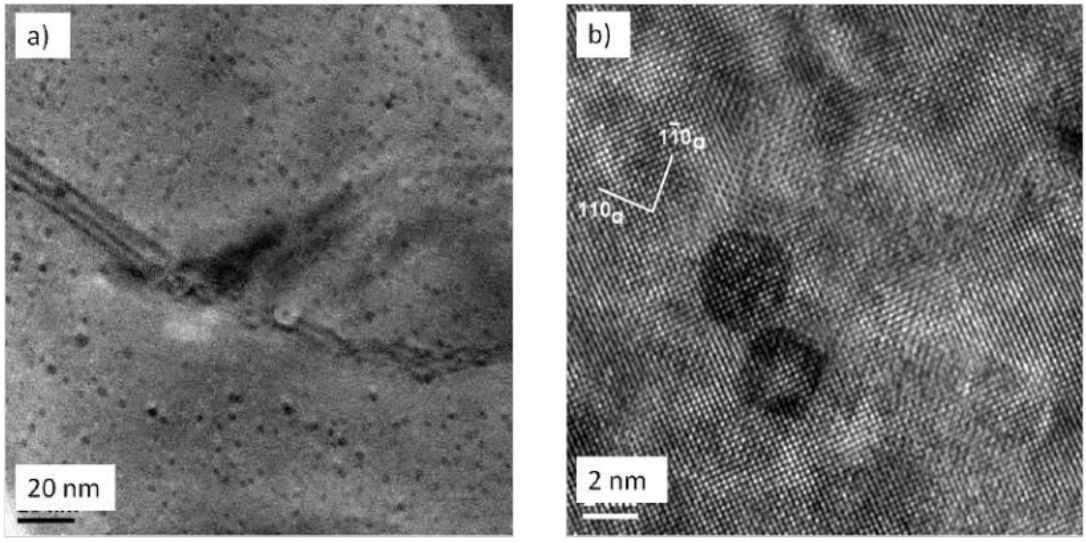


Figure 3.3: a) Bright field TEM images and b) high resolution TEM images of 14YWT1 originally produced by Dr Karl Dawson from the University of Liverpool [44]. 14YWT1 dispersoids in a) can be seen to be randomly distributed. The featured precipitates in b) are coherent with the matrix.

3.1.2.2 14YWT2 and 14YWT3 UCSB alloy

(wt.%)	Fe	Cr	W	Ti	Y	O	N	C
14YWT2	81.87	13.34	2.96	0.39	0.59	0.25	0.08	0.02
	±	±	±	±	±	±	±	±
	0.08	0.20	0.16	0.01	0.24	0.06	0.01	<0.01
14YWT3	83.24	13.19	2.54	0.25	0.27	0.08	0.01	0.02
	±	±	±	±	±	±	±	±
	0.69	0.14	0.18	0.19	0.08	0.06	0.01	0.01

(wt.%)	H	Co	Ga	Si	Mn	Cu	P
14YWT2	0.01	0.25	0.10	0.04	0.07	0.02	0.01
	±	±	±	±	±	±	±
	<0.01	0.12	0.01	0.01	0.02	<0.01	<0.01
14YWT3	-	0.16	0.01	0.07	0.17	-	-
		±	±	±	±		
		0.07	<0.01	0.03	0.06		

Table 3.4: 14YWT2 and 14YWT3 average bulk composition measurements in [wt.%] from APT characterisation studies. The errors quoted are the standard errors calculated from three APT datasets. Hyphens represents elements that were not detected within the sample volumes.

APT measured bulk compositions of 14YWT2 and 14YWT3 are shown in table 3.4 and were averaged across three atom probe datasets. APT experiments of 14YWT2 were conducted by this author. APT experiments of 14YWT3 as-received, were conducted by Nicholas Cunningham at UCSB in the USA and were reconstructed by this author. Both alloys were observed to possess homogenous distributions of Fe, Cr and W. Y, Ti

and O solutes were found mainly in discrete regions thought to be the NFA particles.

TEM images of 14YWT2, which are shown in figure 3.4, show that it contains bimodal grain distributions consisting of fine and coarse grains [279]. Fine grains were around 200nm, whereas coarse grains ranged from 1 to $10\mu m$. No information regarding the grain structure in 14YWT3 is available. Given the similarity in the nominal composition and fabrication process used to produce 14YWT2 and 14YWT3, it is likely that the grain structure in 14YWT2 will resemble that of 14YWT3.

NFA particles in 14YWT2 were seen to be randomly distributed. Average density and radius as measured from APT experiments conducted by this author were seen to be $1.09 \pm 0.39 \times 10^{24} m^{-3}$ and $0.98 \pm 0.04 nm$ respectively. NFA particles in the as received 14YWT3 atom probe datasets were seen to be sparse. NFA particle average density and radius as measured by APT were seen to be $2.39 \pm 1.68 \times 10^{22} m^{-3}$ and $0.87 \pm 0.03 nm$ respectively.

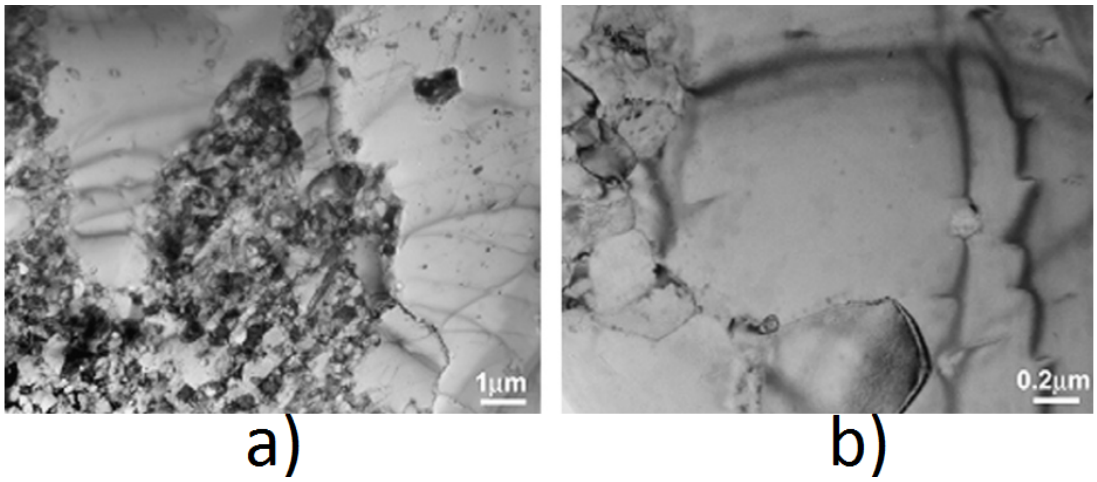


Figure 3.4: TEM images of 14YWT2 at a) low and b) medium magnification [279].

3.2 Isothermal ageing

A vacuum furnace shown in figure 3.5, was used to age the samples of 14WT, 14YWT1, Fe-14Cr binary and 14Y alloys at 475°C for a total duration of up to 8 months. The aged Fe-14Cr binary and 14Y alloys are reserved for a separate study to be conducted in the future. The rig's main components highlighted in figure 3.5, are the Severn furnace, quartz tube, the rotary and diffusion pump. An external Eurotherm thermostat and thermocouple datalogger were also used in this experiment but are not shown.

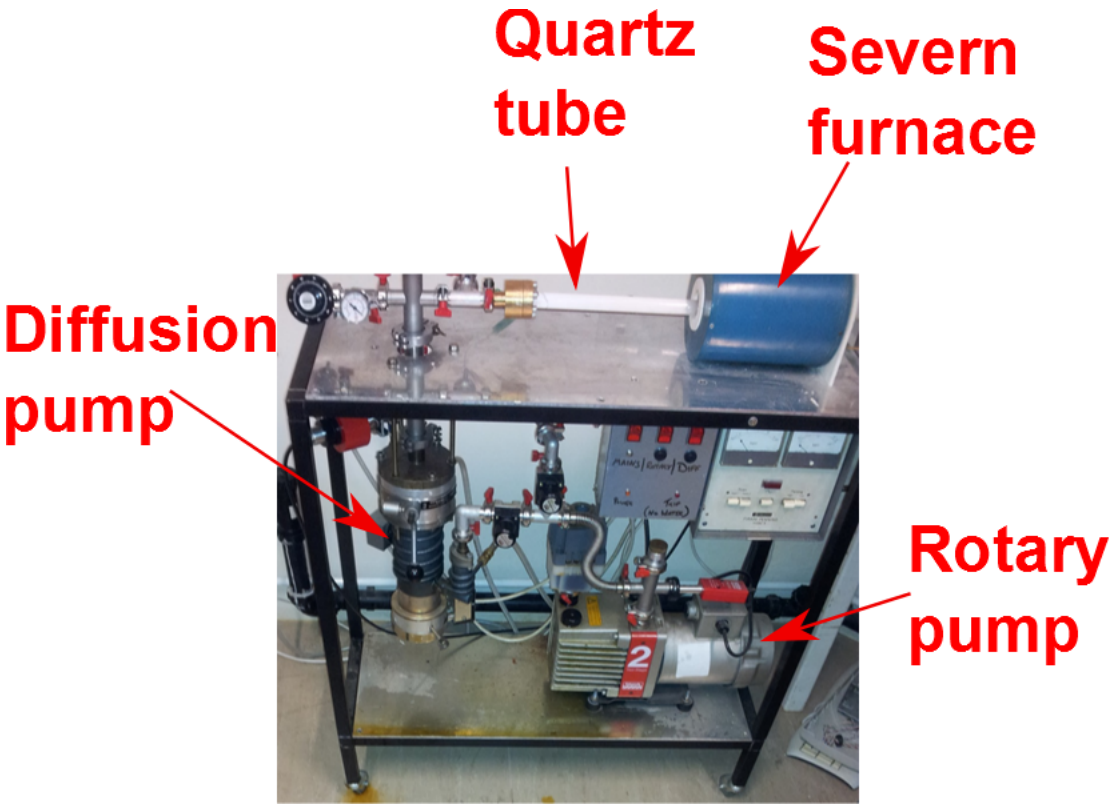


Figure 3.5: The vacuum furnace used to isothermally age the 14WT and 14YWT1 NFA samples at 475°C

3.2.1 Furnace calibration

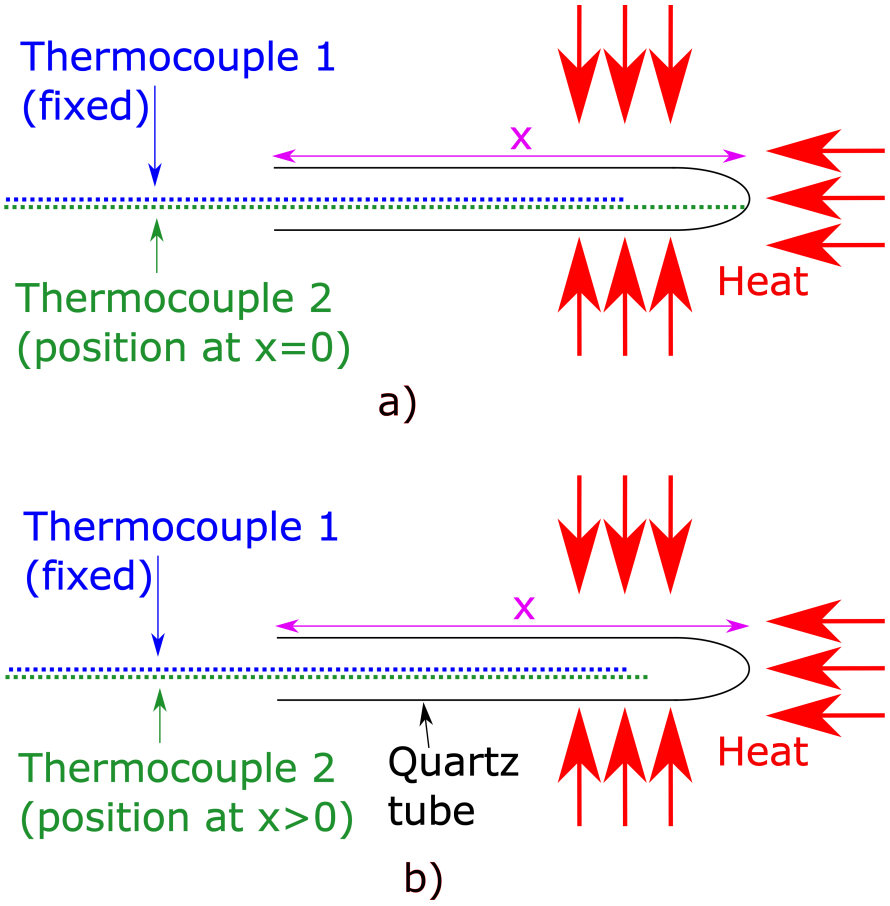


Figure 3.6: Schematic diagram depicting the vacuum furnace calibration

Before the ageing experiment commenced, a furnace calibration was conducted to obtain a 1D temperature profile along the quartz tube length axis, x. The thermostat regulated the temperature based on a fixed thermocouple located inside the quartz tube. The temperature was set and maintained to $475°C$, while the quartz tube was at atmospheric pressure. After thermal steady-state was achieved, a second thermocouple was used to measure the temperature at discrete points along the tube's x axis, as shown in figure 3.6. As depicted in figure 3.6a this commenced from the closed end of the tube.

Once a steady temperature reading from the second thermocouple was observed, the temperature was recorded. Following this, the second thermocouple was retracted and measured a new region at $x > 0$ as shown in figure 3.6b. This calibration experiment was repeated three times to obtain statistical data.

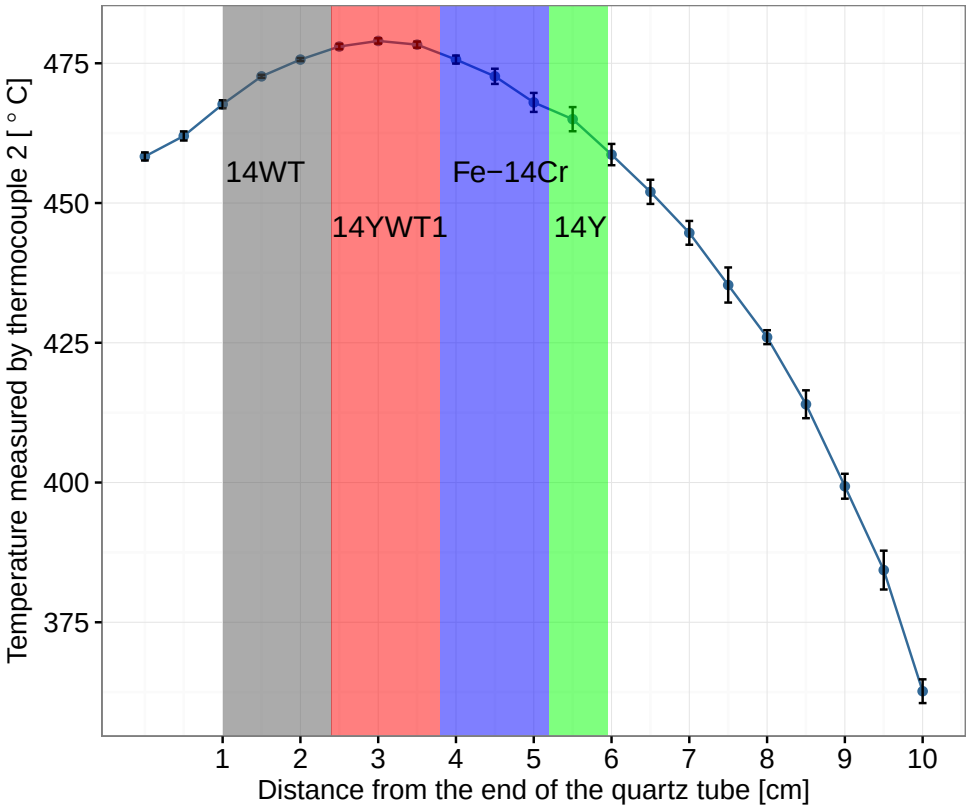


Figure 3.7: Data acquired from the furnace calibration experiment conducted. Blue dots represent the average of the three datapoints acquired. Error bars are shown in black. Shaded areas show the approximate locations of the samples while ageing. Fe-14Cr and 14Y refer to samples of binary $Fe-14Cr$ and $Fe-14Cr-0.25Y_2O_3$ alloys respectively.

The temperature profile along the quartz tube x axis is shown in figure 3.7. As the fixed thermocouple is not the same length as the quartz tube, the temperature at the

end of the quartz tube is below the target temperature of $475°C$. As the thermocouple is drawn out the first 3cm the temperature starts to rise to a maximum of $\sim 476°C$ and then as expected falls again. As the target temperature of $475°C$ is met at 2cm away from the end of the quartz tube, it is that position in which the crucible was placed during the ageing treatment. Also included are the approximate temperatures the 14WT, 14YWT1, $Fe-14Cr$ and $Fe-14Cr-0.25Y_2O_3$ were aged at. As can be seen, the minimum and maximum temperatures the 14WT samples experienced were $467°C$ and $475°C$ respectively. The 14YWT1 resided at a minimum and maximum temperature of $\sim 477°C$ and $479°C$ respectively.

3.2.2 Isothermal ageing experiment

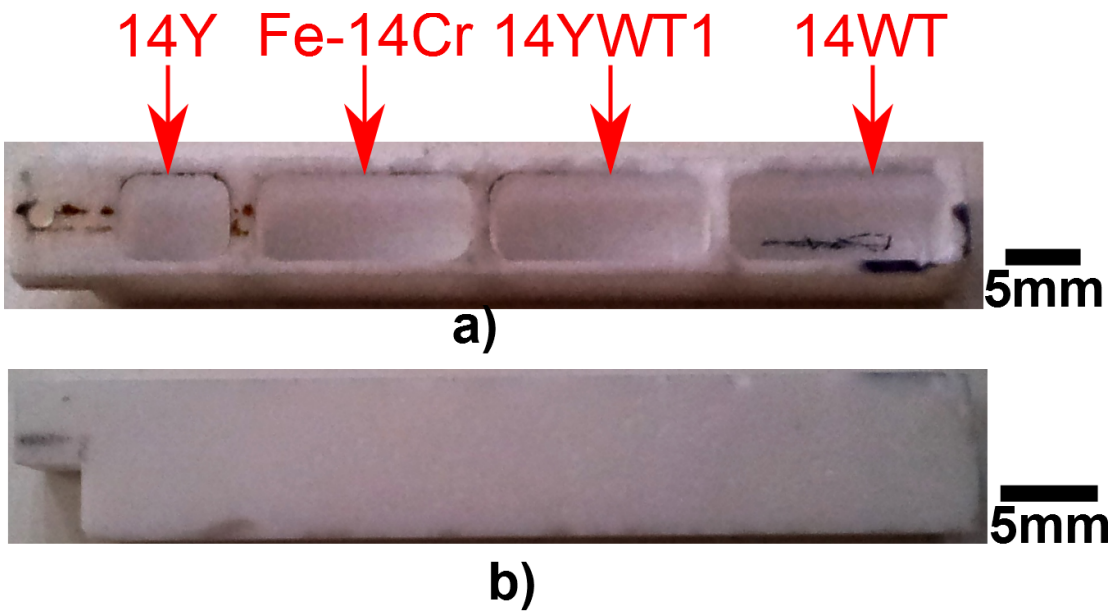


Figure 3.8: a) Top down and b) side views of the Macor crucible used to hold the 14WT and 14YWT1 samples. Labels indicate the sections of the Macor crucible the samples reside within. Fe-14Cr and 14Y refer to samples of binary $Fe-14Cr$ and $Fe-14Cr-0.25Y_2O_3$ alloys respectively.

14WT and 14YWT1 were cut into small chips, roughly $10mm \times 5mm \times 1mm$ using a

precision saw, and polished to a mirror finish using SiC grit paper up to a grade of 4000, followed by a final polishing using $3\mu m$ diamond solution. Polished samples were then placed in a bespoke crucible manufactured from Macor, shown in figure 3.8. Once the samples were loaded into the crucible, both the crucible and samples were transferred into the quartz tube of the furnace.

While the alloys were at temperature, a high vacuum was maintained to pressures $< 10^{-6}Torr$ by a diffusion pump. Pressures were measured via an Edwards CP25K Penning gauge. The temperature was recorded by an external thermocouple datalogger which was connected to a computer throughout the ageing period. Both temperatures and pressures were also regularly monitored via visual inspections as well as an IP camera.

Single chips of 14YWT1 and 14WT were extracted when the target durations had been achieved. These durations were 1, 3 and 8 months, Once the chips were extracted from the furnace, the Macor crucible containing the remaining number of sample chips was reloaded inside the quartz tube. Once a stable vacuum at $< 10^{-6}Torr$ was achieved, the temperatures was ramped to $475°C$ so that ageing recommenced.

3.3 Irradiation experiments

3.3.1 Ion irradiation

Single beam ion implantation experiments on 14YWT2 NFAs were conducted at the JANNuS ion beam facility in France using the 3MV Pelletron accelerator [280]. As shown in figure 3.9a, 14YWT2 and other Fe-Cr based samples were fixed to a bespoke base plate which was manufactured at the University of Oxford. The samples were attached to the surface of the base plate by using a two part silver epoxy, which offers both a conductive and strong bond.

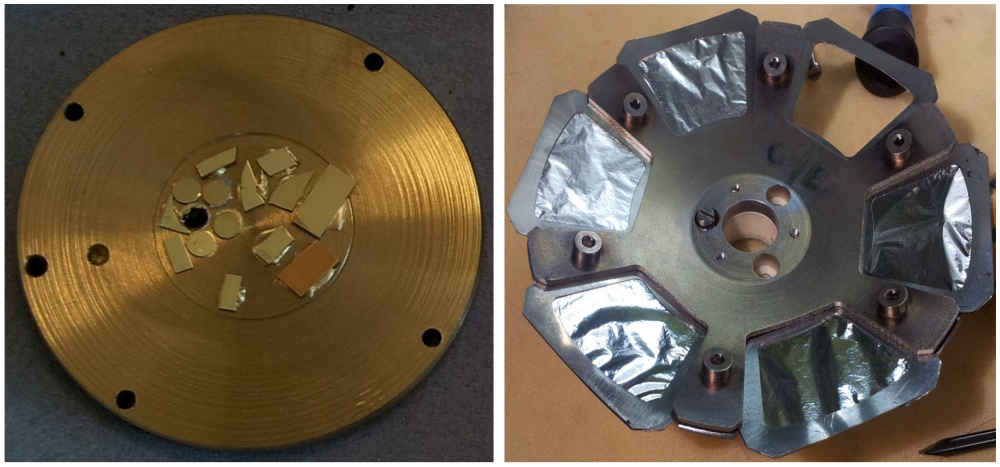


Figure 3.9: a) Samples consisting of Fe-Cr based alloys, including 14YWT2, fixed using a two part silver epoxy, to a JANNuS base plate. b) Degrader foils used in the irradiation experiment at JANNuS

The following implantation specifications were requested in the JANNuS experiment proposal to achieve an irradiation dose of 1.7dpa:

1. 24MeV $^{56}Fe^{8+}$ beam at at flux of $3.70 \times 10^{11} cm^{-2}\, s^{-1}$ and total fluence of $5.40 \times 10^{15} cm^{-2}$
2. 1 rotating frame consisting of 6 windows. 1 window was left "open" (i.e. no foil was placed within it) and the remaining 5 windows were "closed off" with Al degrader foils of varying thicknesses (0.8, 1.6, 3, 4 and 5μm), as shown in figure 3.9b
3. The implantation temperature set to 288°C.

The expected damage profile into the 14YWT2 sample, produced by the beam with the characteristics listed above, is shown by the 'requested' line in figure 3.10. This was calculated by using SRIM 2008 [204] which is a Monte Carlo simulation code which evaluates the interactions between an incident energetic ion and a target [282]. SRIM

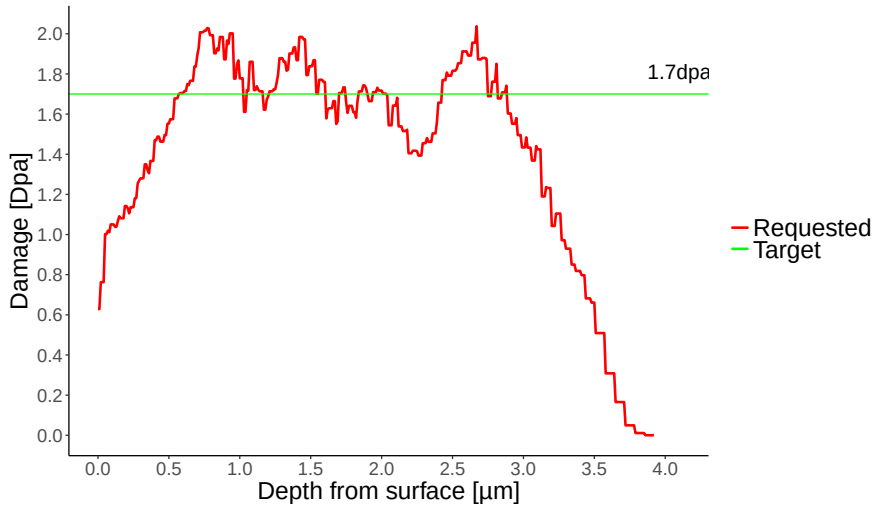


Figure 3.10: Ion implantation profile of 24MeV $^{56}Fe^{8+}$ in pure Fe calculated using SRIM 2008 software [204] which utilises the Kinchin Pease model. By utilising Al degrader foils of varying thicknesses, a $3\mu m$ deep, approximately flat damage profile can be achieved. 'Requested' refers to the profile of the beam using the energy and degrader foils specified in the proposal. 'Target' refers to the target dose required for this ion implantation .

simulations were conducted in a manner that was consistent with the international standards detailed in [283]. This includes running SRIM using the "quick" Kinchin and Pease option, using a displacement threshold of 40eV for Fe and Fe based alloys and finally setting the lattice binding energy to zero, as initially suggested by [284]. Simulations were conducted using 1000 Fe ions into pure Fe. Cr has a similar displacement energy as Fe and therefore is expected to have a minimal influence on the final damage profile.

The damage profile in figure 3.10 lies close to the target dose line of 1.7dpa, and provides an average dose of 1.41dpa over the entire projected range shown. Therefore the implantation conditions listed above and requested in the proposal are adequate for this thesis.

7 Faraday cups measure the current density of the incident beam during the implan-

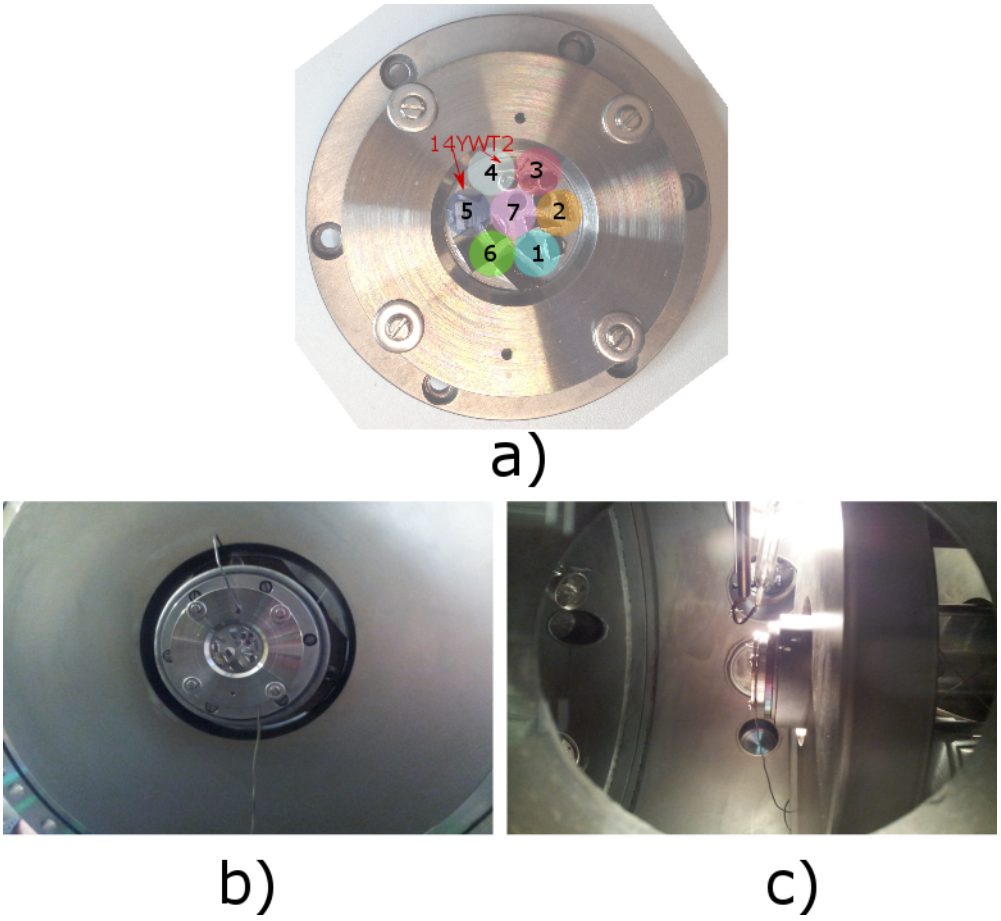


Figure 3.11: a) Top down view of the samples attached to the base plate after the JANNUS irradiation implantation [281]. Overlaid are the outlines of the Faraday cups used to measure the current density during the irradiation experiment. b) The base plate is attached to the irradiation chamber. Two thermocouples can be seen to be attached to the surface at the top and bottom of the base plate. c) Side view of the base plate within the irradiation chamber.

tation. From this, the fluence, that is the ions per unit area, can be evaluated. The positions of each of the 7 Faraday cups relative to the samples and the base plate are shown in figure 3.11a. The positions of the 14YWT2 samples on the baseplate are highlighted and the ion beam these samples are exposed to is monitored by Faraday cups 4 and 5. The irradiation temperature was regulated via two thermocouples that were

fixed to the top and bottom positions of the irradiation target base plate, as shown in figures 3.11b and 3.11c.

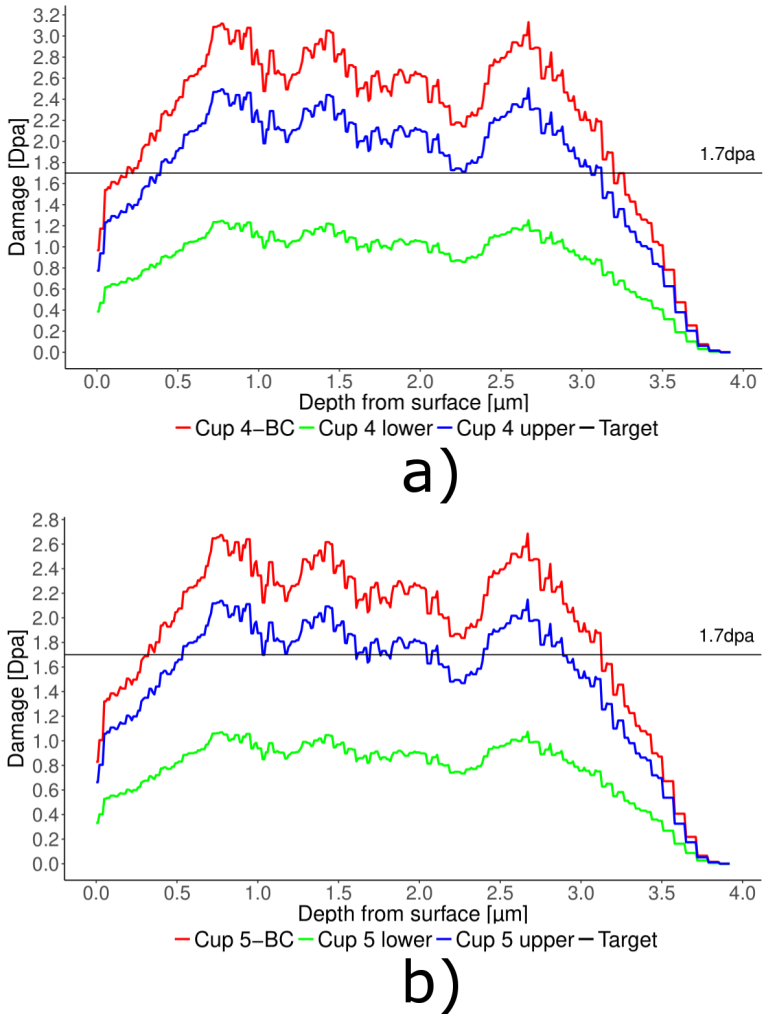


Figure 3.12: Damage profile as a function of depth calculated using SRIM 2008 for the uncorrected beam, corrected beam using the lower correction factor (0.4) and corrected beam using higher correction factor (0.8). The suffix 'BC', 'lower' and 'upper' refer to the damage profile before the correction factor is applied, the lowest correction factor (0.4) and the highest correction factor (0.8) respectively. The Ion beam flux data measured by a) Faraday cup 4 and b) Faraday cup 5 were used in these calculations.

After the experiment had been completed it was revealed that the Faraday cups were positioned incorrectly. This resulted in the incoming beam interacting with one of the tantalum rings within a beam detector. This secondary ion beam interaction resulted in the emission of additional electrons and ions directed at the Faraday cups. Consequently, the irradiation fluence the target 14YWT2 received was reduced, and the incident beam flux was erroneously recorded.

A control experiment was conducted by the implantation team at JANNuS to determine the effects of this secondary emission on the ion flux recorded by the Faraday cups. This involved irradiating an electrically insulated target and measuring the current it collected. This current was measured and recorded using an independent detector and was compared with the measurements from the Faraday cups. They concluded that a correction factor of 0.4-0.8 should be applied to the recorded ion flux measurements.

Accordingly, 3 beam profiles for Faraday cups 4 and 5 are shown in figure 3.12a and 3.12b respectively. One profile is for the uncorrected damage profile and has a suffix 'BC', and the profiles with a suffix 'lower' and 'upper' are the corrected profiles. The suffix 'lower' is for the profile where the lower value of the correction factor, 0.4, has been applied. 'upper' is for the profile where the higher value of the correction factor, 0.8, has been applied.

The differences between the uncorrected damage profiles as measured by Faraday cup 4 and that measured by Faraday cup 5 shows that the ion beam has poor lateral homogeneity. Indeed, the 'lower' and 'upper' damage profiles for the corrected beams for Faraday cups 4 and 5, differ significantly from the uncorrected damage, 'BC', profile. Table 3.5 presents the average doses achieved across the entire depth range shown in figure 3.12.

Table 3.5 shows that the dose achieved in the samples monitored by Faraday cups 4 and 5 range between 0.87-1.73dpa and 0.74-1.49dpa respectively. The dose range

corresponding to Faraday cup 4 is higher than that belonging to Faraday cup 5, and is closer to the target dose of 1.7dpa. However the 14YWT2 sample monitored by cup 5 was chosen as the information regarding the secondary emission during implantation, was disclosed to this author in March 2017. By this time all of the APT experiments and analysis had been completed.

	Average dose [dpa]	
	Cup 4	Cup 5
Uncorrected	2.17	1.86
Lower correction factor applied (0.4)	0.87	0.74
Higher correction factor applied (0.8)	1.73	1.49

Table 3.5: Average doses calculated across the entire depth range shown in figure 3.12, for each of the three beam profiles corresponding to Faraday cups 4 and 5.

Therefore the 14YWT2 sample studied in this thesis was ion irradiated to 0.74-1.49dpa at $3.24 - 6.53 \times 10^{-5} dpa\, s^{-1}$, at $288°C$.

3.3.2 Neutron irradiation

A sample of 14YWT3 NFA was irradiated with neutrons at $288 \pm 6.5°C$ for 54.7 EFPDs (Effective Full Power Day) in position A10 of the Advanced Test Reactor (ATR) in Idaho USA [285], as shown in figures 3.13 and 3.14. Simulations were conducted using the Monte Carlo N-Particle transport code [286] to determine heat rates, fluxes and fluence. It was estimated that the 14YWT3 NFA sample was exposed to a total neutron fluence of $\sim 5.5 \times 10^{21} n\, cm^{-2}$ and an average neutron flux of $\sim 2.4 \times 10^{14} n\, cm^{-2} s^{-1}$ ($E > 0.1 MeV$) which correspond to a maximum dose of 1.82dpa. This corresponds to a dose rate of $3.85 \times 10^{-7} dpa\, s^{-1}$ [285, 186].

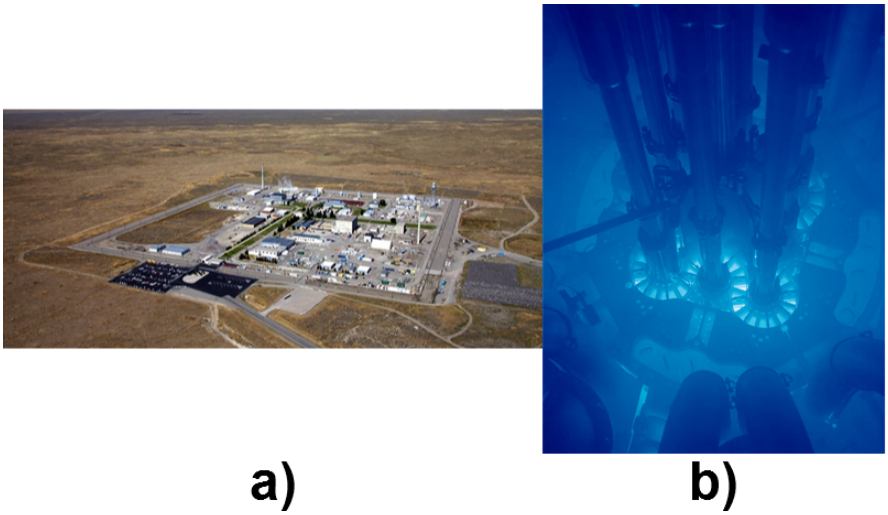


Figure 3.13: a)An aerial view of the ATR facility and a b) picture of the core whilst under operation.

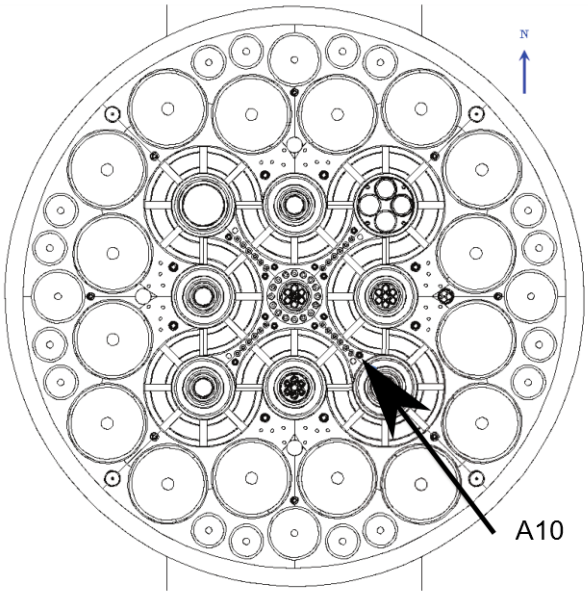


Figure 3.14: Radial cross section view of the ATR core. The black arrow points to where the A10 position is.

Temperature regulation was implemented by packaging the disc shaped samples in a so called "pill box" packet, shown in figures 3.15a, 3.15b and 3.15c. It's primary responsibility is to minimise axial variations in temperature. Additional temperature control measures within the pill box design included a gap between the outer and inner lining of the packet, which was filled with a He-Ar gas mixture to tailor thermal conductivity [186].

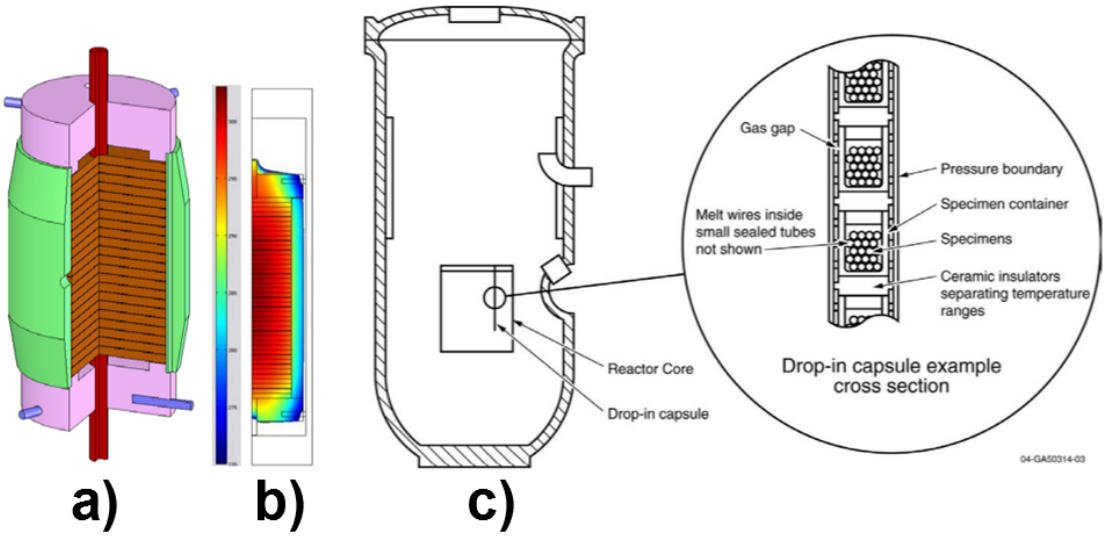


Figure 3.15: a) Schematic of the so called "pill box" packet used to store the samples during the irradiation experiment b) results from a simulation of the thermal energy distribution across the pill box whilst irradiated and c) is a cross section of the side profile of the reactor showing the location in which the samples were situated

3.4 Atom probe tomography

An introduction to APT concepts, APT experimental hardware used in this thesis, analysis parameters used in the experiments, cluster analysis protocols and the shadow effect are presented in this section. Protocols to fabricate APT samples, reconstruct APT datasets, identify mass spectrum peaks and conduct GB analysis within APT datasets are described in appendix A.

3.4.1 A brief introduction to atom probe tomography

First introduced in the 1980's as a development to the field ion microscope, APT has furthered a researchers ability to characterise materials and has provided greater insight into phenomenological mechanisms within nuclear materials research [43, 125, 287, 288]. It offers near atomic scale resolution, 3D imaging capabilities for the mapping and identification of solute distributions. Crystallographic information can also be obtained providing a pole is acquired in the sample volume.

APT works by evaporating surface atoms off of a needle shaped specimen. This is done primarily by applying an appropriate standing electric field, F, to the specimen, in addition to a secondary voltage or laser pulse. It is because of this pulse that controlled evaporation may occur. Equation 3.1 can be used to estimate the magnitude of F required for evaporation to occur [289]. F is the ratio between the voltage applied to the sample, V, and the product of the field reduction factor, k_f, which takes into account the tip shape (e.g. shank angle) and the electrostatic environment, and the tip radius of curvature, R.

$$F = \frac{V}{k_f R} \tag{3.1}$$

As shown in figure 3.16, atom probe machines such as the LEAP 3000X-HR and 4000X-HR also incorporate other additional hardware such as a reflectron energy compensating lens, Micro Channnel Plate (MCP) [291] and Delay Line Detector (DLD) [292]. These pieces of equipment serve together to reduce the uncertainty when attributing a particular ion and also enhance spatial resolution.

Ions of the same type, evaporating off the sample surface may have a distribution of kinetic energies, T. Such differences, as will be shown later, can introduce uncertainty into the calculated mass-to-charge-ratio, M. To mitigate this, the reflectron lens, as can be seen in figure 3.16a, bends the flight path of the incoming ion. If this ion has a higher T, then its flight path will be extended in comparison with those with a lower T. By increasing or decreasing the length of the flight path, the reflectron acts in a similar way to an optical lens and focusses the incoming ions on to the MCP by reducing the difference in arrival times of the ions with varying T to arrive at the detector. While the reflectron decreases uncertainty in M, it is largely responsible for the low detection efficiency, 0.37, for LEAP 3000X-HR and LEAP 400X-HR systems.

Figure 3.16b shows an ion incident to an MCP and a DLD. Once this ion hits the MCP an electron cascade is produced. This electron cascade is focussed onto the conductive wires that make up the DLD. LEAP 3000X-HR and 4000X-HR systems have three sets of DLDs in total. The first two provide the two-dimensional cartesian (x, y) positions of the collision point along the detector. This information is vital for reconstructing the three-dimensional volume sampled. The third is used to firstly resolve multiple hits when they occur and secondly to reduce detector dead time. By assuming the ion evaporated at the start of the pulse, the Time of Flight (ToF), t, to the detector stack can be recorded.

The data generated from the experiment can then be processed by the commercial software package IVAS, which can be used to reconstruct the volume sampled. This thesis

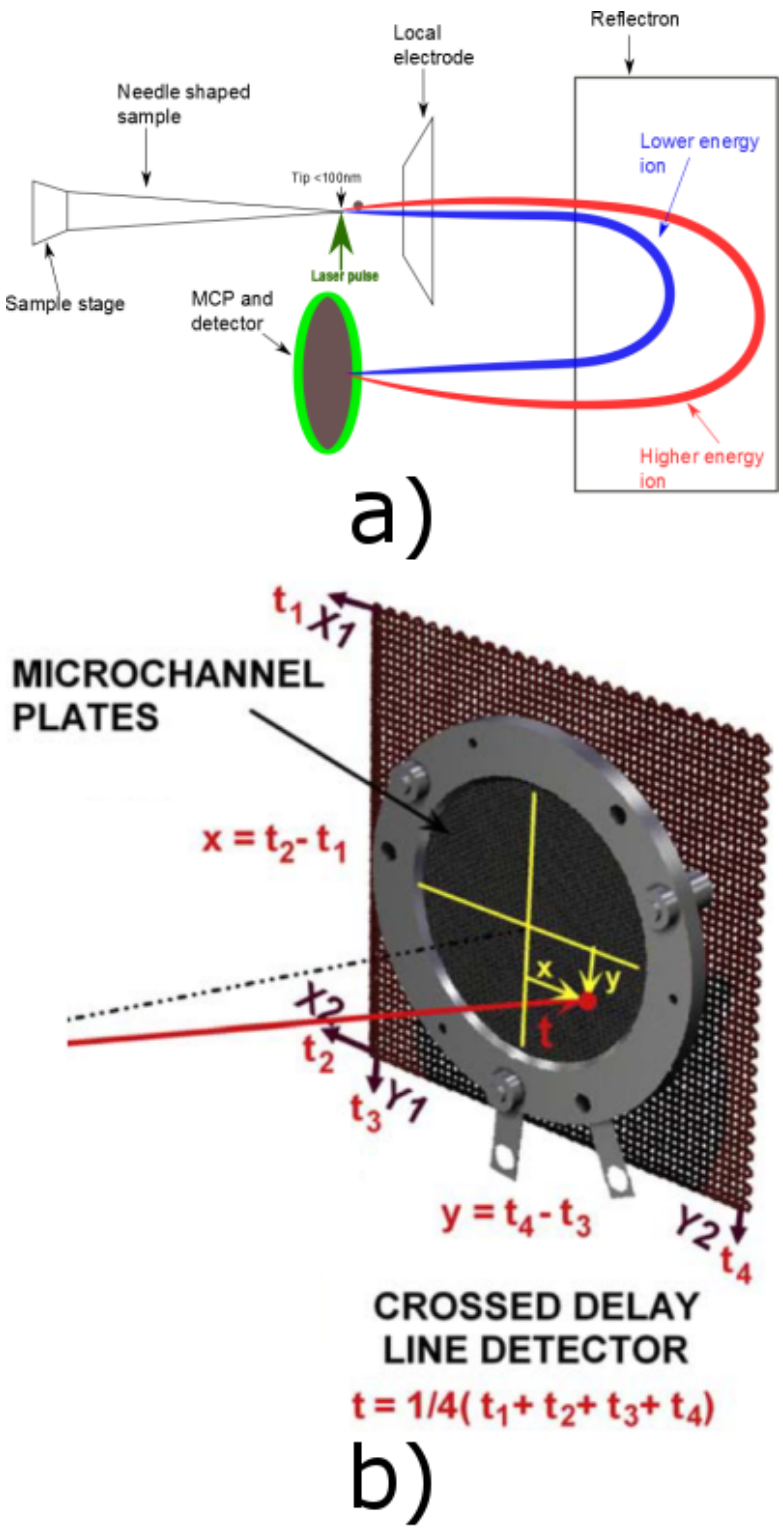


Figure 3.16: a)Simplified schematic of a LEAP 3000X-HR and 4000X-HR atom probe system. b) Schematic, adapted from [290], of an ion (represented by the red circle) incident to the MCP and DLD

utilised version 3.6.8. Reconstruction is primarily based on the hit (x, y) coordinates and the ToFs for each hit event, from the raw detector data. From this information M can be calculated by using equation 3.2, where m is the mass of the ion, n is the charge, e is the charge of an electron, V_0 is the total voltage, t is the ToF and d is the distance between the sample and the detector.

$$M = \frac{m}{n} = \frac{2eV_0t^2}{d^2} \tag{3.2}$$

3.4.2 Field evaporation

The intricate mechanisms that underpin the evaporation of atoms from a sample surface are still not entirely understood and are the subject of much research [289]. However, the consensus belief is that this process occurs as a result of a combination of ionisation and desorption mechanisms due to the presence of a strong electric field [289, 293]. As the surface atom is pulled away from the surface, an electron is transferred to the sample surface causing the surface atom to ionise. The process of this transfer can be thought of as an electron trapped in a potential, known as the Schottky hump [294], in which an energy barrier must be overcome by introducing an appropriate quantity of energy into the system [295]. It is due to this energy barrier that this scheme is often referred to as the 'image hump model'. Though there are other competing models [296] with differences, it is largely agreed that this is a thermally assisted process and therefore the energy barrier can be overcome by introducing thermal energy into the system. As quantum physics states an electron may tunnel through the energy barrier, this may also occur in this context with a given probability. The Schottky hump is a function of the electric field, hence a large electric field could reduce the size of this barrier and increase the likelihood of tunnelling occurring.

3.4.3 LEAP 3000X-HR and LEAP 4000X-HR

APT experiments were conducted on two different Imago atom probe machines: LEAP 3000X-HR at the University of Oxford and the LEAP 4000X-HR located at Centre of Advanced Energy Studies (CAES) in Idaho. The LEAP 3000X-HR was used entirely in the isothermal ageing investigation as well as to study the 14YWT2 as received and ion irradiated 14YWT2. The LEAP 4000X-HR was only utilised to study the neutron irradiated 14YWT3.

The machines differ mainly in terms of their laser pulse wavelength and optics. The LEAP 4000X-HR emits a blue wavelength of 355nm whereas the LEAP 3000X-HR emits a green wavelength 532nm [297]. The LEAP 4000X-HR also has an optics system situated in vacuum which allows for a more focused laser spot [298].

3.4.4 Parameter determination

One of the research objectives of this thesis is to study clustering phenomena, large datasets are required for statistical reasons. Therefore it is advantageous for APT experiments for this thesis to be conducted in laser mode. However, given the influence the parameters have on the data quality, it is beneficial for an calibration experiment to be conducted to determine suitable APT analysis parameters. This calibration experiment is discussed in chapter 4.

Experiments using the LEAP 4000X-HR were conducted in laser mode at $T = 55K$, $E_{laser} = 150pJ$, $\nu = 200kHz$ and $\Phi_{evap} = 0.005\,ions\,pulse^{-1}$. Unlike the experiments conducted on the LEAP 3000X-HR, analysis conditions for the LEAP 4000X-HR were not determined via a parameter determination experiment because of limited access to the instrument. Instead, parameters were based on research outcomes of experiments conducted by Bagot and Edmondson and were discussed via private communication.

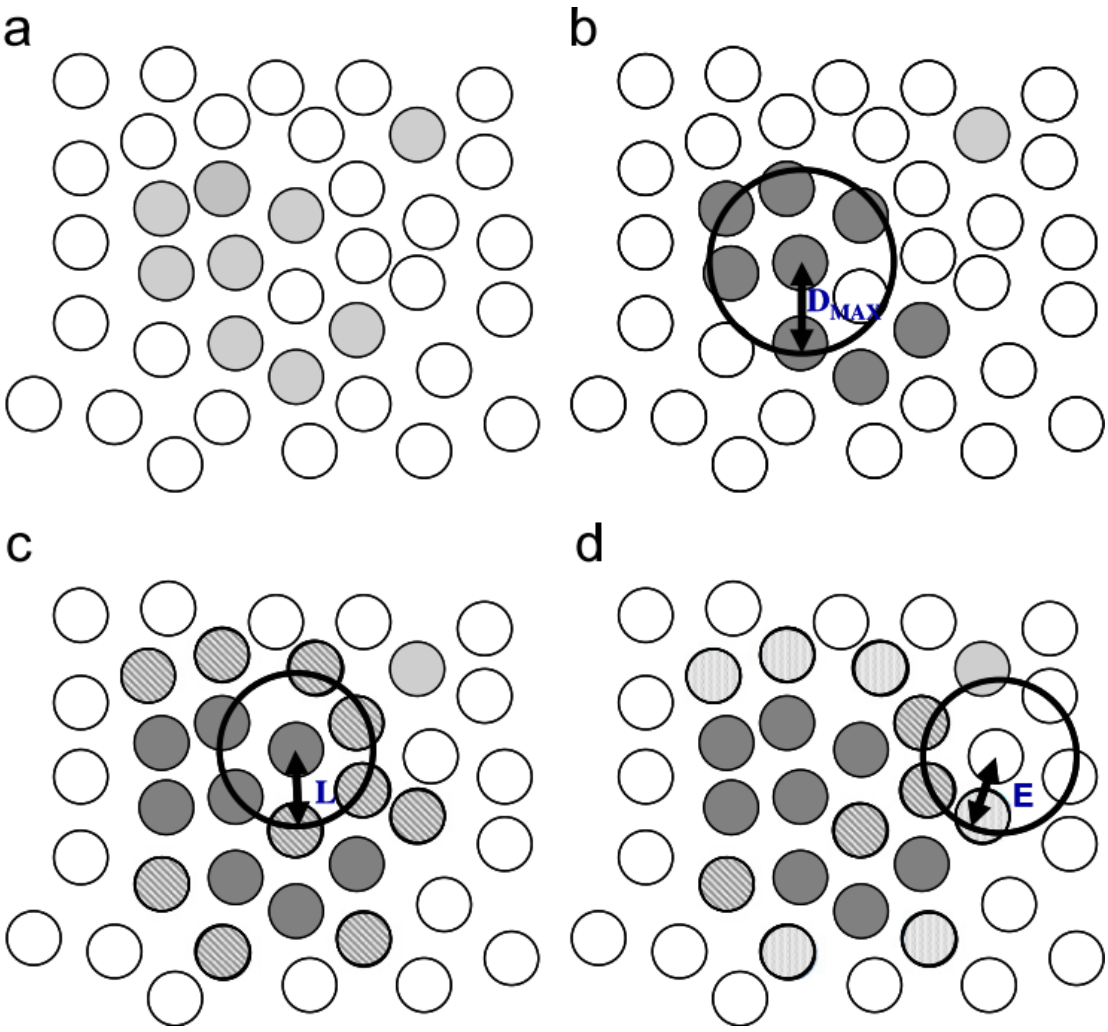


Figure 3.17: A physical representation of each of the maximum separation user-defined parameters [299] for a 1^{st} order ($\eta = 1$) cluster search. A 2D matrix containing cluster solute atoms shown in white and grey respectively (a), D_{max} is the maximum separation between cluster solute atoms (b), L is the maximum separation of cluster solute atoms of a different species (c) and E is the erosion distance in which atoms within a distance less than E are removed (d).

3.4.5 NFA dispersoid cluster analysis

The point cloud data produced from the post experimental processing can be used to determine whether clustering phenomena occurs. If clustering does occur, physical characteristics such as cluster composition and dimensional information can be extracted from the APT dataset. One of many methods used to isolate the clustering ions from the matrix is the maximum separation algorithm [300, 301]. This method is based on the assumption that solute cluster ions that are part of the cluster, are on average likely to be situated closer together in space relative to the matrix. Above this critical separation limit, the inter-solute ion spacing approaches that of the solute distribution in the matrix i.e. unclustered regions.

In addition to the species of the core cluster solutes atoms, 5 separate parameters need to be defined appropriately by the investigator and are referred to as D_{max}, N_{min}, L, E and η. D_{max} is the maximum distance between the core solute ions. N_{min} is the minimum number of core solute ions that have to be present within a cluster. L is the envelope distance where all ions from the solute ion are considered part of the cluster. E is the erosion distance which is responsible for excluding matrix ions from the cluster. Finally, η is the order parameter which specifies the number of nearest neighbours from a core solute atom [301]. Figure 3.17 illustrates the physical representation of D_{max}, L and E for a 1^{st} order ($\eta = 1$) cluster search within a two dimensional dataset.

3.4.5.1 Determining the core clustering solute ions

A χ^2 analysis was performed to determine the core cluster solute species to use within the maximum separation algorithm. The output from this test provides quantitative data that indicates whether specific solute distributions within the sampled volume are

binomially distributed. If the output from this statistical test suggested a departure from a binomially distributed solute, this could indicate micro-chemical phenomena such as clustering or segregation, has occured. Equation 3.3 shows the χ^2 test formula to be applied to the dataset.

$$\chi_e^2 = \sum_{n=0}^{n_b} \frac{(e(n) - f_b(n))^2}{f_b(n)} \tag{3.3}$$

where: $e(n)$ is the measured number of voxels which contain n number of ions out of a total n_b of ionic species and f_b is the corresponding number as determined from a binomial distribution.

The value of χ_e^2 is heavily dependant on the size of the subject dataset and increases with increasing sample size [289]. Therefore in order to fairly compare χ_e^2 from one dataset with that belonging to another, the χ_e^2 value must be normalised with respect to the size of the dataset. This can be done by calculating the Pearson coefficient, μ, using equation 3.4. μ ranges between 0 and 1, where 0 represents a random distribution and 1 indicates a non-random distribution. For a more detailed explanation into the application of χ^2 analysis and μ in atom probe data, the reader is reffered to [302].

$$\mu = \sqrt{\frac{\chi_e^2}{N + \chi_e^2}} \tag{3.4}$$

Table 3.6 shows $\bar{\mu}$ (averaged μ from three experimental repeats for each alloy state) for the Y, YO, TiO and O solutes within the as received 14YWT1, as well as the 14YWT1 aged for 8 months at $475℃$. The calculations were conducted using 1000 ions per voxel. There is no criterion to determine how many ions should be allocated per voxel. However as 1000 ions per voxel is commonly used in APT studies conducted on 14YWT1 [45], it has been used here too.

Table 3.6 suggest the Y and TiO concentration distributions are far from binomial in

both the as received 14YWT1 as well as the 14YWT1 aged for 8 months at 475℃. $\bar{\mu}$ for YO and O do depart away from a pure binomial distribution for both 14YWT1 alloy states. However $\bar{\mu}$ for YO and O is not as high as that belonging to Y and TiO. Though YO and O are highly likely to be part of an NFA dispersoid, their low concentrations within the dataset produces an appparent random solution.

The results in table 3.6 have indicated that Y and TiO ions are not binomially distributed. As these ions are principal NFA dispersoid elements [29, 64] it is likely this non-random distribution is due to clustering of Y and TiO solutes within the dataset. Therefore these ions will be designated as the core solute ions for use in the maximum separation algorithm.

Alloy state	$\bar{\mu}$				Average concentration $[at.\%]$			
	Y	YO	TiO	O	Y	YO	TiO	O
As received	0.80	0.42	0.89	0.27	0.09	0.07	0.22	0.03
8 month aged	0.77	0.39	0.79	0.34	0.11	0.08	0.24	0.03

Table 3.6: Average μ (Pearson coefficient) computed for each principal cluster ion within the as received 14YWT1 as well as the 14YWT1 aged for 8 months at $475°C$. Calculations of μ were conducted using 1000 ions per voxel. Average μ and concentrations were measured and averaged across three APT experimental repeats for each of the two alloys states.

3.4.5.2 Defining D_{max} and N_{min}

D_{max} and N_{min} are fundamental parameters that need to be defined when using the maximum separation algorithm [299]. They influence key metrics such as total cluster population and cluster radius [303] which could impact research outomes. Therefore it is vital that appropriate values are determined in a consistent manner.

Kolli and Seidmann proposed plotting the total number of clusters within the dataset

as a function of D_{max} and N_{min} [304]. Values for D_{max} and N_{min} would be deemed appropriate if a plateau and convergence had occured in the distribution. This is because the total cluster population within the dataset would be invariant to changes to D_{max} and N_{min}. Such a feature within an example Kolli and Seidman (KS) plot is shown in figure 3.18. Since there are multiple combinations of D_{max} and N_{min} that could be used within the maximum separation algorithm, the smallest values of D_{max} and N_{min} should be chosen for consistency [303, 304]. This in principal should maximise the population of smaller clusters [289].

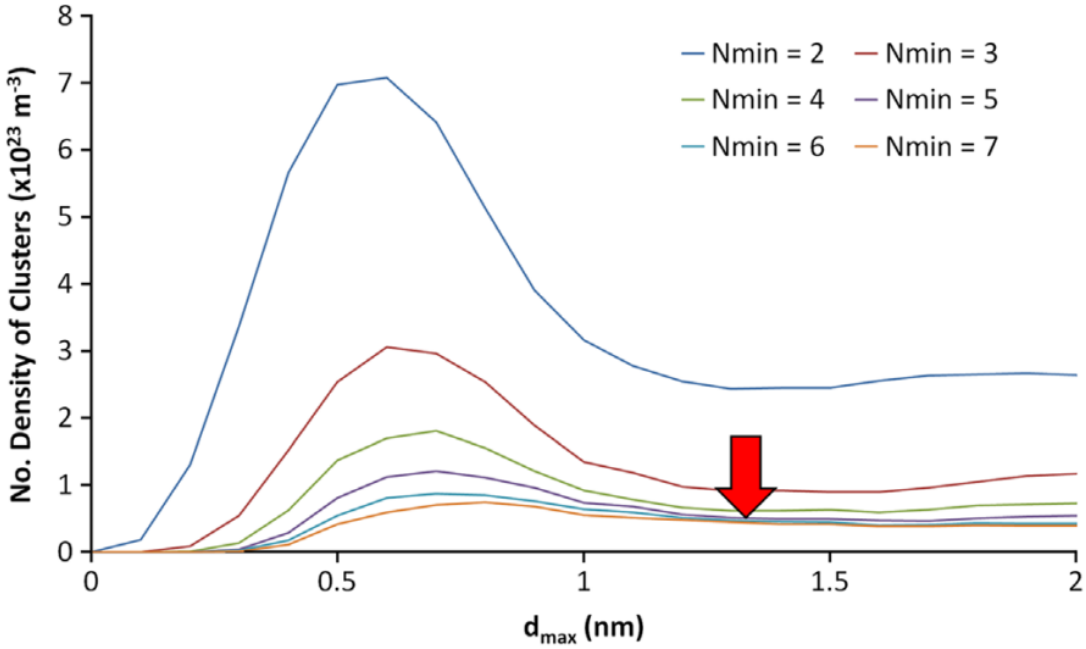


Figure 3.18: Example of a KS plot calculated for the case of an untreated 14YWT variant ($Fe-14Cr-2W-0.3Ti-0.3Y_2O_3$) [303]. As can be seen the distributions start to converge from $D_{max} > 1nm$ and $N_{min} = 5$. The arrow points to the smallest D_{max} and N_{min} at which the plateau and convergence occurs at.

KS plots have been drawn for two separate 14YWT1 APT datasets (as received - 23070 and aged for 8 months at 475℃ - 22826) in figure 3.19. A plateau and convergence of

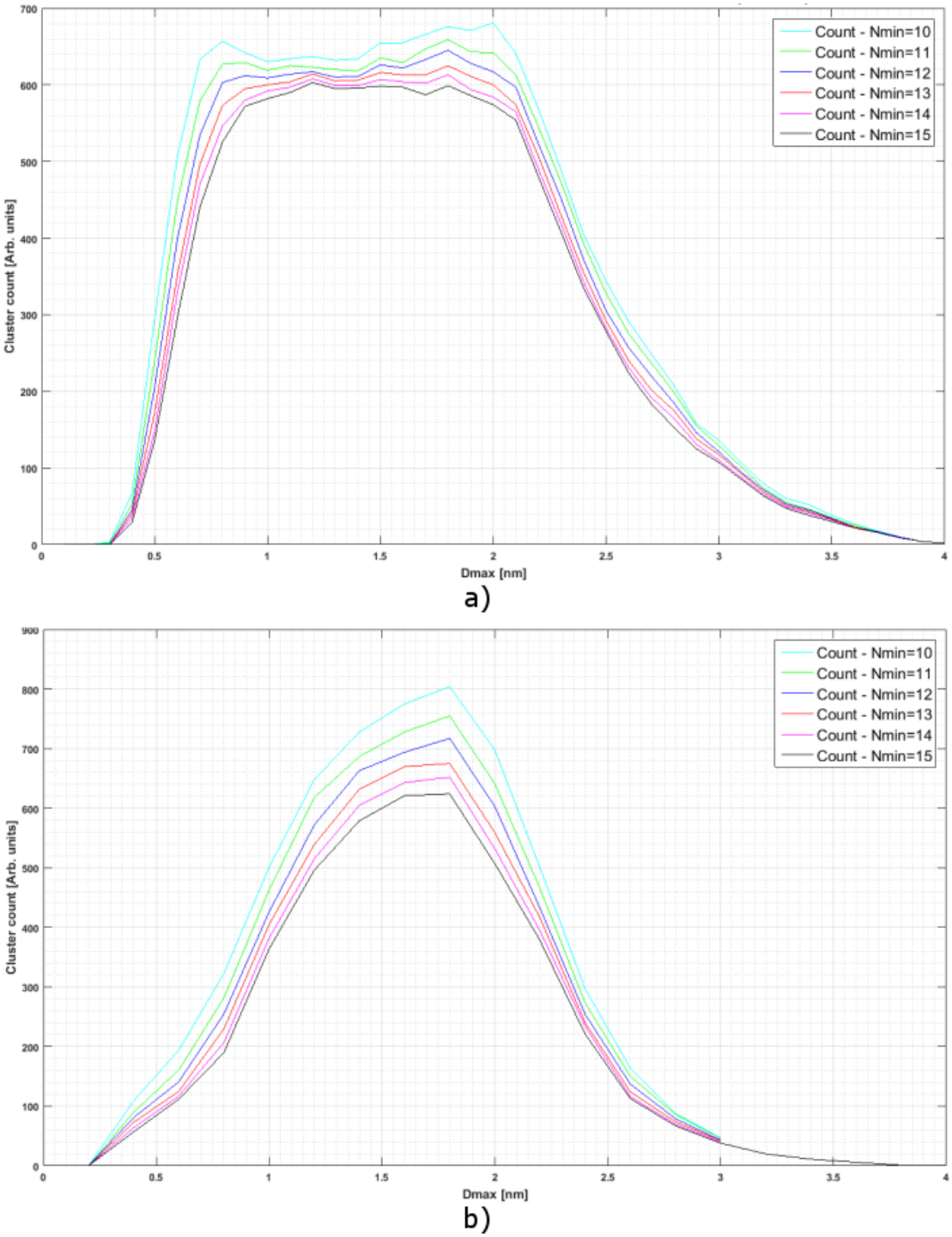


Figure 3.19: Kolli and Seidman plots for a) as received 14YWT1 (dataset 23070) and b) 14YWT1 aged for 8 months (dataset 22826) at $475°C$ using Y, TiO solute ions, $\eta = 1.0$, L and E not defined. Both a plateau and convergence can be seen to occur in a) when both $D_{max} > 1.1nm$ and $N_{min} > 9$, however only a convergence can be seen in b).

the distributions can be seen in figure 3.19a. However, only a convergence occurs in figure 3.19b. As is the case for the KS plot example shown in figure 3.18, values of D_{max} and N_{min} determined from the converged and plateaued regions in figure 3.19a can be substituted into the maximum separation algorithm. The KS plot in figure 3.19b, in which a plateau has not formed, shows that there is variance in the total number of clusters as combinations of D_{max} and N_{min} vary. Therefore values for D_{max} and N_{min} cannot be determined using the KS method for this particular dataset.

Inconsistencies in terms of its ability to determine D_{max} and N_{min} for NFA dispersoid cluster analysis have also been reported by Burrows [45] and Williams [303]. It is suggested that this could be due to varying solute distributions of Y and TiO and their concentrations within the sampled volume [45, 303, 305]. Varying field evaporation behaviour between different NFA dispersoids could also be a contributing factor [84]. Further investigation into the reason behind this inconsistency is beyond the scope of thesis and so wasn't explored further.

As this method performs inconsistently, the KS method cannot be applied to conduct NFA particle analysis in this thesis. Williams et al. proposed using the objective function method as an alternative criterion to reduce the number of possible combinations of D_{max} and N_{min} [303, 305]. This involves plotting the metric 'normalised counts' as a function of D_{max} for various values of N_{min}. The metric 'normalised counts' is calculated by using equation 3.5.

$$Normalised\,counts = \frac{N_{real} - N_{randomised}}{N_{real}} \tag{3.5}$$

Where: N_{real} refers to the total number of clusters found in the dataset for a given combination of D_{max} and N_{min}, $N_{randomised}$ refers to the total number of clusters found in a mass randomised version of the same dataset.

Mass randomisation involves re-assigning ions within the dataset with a new randomly selected mass-to-charge-ratio value whilst retaining their spatial coordinates [289]. This protocol removes the spatial-chemical correlations from the dataset and provides a method to assess clustering phenomena. Comparing the number of clusters that occur within the actual dataset with those that occur within the mass randomised dataset, will provide an indication to the number of "fake" clusters that may be included in the final cluster population.

Applying a threshold to the objective function will reduce the number of D_{max} and N_{min} combinations. Combinations of D_{max} and its corresponding N_{min} that lie above the threshold can be used as input values for the maximum separation algorithm. A conservative threshold of 0.99 was proposed by Williams [303, 305] and Burrows as well as London later applied this to their NFA APT datasets [45, 84]. Williams et al. suggest maximising D_{max} whilst minimising N_{min} as this will ensure that the largest number of small clusters in the sampled volume are considered in the cluster finding algorithm [303].

The objective function method is primarily a method to reduce the number of possible D_{max} and N_{min} combinations to be tried by the investigator and further qualitative analysis is required. This is done by comparing the the cluster index files (output files generated from the maximum separation algorithm) against the corresponding Y and TiO atom maps. If the cluster index files qualitatively resemble the atom maps then the D_{max} and N_{min} combination can be used. If not, then they should be discarded and the next combination that also maximises D_{max}, minimises N_{min} and also lies above the 0.99 threshold should be tried. Sample objective functions used in this thesis are shown in figures 3.20 and 3.21 for the same as-received (23070) and 14YWT1 aged for 8 months at 475℃ (22826) APT datasets.

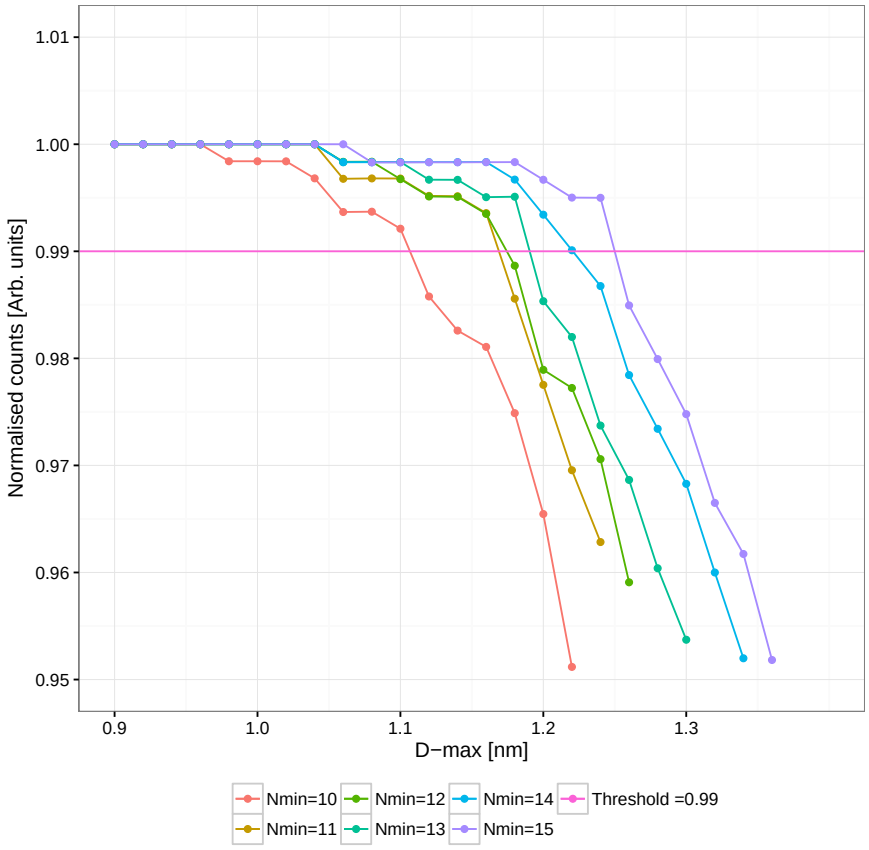


Figure 3.20: Objective function generated for the as-received 14YWT1 APT dataset - 23070

3.4.5.3 Defining L, E and η

The final set of parameters to be defined are the inclusion distance, L, the erosion distance, E and the order parameter, η. Hyde et al. advises setting $L = D_{max}$ [299]. As L is responsible for including atoms around the core solute ions, setting $L > D_{max}$ is likely to include a significant quantity of matrix atoms to the cluster. Hyde also suggests setting $E = L$ so as to minimise the matrix shell around the cluster periphery. Setting $E < L$ may not erode all the matrix ions around the periphery and conversely setting $E > L$ may erode the cluster itself. However it should be noted that the analysis

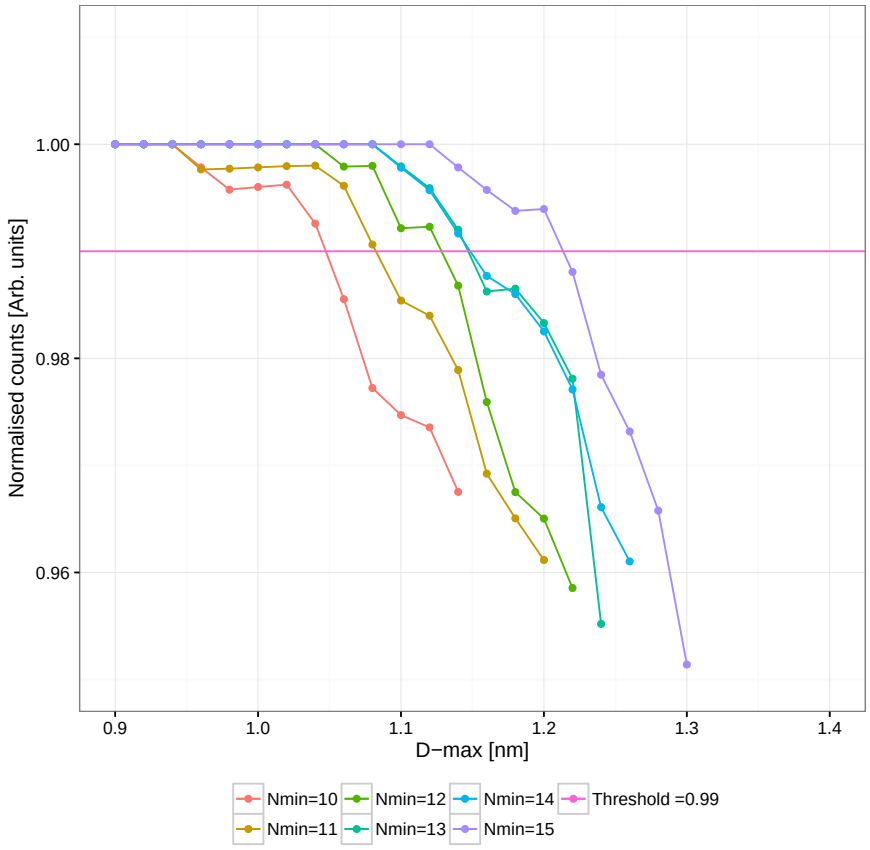


Figure 3.21: Objective function generated for the 8 month aged 14YWT1 APT dataset - 22826

is not strongly dependant on the choice of L or E [299].

Hyde's suggestions were implemented in this work and therefore all cluster analysis utilised $D_{max} = L = E$. $\eta = 1$ was used too. Burrows [45] showed this to be suitable when studying NFA dispersoids within 14YWT1.

3.4.5.4 Cluster analysis output

Combinations of D_{max} and N_{min}, derived from the objective function plots in figures 3.20 and 3.21, were substituted into the maximum separation algorithm for dataset

23070 - 14YWT1 as-received and dataset 22826-14YWT1 aged for 8 months. Three cluster index maps for three D_{max} and N_{min} combinations are shown in figures 3.22 and 3.23. Their corresponding Y and TiO atom map are also shown too.

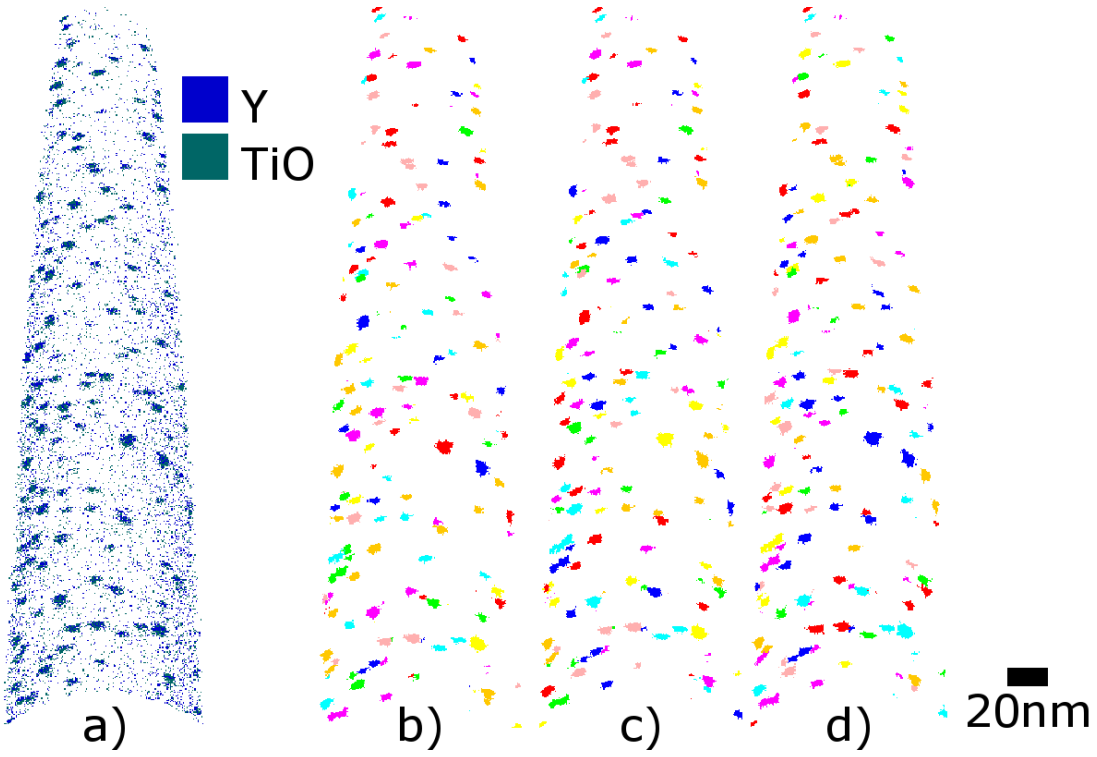


Figure 3.22: a)Y and TiO atom map of the as received 14YWT1 dataset (23070) b) cluster index map generated from the maximum separation method algorithm using the parameters: $D_{max} = 1.11nm$ and $N_{min} = 10$ (finds 611 clusters) c)$D_{max} = 1.15nm$ and $N_{min} = 11$ (finds 622 clusters) d)$D_{max} = 1.25nm$ and $N_{min} = 15$ (finds 601 clusters). $D_{max} = L = E$, $\eta = 1$. The parameters used to generate b) are used for this dataset as an obvious difference in the cluster index maps remains to be seen and N_{min} is also minimsed.

The parameter combinations used to generate the cluster index maps in figure 3.22 are stated in the caption. There isn't a significant difference between the cluster index maps and all three resemble the Y and TiO atom map well. This is probably because the cluster number is invariant to different D_{max} and N_{min} values, as seen in figure

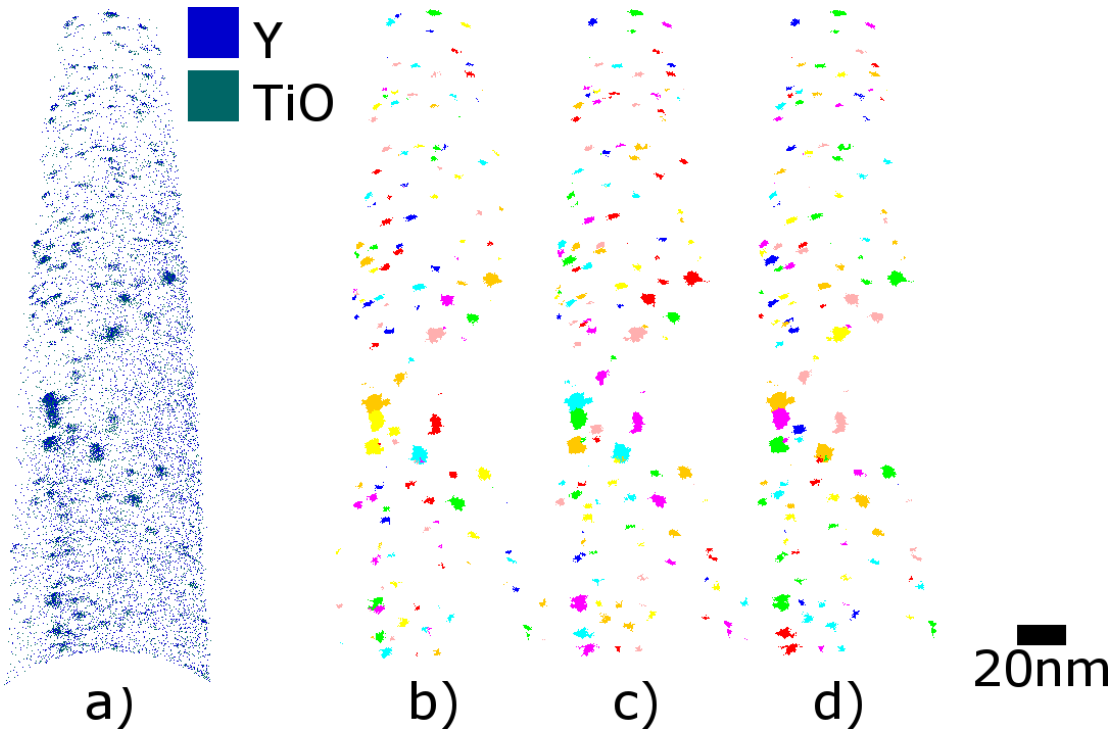


Figure 3.23: a)Y and TiO atom map of the 14YWT1 aged for 8 months APT dataset (22826). Cluster index maps are generated from the maximum separation method algorithm using the parameters: b)$D_{max} = 1.05nm$ and $N_{min} = 10$ (finds 543 clusters) c)$D_{max} = 1.15nm$ and $N_{min} = 13$ (finds 502 clusters) d)$D_{max} = 1.15nm$ and $N_{min} = 14$ (finds 480 clusters). $D_{max} = L = E$, $\eta = 1$. The parameters used to generate c) are used for this dataset as the index map generated resembles a) the most.

3.19a. The parameters chosen to generate figure 3.22b is deemed the most appropriate as D_{max} is maximised whilst minimising N_{min}.

Similarly the parameter combinations used to generate the cluster index maps in figure 3.23 are stated in the caption. The clusters in figure 3.23b look smaller than those in the atom map in figure 3.23a. However, the clusters in both figure 3.23c and 3.23d resemble the atom map well. In the interest of maximising D_{max} and minimising N_{min}, the parameters used to generate figure 3.23c are chosen as the most suitable.

The parameters used to generate the cluster index maps shown in figures 3.22b and 3.23c

are also in range with those used by Williams [303], Burrows [45] and London [306].

3.4.6 α' and Ti cluster analysis

α' and Ti-rich clusters found in the isothermally aged 14WT were analysed using a different analysis protocol. Due to their inconsistent and low number density, relative to the NFA particles in the 14YWT, isoconcentration surface mapping was observed to be more suitable. Isoconcentration mapping has been used to study α' precipitates in the literature e.g. [125, 271, 307]. In these studies isoconcentration thresholds were set at $28at.\%$ [271], $34at.\%$ [125], and $30at.\%$ [307]. The α' isosurface mapping conducted in this thesis was set at $30at.\%$ threshold for decomposed Cr ions only. This threshold was chosen primarily because on average, the precipitates were well replicated.

Ti rich clusters followed the same methodology. However the isosurface threshold placed upon each Ti cluster was varied. This was because they were present in very low number densities. Therefore the isosurface could be adjusted appropriately to capture the entire cluster.

High gradient regions for both types of clusters were then exported to a new cluster pos file so that the spectrum could be re-ranged and ensured that peak overlaps were accounted for.

3.4.7 Trajectory aberrations around clusters

Trajectory aberrations can arise when non-uniform evaporation occurs. The evaporation can be non-uniform as surface atoms from a microstructural feature such as a precipitate, requires a lower field to evaporate relative to the rest of the sample. This leads to preferential evaporation and changes the surface topogrophy of the sample to one similar to that shown in figure 3.24 [309]. As seen, the APT tip has been preferentially evaporated relative to the rest of the sample and a non-hemispherical tip shape has formed.

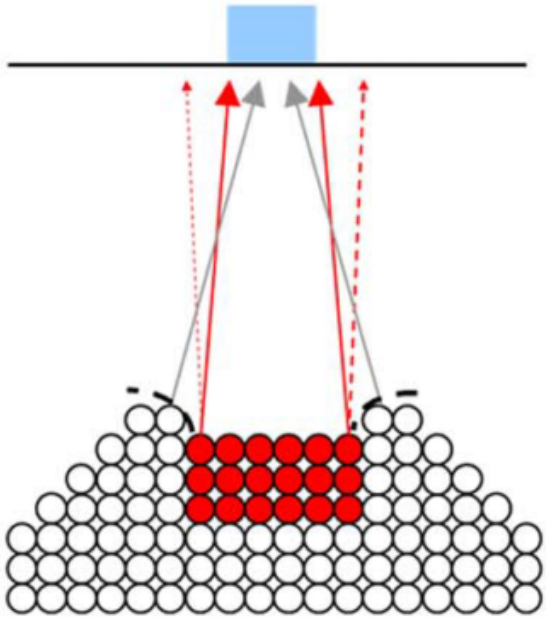


Figure 3.24: Ion trajectories close to the surface of an evaporated 2^{nd} phase (red circles). The second phase has a lower field relative to the parent matrix (white circles). Matrix ions can be seen to cross the interface on the image of the 2^{nd} phase [308].

The flattened region perturbs the field, deflecting the ions evaporating from the higher field region into the lower field region. This perturbs the ion's flight path to the detector and will increase the apparent density of the lower field region [287, 310, 311, 312]. This is depicted in figure 3.25a.

If the precipitate requires a higher field, the curvature on the precipitate surface is larger than the matrix surface and evaporated ions are repelled outwards. This causes an apparent decrease in density within the reconstructed volume, as depicted in figure 3.25b.

Such phenomena is usually observed in alloys possessing more than one phase and GBs [289].

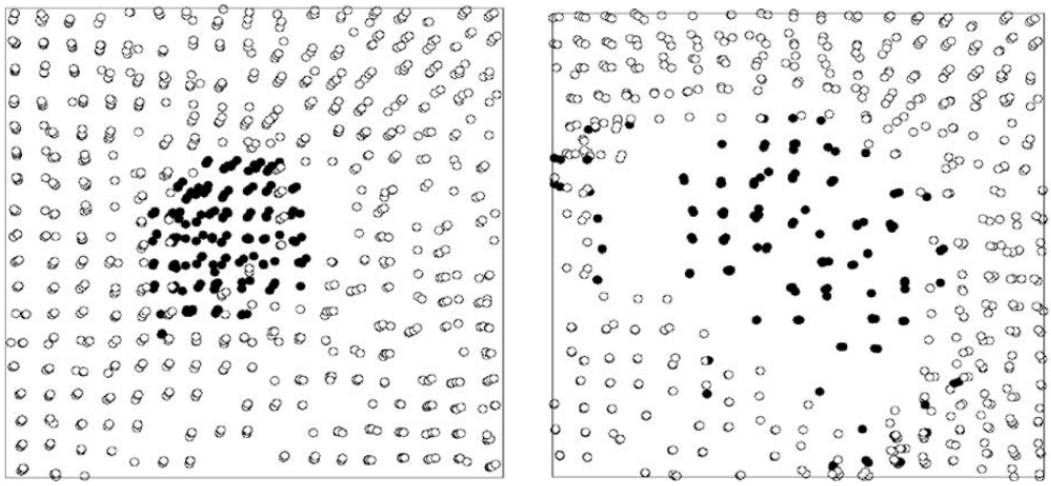


Figure 3.25: Simulations of a reconstructed binary alloy containing a)low field precipitates b) high field precipitates [312]. Grey circles are matrix atoms A and black circles are precipitate atoms B. The reconstructed low field precipitate shows the inclusion of matrix atoms within the compressed precipitate in a). b) shows the a depleted zone where the precipitate atoms fall outside of the particle

3.4.7.1 Trajectory abberations in 14YWT NFAs

The dispersoids within 14YWT NFAs have a lower evaporation field relative to the matrix [313]. This, as described above, results in the preferential evaporation of the NFA dispersoids relative to the matrix [171]. Defocussed matrix ions fall into the precipitate image on the detector as depicted in figure 3.25a. This adulterates the NFA dispersoid composition [84] and increases it's density to around three times higher than the matrix [314, 83]. Another symptom is that NFA dispersoids are usually compressed along the x and y axes. The z-direction is least effected as this phenomena only effects lateral coordinates.

Methods to correct the NFA dispersoid compression along the x and y axes have already been discussed in section A.2.1. To address the increase in cluster density and inclusion of matrix ions within the dispersoids, a matrix correction is often performed [303, 84].

In this protocol, apart from Cr, Y, Ti and O, concentrations of all other elements that may be detected inside inside the cluster is assumed to be 0. The concentration of Cr inside the cluster is 'matrix corrected' using equation 3.6 [306]. Detected concentrations of Y, Ti and O are left uncorrected. This matrix correction protocol shall be applied to all NFA dispersoid internal concentration analysis.

$$Cr_c^* = Cr_c - \frac{Cr_m}{Fe_m} Fe_c \tag{3.6}$$

Where: Cr_c^* is the corrected concentration of Cr in the cluster, Cr_c is the detected concentration of Cr inside the cluster, Cr_m is the matrix concentration of Cr, Fe_m is the matrix concentration of Fe and Fe_c is the cluster concentration of Fe.

3.4.7.2 Trajectory abberations in 14WT

The second family of clusters that are to be studied in this thesis are the Cr rich α' precipitates. Contrary to the NFA dispersoids, α' precipitates are only slightly susceptible to magnification effects. Simulations indicate that only 2% extra Cr from the matrix is included in the reconstructed α' precipitate [312]. Experimental observations disagree with these simulation results - Novy et al. reported that the core concentration of Cr within the precipitates did not have any correlation with the size of the precipitate, and only depended on experimental conditions [33]. However Kuksenko et al. stated that it is not possible to completely exclude the possibility of artifical dilution of the Cr concentration, as the observed density within the clustered region was twice as high as the matrix [271]. Given the conflictions in the literature and that no defined protocol to take into account these potential APT induced effects exists, this thesis will assume the findings from [33] hold true in the 14WT non-NFA alloy too.

The third type of clusters that occur in this thesis are Ti rich precipitates. The litera-

ture does not provide any indication to their susceptibility to the magnification effect. Therefore this thesis ignores magnification effects in relation to the Ti rich precipitates too.

3.4.8 The shadow effect

The shadow effect disturbs the density distribution of ions within a fully reconstructed APT dataset. This phenomenon tends to effect datasets that have been acquired using laser-mode.

During laser-mode APT experiments, the laser pulse illuminates one side of the sample. This induces an inhomogeneous temperature distribution across the tip. As a result, the illuminated side has a higher evaporation rate relative to the shadow region. This asymmetric evaporation behaviour results in a tip shape that has an asymmetric radius of curvature, and therefore is not hemi-spherical [315]. Figure 3.26 shows a TEM micro graph of a 304 stainless steel APT sample after an APT experiment in laser-mode. The illuminated side is seen to have a larger radius at 127nm, than the non-illuminated side which has radius of 110nm.

As stated in section A.2.1, the point project model assumes the tip has a hemi-spherical shape [317]. The detected ions that originate from the illuminated side are, greater in number and are compressed in the reconstructed dataset. This is because the reconstruction assumes a single radius for the reconstruced tip [318]. This causes an apparent higher number density within the illuminated side relative to the shadow region.

The shadow effect has been observed to occur within APT datasets of DSAs acquired by London on the LEAP 3000X-HR in laser mode [89]. In particular, Fe and Cr ion distributions have been most effected.

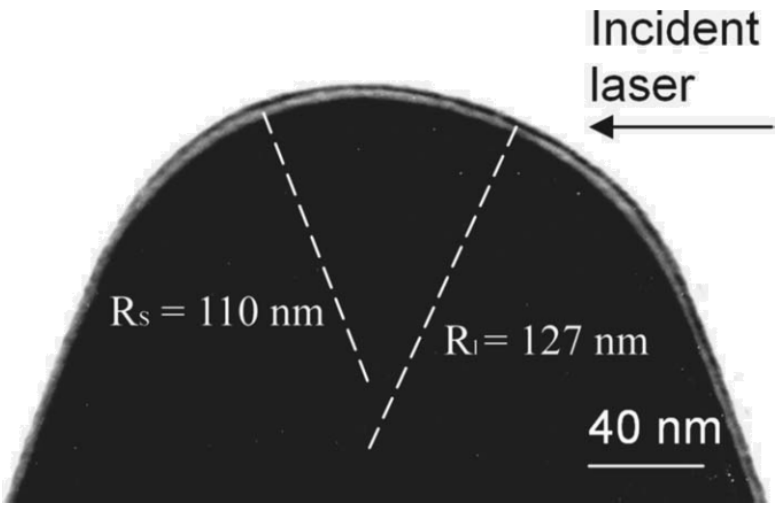


Figure 3.26: TEM micro graph of 304 stainless steel after APT analysis using laser mode, pulse energy of 0.6nJ. The illuminated side is seen to have a larger radius than the non-illuminated side [316].

3.5 Microhardness tests

Microindentations were conducted on the pre-aged and aged samples of 14WT and 14YWT1 at room temperature using a Matsuzawa MHT-1, as shown in figure 3.27a.

The premise of this hardness measuring technique involves the deformation of a sample's surface by applying a load of known weight.

A pyramidal shaped diamond indenter was used to make an impression on the sample's surface using a 200g load, which was held for 20 seconds. This is depicted in figure 3.27b. Using the dimensions of the diagonal lines impressed onto the sample surface after the indentation, the Vickers hardness, H_v, can be calculated using equations 3.7 and 3.8.

$$H_v = \frac{F}{A} \tag{3.7}$$

$$\text{where } A = \frac{d_{rms}^2}{2sin(\frac{\theta}{2})} \tag{3.8}$$

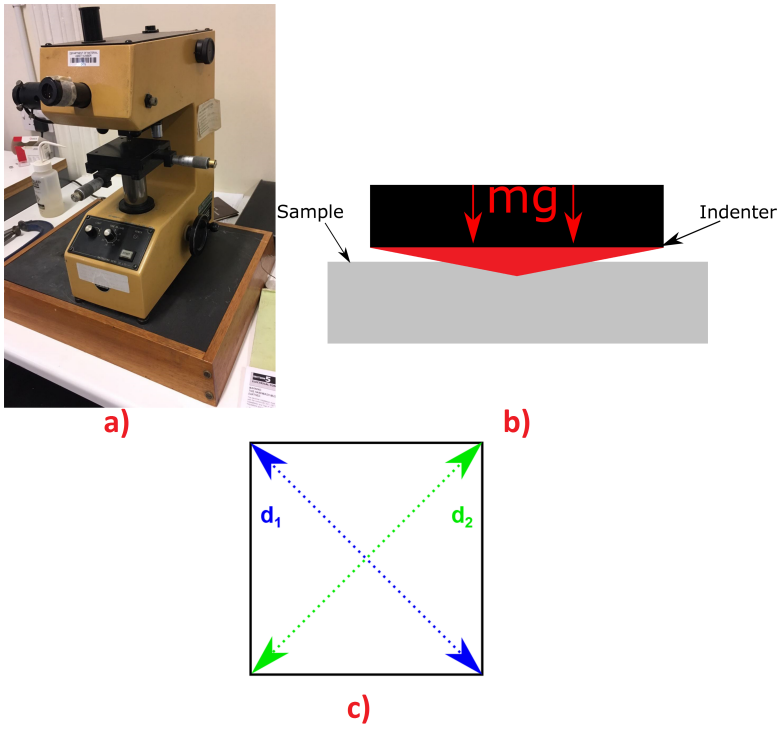


Figure 3.27: a) Microindenter used to measure the Vickers hardness of the aged 14WT and 14YWT1 (Matsuzawa MHT-1) b) schematic depicting how a microindenter indents a sample surface c) a flattened 3D square based pyramid representing the outline of a typical microhardness indent created from the procedure shown in b)

where F, A and d_{rms} represent the force applied, the indenter contact area and the root mean square of the diagonals d_1 and d_2 in figure 3.27c respectively. θ is the indenter tip angle which is 136° for the indentations made using the Matsuzawa MHT-1. Each H_v presented in this thesis is averaged across five indents for each sample and is quoted in $kgf\,mm^{-2}$.

Equation 3.9 can be used to link the indentation hardness of a metal with its bulk properties [319, 320], and remains valid for systems containing NFAs [321, 322].

$$H_v = 3\sigma_y \tag{3.9}$$

where σ_y is the yield stress of the material.

Indentations and their diagonals were analysed using an Scanning Electron Microscopy (SEM). d_{rms} ranged from $42-43\mu m$ for the as-received 14WT and $27-28\mu m$ for the as-received 14YWT1. Accordingly, indentation depths for the as-received 14WT and 14YWT1 ranged from $6-6.14\mu m$ and $3.86-4\mu m$ respectively and was calculated using the relation given in equation 3.10.

$$Indentation\,depth = \frac{d_{rms}}{7} \tag{3.10}$$

Chapter 4

LEAP 3000X-HR calibration for 14YWT

Chapter summary

A series of APT experiments were conducted on 14YWT1 to determine appropriate APT analysis parameters for the LEAP3000X-HR at the University of Oxford. Laser mode analysis parameters were systematically varied for each calibration experiment. The specimen temperature (T) and laser pulse energy (E_{laser}) were varied from 45–55K and 0.2–0.4nJ respectively. Evaporation rate (Φ_{evap}) and pulse repetition rate (ν) were fixed to 0.005 $ions\,pulse^{-1}$ and 200kHz. Parameter combinations were deemed appropriate for use in investigations described in chapter 5 and 6 if they fulfilled three criteria. In order of importance: 1) differences between the APT measured concentrations of Fe, Cr and W within 14YWT1 in comparison with bulk concentrations must be minimised; 2) maximise the dataset Signal to Noise Ratio (SNR) amongst all, 3) Maximise the mass resolution of the $^{56}Fe^{2+}$ peak at 27.97Da and spatial resolution. It should be noted that this calibration experiment does not seek to find the optimum combinations

of parameters. The minimisation or maximisation of particular entitities stated in the three criteria is determined relative to all of the parameter combinations tested here. This calibration study concluded that all three critieria were satisfied when APT experiments, on the LEAP3000X-HR, were conducted in laser mode at $T = 55K$ and $E_{laser} = 0.4nJ$. Therefore all APT experiments on the LEAP3000X-HR conducted in this thesis shall use the following analysis parameters: $\mathbf{T = 55K}$, $\mathbf{E_{laser} = 0.4nJ}$, $\nu = \mathbf{200kHz}$ and $\mathbf{\Phi_{evap} = 0.005\,ions\,pulse^{-1}}$.

4.1 Introduction

As stated in chapter 3, atom probe experiments require a defined set of parameters: cryostat stage temperature, evaporation rate, pulse repetition rate and laser pulse energy for laser mode or pulse fraction for voltage mode. These parameters impact the evaporation physics of APT surface atoms on the sample as well as their detection and may have a significant influence on the outcomes from the research. The relationships between the parameters are complex and are often interdependent such that an adjustment of one parameter may affect the data quality.

While there are numerous calibration studies for APT data acquisition [323, 324], only one study has examined Fe-Cr binary model systems [325]. Adopting the parameters from [325] may be inappropriate for the 14YWT NFA due to the presence of additional alloying elements and two distinct phases: matrix and dispersoids. As a result, it is likely that the field evaporation behaviour encountered in Fe-Cr binary alloys will indeed not be similar [326]. Differences in the field required to evaporate different elements and phases could induce preferential retention or evaporation [118, 327] as well as trajectory aberations. Such phenomena could affect the SNR in the mass spectrum [328, 329], and would have implications for the overall research outcomes yielded from the experiments.

As no systematic APT calibration experiments have been conducted on 14YWT, a series of experiments were conducted in laser mode using varied temperatures and laser energies. If all three of the following criteria are fulfilled the corresponding operational parameters set shall be utilised in the investigations detailed in chapters 5 and 6[1]. The three criteria are: 1) differences between the APT measured bulk concentrations of Fe, Cr and W only within 14YWT in comparison with reference bulk compositions must

[1]As stated in the chapter summary, the minimisation or maximisation of parameters stated in the three criteria may not be the optimum parameter combination. Rather they are the most apropriate parameters relative to the parameter combinations tested in this calibration experiment

be minimised, 2) maximise SNR and minimise background noise, 3) maximise the mass resolution of the $^{56}Fe^{2+}$ peak and dataset spatial resolution.

4.2 Background and objectives

4.2.1 Materials and samples

The subject material used in this parameter determination experiment was 14YWT1 as-received. SEM images of the samples used in the laser mode calibration studies can be seen in figure 4.1. APT samples were prepared via the Focussed Ion Beam (FIB) lift-out technique described in appendix A.1, and have a tip radius of curvature $< 100nm$.
Two samples were used for the laser mode calibration experiments. The sample in figure 4.1a was used for the laser mode experiments at $45K$; the sample in figure 4.1b was used at $50K$ and $55K$. Two samples were required because the first sample, shown in figure 4.1a, fractured during the first experiment at $50K$.

4.2.2 Calibration tests

Given both atom probe modes (laser and voltage) as well as the number of parameters that can be varied, there are many combinations and therefore conditions that can be tested. Smaller datasets are usually obtained during voltage mode acquisition resulting in a lower number of precipitates captured in the reconstructed volume. As such laser-mode was chosen in order to collect larger datasets. Larger datasets offer the possibility of capturing a greater number of precipitates and the opportunity for more robust statistics.
Table 4.1 summarises the parameters used in each of the experiments and the order at which they were conducted. The pulse repetition rate (ν) and evaporation rate (Φ_{evap}) were maintained constant at $200kHz$ and $0.005\,ions\,pulse^{-1}$. The selection of these two

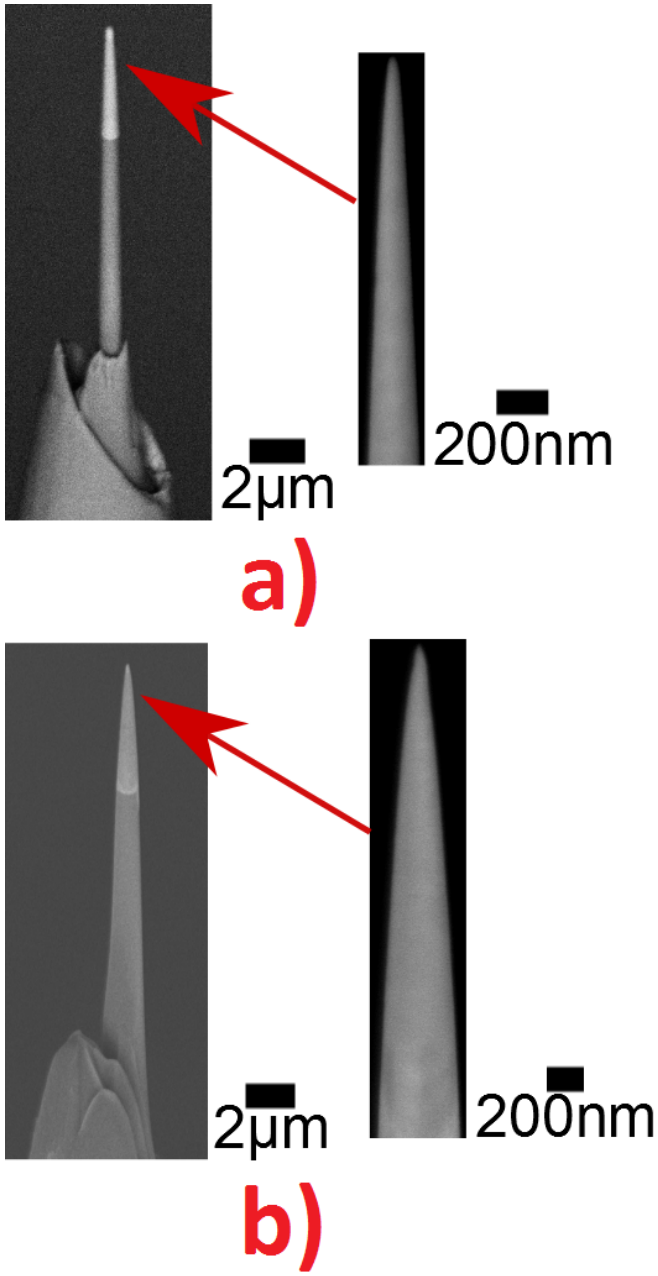


Figure 4.1: SEM images of the two APT samples used in the laser mode calibration experiment. The sample shown in a) was used for experiments at T=45K only, and the sample shown in b) was used in experiments at T=50K and 55K.

Order of execution	1	2	3	4	5	6	7	8	9	10	11	12
Temperature [K]	45				50				55			
Pulse energy [nJ]	0.20	0.25	0.30	0.40	0.20	0.25	0.30	0.40	0.20	0.25	0.30	0.40

Table 4.1: Summary of the parameters used in the laser mode calibration experiments. Target evaporation and pulse repetition were held constant at 0.005 ions/pulse and 200kHz respectively.

parameters were based upon research outcomes from APT experiments conducted by Burrows and Edmondson and were discussed via private communication. The specimen temperature (T) was varied from $45-55K$ in increments of $5K$ and laser pulse energy (E_{laser}) ranged from $0.2-0.4nJ$. Calibration experiments were conducted under ultra-high vacuum ($< 4 \times 10^{-11} torr$) with 3×10^6 ions collected under each parameter combination. Finally, reconstruction of the data followed the protocol described in appendix A.2.1.

4.2.3 Calibration study objectives

The three objectives of this calibration experiment are defined at the end of section 4.1. Accurate concentration measurements of elements via APT is important for investigations described in chapters 5 and 6. As shown in table 3.2, the three main elements within 14YWT1 are Fe ($81.31at.\%$), Cr ($14.14at.\%$) and W ($0.8at.\%$). Previous characterisation studies on 14YWT1 conducted by Gorley [44] have confirmed that these elements have concentrations that fluctuate $> 10\%$ of their mean over an analysis length scale of $20\mu m$. Other minor solutes present in 14YWT1, such as Ti, Y and O, have concentrations that fluctuate more than this, and as such only Fe, Cr and W were tracked in these calibration experiments.

The minimisation of background noise in the mass spectrum is important when trying to identify smaller peaks belonging to elements which are low in quantity within the

sample. A high level of background noise can obscure such peaks, making it hard to identify and range them, which can lead to errors in composition measurements.

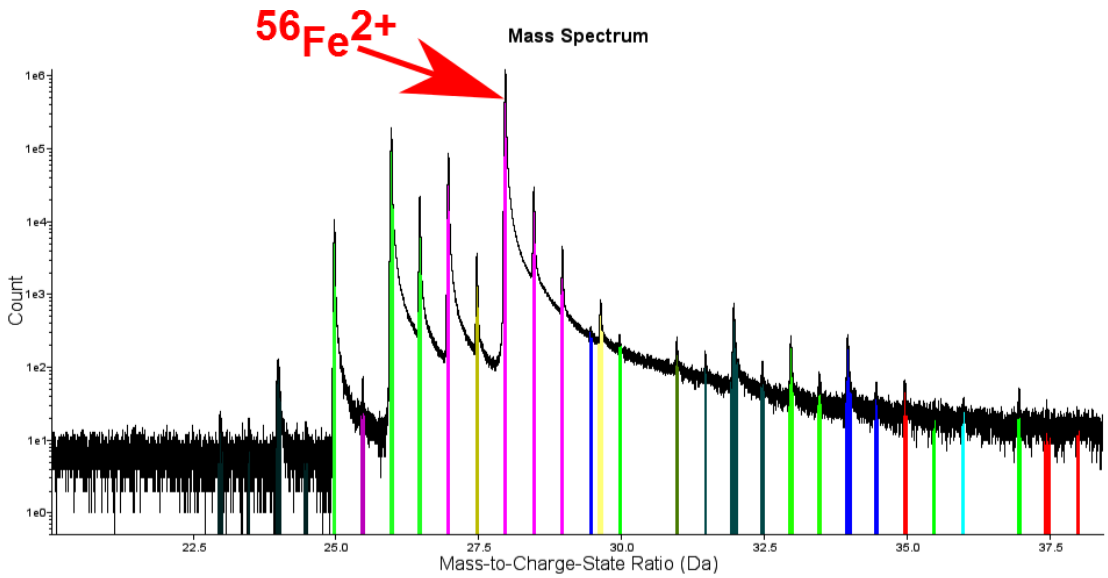


Figure 4.2: A portion of the mass spectrum dataset from an as-received 14YWT1 NFA presenting the realtive heights of the peaks. Counts axis uses a log scale. The $^{56}Fe^{2+}$ contains the most number of ranged ions and therefore is most dominant.

Figure 4.2 shows the dominant peak within the APT spectrum to be the $^{56}Fe^{2+}$ peak which occurs at 27.97Da. It contains the largest proportion of the ions recorded in the experiment. Ion peaks in the mass spectrum collected in laser-mode often have an accompanying thermal tail as shown in figure 4.3a. This is due to the uncertainty over the instant at which a surface atoms are evaporated. As laser energy increases, this thermal tail is expected to increase. This is because the sample resides at a higher temperature longer than the duration of the pulse. In this period, off-pulse evaporation events may occur. This thermal tail can often mask peaks from minor alloying elements of the material such as Y. This could lead to incorrect compositions and atom maps being derived from the data, due to the misidentification of the minor element as absent. As such, minimising the thermal tail, particularly for the case of the materials of interest

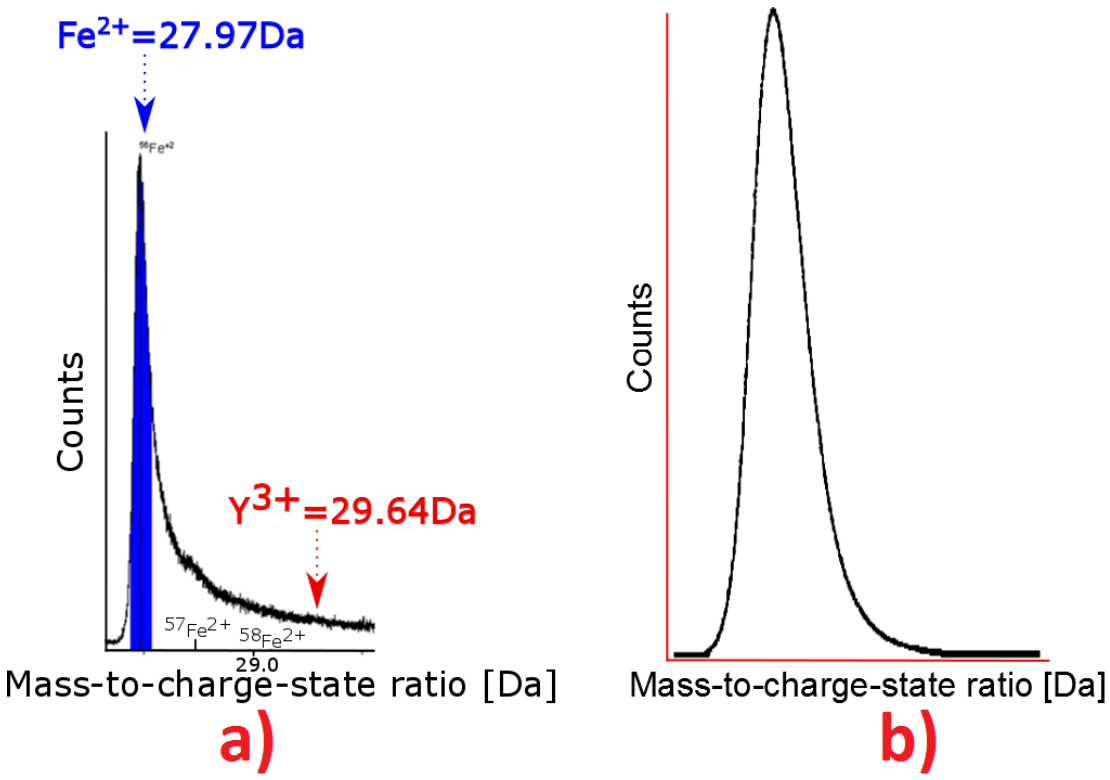


Figure 4.3: a)Example of a $^{56}Fe^{2+}$ at 27.97Da peak with a relatively large thermal tail from the dataset acquired in laser mode at 45K and 0.2nJ. The thermal tail may mask the neigbouring peaks of minor elements e.g. the Y peak at 29.64Da, and increases the spectrum noise. b)Demonstration of the EMG function profile: a sharp rising edge and a long falling tail

in this thesis, is highly desirable.

The mass resolution of the peak can be defined through measurements of a peak breadth using Full Width Half Maximum (FWHM). Often measuring the FWHM is done manually using the IVAS software package, which may introduce ranging inconsistencies. A more consistent approach would be to fit an asymmetric Gaussian function, referred to as the EMG function hereafter. As can be seen from figure 4.3b, the profile of the EMG function provides a reasonable fit to the profile of the $^{56}Fe^{2+}$ peak. The corresponding FWHM for this fitted function can be extracted and recorded.

4.2.3.1 EMG function

To conduct the FWHM analysis, a Matlab function called 'rangeCorrector.m', originally written by London [306], was adapted and applied. This code detects the peaks in the spectrum and fits asymmetric Gaussians functions to the peaks. The EMG function, as it is commonly referred to in the literature [330], is shown in equation 4.1.

$$y = A.\frac{|\lambda|}{2}\left[1 - \text{erf}\left(\frac{(x_g - x)\lambda}{\sigma_g|\lambda|\sqrt{2}} + \frac{\sigma_g}{|\lambda|\sqrt{2}}\right)\right].exp\left(\frac{x_g - x}{\lambda} + \frac{\sigma_g^2}{2\lambda^2}\right) \tag{4.1}$$

where A is the amplitude of the EMG function, λ is the asymmetry coefficient - a dimensionless number ranging from 0.01-0.15 in 14YWT1 APT datasets, x_g is the Gaussian centre, σ_g is the Gaussian width and erf is the error function.

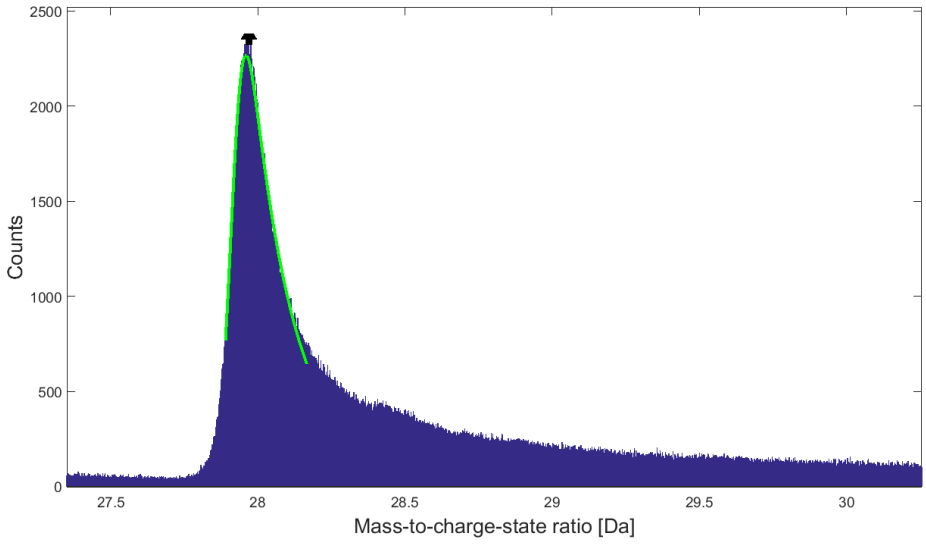


Figure 4.4: A reduced range portion of the full mass spectrum from the dataset acquired in laser mode at 45K and 0.2nJ is shown in blue. The light green line is the outline of the EMG function that has been fitted to the peak.

A demonstration of the Matlab function fitting an EMG function to the $^{56}Fe^{2+}$ peak

shown in figure 4.3a, is presented in figure 4.4. As can be seen the profile of the function fits the $^{56}Fe^{2+}$peak well.

4.3 Results and discussion

4.3.1 Objective 1: minimising the difference between APT measured concentrations and that measured by EPMA

4.3.1.1 Assessing the extent of peak overlaps in the spectrum

Before concentrations of the major elements within 14YWT1 can be measured, ranging errors from peak overlap must be minimised. Once initial ranging was completed, the deconvolution of peaks protocol was implemented on all the datasets acquired from these experiments using IVAS software.

Peaks belonging to principal NFA cluster forming elements such as O, Ti and Y, and more complex molecular ions such as $^{48}Ti^{16}O$, and $^{89}Y^{16}O$, were distinct and did not overlap with neighbouring peaks. Matrix ions were predominantly detached too and generally could be identified by matching the heights of satellite peaks e.g. W.

However, for the case of ^{54}Fe and ^{54}Cr an overlap occurs at both their 2^{nd} and 1^{st} ionisation states ($27Da$ and $54Da$ respectively). A useful protocol to help identify peaks is to compare the measured peak height with that belonging to the expected peak heights for the candidate ion and its isotopes. This has been done in figure 4.5b and 4.5c as well as 4.6b and 4.6c for sections of a mass spectrum belonging to the dataset acquired at $T = 55K$ and $E_{laser} = 0.4nJ$. The height of the labels represents the proportion of the peaks that could belong to the candidate ion inside the label. Considering the mass spectrum ranging from $25Da$ to $28.5Da$ in figure 4.5a, it is evident from figure 4.5b that the peaks occuring at $\sim 27Da$, $\sim 28Da$ and $\sim 29Da$ belong largely to the

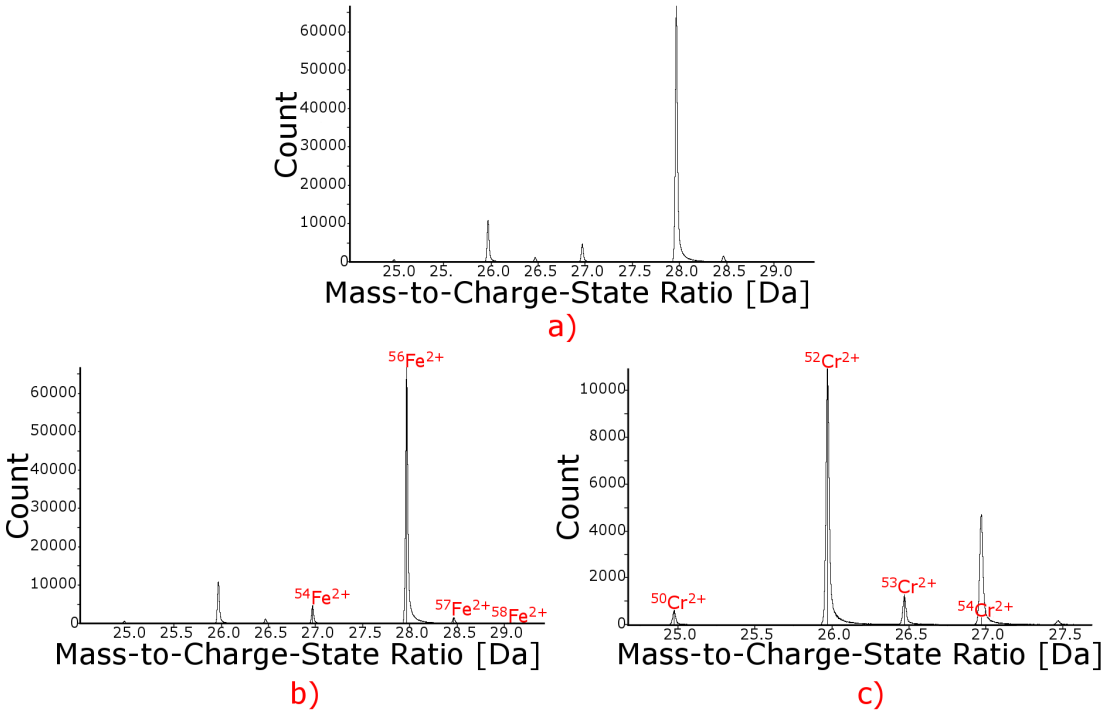


Figure 4.5: a), b) and c) are unranged sections of the mass spectrum from the dataset acquired at $T = 55K$ and $E_{laser} = 0.4nJ$. b) is the same portion of the mass spectrum shown in a), but also includes labels identifying potential Fe peaks. The heights of the labels corresponds with the number of counts contributing to the peak identified. c) is a portion of the mass spectrum ranging from $25Da$ to $27.5Da$ belonging to the same dataset. Peaks thought to belong to Cr have been identified and labelled. The height of the labels in c) also represent the contribution of Cr counts to the corresponding peak. The peak at $\sim 27Da$ can be seen in both b) and c) to overlap with ^{54}Cr and ^{54}Fe, but is comprised $^{54}Fe^{2+}$ more than $^{54}Cr^{2+}$.

family of Fe ions. Figure 4.5c shows that apart from the peak occurring at $\sim 27Da$ the rest of the peaks identified as potentially Cr peaks do indeed belong to the Cr isotopes. Therefore the peak overlap occurring at $\sim 27Da$ can be ranged as Fe as it is predominantly comprised of $^{54}Fe^{2+}$, and not $^{54}Cr^{2+}$ as shown in figure 4.7a.

Now consider the unranged mass spectrum ranging from $\sim 50Da$ to $\sim 58Da$ in figure 4.6a. Potential Fe peaks and Cr peaks have been labelled in figures 4.6b and 4.6c respectively. The peak at $\sim 56Da$ thought to belong to $^{56}Fe^{+}$ in figure 4.6b is the only

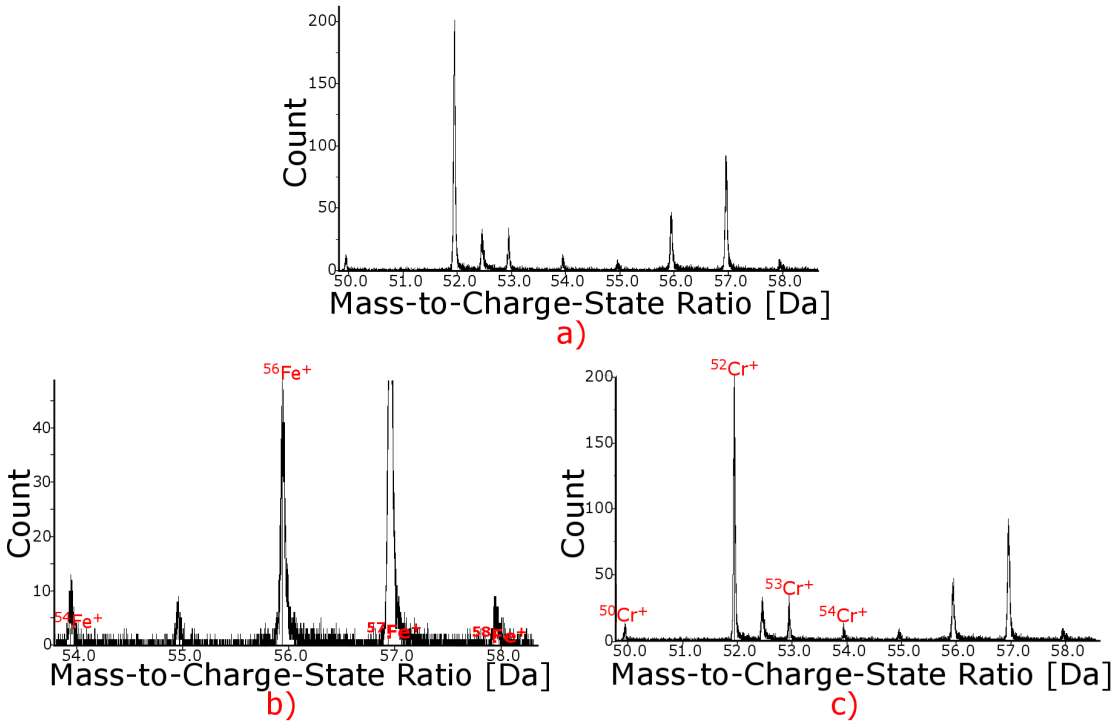


Figure 4.6: a), b) and c) are unranged sections of the mass spectrum ranging from $50Da$ to $58Da$ from the dataset acquired at $T = 55K$ and $E_{laser} = 0.4nJ$. b) is a portion of the mass spectrum ranging from $54Da$ to $58Da$. Peaks thought to belong to Fe have been identified and labelled. The height of the labels in b) represent the contribution of Fe counts to the corresponding peak. c) is the same portion of the mass spectrum shown in a), but also includes labels identifying potential Cr peaks. The peak at $\sim 54Da$ can be seen in both b) and c) to overlap with ^{54}Cr and ^{54}Fe, but is comprised of $^{54}Cr^+$ more than $^{54}Fe^+$.

peak that matches with the expected count. The actual peak height at $\sim 54Da$ does not match with the expected count for $^{54}Fe^+$. The peaks at $\sim 57Da$ and $\sim 58Da$ also do not match the expected peak heights of $^{57}Fe^+$ and $^{58}Fe^+$. Further analysis showed those peaks (at $\sim 57Da$ and $\sim 58Da$) to belong to $(FeH)^+$ ions. Therefore the only Fe peak ranged in this section of the mass spectrum was that occurring at $\sim 56Da$ as shown in figure 4.7b. The Cr candidate peaks are labelled in figure 4.6c. As can be seen, the identified Cr peaks match with the expected counts for those peaks well. This

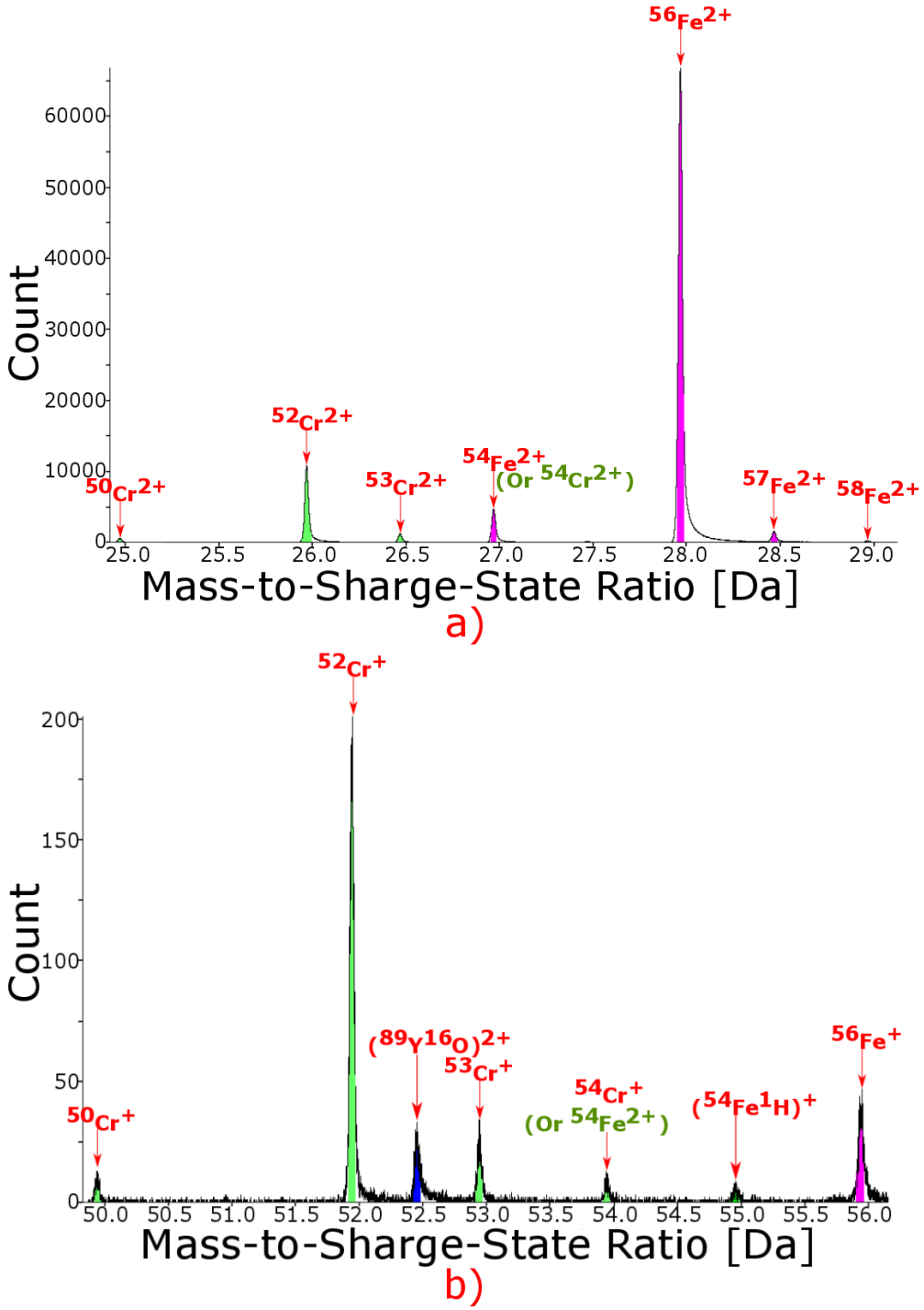


Figure 4.7: An example of peak overlap occuring for ^{54}Fe and ^{54}Cr at $27Da$ and $54Da$. For the case of the peak at $27Da$ in a), it was determined that it was largely made up of $^{54}Fe^{2+}$, whereas the peak at $54Da$ in b) was largely comprised of $^{54}Cr^{+}$.

includes the overlap occurring at $\sim 54Da$. Therefore the peaks occurring at $\sim 52Da$, $\sim 53Da$ and $\sim 54Da$ were ranged as Cr peaks which are also shown in figure 4.7b.

Peak Da	Total number of ions within the peak	Number of Fe ions within the peak	Number of Cr ions within the peak
27	143213	133996 (93.6%)	9217 (6.4%)
54	413	169 (40.9%)	244 (59.1%)

Table 4.2: Results from the 'Decomposition of peaks' protocol showing the count contributions to the 27Da and 54Da peak from Fe and Cr. Brackets show the proportions as a percentage.

As both the $\sim 27Da$ and $\sim 54Da$ of these peaks are comprised of both types of ions, bulk compositions measured from the dataset would yield inaccurate concentrations of Fe and Cr. To account for the mixed content of these peaks the 'Decomposition of peaks' protocol as described in appendix A.2.3 was implemented. Results from the implementation of this protocol are shown in table 4.2 which confirms that the $27Da$ and $54Da$ were ranged correctly as they are comprised mainly of Fe and Cr ions respectively. This process was repeated for all datasets acquired and was taken into account when determining the quantities of Fe and Cr within the APT datasets.

4.3.1.2 Comparing Fe, Cr and W concentrations measured from APT experiments with that from EPMA

The compositions measured by APT were normalised with those determined by EPMA for Fe, Cr and W, and are shown in figure 4.8. Since the concentrations of the minor

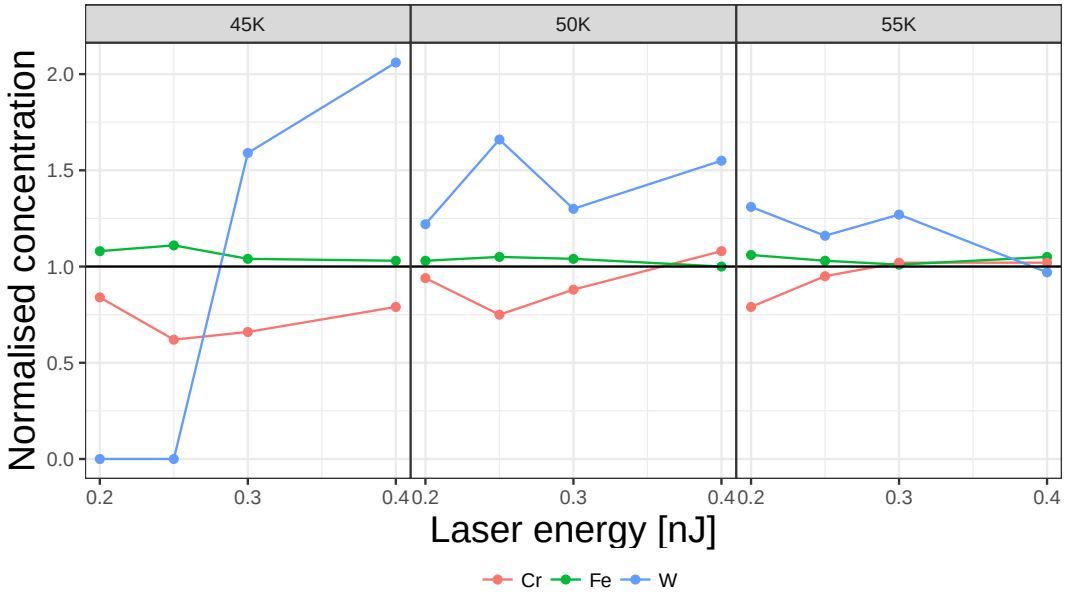


Figure 4.8: Quantities of Fe, Cr and W, normalised to EPMA measured concentrations of these major elements as a function of laser energy. Black solid line represents the reference ratio as measured by the EPMA analysis.

solutes such as Y, Ti, O, Mn and Si fluctuate significantly, these elements have not been considered as part of this calibration experiment. A normalised value of 1 means the APT and EPMA elemental concentrations are equal. Concentrations of Fe are closely matched for most of the conditions while concentrations of Cr and W range significantly. As the temperature increases the difference between the APT and EPMA measured concentrations of these elements reduce.

No W was detected from the experiments conducted at $T = 45K$ and $E_{laser} = 0.2nJ$ as well as $T = 45K$ and $E_{laser} = 0.25nJ$ as shown in figure 4.8. W elemental and molecular ion peaks were absent from the mass spectrum for both of these datasets. Figure 4.9 shows sections of the mass spectrum, belonging to the dataset acquired at $T = 45K$ and $E_{laser} = 0.2nJ$, where the W^{3+}, W^{2+} and W^{1+} peaks should be located (as highlighted in the figure). No W peaks regardless of the charge state, are present within the mass

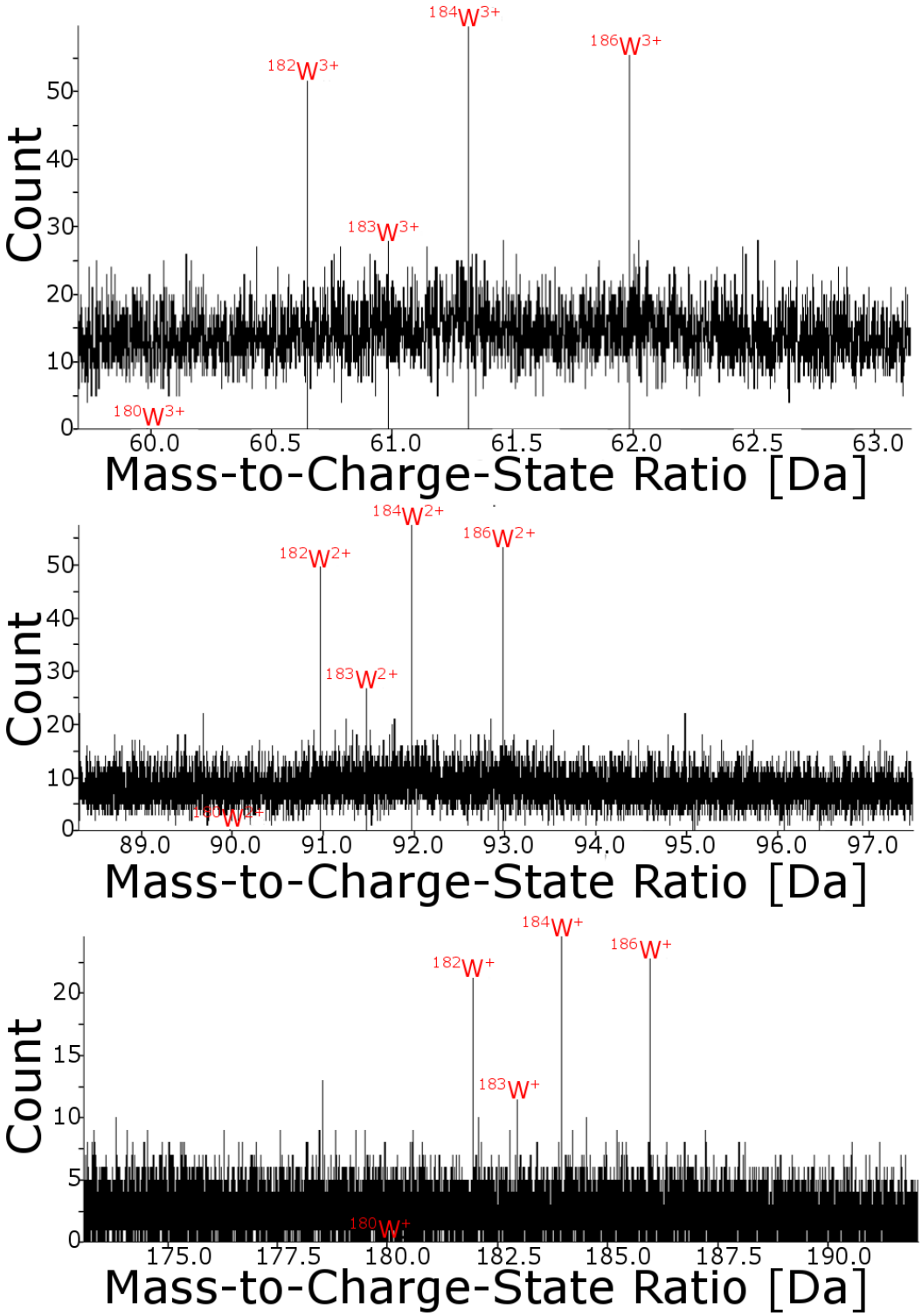


Figure 4.9: Sections of the mass spectrum from the dataset acquired at $T = 45K$ and $E_{laser} = 0.2nJ$. W peaks are not apparent and only background noise is detected. Labels mark the position where the peaks should occur. Their differing heights represent the expected relative counts for each of the W isotopes.

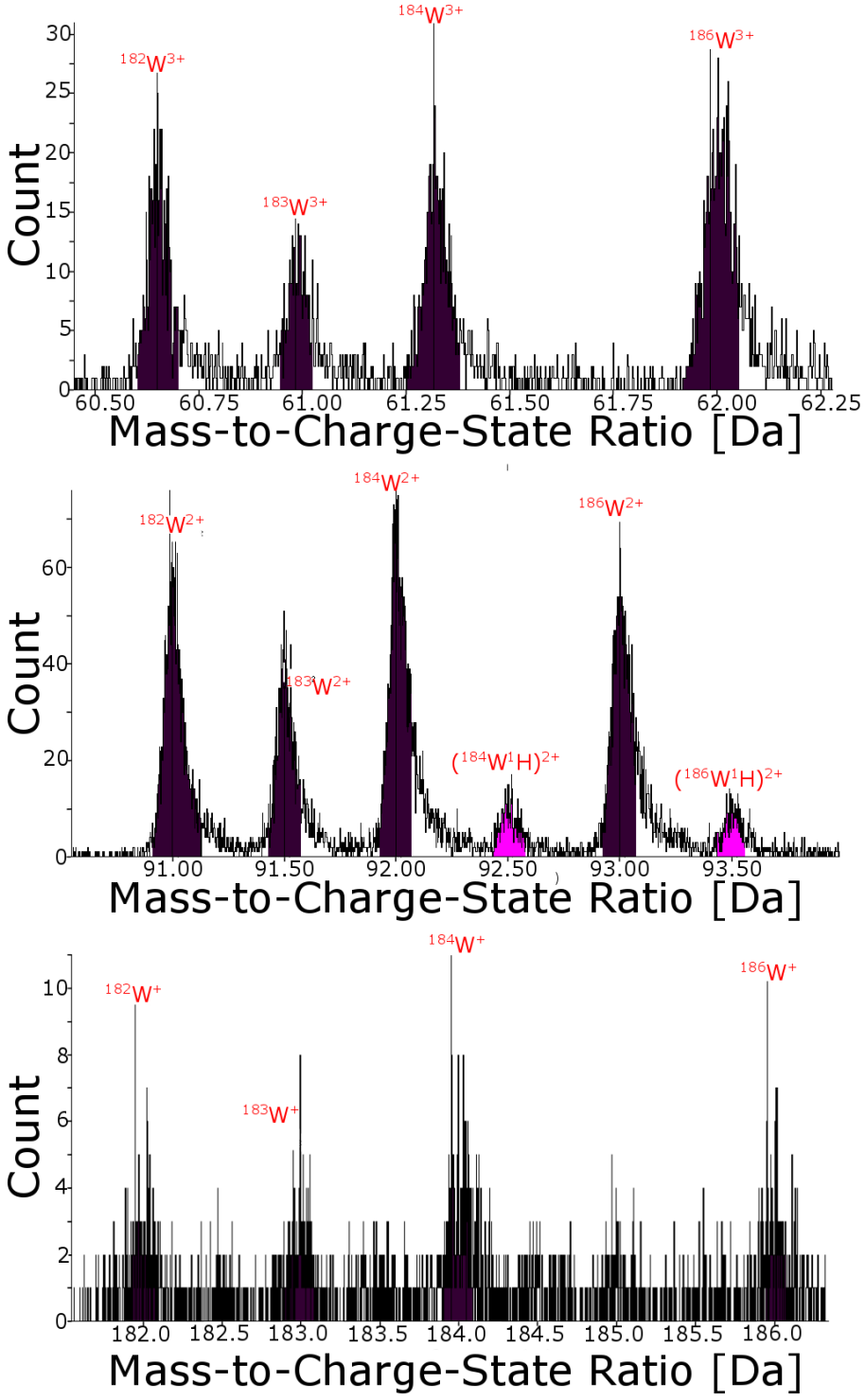


Figure 4.10: Sections of the mass spectrum from the dataset acquired at $T = 55K$ and $E_{laser} = 0.4nJ$ in which W (plum filled) and WH (pink filled) peaks are present.

spectrum belonging to the dataset acquired at $T = 45K$ and $E_{laser} = 0.2nJ$. Therefore W cannot be identified and ranged and does not contribute to the overall bulk W composition. The peaks for the charged states of W listed here are usually observed in 14YWT1 APT datasets including those in these calibration tests. W^{3+}, W^{2+} and W^{1+} peaks can clearly be seen in figure 4.10 which shows portions of the mass spectrum from the dataset acquired at $T = 55K$ and $E_{laser} = 0.4nJ$. Previous characterisation studies have indicated that the main elements are present in varying quantities throughout the sample [44]. As these alloys were made from pre-alloyed powders it is not improbable that there are microstructural regions depleted of W. However as stated in the previous section, extensive characterisation studies have not observed such regions and W was always detected to be present in varying quantities. Further, W was detected in the datasets acquired at $T = 45K$ $E_{laser} = 0.3nJ$ as well as $E_{laser} = 0.4nJ$. Therefore W is present in the sample.

Alternatively, it may be that either W ions are not being evaporated from the sample, or that they are evaporated but are not detected in quantities greater than the background count. According to the image hump model [295], the evaporation fields for Fe, Cr and W are $33V\,nm^{-1}$, $29V\,nm^{-1}$ and $57V\,nm^{-1}$ respectively [331]. These numbers show that a relatively strong electric field is required to evaporate W surface atoms. Therefore it may be that the experiments conducted at $T = 45K$ and $E_{laser} = 0.2nJ$, as well as $T = 45K$ and $E_{laser} = 0.25nJ$ are unable to provide the required conditions to evaporate W and therefore it is preferentially retained. As the surrounding atoms evaporate, the field is enhanced around the remaining W surface atoms leading to their evaporation. As the W is not detected in these datasets, they probably evaporate off pulse and contribute to the background.

Figure 4.8 also shows that Cr and W are often underestimated and overestimated re-

spectively[2]. As temperatures and laser energies increase the Cr and W lines start to converge towards 1.0 - an observation congruent with [332]. The underestimation of the Cr concentration could be due to Cr preferentially evaporating between pulses. The relatively low evaporation fields of Cr, as well as its high abundances relative to W support this theory. As the Cr evaporates between the pulses, many of these evaporation events could remain undetected and identified as background noise. If they are detected, significant errors would be associated with their ToFs as they are not correlated to a pulse. Consequently, these ions would have an incorrect value of M which could either broaden the Cr peaks or contribute to the background spectrum count if their ToFs are distorted enough. These preferential evaporation events lower the proportion of ranged Cr atoms within the dataset. This artificially increases the W concentration within the dataset. As Cr has often been observed to preferentially evaporate within the Fe-Cr binary alloys [33], this proposed scenario is probable.

Fe's profile in figure 4.8 can be seen to reside just above 1.0. This marginally high concentration is unlikely to stem from improper ranging techniques. It is more likely that it is a consequence of overestimating and underestimating W and Cr respectively. APT datasets measure concentration in units of at.%, which compares the relative numbers of one atom to another. If there is a net loss in the combined number of W and Cr atoms, as is the case here, the proportion of Fe atoms will be artificially higher.

At $T = 55K$ and $E_{laser} = 0.4nJ$ all three elemental concentrations are closely matched. It is possible that increasing the temperature or laser energy could further minimise the difference between APT measured concentrations and that measured by EPMA. However for the purposes of this thesis, conducting APT experiments at $T = 55K$ and $E_{laser} = 0.4nJ$ will meet the needs of the experiments described in chapters 5 and 6.

[2]EPMA measured concentration of Fe, Cr and W within 14YWT1 are: 81.31, 14.14 and 0.8 at.% respectively.

4.3.2 Objective 2: maximise the SNR and minimise background count rate

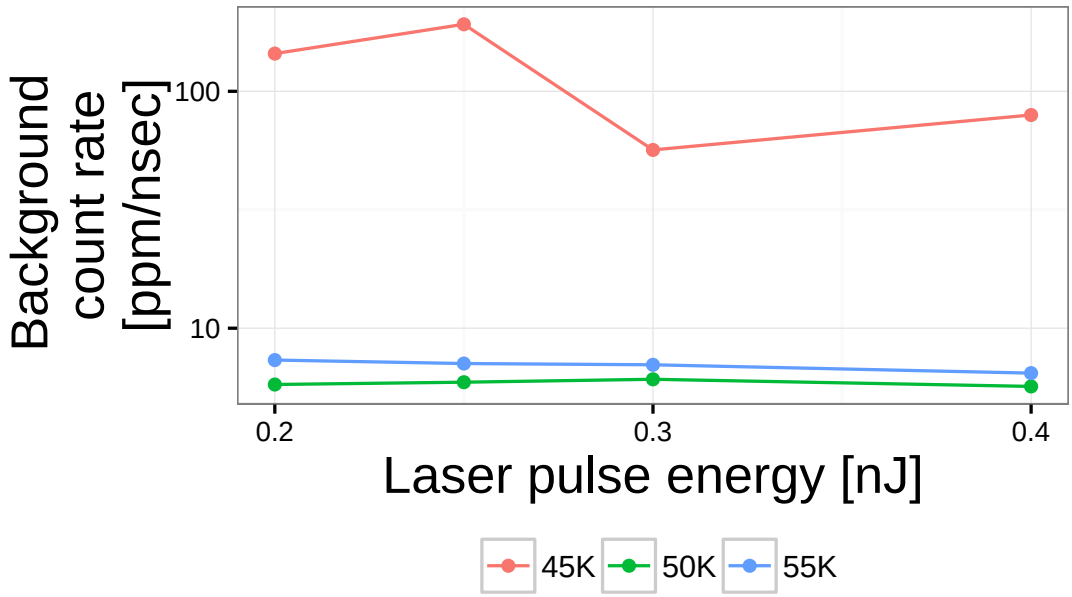


Figure 4.11: Average background count rate as a function of laser pulse energy.

The average background rates during each of the experimental runs are shown in figure 4.11. Ideally, much of these count contributions originate from the residual gas remaining within the vacuum in the analysis chamber. Figure 4.12 shows the SNR for each of the datasets acquired, which was calculated by taking the ratio of the total number of ranged ions and the total number of ions in the dataset.

The disparity in both the background noise and the SNR between the datasets acquired at $T = 45K$ and those taken at $T = 50K$ and $55K$ is significant and unexpected.

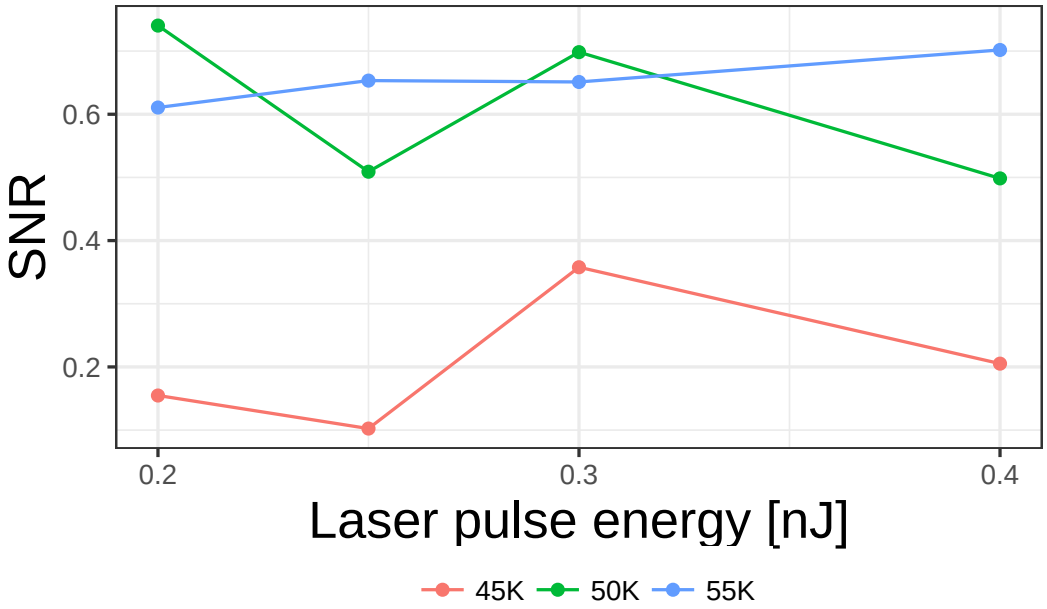


Figure 4.12: Laser mode SNR as a function of laser pulse energy. SNR ratio has been determined by calculating the ratio of the number of ranged ions to the total number of detected ions within the dataset.

The difference in the temperatures are relatively small and was not expected to produce such drastic differences in the background rate and SNR. The background rate shows invariance with E_{laser}, which suggests that it is not a dominating variable. Instead, the argument posed in §4.3.1, in which preferential evaporation of Cr was thought to occur, could account for these drastic changes in the background rate. At lower temperature and laser energy, a higher standing voltage is required to induce the evaporation of surface atoms. It is under these conditions that preferential evaporation is more likely to occur. If preferential evaporation occurred more strongly at $T = 45K$, surface atoms could evaporate between pulses and these events would contribute towards the background count.

Another aspect to consider is the LEAP 3000X-HR itself which can influence the noise

levels in the datasets as a result of vacuum characteristics and electrode status. A poor vacuum containing a high level of residual gas could be ionised by the evaporation field and travel to the detector. After many experiments using the same electrode, material emitted from previous specimens may be deposited onto its surface and could ionise during a pulse. Both additional sources of ions could increase noise levels. However, all experiments were initiated only when the vacuum in the analysis chamber was $\leq 4\times10^{-11}torr$. The electrode is also unlikely to contribute to these effects as an electrode test was conducted before experiments commenced and it was deemed to be "clean" and useable to a high voltage. Therefore the origin of this significant background noise and SNR difference, between datasets acquired at $T=45K$ and those taken at $T=50K$ and $55K$ is unlikely to stem from a poor vacuum and sub-optimal electrode.

The specimens used for the experiments at $T=45K$ were different to those conducted at $T=50K$ and $T=55K$; therefore this must be considered too. No significant difference in the physical appearance of the specimens after FIB manufacturing can be seen from figures 4.1a and 4.1b. Tip radii and shank angles, which are a metrics used to determine how sharp or blunt a tip is, are comparable to each other. If the shank angle were larger in the sample used at $T=45K$, then a higher standing voltage would be required, which would also increase the chances of preferential evaporation. During their fabrication, protruding sections and irregular surface artefacts that were less than $10\mu m$ away from the sample tip were removed. Such features can perturb the electric fields around the specimen which could induce trajectory aberrations to any evaporated ions. They could also act as a secondary emission source, in which atoms could evaporate off and increase the number of multiple hits during an atom probe experiment. However, the physical state of the samples after they were transported from the FIB, situated at Begbroke Science Park, to the atom probe laboratory at Parks Road, is unaccounted for. Therefore the structural integrity of the samples could have been compromised

during this period. However, this is unlikely as the other samples that were transported at the same time were not damaged.

As the main contributors to the high levels of noise found in the dataset acquired at $T = 45K$ have been assessed and deemed to be unlikely, it is unclear why this occurs. The measurements taken at $T = 50K$ have the lowest background rate relative to other datapoints and experiments conducted at $T = 50K$ and $T = 55K$ show invariance in background rate with E_{laser}. Compared to the data acquired at $T = 45K$, the difference in the background count between data acquired at $T = 50K$ and $T = 55K$ is negligible. It is possible that an increase in T could reduce the background rate further but these are likely to be insignificant reductions. Since E_{laser} was seen to be invariant with background, any changes to this parameter is not expected to induce a change in the background rate. Similarly, there is little difference between the SNR of the datasets collected at $T = 50K$ datasets and $T = 55K$ but there are variations with different E_{laser}. From figure 4.12 the SNR is maximised at two different parameter combinations: 1)$T = 50K$ and $E_{laser} = 0.2nJ$ as well as 2)$T = 55K$ and $E_{laser} = 0.4nJ$. It is possible that increasing both T and E_{laser} could improve the SNR, however it is unlikely such improvements would be significant.

4.3.3 Objective 3: maximising the mass and spatial resolutions

4.3.3.1 Maximising the mass resolution

The measured FWHM of the $^{56}Fe^{2+}$ peak mass resolution for each dataset were calculated and are shown in figure 4.13. No data is shown in figure 4.13 for $T = 45K$ and $E_{laser} = 0.25nJ$ as the EMG function was unable to fit to the experimental peak. Figure 4.14 presents portions of the mass spectrum containing the $^{56}Fe^{2+}$ peak and its

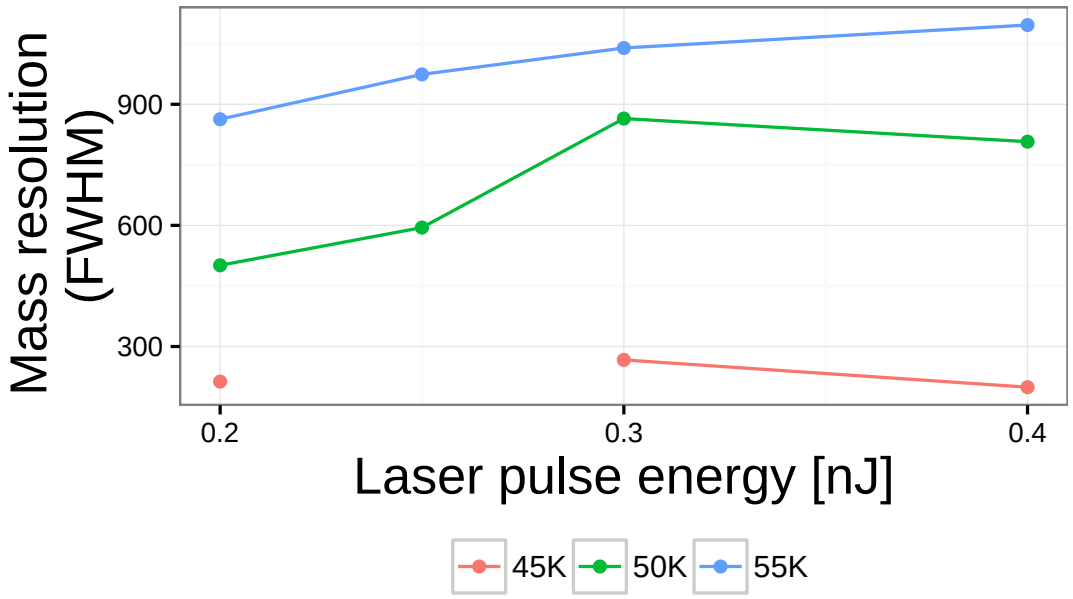


Figure 4.13: Mass resolution of the $^{56}Fe^{2+}$ as a function of laser energy. FWHM analysis for the $^{56}Fe^{2+}$ peak has been conducted using London's 'rangeCorrector.m' code [306].

neighbours for datasets acquired at $T = 45K$, $T = 50K$ and $T = 55K$ at $E_{laser} = 0.25nJ$. Relative to $T = 50K$ and $T = 55K$, the $^{56}Fe^{2+}$ peak at $T = 45K$ is broad and has a high background count. It is probably for these two reasons that the code was unable to fit the EMG function.

From figure 4.13, the mass resolution was maximised in the experiment conducted at $T = 55K$ and $E_{laser} = 0.4nJ$. The reason for this is that the Fe^{2+} peak FWHM is minimised relative to the other datasets.

The primary reason why this peak broadens is because the time of flight for the $^{56}Fe^{2+}$ ions differ [289]. As described in section 3.4.2, the evaporation of ions is inherently a probabilistic phenomenon; some ions may evaporate at different times during the pulse. The data suggests as T and E_{laser} increases, the evaporation of Fe surface atoms become

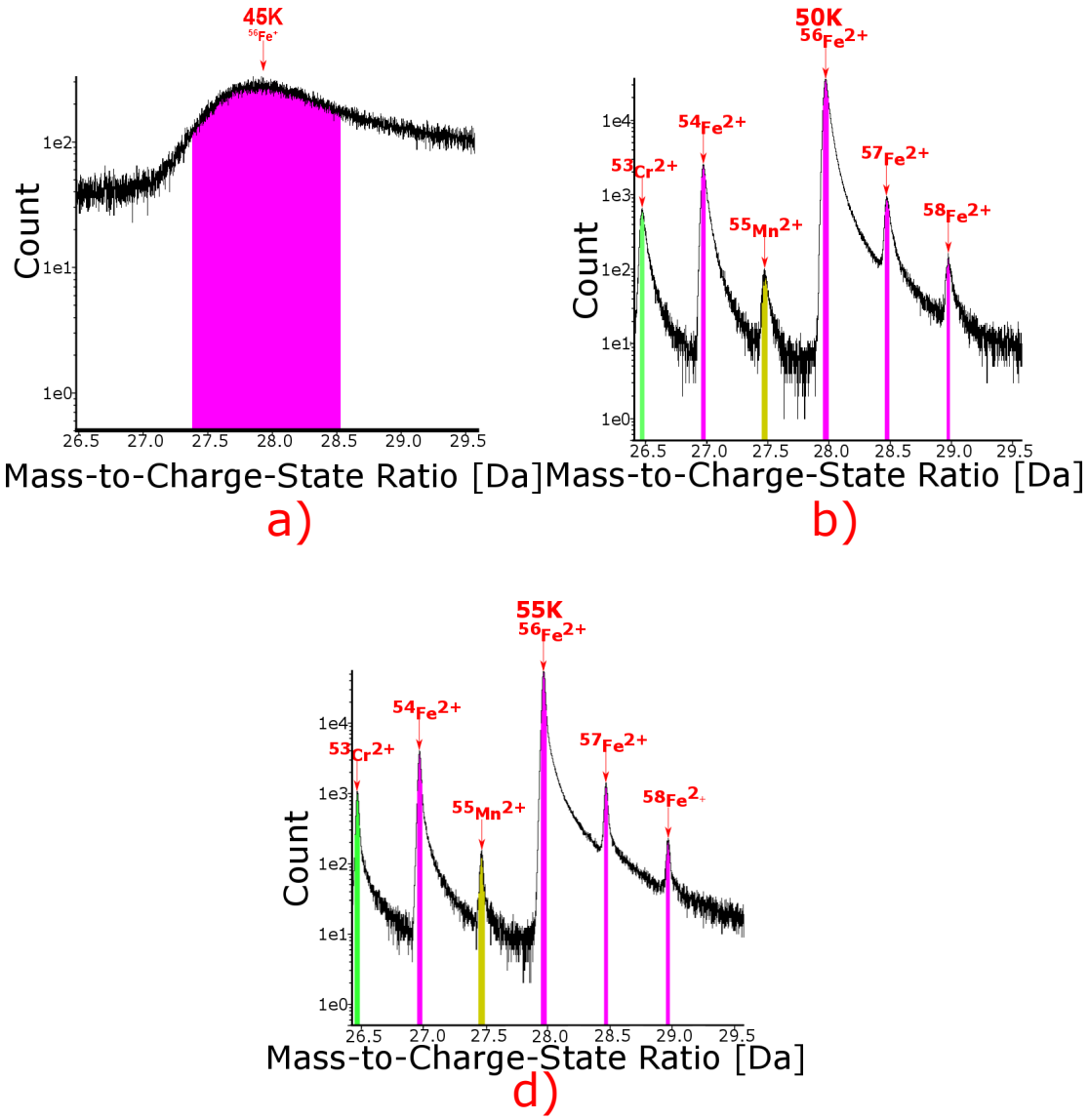


Figure 4.14: Portions of the mass spectrum from datasets acquired at a)45K, b)50K and c)55K at 0.25nJ. As the temperature increases the peaks reduce in width and their apexes become more acute.

more coordinated with the laser pulse. As evaporation under laser pulsing is thought to be a thermally activated mechanism this data also suggests that the tip cools within an appropriate time period. The dataset acquired at $T = 55K$ and $E_{laser} = 0.40nJ$ provides

conditions where the adjacent peaks are most free of the influence of the $^{56}Fe^{2+}$ thermal tail. Therefore it is this parameter combination that maximises the mass resolution. Figure 4.13 indicates further increases in T and E_{laser} would increase the mass resolution further. However the linearly interpolated trendlines indicate these further gains in mass resolution would be insignificant. This is because both the and $T = 50K$ and $T = 55K$ lines seem to be plateauing.

4.3.3.2 Maximising the spatial resolution

Spatial resolution can be separated into its two components; depth resolution along the z-axis, and lateral resolution along the x-y plane. The reconstruction point projection model [333] assumes only surface atoms ions evaporate sequentially. This is a valid assumption for metallic samples specifically as the electric field penetration depth into the surface is $< 5nm$ and therefore is quite low [306, 334]. Hence the depth resolution is unlikely to be affected by different analysis parameters [335]. The lateral resolution however is strongly affected by surface diffusion of surface atoms [336, 337] and the shadow effect as explained in section 3.4.8. Therefore its effect on Fe, Cr and W within 14YWT1 imaged by APT at $T = 55K$ was investigated.

Figures 4.15 and 4.16 show 2D lateral density plots from each of the APT experiments conducted at $T = 55K$ for Fe, Cr and W. From these plots it is evident that no poles were exhibited in the sample volumes. Densely populated zones, which are coloured in red, tend to be predominantly located within the regions closest to where the laser pulse would have made contact with the tip. There are also regions in the top left corner which are sparsely populated with Fe, Cr and W. It is improbable that these alloying elements would be segregated in 14YWT1 in the manner the density plots indicate. Therefore it is likely that these apparent dense regions are due to surface diffusion and the shadow effect.

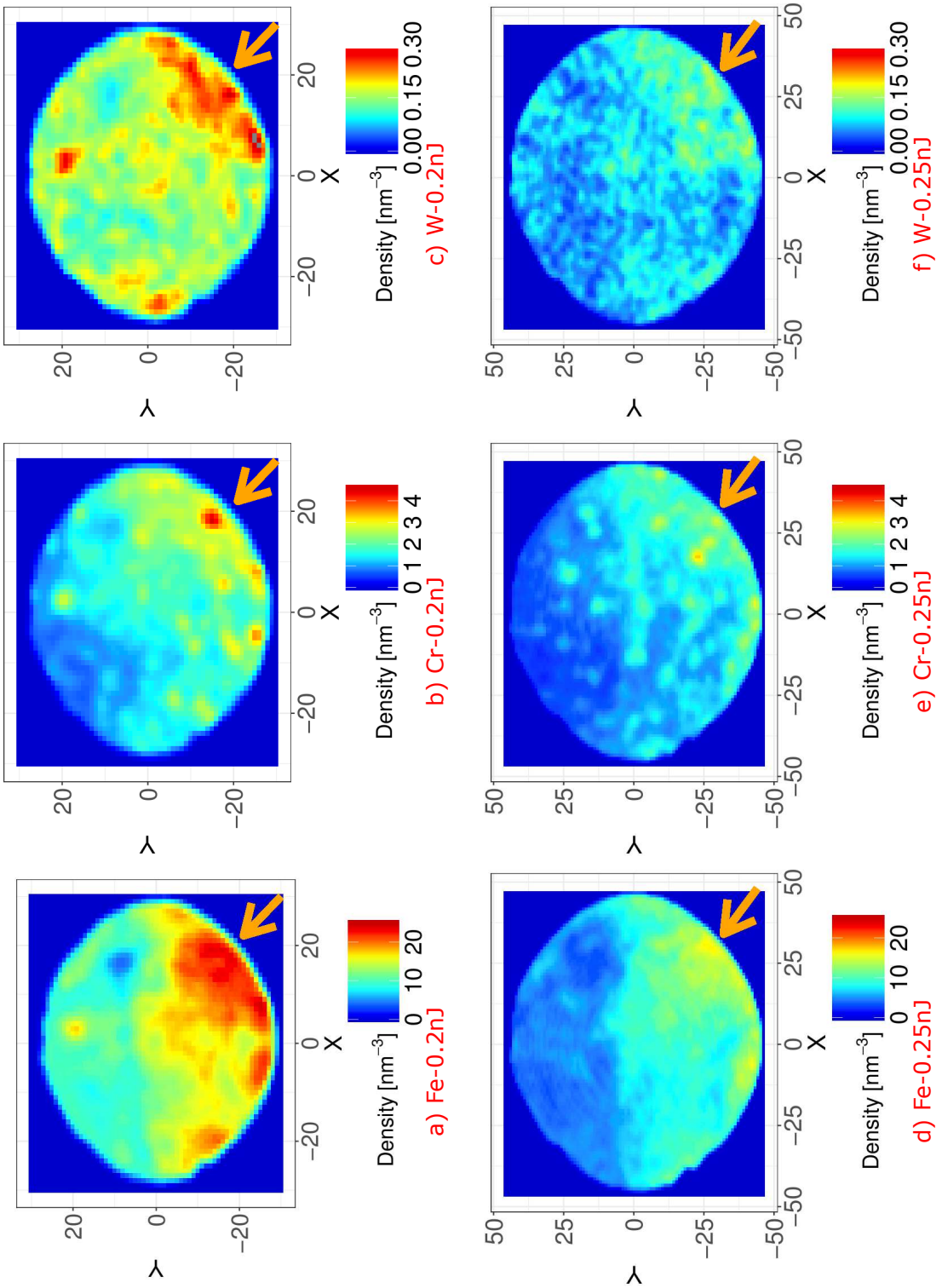


Figure 4.15: 2D density plots of Fe, Cr and W from the datasets acquired at $T = 55K$, $E_{laser} = 0.20nJ$ and $E_{laser} = 0.25nJ$. The orange arrow in the bottom right corner of each 2D density plot represents the approximate orientation the laser pulse strikes the sample tip.

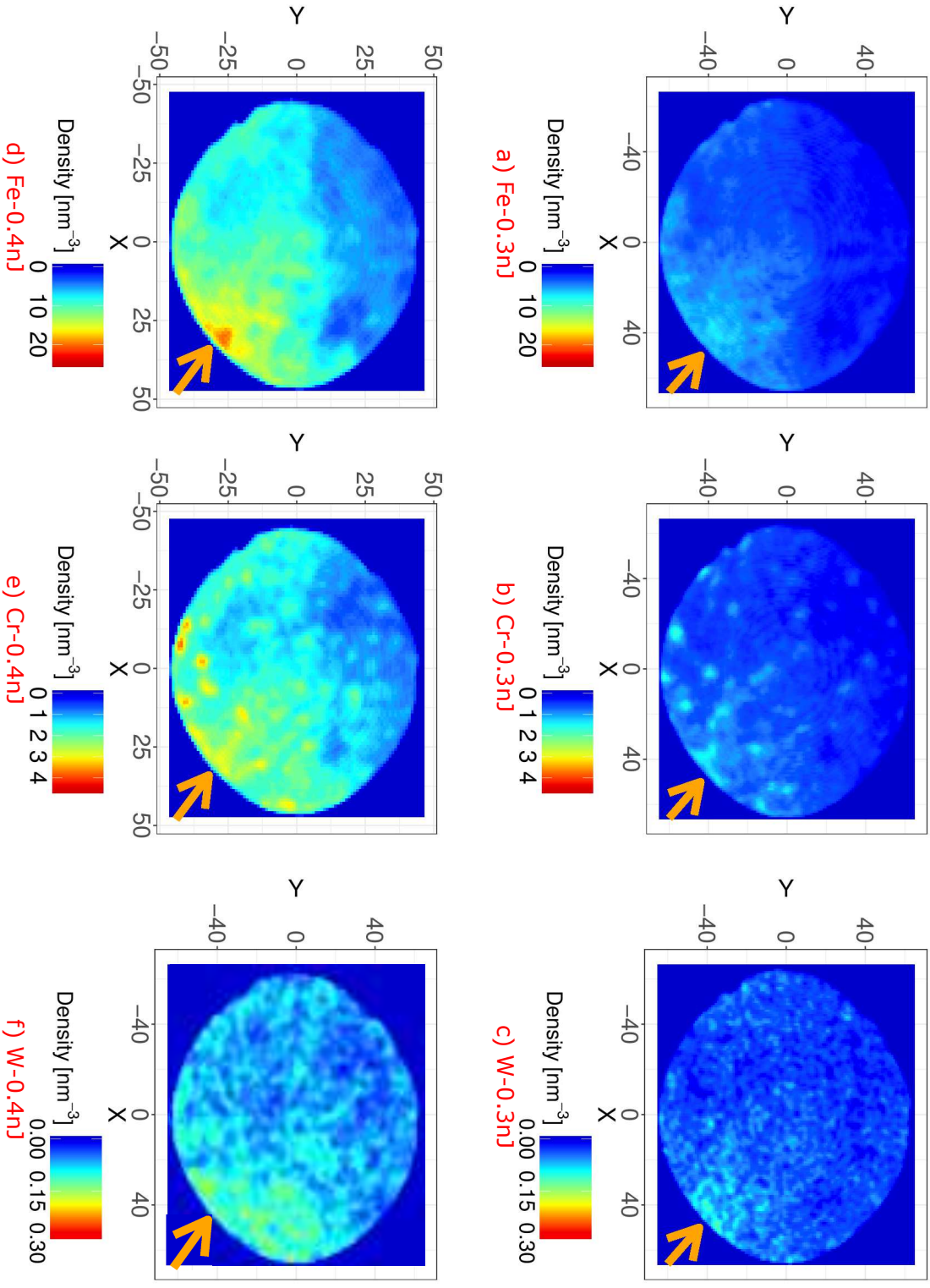


Figure 4.16: 2D density plots of Fe, Cr and W from the datasets acquired at $T = 55K$, $E_{laser} = 0.3nJ$ and $E_{laser} = 0.4nJ$. The orange arrow in the bottom right corner of each 2D density plot represents the approximate orientation the laser pulse strikes the sample tip.

As the laser energy increases the distribution of Fe, Cr and W becomes more evenly distributed. This is likely to be related to the lower standing voltage required for evaporation events to take place. The field generated by this standing voltage plays a large role in this diffusive migration phenomena. Before a surface atom can migrate to another position along the surface, it must detach from its kink site. The field polarises the surface atom causing it to detach from the surface. Once polarised, the atom is likely to translate positions along the field gradient lines [337, 338, 339, 340]. Therefore by reducing the standing voltage, the mobility of the Fe, Cr and W surface atoms are reduced indirectly.

Also evident from these plots, is that the distribution of W seems to be most affected by changes to the laser energy. This could be due to one of two reasons. Firstly, the quantity of W present within 14YWT1 is much lower in comparison to Fe and Cr and therefore lateral movement of this atom would be more easily seen. Secondly, it could be that the kink site detachment activation energy is lower for W [341] than Cr.

Red bright spots can be seen to populate the density maps especially in those belonging to Cr and W. These dense zones of Cr and W are probably due to APT magnification effects. As the NFA dispersoids within the 14YWT1 are of a low-field nature, this results in a deflection of the matrix ion trajectories towards the dispersoids [289, 309]. As a result, artificially high concentrations of the matrix elements, such as Fe, Cr and W here, are shown by APT maps as being part of the dispersoid [303]. While it is possible that surface diffusion [342, 343] of the subject elements and the shadow effect could contribute to the density of these zones, it is likely to be less significant relative to the magnification effects.

The set of 2D lateral density plots acquired at $T = 55K$ and $E_{laser} = 0.30nJ$ show the most spatially homogeneous distributions of Fe, Cr and W relative to the other combinations shown in figures 4.15 and 4.16. It is possible that the spatial resolutions

could be further improved by varying T and E_{laser} further. However, it is probable that these further improvements would be insignificant.

4.4 Conclusion

The data presented in this chapter exhibits the influence atom probe experimental conditions have on the research outcomes. Combinations of atom probe analysis parameters can either promote or deter specific evaporation mechanisms e.g. preferential retention or evaporation. However, this can be managed by conducting a systematic parameter determination experiment to determine appropriate combinations for the subject material.

In this parameter determination study T and E_{laser} parameters were deemed appropriate if they satisfied the following three criteria: 1) differences between the apparent concentrations of Fe, Cr and W within 14YWT1, in comparison with those measured by EPMA must be minimised, 2) minimise background noise and 3) maximise the mass resolution of the $^{56}Fe^{2+}$ peak at 27.97Da as well as the spatial resolution.

Based on the data acquired from this systematic study, atom probe experiments on 14YWT NFAs and 14WT non-NFAs using the LEAP 3000X-HR, should be conducted at: $\mathbf{T = 55K}$, $\mathbf{E_{laser} = 0.4nJ}$, $\nu = \mathbf{200kHz}$ and $\mathbf{\Phi_{evap} = 0.005\,ions\,pulse^{-1}}$.

It should be noted that more suitable APT parameter combinations may exist outside of the range of T and E_{laser} used here. Indeed, the data in figure 4.8, suggests that increasing the temperature could offer APT measured concentrations that were more consistent with that of EPMA. The data shown in figures 4.11 and 4.12 suggest that minor improvements to the background rate and the SNR is achieved by increasing temperature. Figure 4.13 indicates increasing the temperature would improve the mass resolution but this may be to the detriment of spatial resolution. This is because

at higher temperatures surface atoms are more mobile and therefore surface diffusion may be more prominent. Generally, the laser energy was not seen to be significantly influential on the quality of the data, which suggests higher E_{laser} are required to observe significant effects this parameter has on data quality.

Future work should be conducted to investigate whether higher temperatures would offer higher data quality. Though fixed here, ν and Φ_{evap} should also be varied to determine whether further improvements could be made to the quality of data and the data acuisition rate.

Chapter 5

Isothermal ageing of 14WT and 14YWT at 475℃

Chapter summary

14WT non-NFA and 14YWT1 NFA specimens have been isothermally aged at 475°C for 1, 3 and 8 months. Post-ageing characterisation of both alloys includes a combination of APT and microhardness tests. APT indicated Cr-rich α' precipitates have not formed in the 14WT non-NFA aged for 1 month, but have formed in the 14WT aged for 3 and 8 months. This indicates an incubation period between 1 and 3 months before the α' precipitates nucleate.

α' precipitates have not formed in the 14YWT1 NFA after 8 months of ageing. Cr, W, Si and Mn are seen to segregate and enrich the GBs in the aged 14YWT1. Significant variation in the level of GB enrichment was observed, and no trend as a function of ageing duration can be determined. The 14YWT1 NFA clusters distributed across the matrix seem to be stable after 8 months of low-temperature ageing as their composition and radii remain unchanged.

Microhardness indentations show an increase in hardness in 14WT aged for 8 months by $\Delta Hv_{14WT} = +32 \pm 4kgf\,mm^{-2}$. Conversely, 14YWT1 aged for 8 months has softened by $\Delta Hv_{14YWT} = -26 \pm 10kgf\,mm^{-2}$.

5.1 Introduction

Fe-Cr binary alloys [33] and ODS steels [167] with Cr concentrations $> 9wt.\%$ aged at $475°C$ are susceptible to the formation of α' precipitates [32]. It is unclear whether 14YWT NFAs are also susceptible to this phase formation. Moreover, if α' precipitates do form in 14YWT, how do the ultrafine dispersoids affect α' precipitate formation; and what are the implications for mechanical properties such as hardness? The work presented in this chapter aims to answer these questions by presenting the results from an 8 month isothermal ageing study conducted on 14WT non-NFA and 14YWT1 NFA at $475°C$.

5.2 Materials and methods

The alloys used in this isothermal ageing study are 14WT non-NFA and 14YWT1 NFA. Both were fabricated at the University of Oxford. Descriptions of their processing history and as-received microstructures are in sections 3.1.1.1 and 3.1.2.1 respectively. Details regarding the isothermal ageing experiment are given in section 3.2. Elemental distributions within the as-received and aged alloys were studied by APT and their mechanical hardness was measured by microhardness indentation tests. APT sample fabrication, experimental and analysis methods are described in appendix A. Methods employed for the microhardness tests are described in section 3.5.

Three atom probe datasets for each ageing duration and alloy were acquired in an attempt to obtain statistically robust data. All three APT datasets for 14WT for each ageing duration are shown in the results section. However, only one set of 14YWT1 atom maps out of the three experimental repeats, for each ageing duration, is shown in the results section as they are representative of the remaining two datasets. The

remaining two 14YWT1 APT datasets are provided in appendix B for reference. All APT measured values presented in this study are averaged across 3 APT datasets. Uncertainty in these values was calculated using the standard error formula.

Similarly, the average microhardness data presented here are the average of five Vickers hardness tests conducted on 14WT and 14YWT1 specimens, each aged for different durations. The uncertainties in the hardness values quoted in this study were calculated by using the standard error formula.

5.3 Results

As part of this isothermal ageing experiment, 24 APT datasets were acquired and will be referred to in this and succeeding sections. These datasets are summarised in table 5.1 for reference.

Ageing duration [$Months$]	14WT dataset	14YWT1 dataset
0	23301	23070
	23328	23146
	23818	23181
1	22843	20713
	22860	21112
	22923	21240
3	21350	20823
	21514	22468
	22361	23065
8	24511	22826
	24508	22894
	23604	22920

Table 5.1: Index of all the APT datasets acquired in the isothermal ageing study conducted on 14WT and 14YWT1

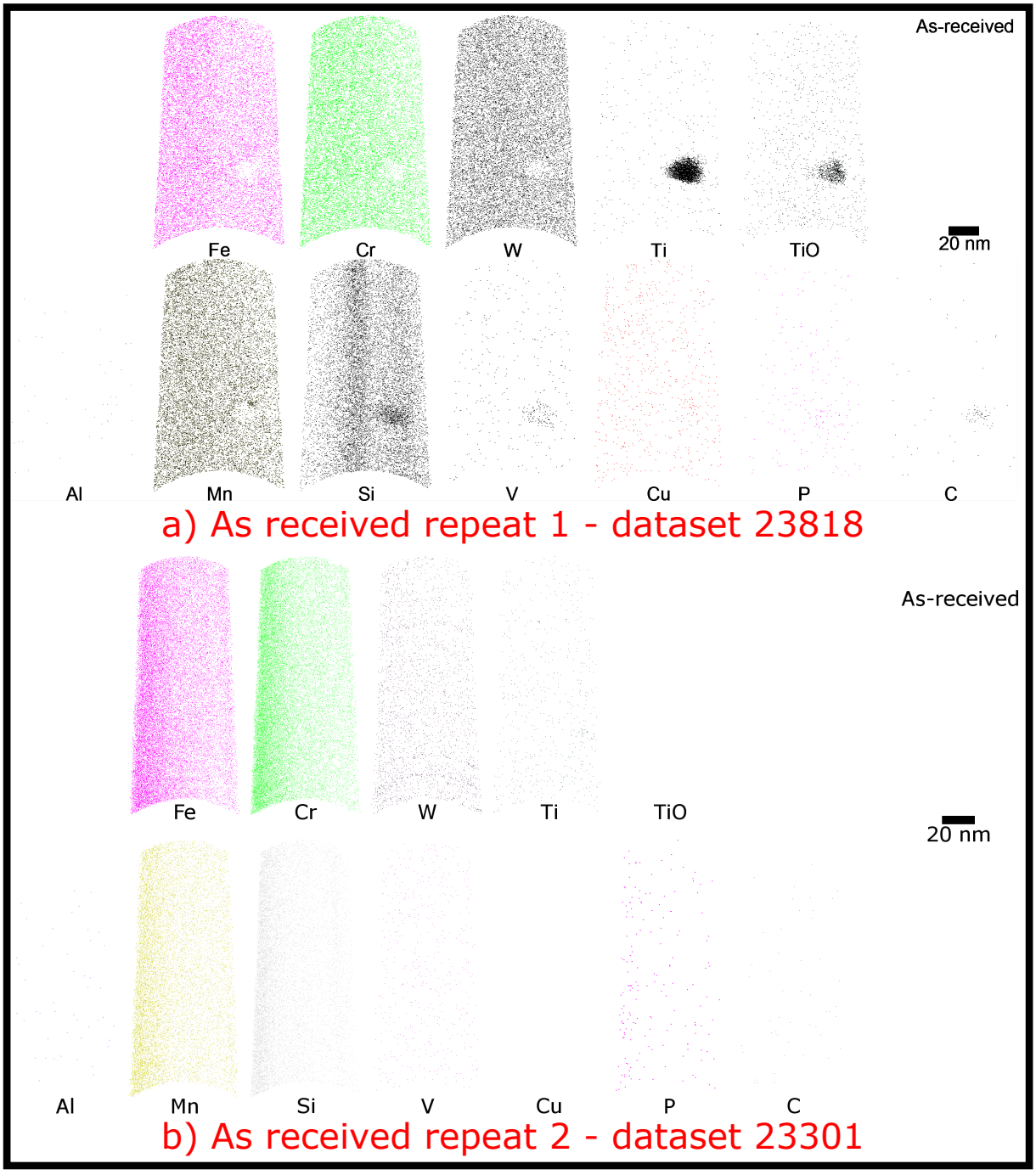


Figure 5.1: Atom map slices of as-received 14WT

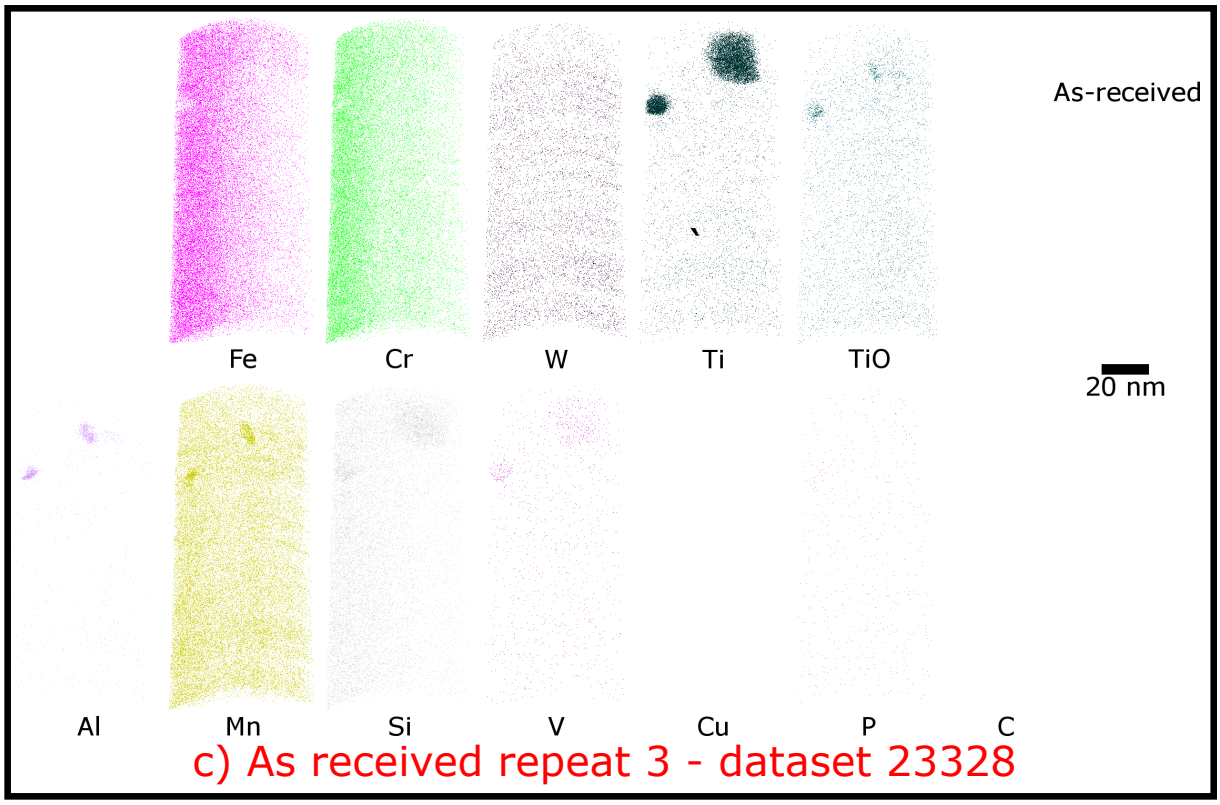


Figure 5.1: Atom map slices of as-received 14WT

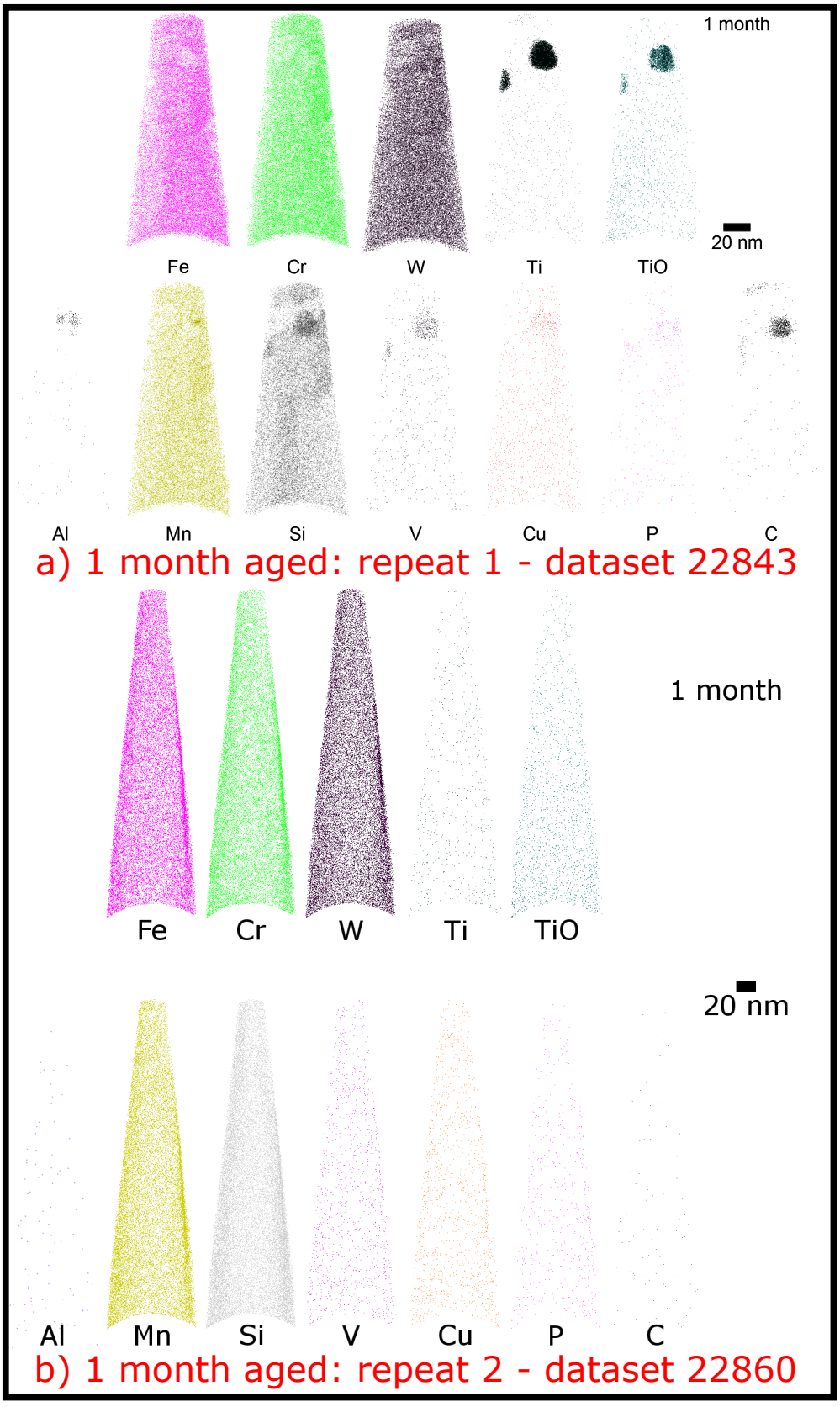


Figure 5.2: Atom map slices of 14WT aged for 1 month at $475°C$

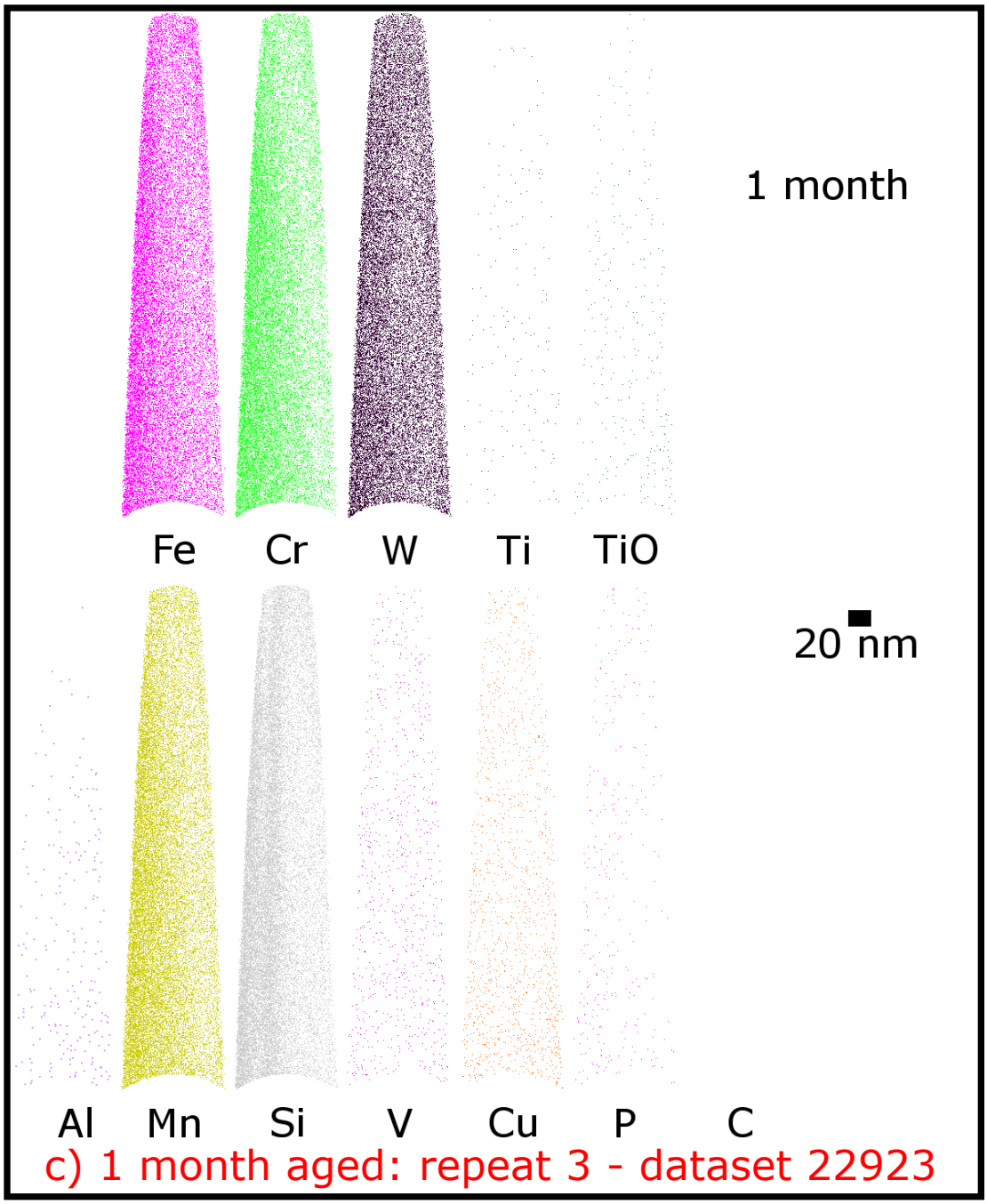


Figure 5.2: Atom map slices of 14WT aged for 1 month at 475°C

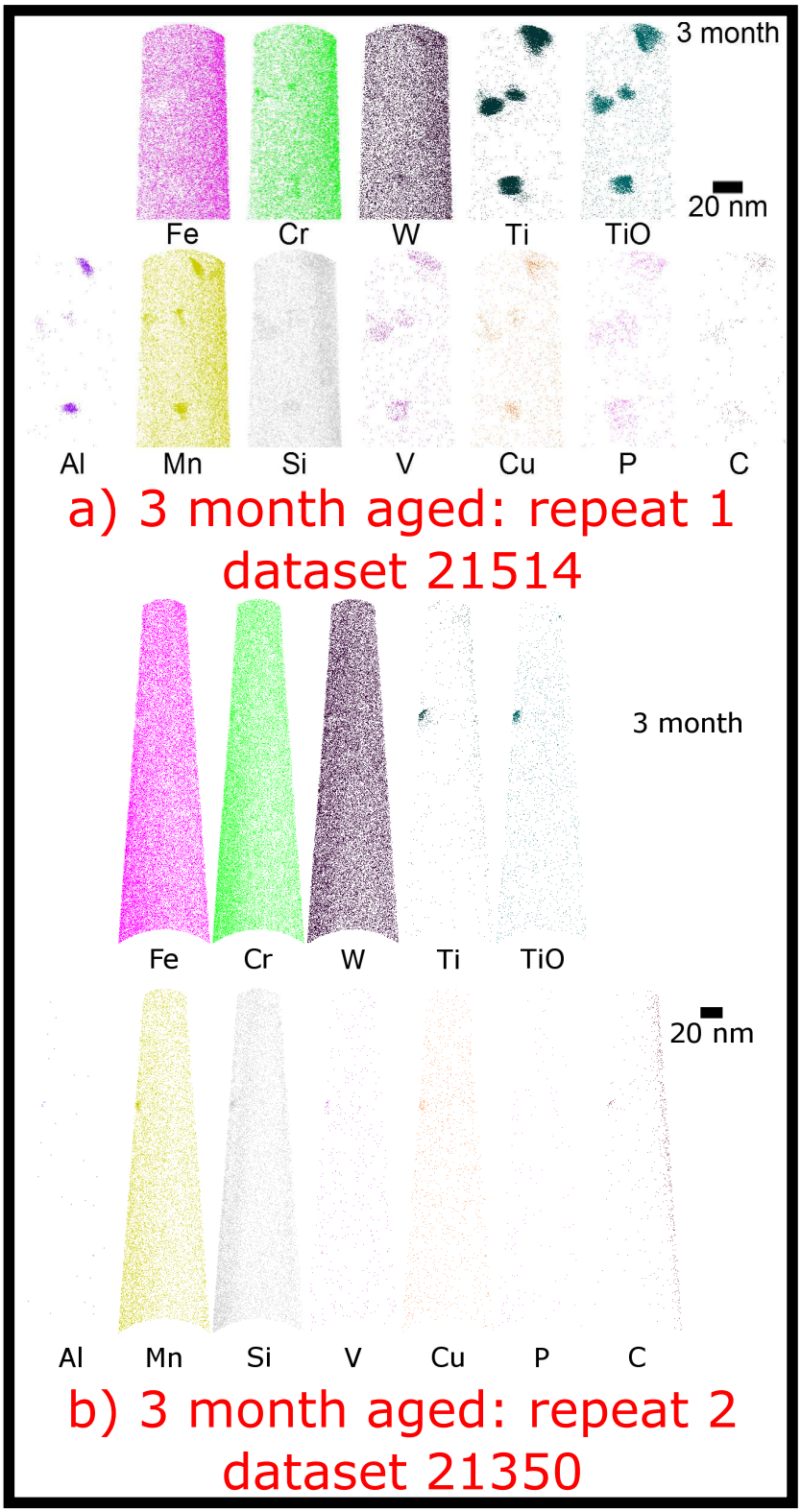


Figure 5.3: Atom map slices of 14WT aged for 3 months at 475°C

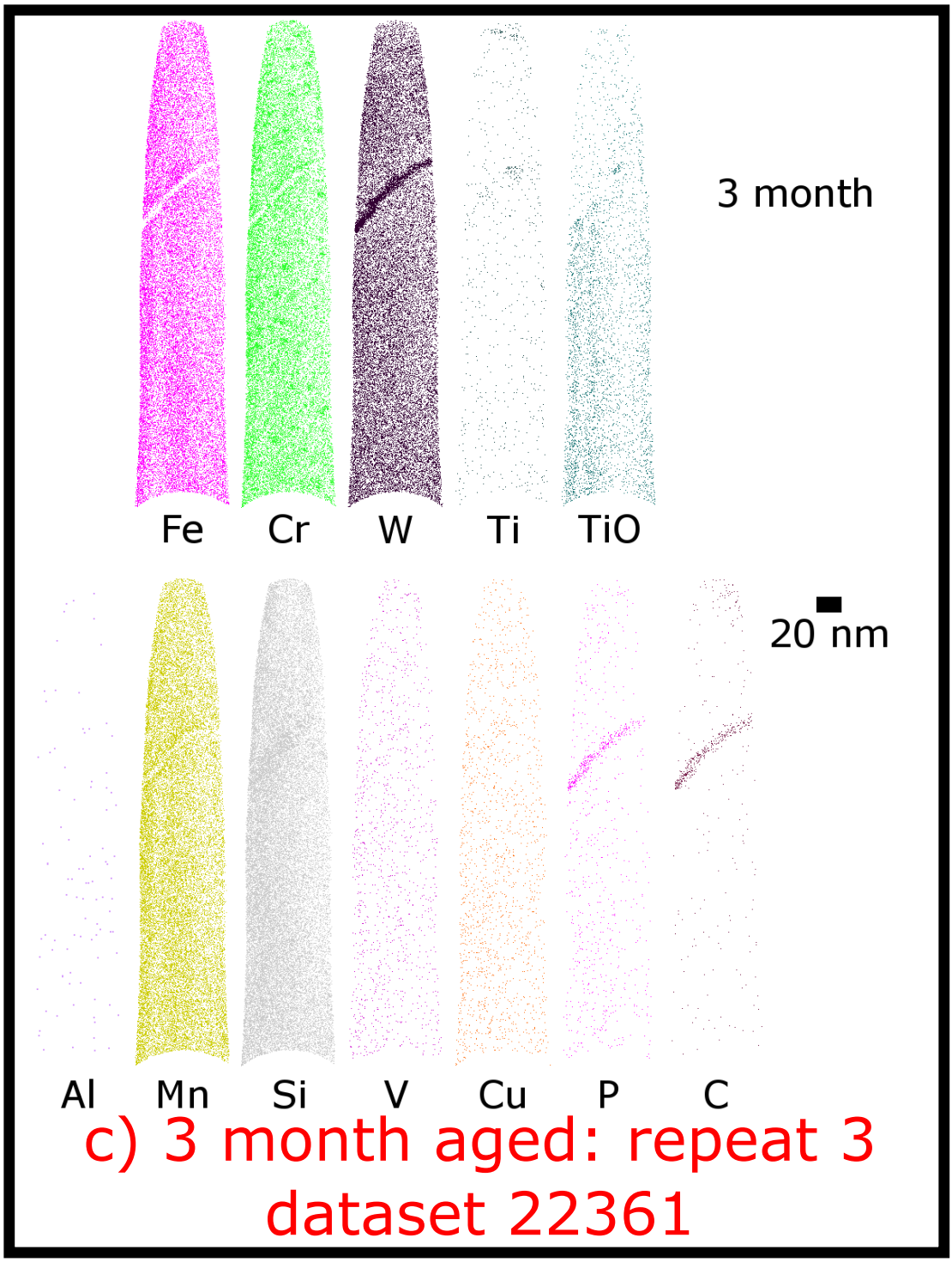


Figure 5.3: Atom map slices of 14WT aged for 3 months at 475°C



Figure 5.4: Atom map slices of 14WT aged for 8 months at 475°C

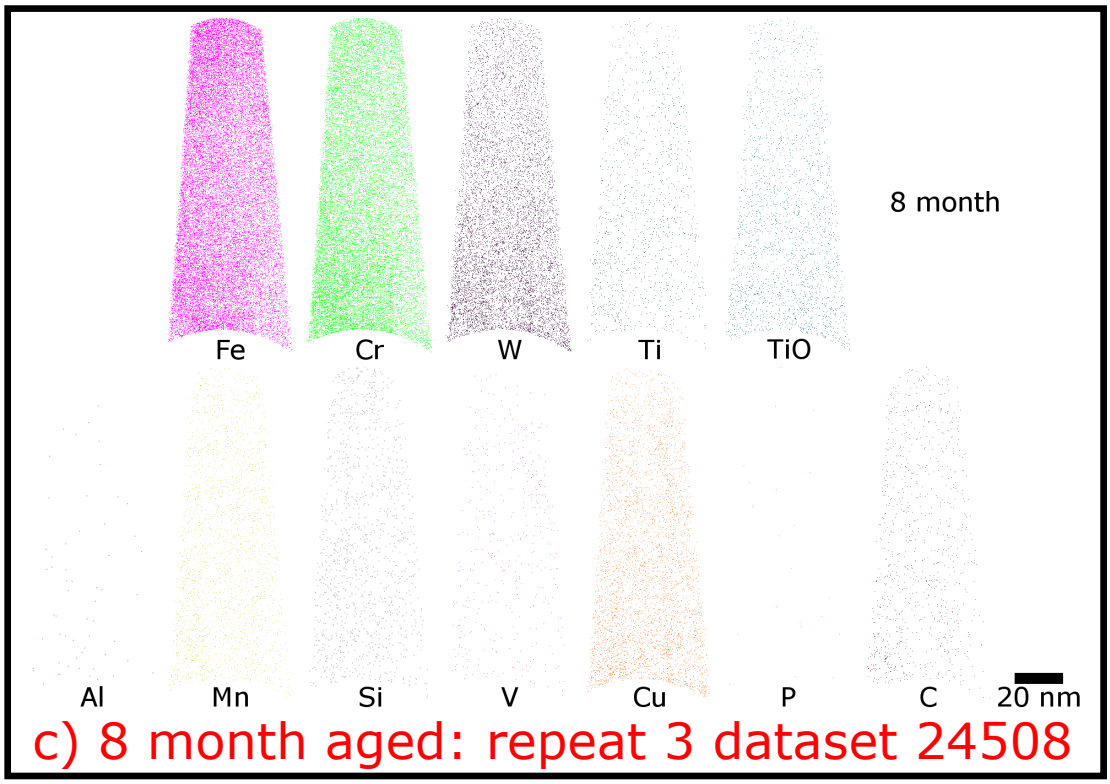


Figure 5.4: Atom map slices of 14WT aged for 8 months at $475°C$

5.3.1 APT characterisation of isothermally aged 14WT

Atom maps from all three experimental repeats for each ageing duration are shown figures 5.1, 5.2, 5.3 and 5.4. By comparing the atom maps for each of the as-received atom maps in figure 5.1, it is evident that that the microstructure within 14WT is inhomogeneous.

Microchemical phenomena (i.e. clustering or segregation) affecting the distributions of Fe, Cr and W, within the as-received 14WT was not observed in any of the three datasets shown in figure 5.1. Ti-rich precipitates can be seen in figures 5.1a and 5.1c. Apart from Al, other impurity solutes such as Mn, Si, V, Cu, P and C are seen to be highly correlated with the Ti-rich precipitates.

Figure 5.2 presents atom maps from the 14WT aged for one month. Microchemical phenomena involving Fe, Cr and W appears to have not occurred. Concentrated zones containing Al, Mn, Si, V, Cu, P and C are seen to be correlated with the position of the Ti dense zone.

After three months of ageing at $475°C$ dense zones of Cr atoms can be seen in each of the experimental repeats shown in figure 5.3. W appears to remain microchemically neutral. All minor impurity elements continue to be highly correlated with the concentrated Ti zones but not with the Cr-rich zones.

Finally, after 8 months of ageing, Cr-rich zones continue to occur in figures 5.4a and 5.4b. W, Ti, TiO and other minor impurity elements appear unsegregated and sparse.

5.3.1.1 Cr rich α' precipitates within 14WT alloys aged for 3 and 8 months at $475°C$

Cr-rich regions were identified in the Cr atom maps belonging to the 14WT aged for 3 and 8 months, and are indicative of clustering. Clustering of Cr in each of the

14WT APT datasets has been investigated by calculating the Pearson coefficients, μ, associated with the Fe and Cr elemental species. As explained in section 3.4.5.1, values of μ close to 0 are indicative of a distribution of the subject element that is close to binomial (random). μ close to 1 indicates microchemical phenomena such as segregation or clustering of the subject element has occurred. μ for each experimental dataset is plotted as a function of ageing duration in figure 5.5. The results of this analysis show that Fe and Cr within all the APT datasets belonging to the 14WT aged for 3 months deviate significantly from a binomial (random) distribution. Apart from dataset 24508, the Fe and Cr within APT datasets belonging to the 14WT aged for 8 months, also deviate away from a random solution. The calculated μ for each dataset is consistent with the qualitative assessment of their corresponding Cr atom maps.

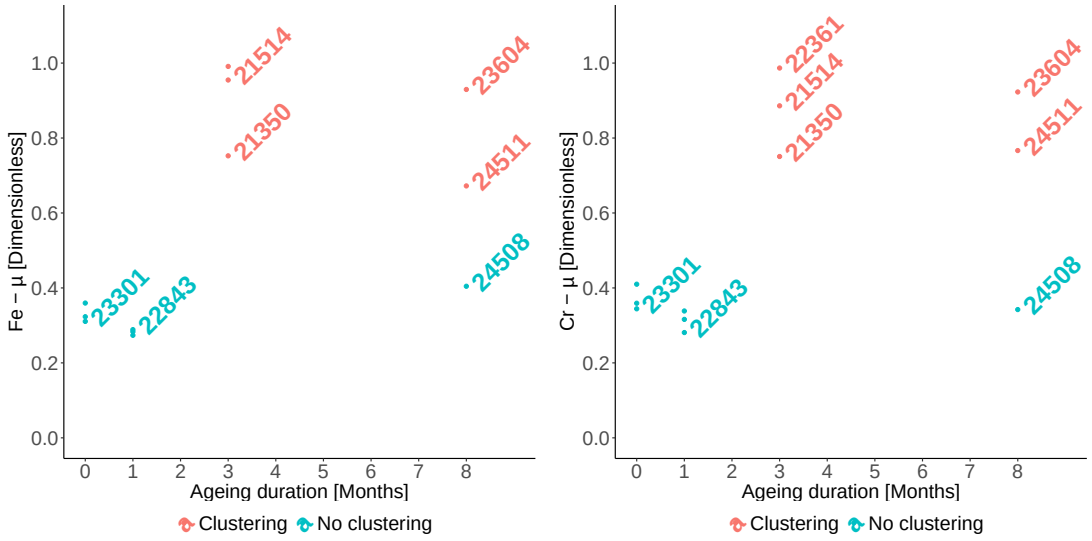


Figure 5.5: μ for Fe and Cr plotted as a function of ageing duration for each dataset acquired. Data point labels refer to the individual APT dataset number. Labels are missing for points that either overlap with one another or are very close. Clustering or no clustering refers to whether Cr-rich zones were observed in the Cr atom maps

Figure 5.6 shows concentration profile through 6 randomly selected Cr-rich regions from

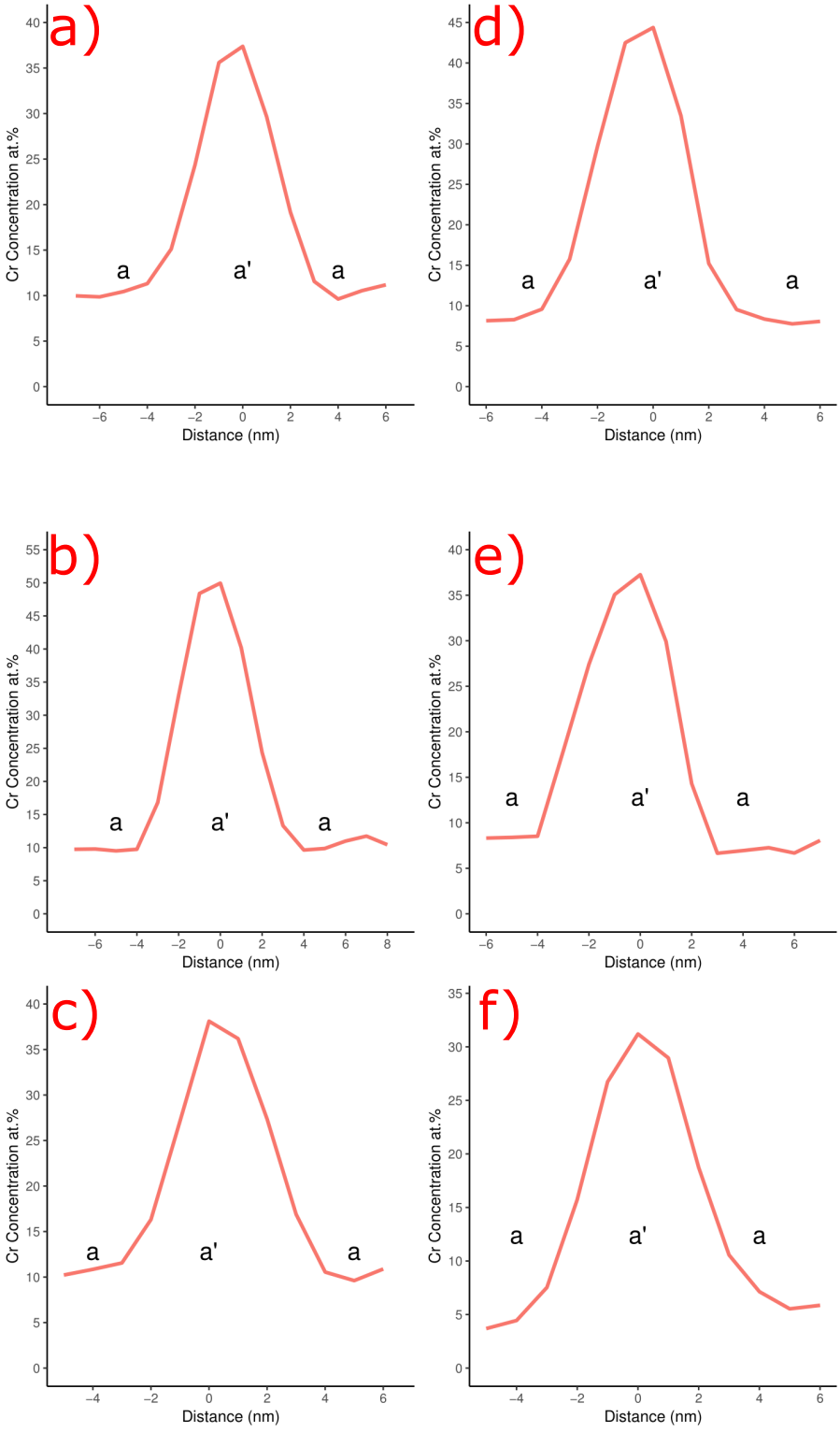


Figure 5.6: Cr concentration profiles through 6 different Cr-rich regions within the 14WT aged for 8 months that contain them. a), b), and c) are from dataset 23604. d), e) and f) are from dataset 24511

dataset 24511 and 23604, shown in figure 5.4a and 5.4b, which are from 14WT aged for 8 months. Generally, it can be seen that the matrix (labelled as α) Cr content falls as the boundary of the Cr-rich region (labelled as α') is approached. As the x-axis ('Distance') increases towards 0, the Cr content increases rapidly. As the position along the x-axis increases above 0, the Cr concentration starts to reduce rapidly.

Concentration profiles belonging to phases that form via nucleation and growth are expected to be similar to that of a top hat function [41]. Instead, the concentration profiles in figure 5.6 are seen to be bell shaped and this is because of two main reasons. Firstly the lateral resolution limit, which is 0.2nm on the LEAP 3000X-HR, and trajectory aberations due to differences in evaporation fields reduce the ability of this technique to sample the interface accurately. Secondly, the generation of concentration profiles through the Cr-rich regions required the use of cylindrically shaped volumes. These volumes have a finite width (1nm) and will therefore average out the concentration across the cross-sectional area of this volume. This is exacerbated since the interface between the matrix and these precipitates is a curved surface.

Though the peak Cr concentration achieved in the centre of the Cr-rich zones vary, the shape of the concentration profiles in figure 5.6 are similar. Therefore, it is likely they are representative of all the Cr-rich regions within the aged 14WT.

Using the analysis protocol described in section 3.4.6, the Cr-rich regions found within the APT datasets belonging to the 14WT aged for 3 and 8 months, have been isolated and studied. Slices of the datasets containing these Cr-rich regions are shown in figures 5.7 and 5.8.

Figures 5.7 and 5.8 indicate qualitatively that the number density of the Cr-rich zones varies significantly between the experimental repeats for a given ageing duration. Due

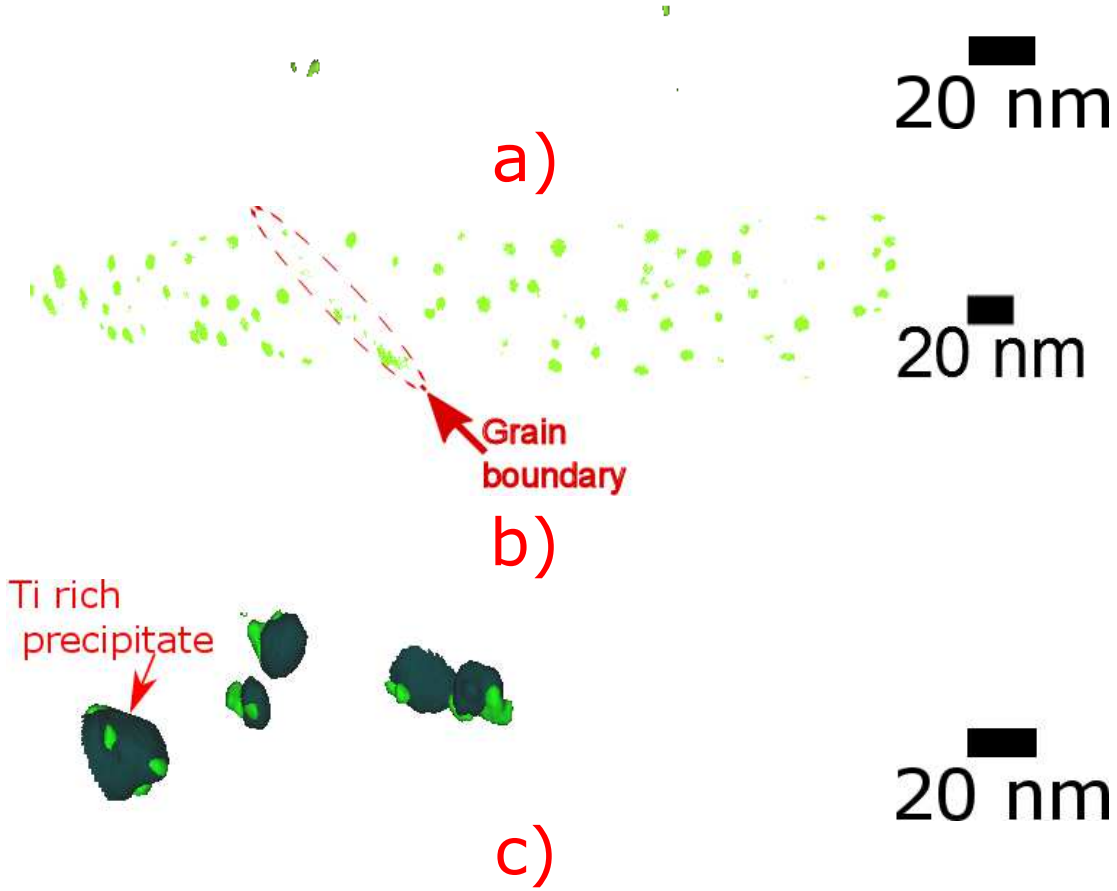


Figure 5.7: Slices of Cr isoconcentration maps from 14WT aged for 3 months APT datasets using a threshold of $30at.\%Cr$. All three experimental repeats are shown: a)21350 b) 22361 and c) 21514. The Cr-rich zones are seen to be present within all of the repeats in varying number densities. Ti-rich precipitates shown in c) are defined using Ti isoconcentration surfaces using a threshold of $5at.\%Ti$.

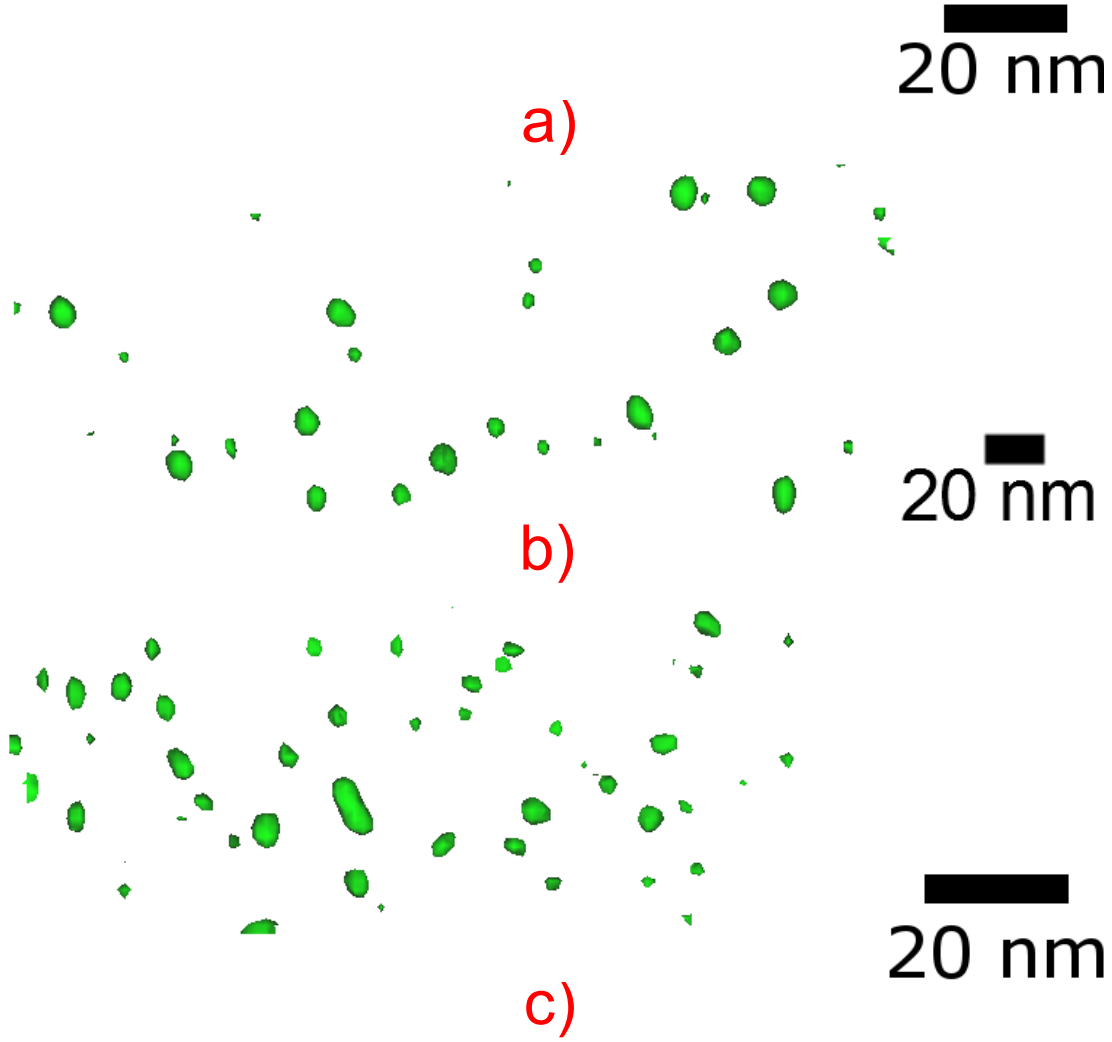


Figure 5.8: Slices of Cr isoconcentration maps from 14WT aged for 8 months APT datasets using a threshold of $30at.\%Cr$. All three experimental repeats are shown: a)24508 b)23064 and c)24511. Cr-rich zones are seen to be present within b) and c) in varying number densities but not in a).

to the inhomogeneous distribution of the Cr-rich zones, they have been studied on an individual dataset basis. Table 5.2 presents the physical characteristics associated with the Cr-rich zones in each of the three APT datasets belonging to the 14WT aged for 3 and 8 months, and also includes the matrix Cr concentrations. In addition, the average of these metrics across a particular ageing duration has been calculated and presented in table 5.3.

Variation in the physical characteristics of the Cr-rich zones is observed. Firstly, the number densities of the Cr-rich zones in 14WT aged for 3 and 8 months vary significantly between the experimental repeats. For the 14WT aged for 3 months, the number density of the Cr-rich zones within 22361 is greater by one order of magnitude compared to dataset 21350 and 21514. As the ageing duration increases to 8 months, the variation in the number densities of these zones increases substantially. Dataset 24508 does not contain any of these zones while the remaining two datasets have a number density of $\sim 10^{22} - 10^{23} m^{-3}$. This number density data is consistent with the qualitative assessment of the slices in figures 5.7 and 5.8. Secondly, the radius of these zones are seen to vary within table 5.2.

The averaged data in table 5.3 show that the average zone radius decreases while the average number density increases with ageing duration.

The Cr concentrations within the zones do not vary between the experimental datasets. It's average, as presented in table 5.3, increases as ageing duration increases. A breakdown in the compositions of these zones within the 14WT aged for 3 and 8 months are presented in table 5.4.

The isolated Cr-rich zones found within 14WT aged for 3 and 8 months were observed to contain: Fe, Cr, W, Ti, Mn, C, Si, N, Cu, V, O, H, P, Co in varying quantities. Cr-rich zones within the 14WT aged for 3 months have concentrations of Fe, Cr and W that vary slightly between the datasets. However there are large variations in the

	14WT aged for 3 months		
	Dataset 21350 (figure 5.7a)	Dataset 22361 (figure 5.7b)	Dataset 21514 (figure 5.7c)
Number of Cr-rich zones in dataset	5	244	14
Number of ions acquired in dataset	117.3×10^6	42.4×10^6	35.2×10^6
Dataset volume $[m^3]$	3.83×10^{-22}	1.38×10^{-21}	1.15×10^{-21}
Cr-rich zone number density $[m^{-3}]$	1.31×10^{22}	1.77×10^{23}	1.22×10^{22}
Average Cr-rich zone radius [nm]	1.43 ± 0.20	2.80 ± 0.06	2.70 ± 0.31
Average Cr-rich zone Cr concentration [wt.%]	39.61 ± 1.01	46.32 ± 0.07	47.47 ± 0.31
Matrix Cr concentration [wt.%]	10.84 ± 0.01	10.82 ± 0.01	10.95 ± 0.01
	14WT aged for 8 months		
	Dataset 24508 (figure 5.8a)	Dataset 23604 (figure 5.8b)	Dataset 24511 (figure 5.8c)
Number of Cr-rich zones in dataset	0	27	60
Number of ions acquired in dataset	34×10^6	37.9×10^6	2.7×10^6
Dataset volume $[m^3]$	1.11×10^{-22}	6.46×10^{-22}	8.76×10^{-23}
Cr-rich zone number density $[m^{-3}]$	0	4.18×10^{22}	6.85×10^{23}
Average Cr-rich zone radius [nm]	0	1.64 ± 0.14	1.12 ± 0.05
Average Cr-rich zone Cr concentration [wt.%]	0	52.04 ± 0.52	58.31 ± 0.61
Matrix Cr concentration [wt.%]	9.68 ± 0.02	9.08 ± 0.01	9.50 ± 0.02

Table 5.2: Physical characteristics of the α' precipitates found within each of the three APT datasets belonging to the 14WT aged for 3 months and 8 months.

Ageing duration [Months]	Matrix Cr concentration [$wt.\%$]	Average Cr-rich zone Cr concentration [$wt.\%$]	Average Cr-rich zone number density [$\times 10^{22} m^{-3}$]	Average Cr-rich zone radius [nm]
0	12.51 ± 0.46	-	-	-
1	11.03±0.63	-	-	-
3	11.66±0.52	44.47±2.00	7±5	2.31±0.36
8	9.29±0.22	52.17±3.39	36±32	1.38±0.26

Table 5.3: A summary of the average physical characteristics of the Cr-rich zones found in the aged 14WT samples as measured by APT. Metrics for the Cr-rich zones within 14WT aged for 3 months are averaged across all 3 experimental repeats. Whereas they are averaged across 2 datasets (23604 and 24511) for the 14WT aged for 8 months.

concentration of Ti and minor elements such as Mn, Si, O, C, N, Cu and V. Indeed, the concentration of the minor elements in datasets 21514 and 22361 are not as high as dataset 21350. However, Si and Mn are consistently the most abundant minor elements across the 14WT aged for 3 month datasets.

The Cr-rich zones in the 14WT aged for 8 months show the opposite trends, as there is significant variation in the Fe, Cr and W content but little variation in the Ti and the minor elements. Table 5.4 also shows the total minor elements concentrations are dominated mainly by Si and Mn, which is similar to the 14WT aged for 3 months.

As shown in table 3.3 and 5.3, the average as-received 14WT matrix concentration of Cr is $12.51 \pm 0.46 wt.\%$. At the ageing temperature ($475°C/748K$) 14WT is expected to reside within the $\alpha + \alpha'$ region in the Fe-Cr phase diagram (figure 2.10) [32], thus indicating that it is favourable for α' phases to form. For Fe-Cr binary alloys with Cr

	14WT aged for 3 months Concentrations [wt.%]			14WT aged for 8 months Concentrations [wt.%]	
	Dataset 21350	Dataset 21514	Dataset 22361	Dataset 23604	Dataset 24511
Fe	42.55	41.42	49.21	52.04	34.46
Cr	39.61	47.47	46.32	44.26	58.31
W	5.50	4.65	3.78	2.90	5.51
Ti	3.00	3.31	0.03	0.02	0.08
Mn	1.95	1.05	0.21	0.48	0.71
Si	0.94	0.52	0.33	0.20	0.44
O	3.33	0.14	0.03	0.00	0.24
C	1.56	0.32	0.04	0.00	0.06
N	0.56	0.61	0.01	0.00	0.02
Cu	0.47	0.14	0.00	0.01	0.05
V	0.23	0.14	0.01	0.00	0.04
Others	0.30	0.23	0.03	0.09	0.08

Table 5.4: Composition breakdown of the isolated Cr-rich zones within 14WT aged for 3 and 8 months. Others refer to the sum total concentration of the minor elements within the precipitate: H, Al, P and Co. Units of concentration are wt.%.

concentrations similar to 14WT, the α' phase is observed as spherical isolated precipitates rich in Cr, as shown in figure 2.16. As the precipitates observed to have formed in the 14WT aged for 3 and 8 months are similar to that described in section 2.3.1.4, the highly Cr-rich zones are α' precipitates.

5.3.1.2 No segregation of minor elements towards α' precipitates

The atom maps in figures 5.3 and 5.4 indicated no minor elements were segregated at the interfaces of any α' precipitates within the 14WT aged for 3 and 8 months. Magnified atom maps of W, Ti, Al, Mn, Si containing a single typical α' precipitate are shown in figure 5.9. These atom maps have been generated from dataset 24511 which is from the 14WT aged for 8 months. Each of the atom maps shown shows that there aren't any highly concentrated zones around the α' precipitate. This shows that W, Ti, Al, Mn and Si are not segregated at the α' precipitate-matrix interface. Indeed, no segregation of minor elements was observed in any of the APT datasets containing α' precipitates.

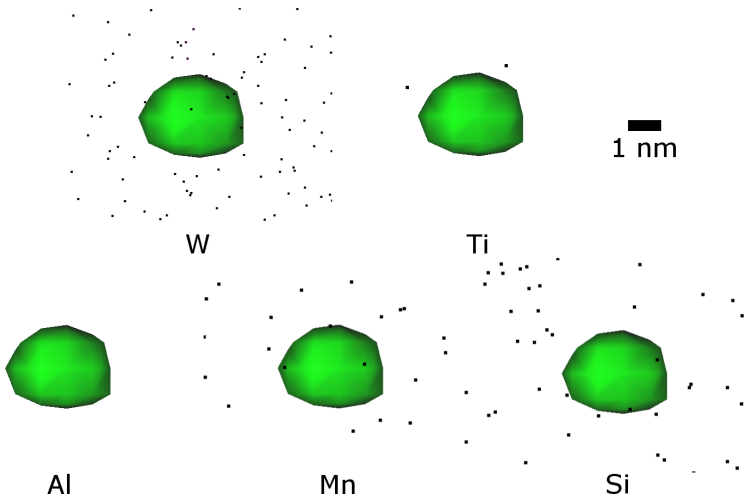


Figure 5.9: A single α' precipitate has been cropped from dataset 24511 and an atom map of a particular minor element has been overlaid. The α' precipitate here is represented by a 30at.%Cr isoconcentration surface map.

5.3.1.3 14WT Ti rich precipitates

The 14WT atom maps, with the exception of those from the 8 month aged APT datasets, show the existence of zones containing a high density of Ti and TiO ions. These features have been identified as Ti-rich precipitates [344]. As they are present in the as-received

samples, they probably have formed during the fabrication process.

Table 5.5 presents the Ti-rich precipitate data as a function of time for each of the experimental repeats. In total 21 Ti-rich precipitates were observed across all 12 14WT APT datasets acquired in this study. Not all datasets contained Ti-rich precipitates and this was the case for datasets 23301, 22860, 22923 and all three APT datasets belonging to the 14WT aged for 8 months (23064, 24508 and 24511). Like the Cr-rich precipitates, the Ti-rich precipitate radius data presented in table 5.5 have large uncertainties associated with it, and there is significant variation in the number densities. Table 5.5 also shows that the matrix Ti concentrations measured here range from 0.06-0.28at.%. Given that the nominal concentration of Ti in 14WT is 0.2wt% or 0.21at.%, there is significant variation.

As part of the 14WT characterisation process, Gorley measured the distribution of Ti solute using EPMA over a $20\mu m$ distance [44]. He showed that there were significant fluctuations in the concentration of Ti, and that there were regions in the microstructure that had a concentration as low as 0.06wt%, and as high as 0.32wt%. Therefore the inhomogeneous concentration of Ti in 14WT measured here and reported in table 5.5 is not surprising.

The varying matrix concentration of Ti can also explain the inhomogeneity in the distribution of the Ti-rich precipitates. The solubility limit of Ti in Fe at $475°C$ is $\sim 1.7at.\%$ [345]. Therefore only regions that exceeded this concentration of Ti should have formed a Ti-rich precipitate. Regions that greatly exceed this threshold concentration should contain larger precipitates that have high precipitate concentrations of Ti, whereas those that exceed it marginally should contain smaller precipitates and lower precipitate Ti concentrations.

The atom maps in figures 5.1, 5.2 and 5.3 indicated that minor impurity elements such as Al, Mn, Si, V, Cu, P and C are concentrated in approximately the same space as the

Ageing duration	Dataset #	# of Ti rich precipates in dataset volume	Dataset volume $[10^{-22}m^3]$	Ti-rich precipitate number density $[10^{21}m^{-3}]$	Average radius [nm]	Average precipitate Ti concentration $[at.\%]$	Ti matrix concentration $[at.\%]$
	23301	0	3.79				0.23
As-received	23328	3	3.23	9	5.24±1.51	44.17	0.15
	23818	2	7.17	3	11.09± 1.46	30.69	0.08
	22843	2	4.86	4	7.46±1.49	26.69	0.15
1 month	22860	0	16.3				0.08
	22923	0	9.87				0.07
	21350	4	3.83	10	63.97±0.39	4.09	0.14
3 months	21514	5	11.5	4	8.27±1.02	18.04	0.26
	22361	5	13.8	3	3.82±0.77	4.65	0.12
	23064	0	12.4	0	0	-	0.07
8 months	24508	0	1.11	0	0	-	0.28
	24511	0	0.88	0	0	-	0.06

Table 5.5: Physical characteristics of the Ti-rich precipitates found in each of the aged 14WT APT datasets.

Ti-rich precipitates. Concentration profiles through Ti rich precipitates such as that shown in figure 5.10a have been obtained. The Ti rich precipitate shown in figure 5.10a is through the largest Ti-rich precipitate in dataset 22843 (14WT aged for 1 month). The minor impurity elements such as C, Si in figure 5.10c as well as Al, P, V, Mn, Cu in figure 5.10d contribute to the total composition of the Ti rich precipitate. Only Mn, P and Cu appear to be segregated at the matrix-Ti rich precipitate interface.

All of the Ti-rich precipitates in dataset 21514 can also be seen to be correlated with α' precipitates. This is shown in figure 5.7c and figure 5.11. This is an anomalous observation as only one dataset out of all the aged 14WT APT datasets containing α' precipitates exhibited this. It is possible that the Ti rich precipitates in dataset 21514 may have participated or promoted α' precipitation via heterogeneous nucleation. However heterogeneous nucleation of α' precipitates was not observed in any of the other 14WT datasets containing both α' and Ti rich precipitates. Indeed, the majority of α' precipitates have been seen to form away from surfaces such as the grain boundary in dataset 22361 or Ti rich precipitates in the datasets that contain them. Overall only 5 out of the entire population of Ti-rich precipitates (21 in total) exhibited this.

5.3.1.4 Concentrations of Ti and W within 14WT aged for 8 months

Each of the datasets for the 14WT aged for 8 months, which are shown in figure 5.4, were seen to contain sparse distributions of Ti and W, and suggests that these alloying elements are depleted in the samples. Table 5.5 and the preceding section explained that the concentrations of Ti within 14WT were all within the range of concentrations as initially characterised by Gorley [44].

Table 5.6 presents the concentrations of W within the as-received 14WT and the 14WT aged for 8 months APT datasets. W can be seen to range between 0.77-0.91at.%. Gorley also characterised the W distributions using EPMA and showed that W concentrations

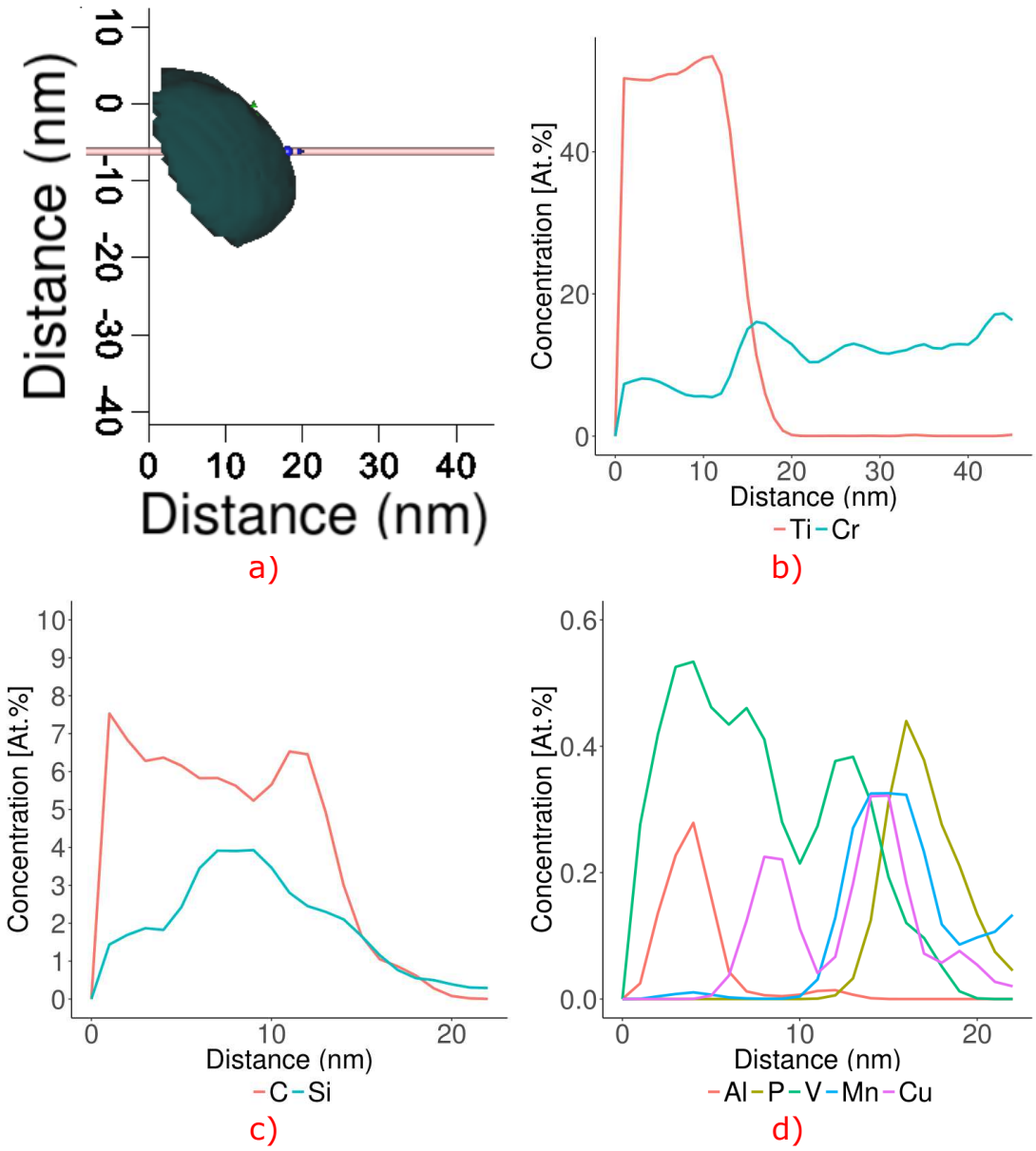


Figure 5.10: a) Ti Isoconcentration surface map showing the largest Ti rich precipitate in dataset 22843 (14WT aged for 1 month) which is approximately 20nm in diameter. The Ti threshold is set to 5at.%. b), c) and d) are concentration profiles through precipitate shown in a). b) shows a Ti and Cr concentration profile. c) C and Si concentration profiles. d) Al, P, V, Mn, Cu concentration profiles inside the Ti rich precipitate shown in a).

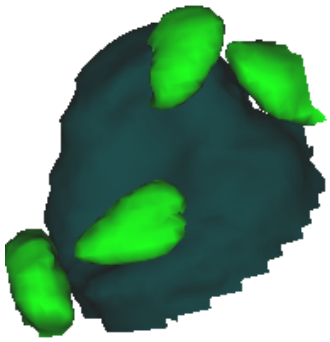


Figure 5.11: Zoomed in rotated 90° anti-clockwise section of the Ti rich and α' precipitates labelled in figure 5.3a. Isconcentration Ti and Cr surfaces have been used to highlight these two features. The presence of α' precipitates on the surface of these Ti rich precipitates suggests that they nucleated heterogeneously

fluctuated between 0.74at.% and 0.94at.% over a $20\mu m$ distance [44]. Given the nominal composition and inherent inhomogeneity associated with 14WT alloys, the concentrations reported in table 5.6 are expected. Therefore, the perception of W depleted in the 14WT aged for 8 month APT datasets, in figure 5.4, is false.

Nominal	As-received 14WT			14WT aged for 8 months		
concentration	23301	23328	23818	24511	23064	24508
0.92	0.77	0.94	0.71	0.8	0.77	0.81

Table 5.6: Bulk concentrations of W as measured by the atom probe in the as-received 14WT and 14WT aged for 8 months. Concentrations are quoted in at.%

5.3.1.5 14WT grain boundary segregation

As shown in table A.2, as well as the 14WT atom maps presented here, only one 14WT APT sample volume contained a GB. This GB was found in dataset 22361 which is from the 14WT alloy aged for 3 months.

GIE values have been calculated for this GB using the method described in appendix

A.2.4. Cr, W, Mn and Si were on average present at the GB by 35.62±11.78, 22.48±3.64, 0.38±0.07 and 6.06±1.52 $atoms\,nm^{-2}$ respectively. Whereas, Ti was on average depleted at the GB by -0.54 ± 0.25 $atoms\,nm^{-2}$.

As a GB has not been captured in any of the as-received 14WT datasets acquired in this thesis a comparison cannot be made. Instead, the data is presented in appendix C for use in future studies.

5.3.2 APT characterisation of isothermally aged 14YWT1

Atom maps from one dataset from each of the ageing states are shown in figure 5.12. Atom maps from the remaining two datasets acquired from each aged state are shown in appendix B.

The atom maps from all three APT datasets belonging to the as-received 14YWT1 show trends that are consistent across all experimental repeats. Firstly, zones that are depleted of Fe occur in the Fe atom map. These zones tend to be correlated with regions containing a high concentration of Cr. Both of these features are correlated with the positions of the NFA particles, which can be identified from the Y, Ti and O ion maps. W is not concentrated in any particular region and can be seen to be spread uniformly. Regions containing a high density of Al, Mn and Si, which are impurity elements within 14YWT1, can be seen to be correlated with the NFA dispersoids. An example of such an occurrence is highlighted by the arrow on the Mn atom map within figure 5.12a.

As ageing duration increases little change is observed when comparing the as-received sample atom maps with those belonging to the aged atom maps. Indeed, little change occurs between aged states too. This general observation is consistent across all atom maps shown in figure 5.12 as well as those in appendix B. The zones depleted in Fe and enriched in Cr, first identified in the as-received 14YWT1, continue to be present in all the atom maps belonging to the aged material. These features also continue to

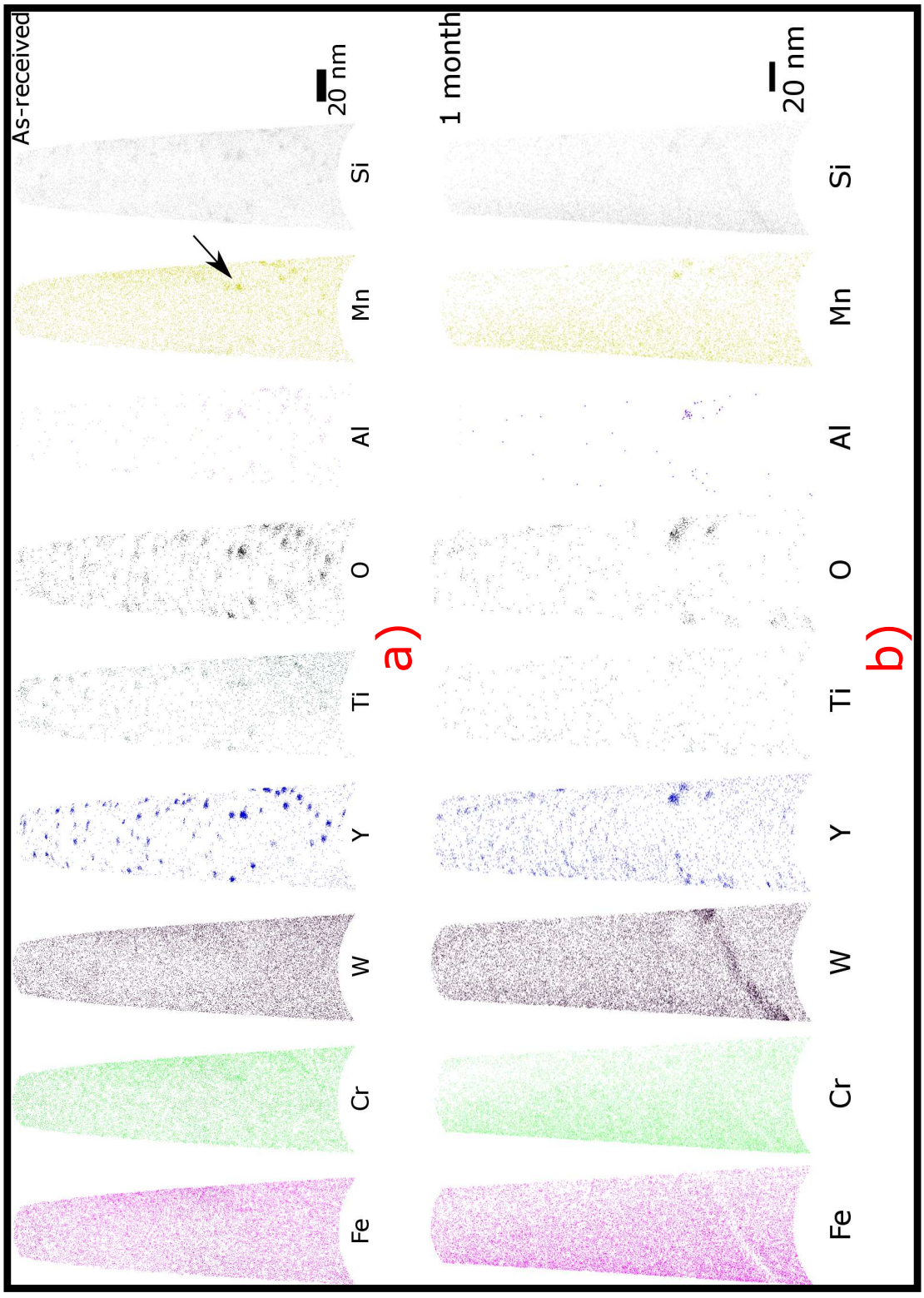


Figure 5.12: Atom map slices of solute and impurities within as-received and aged 14YWT1

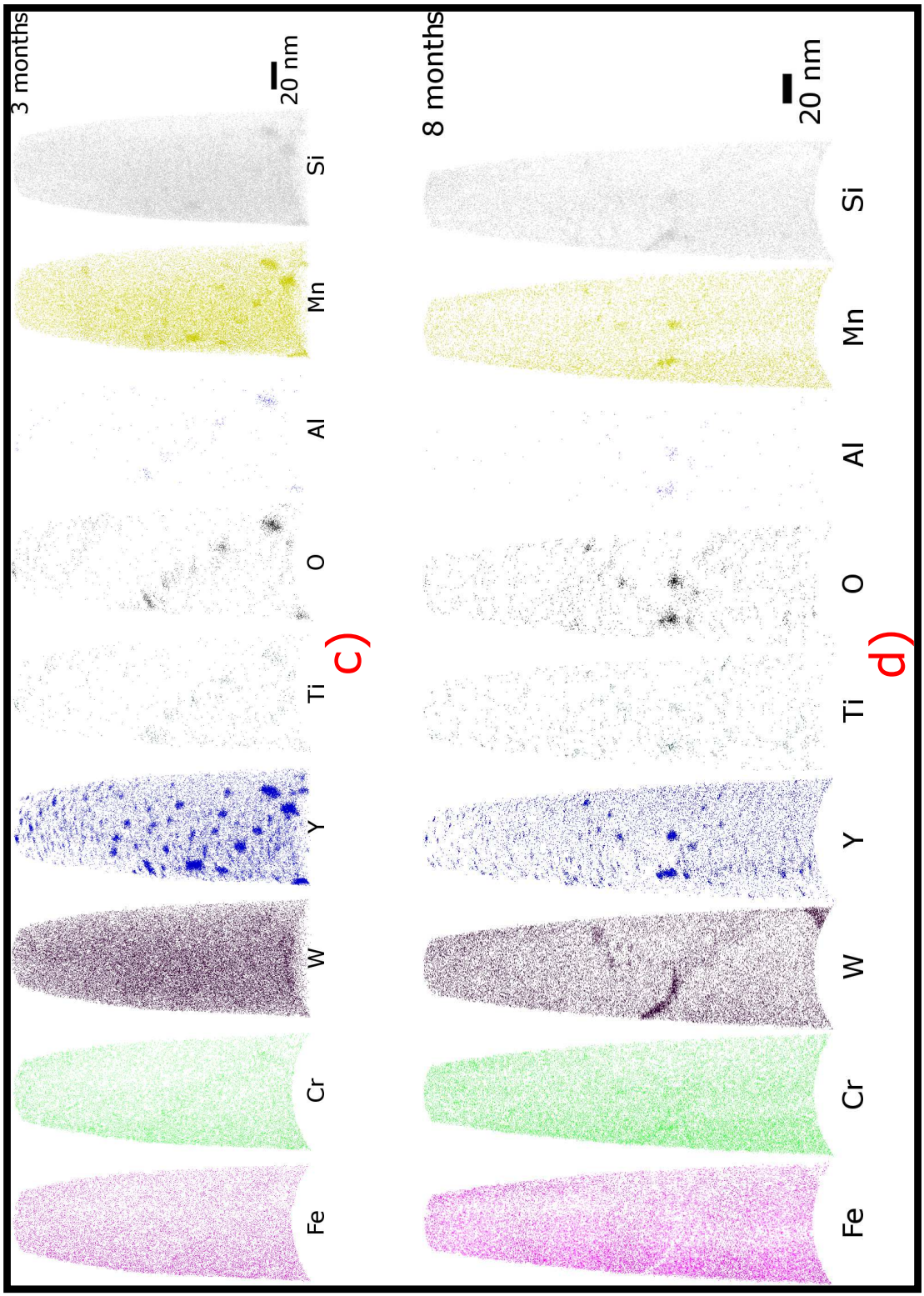


Figure 5.12: Atom map slices of solute and impurities within as-received and aged 14YWT1

be correlated with the NFA particles. Y, Ti and O atom maps also retain their highly concentrated and discrete positions within the matrix. Regions containing a high density of Al, Mn and Si continue to be correlated with the positions of NFA particles for all 14YWT1 atoms at all ageing durations. However, the distribution of W is varied in the aged 14YWT1. W can be seen to segregate to grain boundaries in figure 5.12b and a dislocation in figure 5.12d.

5.3.2.1 Fe and Cr distributions within the as-received and aged 14YWT1

The as-received and aged 14YWT1 atoms maps in figure 5.12 indicate that Fe and Cr distributions are non-binomial. A magnified Fe, Cr and Y+TiO atom map is shown in figure 5.13. Within it is a zone which is depleted of Fe but rich in Cr, Y and TiO. There are also zones rich in Y and TiO that are smaller than that highlighted in figure 5.13, where Fe is not depleted and Cr is not enriched.

As explained in section 3.4.5.1, Pearson coefficients, μ, can be calculated to quantitatively determine whether concentration distributions of an ionic species within a dataset is binomial. μ has been calculated for the Fe and Cr ion distributions, for each of the 3 experimental repeats for each 14YWT1 state, to determine the degree to which these elements deviate from a binomial distribution. $\bar{\mu}$ has been calculated by averaging μ across all three experimental repeats for an ageing duration and is presented in table 5.7. The data in table 5.7 show that both Fe and Cr deviate away from a perfect binomial distribution as μ is close to one. The results from this quantitative analysis are consistent with the qualitative observations made from the atom maps in figures 5.12, appendix B and figure 5.13.

A concentration profile through the area of interest in figure 5.13 is shown in figure 5.14. The dispersoid region is clearly outlined by the Y and Ti concentration profile. This region contains a significant concentration of both Fe and Cr. The enriched part

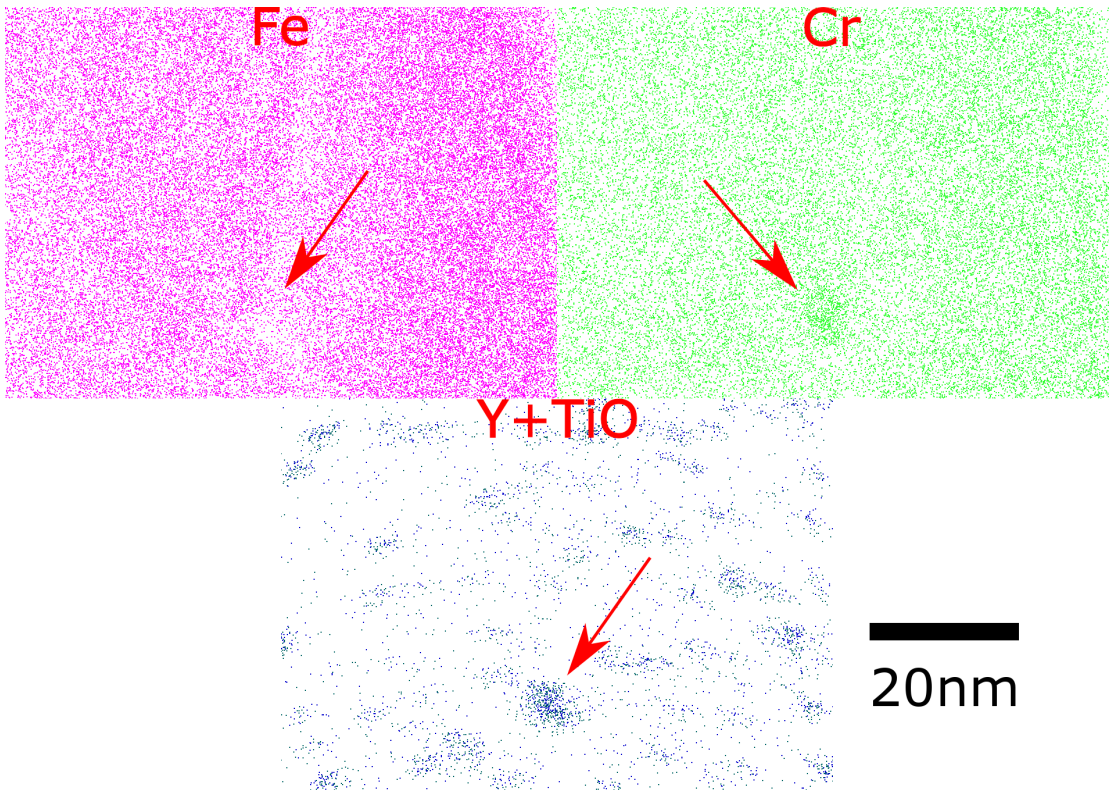


Figure 5.13: Magnified image of an Fe, Cr and Y+TiO atom map from dataset 22920 (14YWT1 aged for 8 months). The arrows point to the same zone in each of the three different atom maps.

of the Cr profile extends spatially beyond the profile of Y and Ti, which indicates the presence of a Cr shell around the dispersoid.

One concentration profile through a randomly selected NFA dispersoid from the as-received 14WT, 14WT aged for 1 month, 3 months and 8 months datasets are shown in figure 5.15. All of these concentration profiles showed the same trends as those in seen in figure 5.14, that is a region enriched with Cr, depleted of Fe and enriched with Y and Ti.

Previous studies have confirmed via electron microscopy that Fe is not present within NFA dispersoids. These features also tend to be enriched with higher concentrations of

Ageing duration [$Months$]	Dataset	μ_{Fe}	μ_{Cr}	$\bar{\mu}_{Fe}$	$\bar{\mu}_{Cr}$
0	23070	0.72	0.72	0.78 ±0.10	0.80 ±0.04
	23146	0.64	0.85		
	23181	0.97	0.83		
1	20713	0.79	0.64	0.89±0.05	0.81±0.09
	21112	0.90	0.82		
	21240	0.98	0.95		
3	20823	0.82	0.69	0.79±0.02	0.76±0.04
	22468	0.81	0.79		
	23065	0.74	0.80		
8	22826	0.92	0.76	0.92±0.02	0.79±0.0.07
	22894	0.88	0.70		
	22920	0.97	0.92		

Table 5.7: Pearson coefficients, μ for the Fe and Cr ions distributions within each 14YWT1 dataset acquired for this isothermal ageing experiment. Averages are calculated from all three experimental repeats for each duration.

Cr when imaged by APT [346]. This is due to APT magnification effects, as explained in section 3.4.7.

Figure 5.16 shows two-dimensional density plots of Fe, Cr and Y+TiO in the same region shown in figure 5.13. The black arrows represent the direction of the incoming laser pulse and the red arrow highlights the same dispersoid highlighted in figure 5.13. It can be seen that a highly dense region within the Fe and Cr density maps is situated closest to where the laser pulse initially interacts with the sample. Accordingly, a density gradient

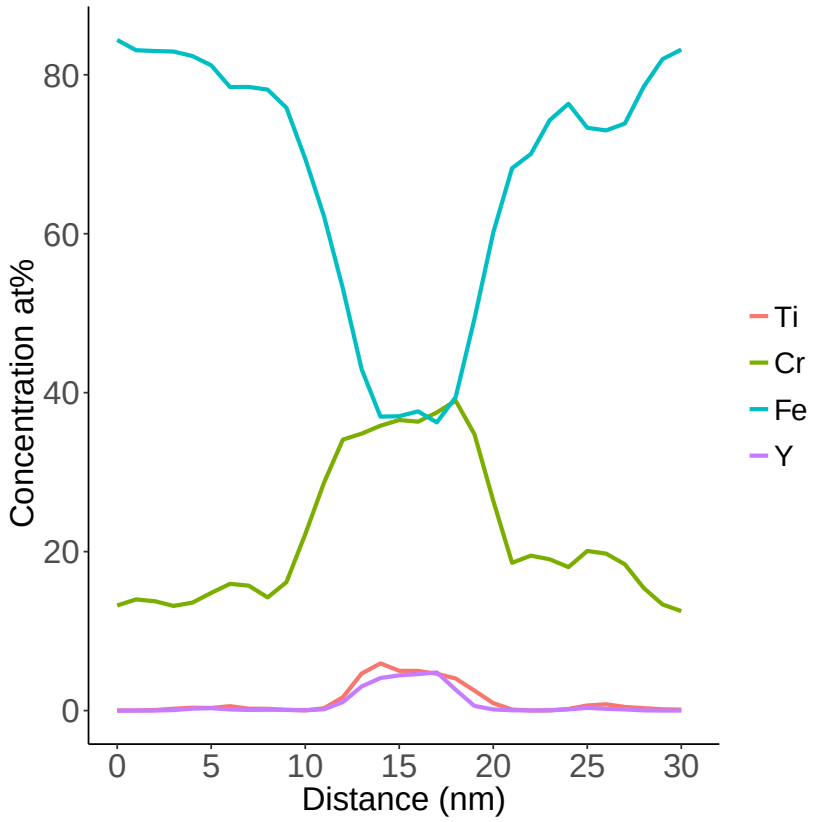


Figure 5.14: Concentration profile through the area of interest in figure 5.13

occurs for these solvents. The Y+TiO map also exhibits highly dense regions distributed within the region sampled, which is representative of the dispersoids. Y+TiO density maps do not exhibit a gradient along the Y-axis. The highly dense regions closest to the laser pulse are indicative of the shadow effect as described in appendix 3.4.8. Finally, consistent with the concentration profiles shown in figures 5.14 and 5.15, localised dense regions of Fe and Cr are correlated with the dispersoids.

Therefore the distribution of Fe and Cr are not homogeneous as a result of magnification effects and the shadow effect, and not due to α' formation.

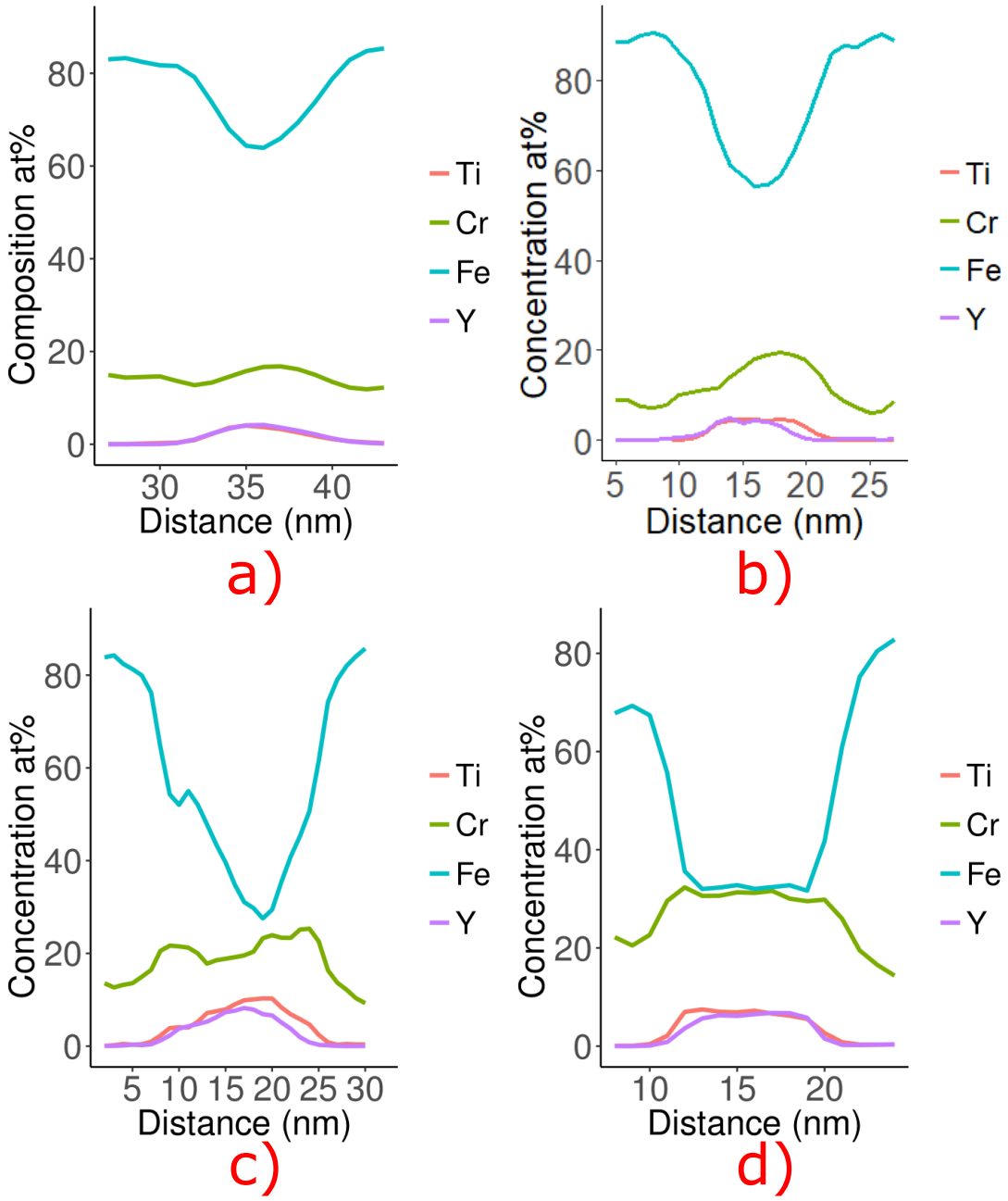


Figure 5.15: Concentration profile through randomly selected NFA dispersoids in a) dataset 23070 - as-received 14YWT from b) dataset 20713 - 14YWT aged for 1 months c) dataset 20901 - 14YWT aged for 3 months d) dataset 22894 - 14YWT aged for 8 months.

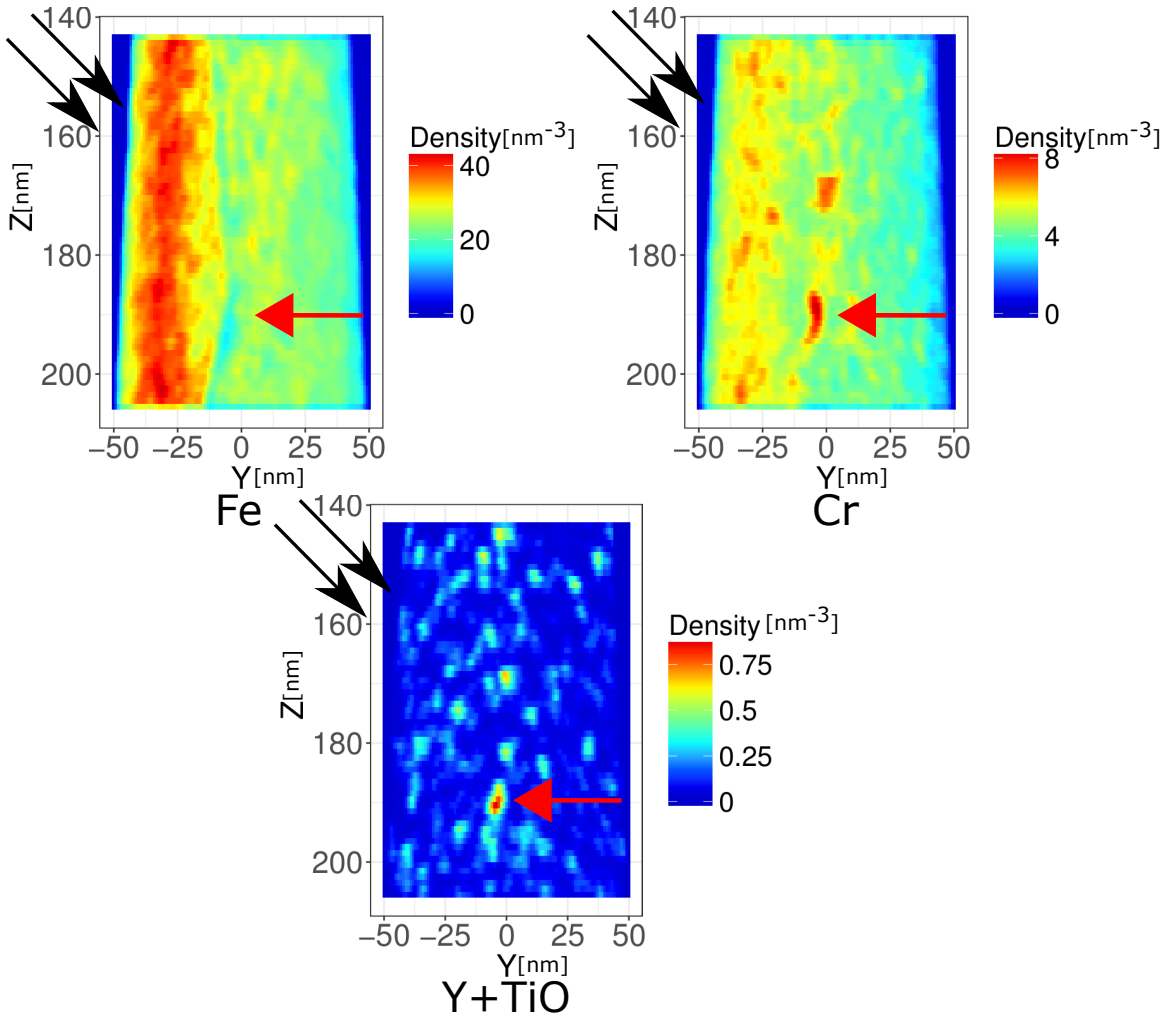


Figure 5.16: 2D density maps of Fe, Cr, Y_TiO within dataset 22920 -14YWT1 aged for 8 months. The black arrows show the direction of the laser beam within the APT analysis chamber. The red arrow is the same dispersoid highlighted in figure 5.13.

5.3.2.2 Mn, Si and Al distributions within the as-received and aged 14YWT1

The atom maps in figure 5.12 and those in appendix B indicated that Mn, Si and Al enriched zones were correlated with the larger NFA dispersoids. Figure 5.17 shows atom maps for Mn and Al in a), Si only in b) and TiO and Y in c). This is the same region as highlighted in figure 5.12a but has been magnified.

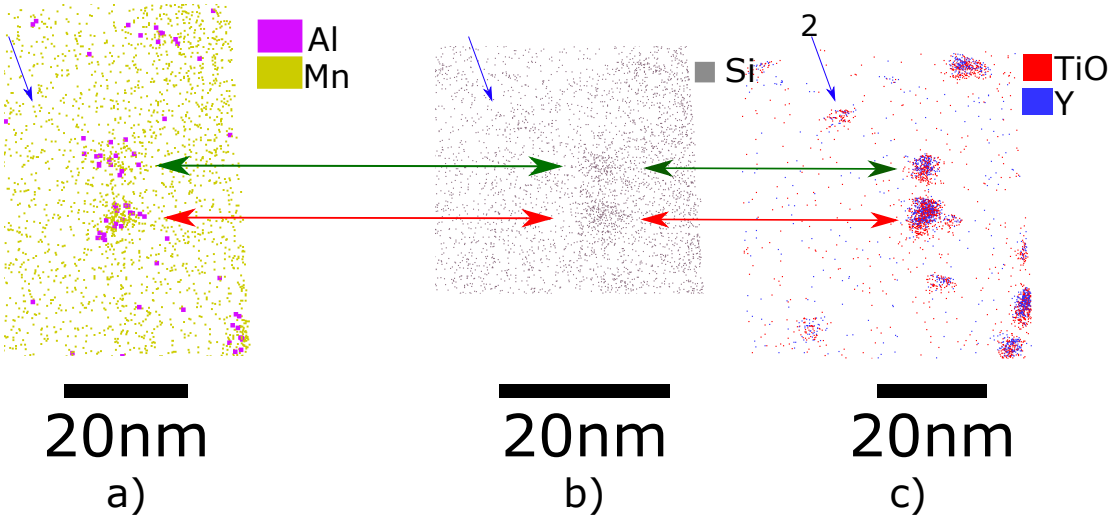


Figure 5.17: a), b) and c) are magnified atom maps of the zone highlighted by the black arrow in figure 5.12a. a) shows Mn and Al ions, b) shows Si ions only and c) shows Y and TiO ions. The size of the Al atoms shown are 3 times as large as the Mn atoms to ensure visibility. The red, blue and green arrows highlight the same region within a) b) and c).

The region magnified in figure 5.17 contains two large dispersoids, which are highlighted by the red and green arrows, and many small dispersoids. One of the many smaller dispersoids is highlighted by the blue arrow. The position of the dispersoids are clearly marked in the TiO and Y atom map in figure 5.17c.

The larger NFA dispersoids, which are highlighted by the red arrow, are seen to be enriched with Al, Mn and Si. Whereas the smaller dispersoids, including the one highlighted by the blue arrow, are not enriched with any of these elements.

A concentration profile through dispersoids highlighted in blue and red in figure 5.17 is shown in figure 5.18. Both concentration profiles show a large Y and Ti peak which

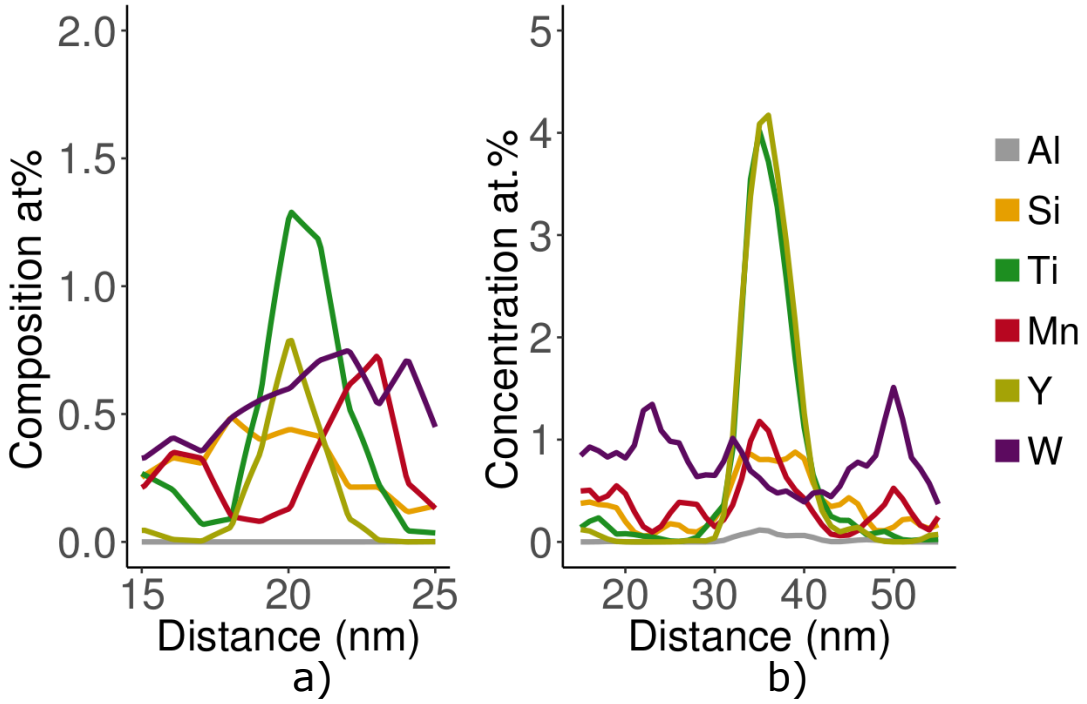


Figure 5.18: Concentration profile through a) the small dispersoid (diameter is 6nm) highlighted by the blue arrow in figure 5.17 and b) the larger dispersoid (diameter is 14nm) highlighted by the black arrow in figure 5.12a and the red arrow in figure 5.17

is expected, given that they are both NFA dispersoids. The concentrations of Mn, Si and Al within the smaller dispersoid are lower than in the larger dispersoid. Table 5.8 show the concentrations at the centre of each of the dispersoids as well as the corresponding bulk composition within the dataset. The larger dispersoid contains a higher quantity of Mn and Si and Al relative to the bulk concentration. The smaller dispersoid is seen to contain significantly more Si but the quantities of Mn and Al are below the bulk concentrations. This quantitative data is consistent with the qualitative assessment from the atom maps, that is the larger dispersoids are seen to contain larger concentrations of Mn, Si and Al.

Electron microscopy has shown that NFA dispersoids tend to contain Cr, Y, Ti and O

	Smaller dispersoid	Larger dispersoid	Bulk concentration
Mn	0.13	1.17	0.23
Si	0.44	0.86	0.3
Al	<<0.01	0.12	0.01

Table 5.8: Concentrations of Mn, Si and Al, in at.%, at the centre of the dispersoids shown in figure 5.17. The smaller dispersoid is that highlighted by the blue arrow in figure 5.17 and the larger dispersoid is highlighted by the red arrow in figure 5.17. For comparison, the bulk concentrations of these elements from the same dataset as measured by APT is shown.

only [84, 313]. Therefore the quantities of Si, Mn and Al within the NFA dispersoids are due to APT magnification effects.

5.3.2.3 14YWT1 grain boundary segregation

The atom maps in figure 5.12b indicated that the 14YWT1 GBs were enriched in W and Si. Accordingly, Gibbsian Interfacial Excess (GIE) values have been calculated via the method described in appendix A.2.4. Gibbsian Interfacial Excess (GIE) values were calculated at three different regions along the same GB for each dataset containing a GB (see table A.2 in the appendix for a summary of the datasets containing a grain boundary). Averages across the three Gibbsian Interfacial Excess (GIE) values for a particular GB are plotted as a function of ageing duration and is shown in figure 5.19. The numbers adjacent to each datapoint refer to the dataset number.

Cr GIE values shown in figure 5.19a for the as-received datasets are clustered together and have small error bars. This indicates little variation between the measurements across the GBs within the as-received datasets occurs. Though there is signficant variation in the data, the data suggests GBs within the aged 14YWT1 are enriched with Cr. W GIE values are shown in figure 5.19b and suggest that GBs are enriched with

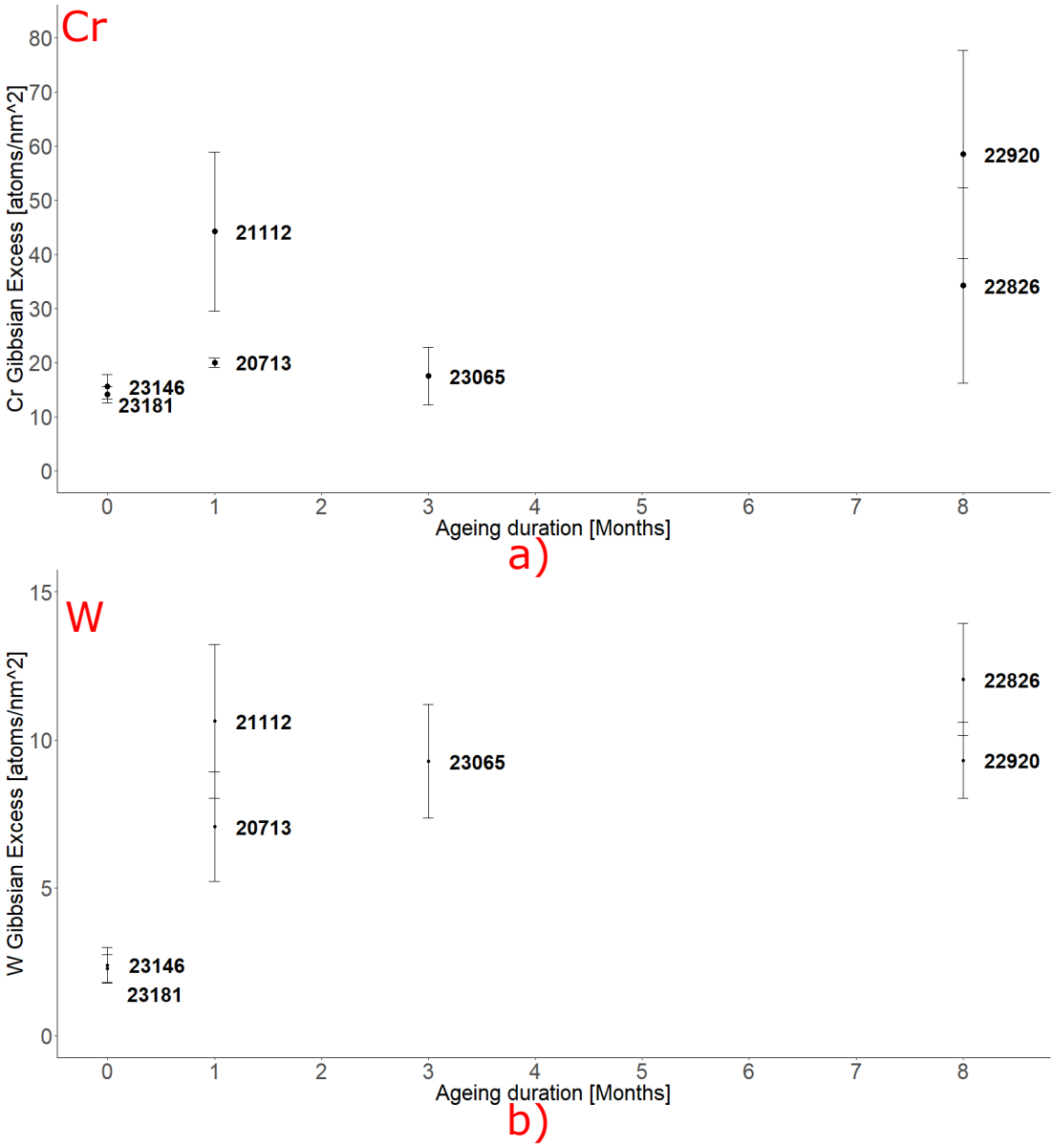


Figure 5.19: Average GIE values for a) Cr, b) W, c) Si and d) Mn within the GBs captured in the 14YWT1 APT datasets. For Cr and W, some GBs seem to enrich further with ageing, but some do not undergo any change. For Si and Mn, no change occurs with ageing.

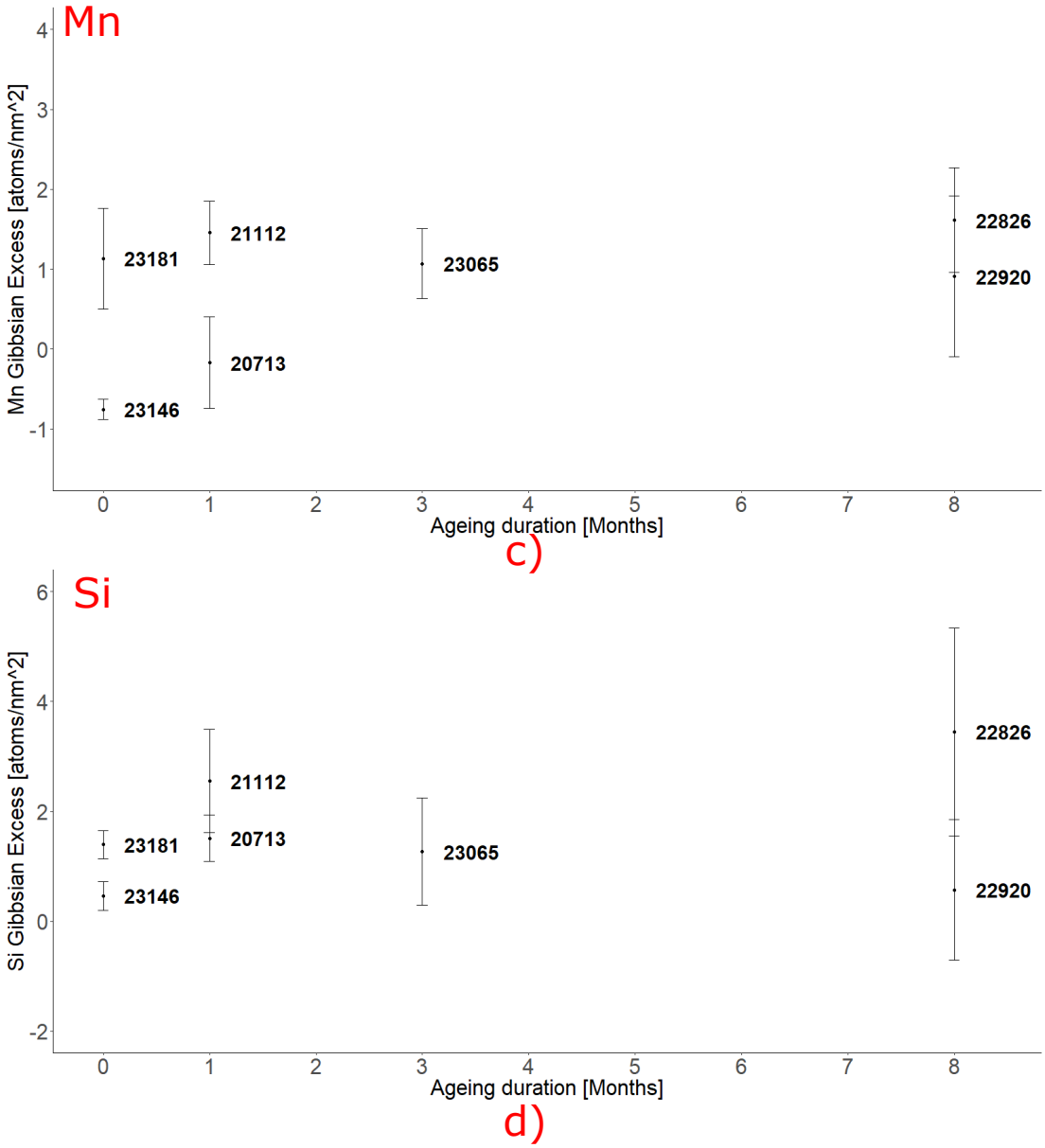


Figure 5.19: Average GIE values for a) Cr, b) W, c) Si and d) Mn within the GBs captured in the 14YWT1 APT datasets. For Cr and W, some GBs seem to enrich further with ageing, but some do not undergo any change. For Si and Mn, no change occurs with ageing.

W during ageing. The increase in the quantity of W at the GBs is seen to plateau after ageing for one month. Figures 5.19c and 5.19d indicate that ageing does not increase the quantity of Mn and Si respectively.

5.3.2.4 NFA particles within the as-received and aged 14YWT1

	As-received			1 month		
Dataset	23070	23146	23181	20713	21112	21240
Number of dispersoids within dataset	633	157	424	366	577	440
Total number of dispersoids across all datasets	1214			1383		

	3 month			8 month		
Dataset	20823	20901	22468	22826	22894	22920
Number of dispersoids within dataset	205	136	593	543	499	1034
Total number of dispersoids across all datasets	934			2076		

Table 5.9: Number of dispersoids found, isolated and studied in each of the 14YWT1 APT datasets

The 14YWT1 Y, Ti and O atom maps, in figure 5.12, show the positions of the NFA dispersoids. These atom maps show that the dispersoids continue to populate the 14YWT1 matrix throughout the ageing process. The inhomogeneous distribution of the dispersoids is evident by comparing figure 5.12a with atom map slices of the as-received

14YWT1 in appendix B. Indeed, the atom map slices do not represent the dispersoid distributions adequately as there is significant variation between planes within the APT dataset volumes.

The dispersoids have been isolated from the APT datasets so that their radius and Y, Ti and O contents can be studied. Table 5.9 shows the number of dispersoids that are present in each of the 14YWT1 datasets. The number of dispersoids varies significantly and this is due to both inhomogeneous distributions of dispersoids as well as varying APT dataset volumes.

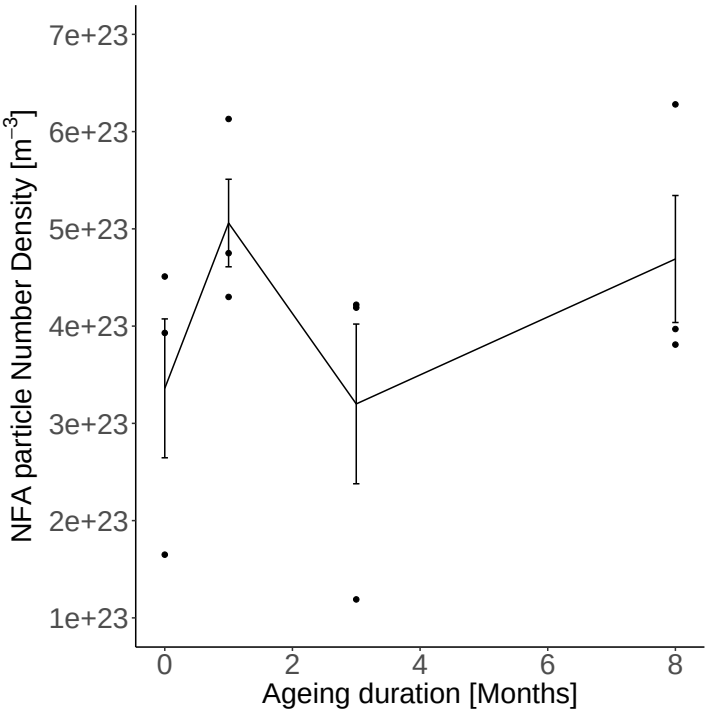


Figure 5.20: NFA cluster densities as a function of ageing duration for each 14YWT1 dataset acquired. The solid line is the average NFA particle density for a particular 14YWT1 state. Averages and standard errors are calculated from the three experimental repeats for each ageing duration

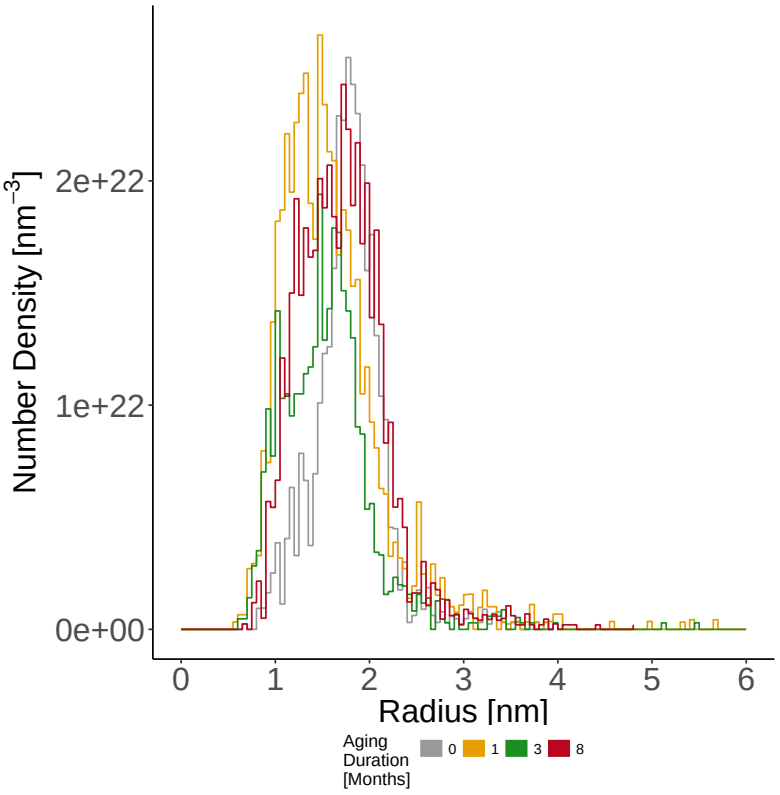


Figure 5.21: NFA cluster radius distribution within the as-received and aged 14YWT1. Averages and standard errors are calculated from the three experimental repeats for each ageing duration

NFA particle number density as function of ageing duration for each 14YWT1 APT dataset is shown in figure 5.20. The solid line shows the average NFA particle number density as a function of ageing duration. There are large variations in the NFA particle number densities between the individual datasets for a single ageing state, which confirms that the dispersoids are inhomogeneously distributed. No significant change in the NFA particle density as result of the ageing can be identified from either the scatter points or the solid line.

14YWT1 NFA cluster radii distributions for each of the ageing durations are shown in figure 5.21. It has been constructed by averaging the dispersoid radius distributions

from each of the experimental repeats for a given ageing duration. Figure 5.21 exhibits no significant change between the four different distributions. Therefore no change in the dispersoid radius within the aged 14YWT1 NFA clusters relative to the as-received 14YWT1 is observed.

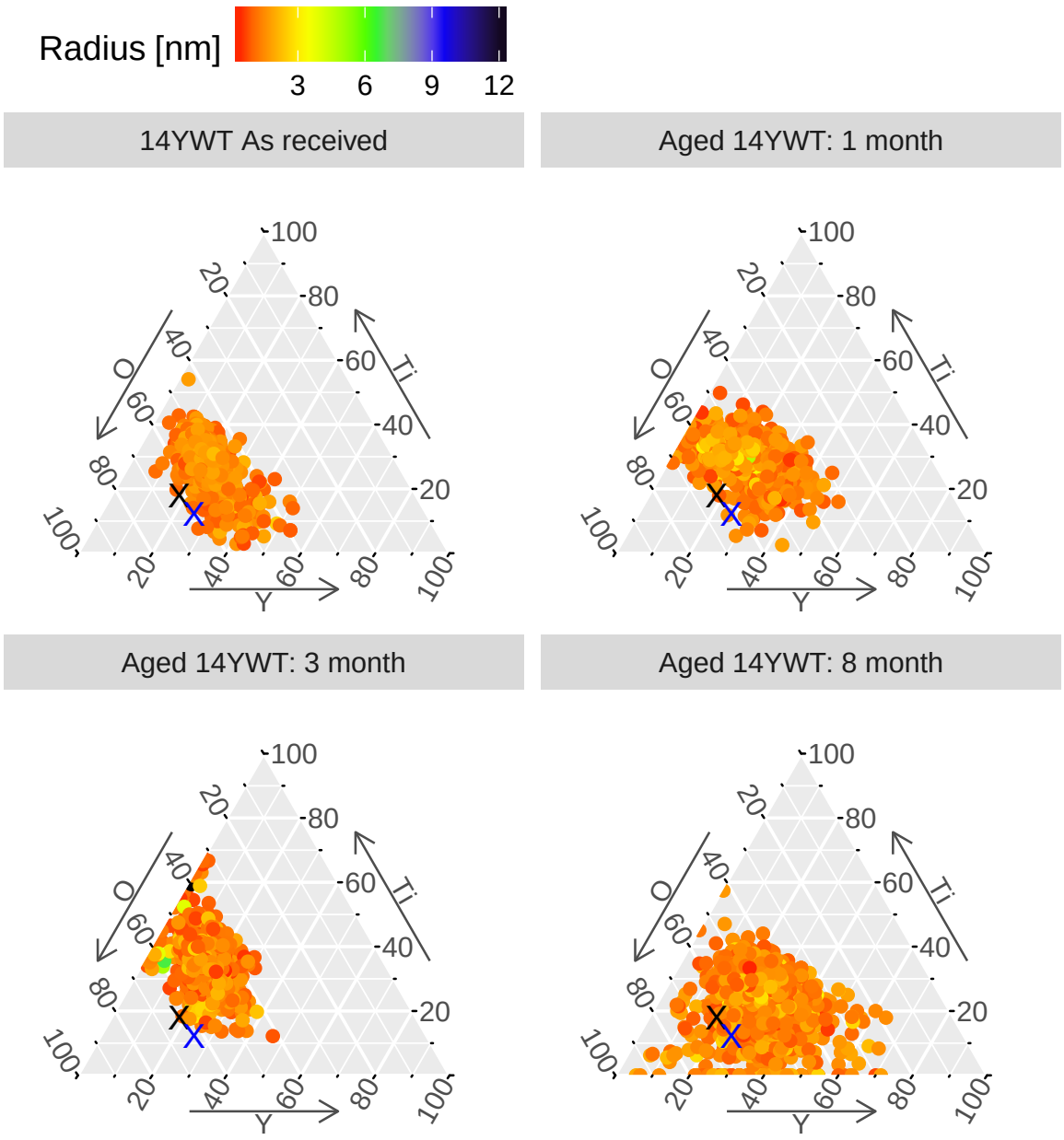


Figure 5.22: Ternary NFA dispersoid composition diagrams. The colours of the spots represent the radius of the individual clusters present in each of the three APT datasets acquired for a given time period. The black and blue crosses mark the positions of the stoichiometric $Y_2Ti_2O_7$ and Y_2TiO_5 respectively.

Figure 5.22 presents tenerary diagrams that show the NFA cluster Y, Ti and O content as a function of radius for all the NFA particles analysed in this study. These ternary diagrams have been calculated by counting the number of Y, Ti and O atoms within each of the dispersoids for a given ageing duration. Particles larger than 3nm do occur but are few in number with respect to the more abundant smaller particles. There is significant variation in the data for each alloy state. This is consistent with the APT characterisation of various Fe-Cr DSAs by London [306] and Williams [347]. The compositions tend to reside in the O-rich corner of the ternary diagram for all 14YWT1 samples. No obvious NFA particle radius-composition relationship can be seen and no significant change in the composition of the NFA particles has occurred during ageing. However, there is significantly more spread in the compositions within the ternary diagram for the 14YWT1 aged for 8 months. Table 5.9 shows that the compositions from 2076 dispersoids are used to construct the ternary diagram for the 14YWT1 aged for 8 months. This is significantly greater than the other aged states, and so the greater spread is attributed to the increased number of dispersoids sampled at this ageing duration relative to others aged states.

The ternary diagrams also show that the majority of the dispersoid populations are centred away from the black and blue crosses which show the positions of the stoichiometric stable $Y_2Ti_2O_7$ and Y_2TiO_5 respectively. This indicates the majority of dispersoids in all of the 14YWT samples studied here have non-stoichiometric compositions. This data is consistent with the a large number of studies in the literature [74, 77, 348, 349]. This includes APT data presented by London [306] and Williams [347]. This non-stoichiometry is thought to be due to the highly deffective structure within the dispersoids [75]. The average metal (Y+Ti) to oxide ratios (M:O) are often published in the literature and are a useful metrics to compare dispersoid compositions. This metric for a variety of 12YWT and 14YWT alloy variants are presented in table 5.10. M:O for each 14YWT

state in this study are shown in table 5.11 and are consistent with each other. This indicates little change in terms of Y, Ti and O dispersoid concentrations has occured during ageing. Apart from the M:O reported by [351], the M:O for the 14YWT as-received and the 14YWT aged alloys studied here are largely consistent with those from the studies in table 5.10.

Alloy	Nominal composition (wt%)	Treatement	Metal:Oxygen $((Y+Ti):O)$	Source
12YWT	$Fe-12Cr-3W-0.4Ti-Y_2O_3$	As-rec.	1.35	[350]
12YWT	$Fe-12.3Cr-3W-0.39Ti-0.25Y_2O_3$	As-rec.	1.2	[171]
14YWT	$Fe-14Cr-3W-0.4Ti-0.25Y_2O_3$	As-rec.	1.2	[62]
14YWT	$Fe-14Cr-3W-0.4Ti-0.3Y_2O_3$	As-rec.	1	[91]
14YWT	$Fe-14Cr-3W-0.4Ti-0.25Y_2O_3$	As-rec.	1.25	[62]
14YWT	$Fe-14Cr-3W-0.4Ti-0.3Y_2O_3$	As-rec.	4	[351]
12YWT	$Fe-12Cr-3W-0.4Ti-0.25Y_2O_3$	Aged at $1300°C$ for 10hrs	1	[170]
12YWT	$Fe-12Cr-3W-0.4Ti-0.25Y_2O_3$	Fe^+ irrad. 0.7dpa at $300°C$	1.04	[352]

Table 5.10: Published metal to oxygen ratios $((Y+Ti):O)$ for a variety of 12YWT and 14YWT alloys. As-rec. means as-received

14YWT State	M(Y+Ti):O
As-received	0.95
1 months	1.01
3 months	1.09
8 months	1.02
Average	1.01

Table 5.11: Metal (Y+Ti) to Oxide ratios (M(Y+Ti):O) for each 14YWT state

5.3.3 Aged 14WT and 14YWT1 microhardness measurements

Figure 5.23 shows the average Vickers hardness as a function of time for both the aged 14WT and 14YWT1. After 8 months of ageing the 14WT had hardened slightly from $238 kgf\,mm^{-2}$ to $269 kgf\,mm^{-2}$ ($\Delta Hv_{14WT} = +32 \pm 4 kgf\,mm^{-2}$), while the 14YWT1 had softened slightly from $575 kgf\,mm^{-2}$ to $548 kgf\,mm^{-2}$ ($\Delta Hv_{14YWT} = -26 \pm 10 kgf\,mm^{-2}$). The profile of the change in hardness within 14WT is peculiar as the values increase by $36 kgf\,mm^{-2}$ after one month of ageing and then softens to $+11 kgf\,mm^{-2}$ relative to the as-received hardness, after 3 months of ageing. By the time the full ageing period of 8 months is completed a net hardening of $+32 kgf\,mm^{-2}$ relative to the as-received state.

Similar to the 14WT, the Vickers hardness profile for 14YWT1 also fluctuates as ageing duration increases. Relative to the as-received sample, an initial loss in hardness by $-1 kgf\,mm^{-2}$ occurs after one month of ageing, the 3 month aged 14WT samples increases by $11 kgf\,mm^{-2}$ and then softens again by $26 kgf\,mm^{-2}$ after residing at temperature for 8 months. These changes in the hardness of 14YWT1 are well within the error bars, as shown in figure 5.23.

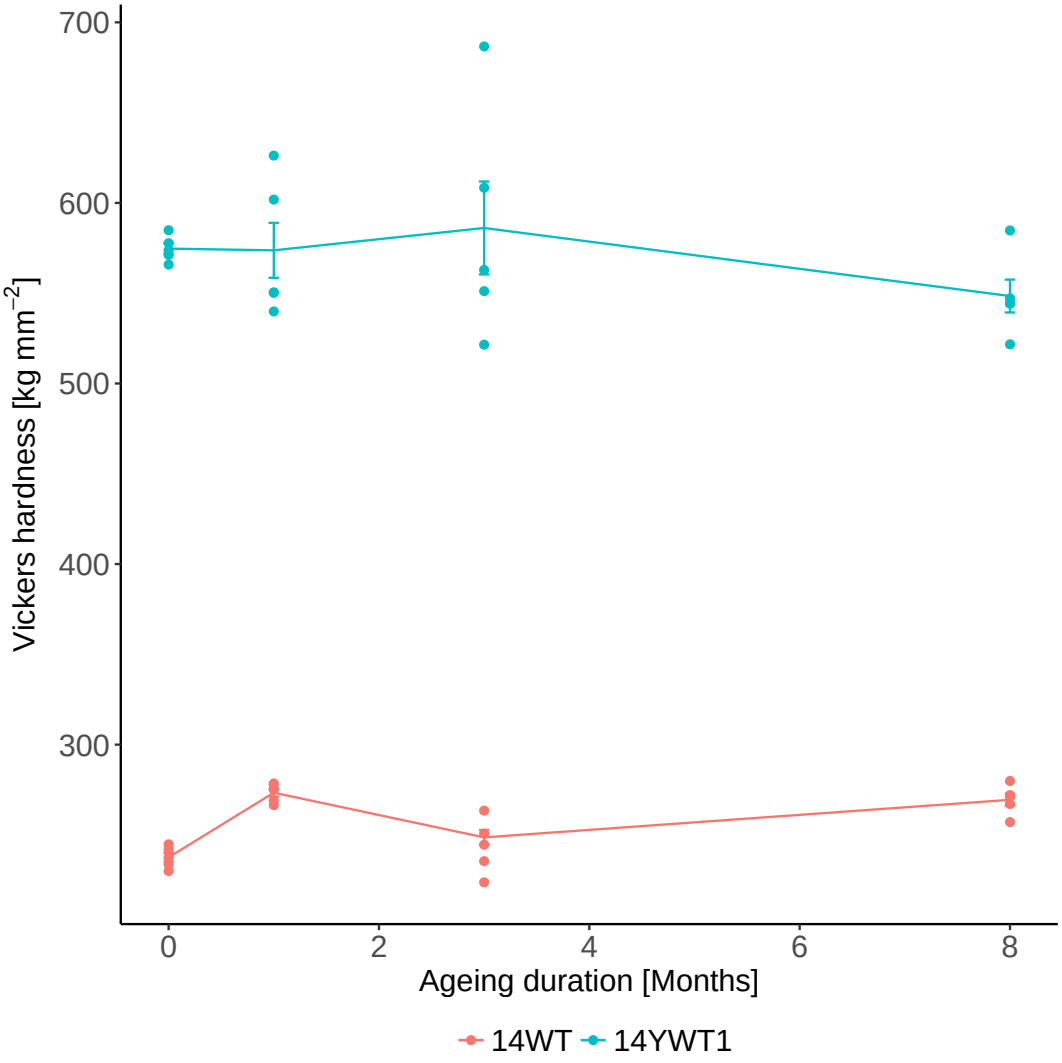


Figure 5.23: Microindentation hardness as a function of ageing. The points are the five repeated measurements and the solid line is the average of the repeated measurements.

5.4 Discussion

5.4.1 α' precipitate characteristics in the aged 14WT

α' precipitates were observed after isothermal ageing 14WT at $475°C$ for three months, but not after one month. This indicates that there is an incubation period that lasts sometime between 1 and 3 months. Ageing studies on PM2000 ODS at $475°C$ observed α' precipitates after 10hrs [40], and Fe-20Cr binary alloy samples aged at $500°C$ formed α' precipitates after 50 hrs [33]. Therefore relative to these examples this is a significantly long incubation period.

Table 5.12 presents α' precipitate characteristics from four studies in the literature. Averaged characteristics of α' precipitates that formed within the 14WT aged for 8 months are also included for comparison. 14WT aged for 8 months has a lower number density of α' relative to those found in [33], [40], [125] and [271]. Internal concentrations of Cr within the α' precipitates in 14WT are also much lower than [33], [40], [125] and [271], even though the 14WT ageing duration is much longer. The measured Cr solubility limit in Fe-Cr binary alloys at $300°C$ is $8.8at.\%$ [116] and is approximately consistent with the boundary between the α and $\alpha+\alpha'$ regions in figure 2.11. Using this boundary, the Cr solubility limit at $475°C$ is approximately $9at.\%$. As seen in table 5.3, the matrix Cr concentration within the 14WT aged for 8 months is much higher than this solubility limit ($9.29wt.\% \sim 11.5at.\%$). This means Cr is still supersaturated in the matrix and therefore a longer ageing duration is required to coarsen the α' precipitates further. This would increase the average internal concentration of Cr and increase the average radius.

Alloy	Ageing temperature [$°C$]	Ageing duration [Days]	α' radius [nm]	α' Cr concentration [at.%]	α' number density [m^{-3}]	Matrix Cr concentration [at.%]	Source
Fe-20at.%Cr binary	500	45	2.53	∼80	10^{24}	∼14	[33]
PM2000 ODS (18.5at.%Cr)	475	2.5	9	86	$\gg 10^{22}$	17	[40]
Fe-15at.%Cr binary	290*	62	1.3	87.2	3.2×10^{24}	9.7	[125]
Fe-12at.%Cr binary	300**	73.87	1.1	58.5	5×10^{24}	8.24	[271]
14WT	475	240	1.38	44.34	3.6×10^{23}	$\sim$ 11.5	This work

Table 5.12: A summary of α' characteristics in four separate studies. * Fe-15Cr binary alloy was neutron irradiated to 1.82dpa.**Fe-12at.%Cr was neutron irradiated to 0.6dpa.

5.4.1.1 Inhomogeneity in the α' precipitate distribution

Significant variation in the α' precipitate number density was observed across all three of the experimental repeats within the 14WT aged for 3 and 8 months. Figures 5.7 and

	Dataset		
	23301	23328	23818
Cr [wt.%]	13.18	12.74	11.62

Table 5.13: Concentrations of Cr as measured by APT, in the as-received 14WT. Each of the three measurements are from the three experimental datasets acquired: 23301, 23328, 23818.

5.8 show this qualitatively and table 5.2 shows this quantitatively.

APT compositional analysis of the as-received 14WT here and in [44] showed that there were variations in the matrix Cr concentrations. Table 5.13 presents the APT measured Cr concentrations in wt.% for all three as-received experimental repeats. The Cr concentration is seen to range from 11.6-13.1 wt.%. As APT characterisation only provides information from very small sample volumes, it is possible that the Cr concentration ranges are larger than that shown in table 5.13.

The critical radius for the nucleation of α' precipitates is highly dependent on the local concentrations of Cr [41, 121]. Therefore a local depletion or enrichment in Cr is likely to reduce or increase the probability of nucleation respectively. In the the event that a depletion of Cr occurs, this would reduce the driving force for phase separation and reduce the probability of nucleation. Therefore the number of precipitates that are formed within a given duration are likely to be lower.

The relationship between Cr matrix concentration and nucleation rate of α' precipitates has been investigated by Schwen et al. for the case of Fe-Cr binary alloys only [353]. This work reinforces the notion the depletion of Cr will lead to a lower number of precipitates within the matrix. Schwen's Fe-Cr binary free energy was used within the classical nucleation model to predict the nucleation rates at 300K, 500K and 700K, and is shown in figure 5.24. The predicted nucleation rate increases with higher Cr

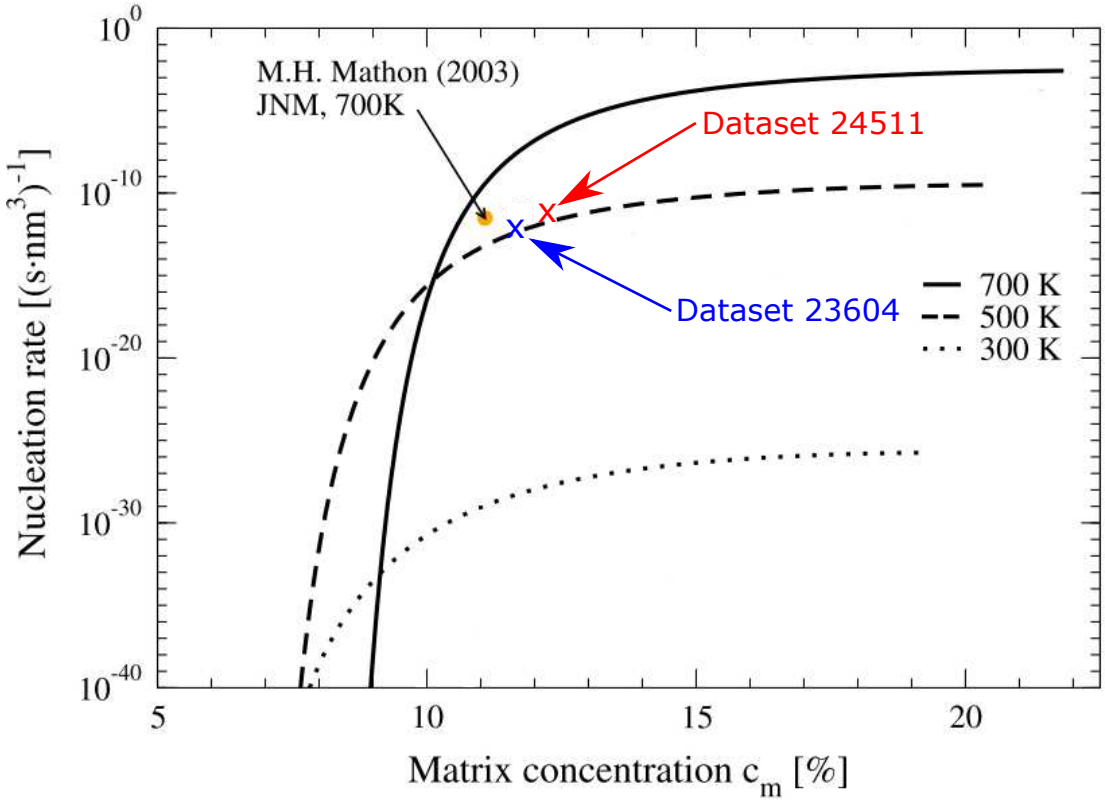


Figure 5.24: Nucleation rate as a function of matrix concentration of Cr taken and adapted from [353]. The yellow circle shows the nucleation rate in the alloys studied by Mathon [42]. The red and blue crosses are the α' precipitate nucleation rates for datasets 24511 and 23604, which are two of the three datasets belonging to the 14WT aged for 8 months at $475^{\circ}C$.

concentration and temperature because more Cr in the system increases the driving force for phase separation, and higher temperatures enhances Cr diffusion within the predominantly Fe-Cr matrix.

Overlaid on figure 5.24 are three empirical α' precipitates nucleation rates represented by the orange circle and two crosses. The orange circle is from an LA4TA steel (11.08Cr-0.72W-0.78Mn-0.07Ta-0.23V-0.03Si-0.142C-0.041N wt.%) aged at 700K for 10,000 hours [42]. The red and blue crosses are from datasets 24511 and 23604 which are two of the three datasets belonging to the 14WT aged for 8 months at $475^{\circ}C$. The nucleation

rates from dataset 24511 and 23604 has been calculated by dividing the number density of α' precipitates in each dataset (presented in table 5.2) by the number of seconds in 8 months. This calculation serves as a simple and quick method to estimate a minimum value for the nucleation rate and does not take into account the 1-3 month incubation period.

The nucleation rates for the aged LA4TA are similar to that in the 14WT aged for 8 months despite the higher Cr concentrations. However, these nucleation rates are minimum values. Therefore the real nucleation rates should be higher and more aligned with Schwen's model. This would suggest that the free energies for Fe-Cr binary alloys are consistent with that of 14WT.

5.4.2 14YWT1 NFA resistance to α' precipitate formation

The average as-received 14YWT1 matrix concentration of Cr, as shown in table 3.2 is $13.34\,wt.\%$. Ageing at $475°C$ is expected to produce spherical isolated α' precipitates [32] within 14YWT1. However, the 14YWT1 studied here deviates from this theory as it does not form α' precipitates.

ODS alloys containing second phase dispersoids have been observed to form α' precipitates after isothermal ageing at $475°C$ (PM2000-18.6wt.%Cr and K2-13.64wt.%Cr ODS alloys) [130, 151, 167] and after neutron irradiation (MA957-12.6wt.%Cr ODS alloys) [354]. However, as presented in table 2.1, the dispersoids in these alloys have different characteristics to those in 14YWT1. It is unlikely that the fine dispersoids directly inhibit α' precipitate formation, as their surfaces could be heterogeneous nucleation sites.

Even though Y is known to be insoluble within the Fe-Cr matrix [355], APT atom maps in figure 5.12 show residual quantities of Y within 14YWT1. Calculations to determine the influence Y has on the free energy have not been conducted in the literature and so

its effects on the formation of α' is largely unknown. However as the concentration of residual Y across the datasets is only $\sim 0.05at.\%$ it is not likely that it would perturb the free energy of the Fe-Cr system significantly. Therefore positions of the phases should, in theory, be similar to those found in the Fe-Cr binary system.

	22920	22894 (no GB)	22826
Cr [wt%]	13.10	13.35	13.16

Table 5.14: Matrix Cr concentration in the three APT datasets belonging to 14YWT1 aged for 8 months. Datasets 22920 and 22826 contains a GB, but dataset 22894 does not.

Figure 5.19a shows that GB enrichment of Cr occurs as a result of ageing. Intragranular depletion of Cr is a possible explanation for why α' precipitates do not form in the aged 14YWT1. Table 5.14 presents the Cr concentrations within each of the three experimental repeats belonging to 14YWT1 aged for 8 months. These concentrations have been measured from an area away from the GB and with the dispersoids removed from the matrix. It can be seen that the matrix concentrations of Cr are fairly consistent across all three experimental repeats. The dataset that does not contain a GB has a slightly higher Cr concentration, and this is probably due to the absence of a GB. Overall, the concentrations of Cr in the matrix mean that the alloy should, in theory, remain within the miscibility gap and therefore α' precipitates might still be expected to form.

The major factors and mechanisms that influence the formation of α' precipitates have been explored and have not been able to explain why α' precipitates do not form. It is evident that 14YWT1 is overall resistant to the formation of α' precipitates at $475^{\circ}C$.

5.4.3 14YWT1 grain boundary enrichment

Section 5.3.2.3 showed that GBs the aged 14YWT1 were enriched with Cr and W. This trend was observed to be more prominent for W then it was for Cr. Generally, GBs contained Si and Mn but ageing did not seem to effect the quantity of these solutes at these interfaces. There was also signficant variation in the quantity of Cr, W, Mn and Si at GBs within alloys aged for the same durations (e.g. dataset 21112 and 20713).

Higher intragranular concentrations of Cr, W, Si and Mn will result in a higher tendency of GB enrichment from these elements. Table 5.15 shows the concentrations of Cr, W, Si and Mn within the as-received 14YWT1 across all three experimental repeats. There is some variation in the concentrations of Cr, W and Si within the relatively small volumes sampled by APT, but there is little variation in Mn. Gorley characterised the distributions of Cr and W over a $20\mu m$ length using EPMA [44]. Cr was seen to fluctuate but it is unclear which regions contained dispersoids, and therefore the highest and lowest matrix concentrations of Cr are ambiguous. He also showed concentrations of W could be as high as 4.25wt%, and as low as 2.25wt% in some regions. Therefore the variation in GIE values for 14YWT1 aged for a given duration (e.g. dataset 21112 and 20713), could be accounted for by considering the inhomogeneous intragranular distribution of elements within 14YWT1.

The second potential source of this variation could be due to APT related limitations. Evaporation behaviour around interfaces, such as GBs, are known to differ from the parent matrix. This results in trajectory aberrations which can distort local atomic densities. Due to this, atoms can be artificially included or depleted from the GB region. Therefore concentration measurements of alloying elements, especially if they are present at the GBs in very low quantities, can be erroneous. In addition, the LEAP 3000X-HR has a lateral and depth resolution of 0.2nm and 0.1nm respectively.

	23070	23146	23181
Cr	13.28	14.88	13.42
W	2.44	2.69	2.65
Si	0.14	0.29	0.15
Mn	0.22	0.23	0.22

Table 5.15: Concentrations of Cr, W, Si and Mn within the as-received 14YWT1 as measured by APT. Concentrations are in at.%.

Variations in the GIE measurements for Si and Mn seem significant however the excesses are on the order of 1 atom nm^{-2}. This is near the resolution limit of the LEAP 3000X-HR and therefore these results are susceptible to error from noise.

It is probable that the variations seen in the Cr and W excesses are due to inhomogeneous distributions of these alloying elements. The variation in the Mn and Si is probably due to the both low concentrations of these impurity elements and APT resolution limits.

A greater number of interfaces are required given the large error bars associate with the datapoints. Ideally, 3 GBs should be captured for each alloy state. Apart from the data for the 14YWT1 aged for 3 months, this study has on average captured two GBs per ageing duration. Therefore it is challenging to determine which points are anomalous. This is especially the case for Cr as the data fluctuated significantly (e.g. dataset 21112 and 201713 as well as dataset 22920 and 22826). It is due to this reason that the signifcance of this analysis is low.

5.4.4 14YWT1 NFA cluster thermal stability at low-temperatures

The data shown in figures 5.20, 5.21 and 5.22 showed no significant changes to the density of NFA particles in the microstructure, their radii or their internal Y, Ti and

O concentration occurred after ageing. Therefore the NFA dispersoids here are thought to be thermally stable after ageing at $475°C$ for up to 8 months.

NFA dispersoid solutes can dissolve back into the 14YWT matrix after irradiation at very low temperatures e.g. $-75°C$ [356]. This is due to the ejection of an Y, Ti or O atom, via ballistic collisions, from the dispersoid. The NFA's high tolerances to irradiation are closely linked to the capabilities of an ejected solute to diffuse back into the dispersoid [357]. Therefore the temperature the matrix resides at is a highly influential parameter that determines whether this occurs or not. As these ageing experiments have been conducted without irradiation and at relatively low temperatures, these findings are not anomalous and are expected.

5.4.5 Establishing the origins of the hardening in 14WT and softening in 14YWT1

Figure 5.23 shows large fluctuations in ΔHv for both 14WT and 14YWT1. This is likely to be due to the inhomogeneous microstructures within 14WT and 14YWT1.

Features such as α' precipitates [34, 35] and spinodal structures [358] inhibit dislocation motion because they are either difficult to cut through or bypass [147]. The ageing provides an environment in which recovery can occur, thus reducing the intragranular dislocation density. The application of the dispersed barrier hardening model on neutron irradiated Fe-Cr binary alloys has shown that relative to dislocation loops, α' precipitates are a weak obstacle [148]. This is because BCC Fe and BCC Cr have a similar lattice parameter ($a_{Cr} = 2.88\mathring{A}$, $a_{Fe} = 2.87\mathring{A}$ [35]) and therefore the lattice mismatch between the matrix and Cr rich precipitate is small, and a coherent interface between the two regions is expected.

As dislocation loops are not produced under ageing conditions, the dominant obstacle to dislocation motion within the aged 14WT is likely to be the α' precipitates. As 14WT

hardened after 8 months of ageing, it is very likely that it is due to the presence of the α' precipitates.

Alloy	Ageing duration	α' type	ΔHv	Source
14WT (13.06wt.%Cr)	8 months	Precipitate	+32	This work
AISI 444 (17.56wt.%Cr)	1.39 months	Precipitate	$\sim$+88	[359]
18Cr-2MoTi	1.39 months	Precipitate	$\sim$+102	[124]
18Cr-2MoTi	13.89 months	Precipitate	$\sim$+172	[360]
2205 duplex stainless steel (23.8wt.%Cr)	64 hrs	Spinodal	$\sim$+70	[133]

Table 5.16: ΔHv measurements from isothermally aged non binary Fe-Cr alloys at $475°C$ reported in the literature. Hardness has been determined by Vickers tests at differing loads.

Alloy	Ageing duration	α' type	ΔHv	Source
14YWT1 NFA (13.34wt.%Cr)	8 months	None detected	-26	This work
K2 ODS (13.64wt.%Cr)	150 days	Precipitate	$\sim$+25	[130]
PM2000 ODS (18.60wt.%Cr)	42 days	Precipitate	$\sim$+130	[40]
MA956 (21.26wt.%Cr)	1.025 months	Precipitate	$\sim$+120	[361]

Table 5.17: ΔHv measurements from isothermally aged Fe-Cr NFAs and ODS alloys at $475°C$ reported in the literature. Hardness has been determined by Vickers tests at differing loads.

Tables 5.16 and 5.17 summarises ΔHv measurements from isothermal ageing studies on higher order non-DSAs and DSAs respectively. All the hardness measurements quoted have been determined by Vickers hardness tests with varying loads. The large variations in ΔHv between the experiments are due to the isothermal ageing duration, temperature and intrinsic properties such as dislocation type, shear modulus and matrix coherency

amongst others [127].

Relative to the other ΔHv measurements in table 5.16, 14WT has not hardened significantly despite the long ageing duration in this study. Since the hardening effect is enhanced with increasing Cr matrix content [148], the low ΔHv_{14WT} measured here could be due to its relatively low quantity of Cr.

ΔHv for 14YWT1 varies significantly relative to the others studies listed in table 5.17. In the PM2000 ODS [40] and K2 ODS [130] ageing experiments, the positive ΔHv was attributed to the formation of α' precipitates. As α' precipitates did not form within the aged 14YWT1 the small net softening effect observed in the aged 14YWT1 is likely to be due to recovery occurring during ageing i.e. decreasing dislocation density per grain.

Overall the hardness changes within the aged 14WT and 14YWT1 are negligible especially when comparing them to the other investigations listed in table 5.16 and 5.17.

5.4.5.1 Estimating the dislocation breakway angle in 14WT alloys aged for 3 and 8 months

The hardening effect observed in the 14WT aged for 3 and 8 months is less pronounced than that seen in the aged alloys listed in 5.16. This is probably because the dislocation obstacles (α' precipitates) are weaker in the 14WT. To understand quantitatively how weak these obstacles are, the dislocation breakaway angle can be estimated using the Friedel weak coherent obstacle model. This is only applied to the 14WT aged for 3 and 8 months as they are the only samples that contain α' precipitates.

According to the Friedel treatment, the change in the shear yield stress, $\Delta\tau_y$, due to the dispersion of weak coherent obstacles to dislocation motion is given by equation 5.1 [362]. This is a weak obstacle version of the hardening theory, where the dependence on particle breakaway angle is to the power of 3/2, as several obstacles can release the

dislocation segment in one event.

$$\Delta\tau_y = \frac{Gb}{\lambda}\left[cos\left(\phi_c\right)\right]^{\frac{3}{2}} \tag{5.1}$$

where G is the shear modulus, b is the length of the matrix Burgers vector, ϕ_c is the breakaway angle between the edge dislocation and the obstacle (α' precipitate in this context) and λ is the inter-obstacle spacing as determined by equation 5.2.

$$\lambda = [\rho.d]^{\frac{1}{2}} - d \tag{5.2}$$

where ρ is the number density of the obstacles, d is the diameter of the obstacles.
To compare this model with the hardness data obtained from the microhardness measurements the relation between $\Delta\tau_y$ and H_v given in equation 5.3 is used:

$$\Delta\tau_y = \frac{\Delta H_v[MPa]}{6} \tag{5.3}$$

Equation 5.3 is derived by combining the empirical relations in equation 5.4 with 5.5.

$$\Delta\sigma_y = \frac{\Delta H_v[MPa]}{3} \tag{5.4}$$

and

$$\Delta\tau_y = \frac{\Delta\sigma_y}{\underbrace{2}_{Tresca\,yield\,criteria}} \tag{5.5}$$

where $\Delta\sigma_y$ is the tensile yield stress and ΔH_v is the change in hardness in units of MPa.
The data from table 5.3 can be substituted into equation 5.2 to deduce λ. The G for an Fe-Cr model alloy is $\sim 85GPa$ [148], b for a $\frac{1}{2}\langle 111\rangle$ edge dislocation is $0.248nm$. ϕ_c

is left as an adjustable parameter so that the model can be fitted to the hardness data. ϕ_c is a metric that provides insight into the obstacle strength. Therefore this will indicate the extent to which α' precipitates contribute to the overall increase in hardness within the 14WT aged for 3 and 8 months.

Ageing duration [Months]	Measured ΔH_v $\left[\frac{kgf}{mm^2}\right]$	ϕ_c [°]
3	8.6	83.7
8	36.2	60.0

Table 5.18: ϕ_c as predicted by Friedel's weak obstacle hardening model. ΔH_v quoted here is the difference between the hardness measured in the aged alloy and the as-received alloy.

ϕ_c has been predicted by implementing Friedel's weak obstacle model and is given in table 5.18. Overall, for very small changes in ϕ_c the predicted hardness increases significantly. ϕ_c within the 14WT aged for 3 and 8 months was predicted to be 89.5° and 74.8° respectively. The higher ϕ_c is, the weaker the obstacle is. In the case for both aged states, ϕ_c is close to the upper limit (90°) and so the α' precipitates are extremely weak obstacles. This is consistent with the outcomes from [148].

Therefore the implementation of the Friedel model predicts that these features contribute very little to the measured increase in hardness. Indeed, any contribution to the increases in hardness would be below experimental error.

5.5 Conclusion

Isothermally aged 14WT and 14YWT1, at $475°C$, have been studied using APT and microhardness indentation tests. Atom maps showed the formation of α' within 14WT

but not in 14YWT1.

Surprisingly there was an incubation period of 1 to 3 months before α' precipitates were observed in the 14WT microstructure. This is a significantly longer period in comparison to other isothermal ageing experiments that have observed α' e.g. [33] and [40]. α' precipitates were characterised and found to contain concentrations of Cr well below that found in Fe-Cr binary alloys [33, 125]. Further, the Cr concentration within the matrix had not plateaued. Ergo it is likely that if ageing durations were increased, the α' precipitates would evolve further in terms of their radii and Cr concentration. Number densities of α' between experimental repeats varied by one order of magnitude. This was congruent with atom probe maps which exhibited significant differences in the number of α' precipitates between experimental repeats.

It is unclear why 14YWT1 is resistant to α' phase formation.

No W laves, W rich or minor solute rich precipitates had formed as a result of the ageing experiment.

GB enrichment of Cr, W, Si and Mn was observed to occur in the aged 14YWT1 NFAs. No specific trend relating enrichment with ageing duration can be obtained as there is significant variation in the magnitude of enrichment in the aged alloys for each of the 4 elements.

Analysis conducted on the NFA clusters within the aged 14YWT1 suggest that they are stable as average cluster radii distribution had not changed significantly throughout the ageing process. NFA cluster content does not change significantly either.

Finally Microhardness tests revealed that overall hardness for 14WT and 14YWT1 changed by $\Delta Hv_{14WT} = +32 kgf\,mm^{-2}$ and $\Delta Hv_{14YWT1} = -26 kgf\,mm^{-2}$ respectively. It is likely that the increase in hardness in 14WT is due to the presence of α' clusters [36]. 14YWT1's reduction in hardness is likely to be due to a reduction in dislocation density but requires confirmation via electron microscopy.

Chapter 6

Phase stability of ion and neutron irradiated 14YWT

Chapter summary

A systematic investigation to determine whether ion-irradiation or neutron irradiation destabilises the α-matrix and forms α' 14YWT NFA has been conducted. Bulk samples of 14YWT2 were irradiated with 24MeV $^{56}Fe^{8+}$ to 0.74-1.49dpa at a dose rate of $3.24 - 6.53 \times 10^{-5} dpa\, s^{-1}$, at $288°C$. Bulk samples of 14YWT3 were neutron irradiated to 1.82dpa at $3.85 \times 10^{-7} dpa\, s^{-1}$ (E>0.1MeV) in the ATR in the USA.

The ion-irradiated 14YWT2 atom maps resembled those of the neutron irradiated 14YWT3. This shows that distributions of alloying elements within fission neutron-irradiated samples are well replicated by ion-irradiated samples for irradiation conditions used here. No α' precipitates or any other tertiary intermetallics were observed to have formed in the ion-irradiated 14YWT2 or the neutron irradiated 14YWT3 NFAs.

6.1 Introduction

As stated in section 2.5, irradiation can induce phase instability [126] and enhance the formation of α' precipitates [42]. It is currently unknown whether the 14YWT matrix destabilises and forms α' precipitates under certain irradiation conditions.

Further, the notion that ion irradiation is a surrogate for neutron irradiation relies on the assumption that the cumulative effects of ion irradiation e.g. RIS, irradiation induced hardening and dislocation networks are equivalent to those in neutron irradiated samples. However, the literature, as discussed in section 2.4.3, has many examples where this is not the case. Most relevant to this thesis is the study conducted by Pareige et al. described in section 2.5.2.2. Pareige reported significant differences in the distributions of Cr, P, Si and Ni within Fe-Cr binary alloys irradiated with neutrons and ions [43]. It is unknown whether this difference occurs in Fe-Cr alloys containing high defect sink densities e.g. 14YWT NFA.

The focus of this work is to characterise solute distributions within 14YWT NFA samples that have been self-ion irradiated and neutron irradiated separately to similar peak doses and irradiation temperatures.

6.2 Materials and methods

Samples of 14YWT2 NFA were ion irradiated at the JANNuS facility in France. 14YWT3 NFA was neutron irradiated at the ATR in the USA. Both alloys were fabricated at UCSB in the USA and a description of their processing history is given in section 3.1.1.2. Information regarding the as-received microstructures are provided in section 3.1.2.2. A description of both the ion and neutron experimental campaigns can be found in section 3.3.

Distributions of elements within all four samples were characterised by APT only. This author acquired APT datasets of 14YWT2 as-received, ion-irradiated 14YWT2 and neutron irradiated 14YWT3. APT datasets of 14YWT3 as-received were obtained from Cunningham of UCSB. Methods utilised to fabricate samples as well as atom probe reconstruction protocols are described in appendix A. APT analysis parameters for the 14YWT2 and neutron-irradiated 14YWT3 are detailed in section 3.4.3 and are also summarised in table 6.1. APT analysis parameters for the 14YWT3 as-received differed from that of the neutron irradiated 14YWT3 and are shown in table 6.1.

Alloy	APT system	APT mode	Analysis temp. $[K]$	Pulse rate $[kHz]$	Pulse fraction [%]	Laser energy	Evaporation rate $[ions\,pulse^{-1}]$
14YWT2 As-received and Ion-irradiated	3000X	Laser	55	200	-	0.4nJ	0.005
14YWT3 As-received	4000X	Voltage	60	200	20%	-	0.005
14YWT3 Neutron irradiated	4000X	Laser	55	200	-	150pJ	0.005

Table 6.1: Summary of the APT analysis parameters used in this study. 3000X and 4000X are abbreviations for LEAP 3000X-HR and LEAP 4000X-HR systems respectively

6.3 Results

12 APT datasets were acquired for this ion and neutron irradiation comparative study, and are listed in table 6.2. Atom map slices from one dataset for each of the 4 alloys states are presented here in this chapter, and are typical of the experimental repeat datasets. Atom map slices from experimental repeat datasets are shown in appendix D.

14YWT2		
Treatment	Dataset	Presented in
As-received	24102	Figure 6.1a
	24154	Appendix D figure D.1a
	24344	Appendix D figure D.1b
Ion-irradiated	24491	Figure 6.1b
	24492	Appendix D figure D.2a
	24493	Appendix D figure D.2b
14YWT3		
Treatment	Dataset	Presented in
As-received	5209	Appendix D figureD.3a
	5210	Appendix D figure D.3b
	5213	Figure 6.6a
Neutron irradiated	4724	Appendix D figure D.4a
	4731	Figure 6.6b
	4732	Appendix D figure D.4b

Table 6.2: Index of all the APT datasets acquired in this ion and neutron irradiation comparative study

6.3.1 14YWT2 as-received and ion-irradiated

Atom maps from one dataset of the 14YWT2 as-received are shown in figure 6.1a. Figure 6.1b shows one set of atom maps from the ion-irradiated 14YWT2. Both are representative of the other two experimental repeats, which are shown in appendix D. The Fe, Cr and W atom maps in the 14YWT2 as-received, shown in figure 6.1a, are seen to be unclustered and unsegregated. Y and TiO atom maps show these solutes to be concentrated in discrete zones and clustered. Y rich regions are correlated with TiO rich regions, and therefore these represent the dispersoids distributed within 14YWT2. Co, Si and Mn, which are impurity solutes are unsegregated and unclustered.

After ion-irradiation, Fe, Cr, and W, atom maps in figure 6.1b indicate no changes have occurred as a result of ion-irradiation. All three continue to be unclustered and are unsegregated. Y and TiO atom maps continue to be concentrated within discrete zones and are correlated with each other. Impurity solutes, Co, Si and Mn continue not to be clustered or segregated.

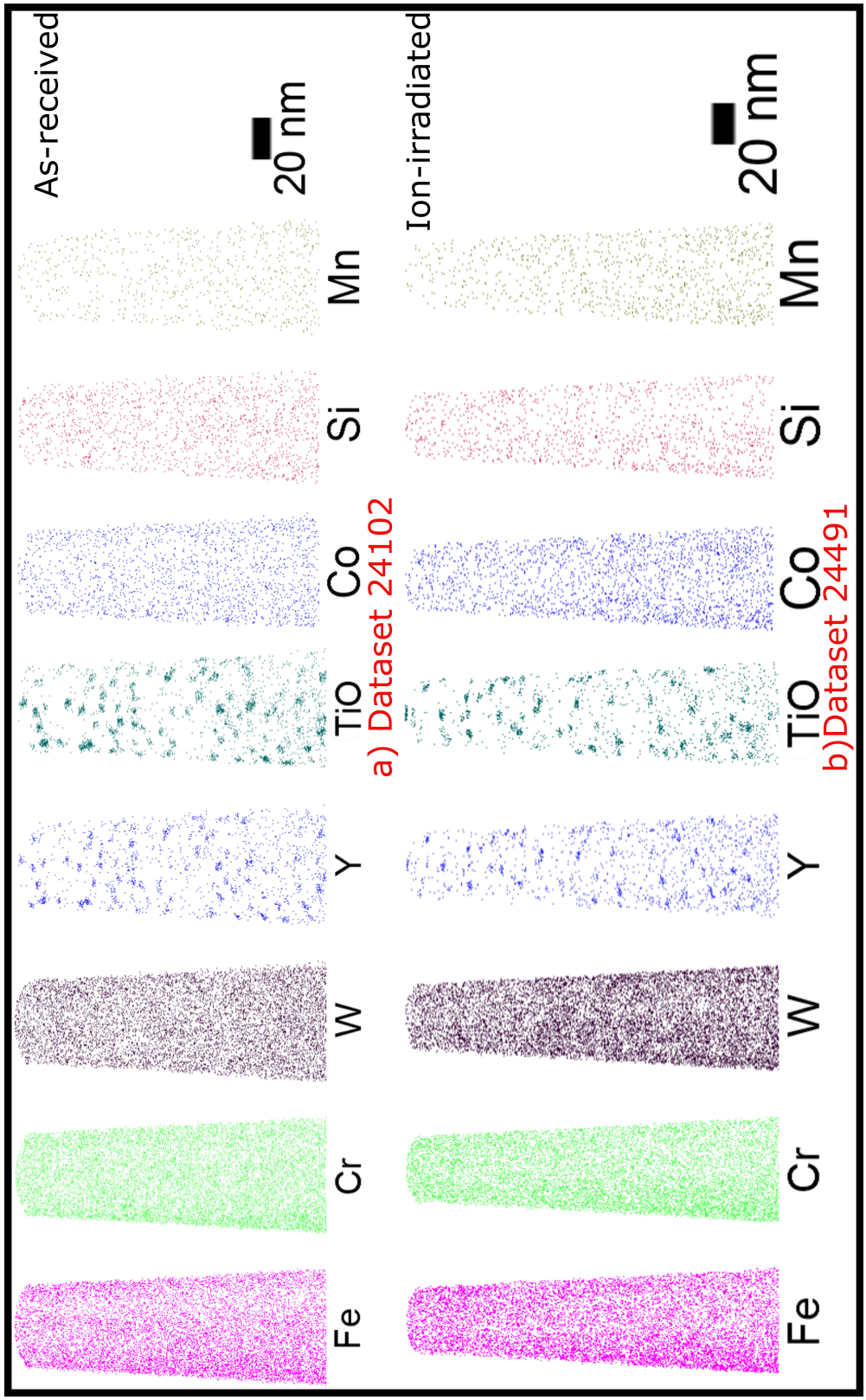


Figure 6.1: Atom map slices of 14YWT2 a) as-received and b) ion-irradiated

6.3.1.1 Fe and Cr solvent distributions

Treatment	Dataset	μ_{Fe}	μ_{Cr}	$\bar{\mu}_{Fe}$	$\bar{\mu}_{Cr}$
As-received	24102	0.94	0.49	0.97 ± 0.01	0.63 ± 0.09
	24154	0.99	0.80		
	24344	0.98	0.59		
Ion-irradiated	24491	0.78	0.51	0.78 ± 0.02	0.59 ± 0.04
	24492	0.74	0.60		
	24493	0.81	0.66		

Table 6.3: Pearson coefficients, μ for the Fe and Cr ions distributions within each 14YWT2 datasets acquired. Averages are calculated from all three experimental repeats for each duration.

Pearson coefficients, μ, have been calculated for Fe and Cr for each 14YWT2 APT dataset. The protocol to do this and the interpretation of μ is explained in appendix 3.4.5.1. This will show whether concentrations of Fe and Cr are, as the atom maps suggest, homogeneous. These are shown in table 6.3. μ_{Fe} is consistently greater than μ_{Cr}. μ_{Fe} and μ_{Cr} for both 14YWT2 states indicate that the concentration distribution of Fe and Cr deviate from a random binomial solution since they are much larger than 0.

Magnified Fe, Cr, and Y+TiO atom maps from dataset 24102 (14YWT2 as-received) are shown in figure 6.2a. The Fe and Cr atom maps indicate homogeneous distributions of Fe and Cr. Two dispersoids are also highlighted in figure 6.2a. Contrary to 14YWT1 in section 5.3.2.1, Fe and Cr atom maps indicate that Fe and Cr distributions do not change in the presence of these dispersoids.

Concentration profiles through both dispersoids are shown in figures 6.2b and 6.2c.

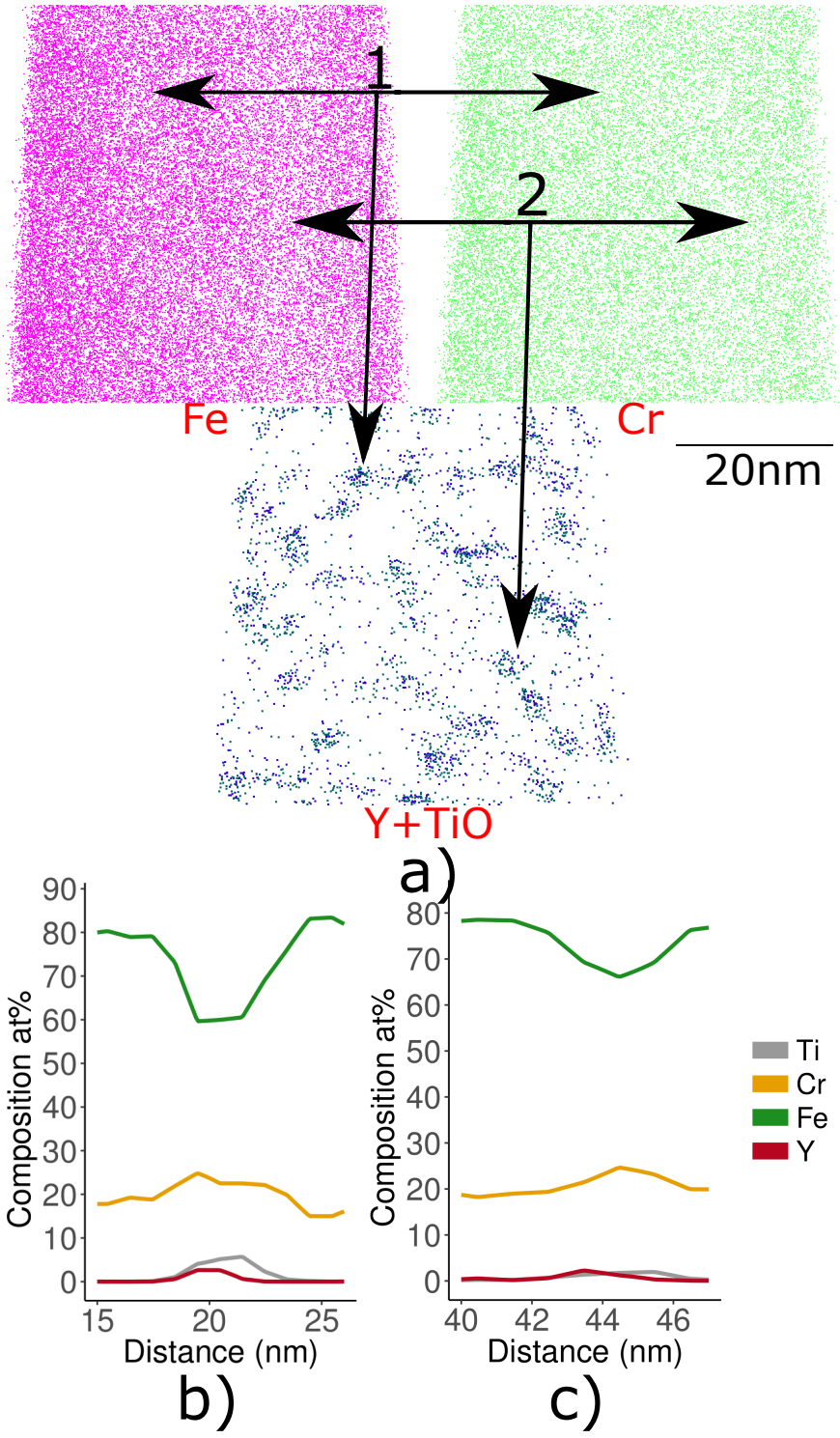


Figure 6.2: a) Zoomed in Fe, Cr, Y+TiO atom maps from 14WT2 as-received, dataset 24102. b) and c) are concentration profiles through region 1 and 2 in a)

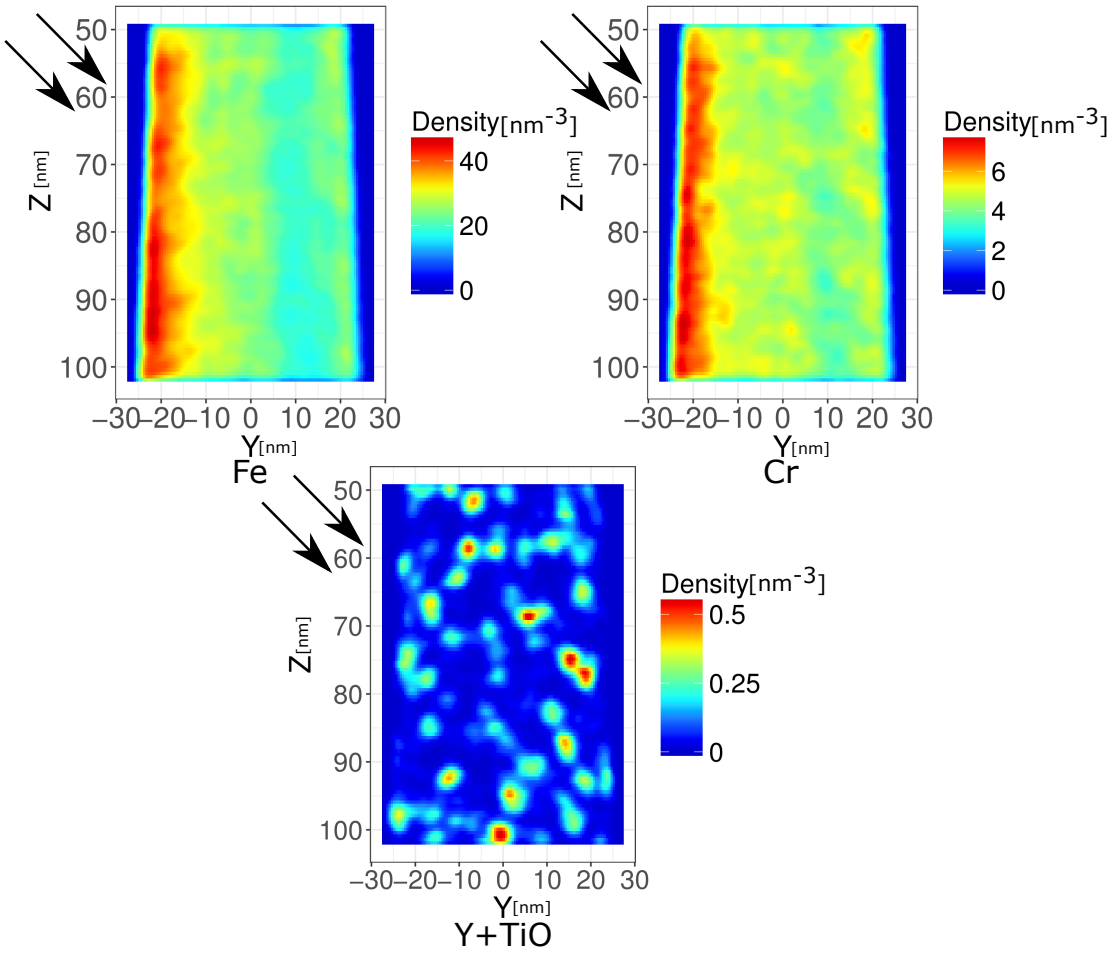


Figure 6.3: 2-dimensional density maps of Fe, Cr, Y+TiO within the same region shown in figure 6.2a. The black arrows show the direction of the laser pulse.

Inside the dispersoids, Fe is seen to be depleted and Cr is enriched.

Two-dimensional density plots of Fe, Cr and Y+TiO distributions are shown in figure 6.3. The black arrows show the direction of the laser pulse, which is targeted at the apex of the specimen. The density plots show that there is a gradient in terms of the density of Fe and Cr, along the y axis. The highest density of Fe and Cr is situated on the side of the sample that is closest to the laser pulse. The number density of Fe and Cr reduces with increasing distance from this position.

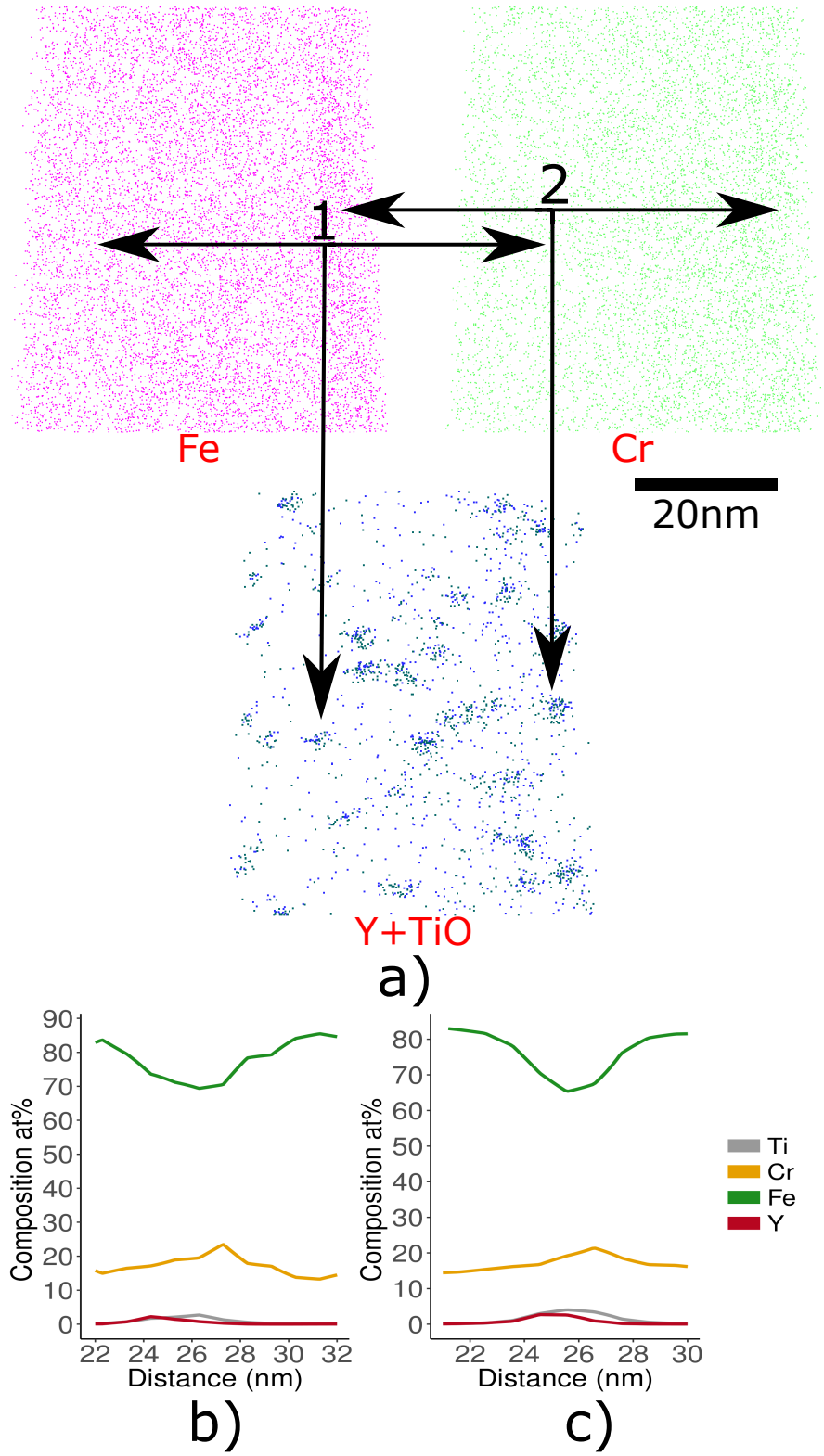


Figure 6.4: a) Zoomed in Fe, Cr, Y+TiO atom maps of the ion irradiated 14YWT2, dataset 24491. b) and c) are concentration profiles through region 1 and 2 in a)

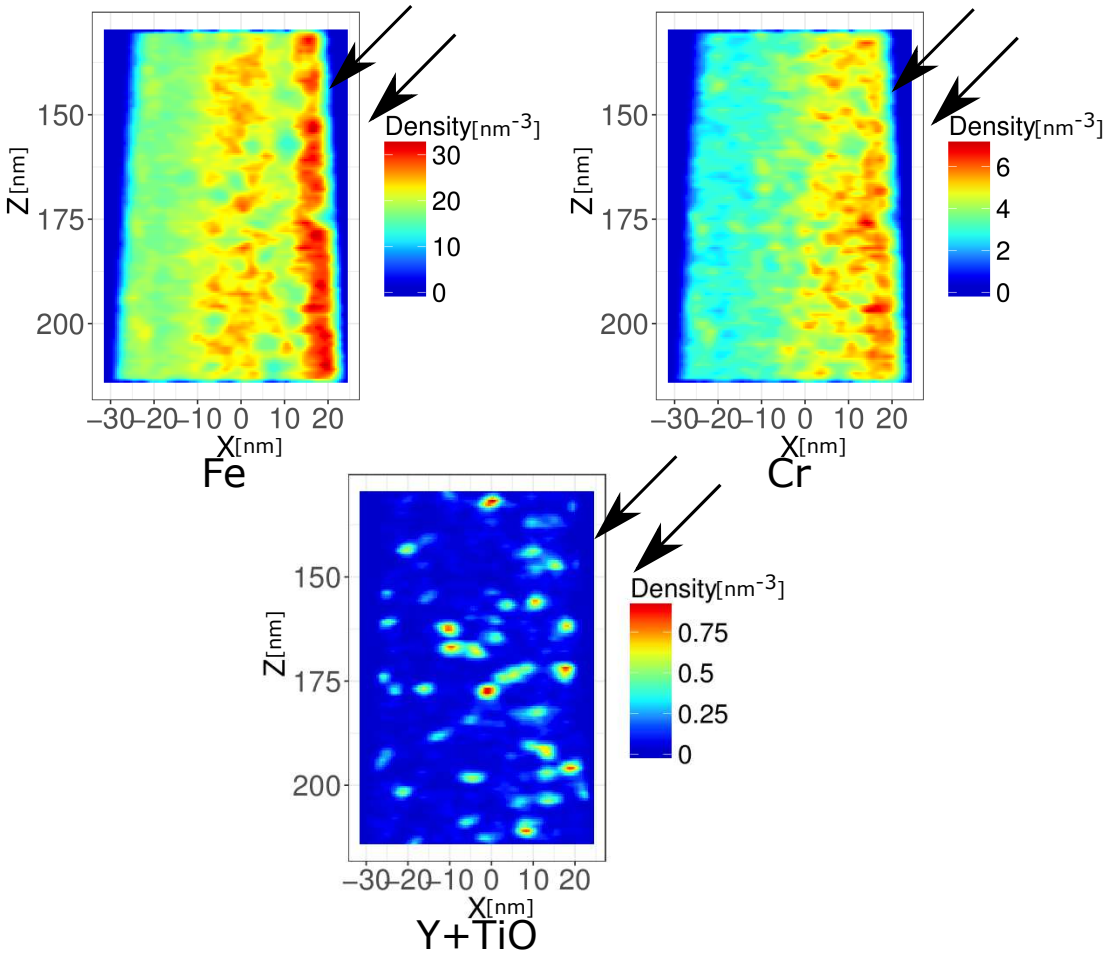


Figure 6.5: Two-dimensional density maps of Fe, Cr, Y+TiO within the same region shown in figure 6.4a. Black arrows represent the approximate direction of the laser pulse

Y+TiO density plots show discrete regions where there is a high density of these elements. These highly dense regions of Y+TiO are representative of the dispersoids and do not indicate similar behaviour to that seen for Fe and Cr. Figure 6.3, also shows that denser regions of Fe and Cr are correlated with the positions of the dispersoids.

Magnified Fe, Cr and Y+TiO atom maps from dataset 24491 (ion-irradiated 14YWT2) are shown in figure 6.4a. Fe and Cr atom maps indicate homogeneous distributions of

both solvents, even in the regions dispersoids reside within. Concentration profiles of the two highlighted dispersoids in figure 6.4a are shown in figure 6.4b and c. They show that the dispersoids are depleted of Fe and enriched with Cr. Density plots of Fe and Cr distributions within this sample are shown in figure 6.5 and exhibit the same four trends seen for the 14YWT2 as-received. That is, 1) highly dense regions of Fe and Cr are situated closest to where the laser pulse initially interacts with the sample. 2) Fe and Cr density gradients occur along the Y-axis. 3) Y+TiO do not exhibit the same gradients as that seen for Fe and Cr. 4) Localised highly dense regions of Fe and Cr are correlated with the dispersoids (localised highly dense regions of Y+TiO).

Contrary to observations from the atom maps of 14YWT2 as-received and the ion-irradiated 14YWT2, concentration distributions of Fe and Cr are not homogeneous. Dispersoid regions do perturb the distribution of Fe and Cr as dispersoids are depleted of Fe and enriched with Cr. As explained in section 5.3.2.1 and appendix 3.4.7, this is indicative of magnification effects.

The higher density of Fe and Cr seen on the side closest to where the laser hits the sample is indicative of the shadow effect as explained in appendix 3.4.8.

Therefore, the distribution of Fe and Cr are not homogeneous in terms of concentration nor density. This is because of magnification effects and shadow effects, and are not due to the formation of α' precipitates.

6.3.1.2 Grain boundary segregation of alloying elements

One 14YWT2 APT sample volume contained a GB. This GB was found in dataset 24154, 14YWT2 as-received, and is shown in appendix E figure E.1.

GIE values have been calculated for this GB using the method described in appendix A.2.4. A positive GIE value for a given element indicates the GB is enriched with that element. The GB was seen to contain on average $+13.4 \pm 1.6 atoms\, nm^{-2}$ of Cr,

$+2.3\pm0.4 atoms\,nm^{-2}$ of W, $0.0\pm0.3 atoms\,nm^{-2}$ of Mn and $+0.2\pm0.1 atoms\,nm^{-2}$ of Si.

As a GB has not been captured in any other 14WT2 APT datasets in this thesis, a comparison cannot be made. Instead, the data is presented in appendix E table E.1 for use in future studies.

6.3.1.3 14YWT2 minor solute distributions

Atom maps in figure 6.1, showed Co, Si and Mn to be unclustered and unsegregated. This qualitative assessment has been confirmed by calculating Pearson coefficients, μ for Co, Si and Mn, and are presented in table 6.4. μ for Co, Si and Mn are close to 0, before and after ion-irradiation. Therefore these solute distributions are random in the as-received and continue to be so after ion-irradiation.

14YWT3 as-received				
	24102	24154	24344	$\bar{\mu}$
μ_{Mn}	0.05	0.17	0.08	0.10 ($\pm$0.04)
μ_{Si}	0.12	0.04	0.13	0.10 ($\pm$0.03)
μ_{Co}	0.04	0.08	0.05	0.06 ($\pm$0.01)
Ion-irradiated 14YWT2				
	24491	24492	24493	$\bar{\mu}$
μ_{Mn}	0.02	0.04	0.06	0.04 ($\pm$0.01)
μ_{Si}	0.04	0.02	0.01	0.03 ($\pm$0.01)
μ_{Co}	0.08	0.05	0.09	0.07 ($\pm$0.01)

Table 6.4: Pearson coefficients, μ, calculated for Mn, Si and Co within each of the 14YWT2 APT datasets

6.3.2 14YWT3 as-received and neutron irradiated

One set of atom maps of the 14YWT3 as-received and neutron irradiated is shown in figure 6.6. It is representative of the other two experimental repeats which are shown in appendix D.

The Fe, Cr and W atom maps in the 14YWT3 as-received, shown in figure 6.6a, are seen to be unclustered and unsegregated.

The Y atom map shows four Y dense regions in the top left region and the rest of the map look unclustered. The left side of the TiO atom map shows there are more than four regions concentrated with TiO. The 4 regions concentrated with Y are seen to be correlated with the 4 regions concentrated with TiO, and therefore these regions represent the dispersoids distributed within 14YWT3. Co, Si and Mn, are unsegregated and unclustered.

After neutron irradiation, Fe, Cr, and W, atom maps in figure 6.6b show all three continue to be unclustered unsegregated. Y and TiO atom maps are highly concentrated within discrete zones and are correlated with each other. Therefore these Y and TiO-rich regions represent the dispersoids. Relative to the 14YWT3 as-received Y and TiO atom maps, which are shown in figure 6.6a, there are significantly more dispersoids. Impurity solutes such as Co, Si and Mn continue to not be clustered or segregated.

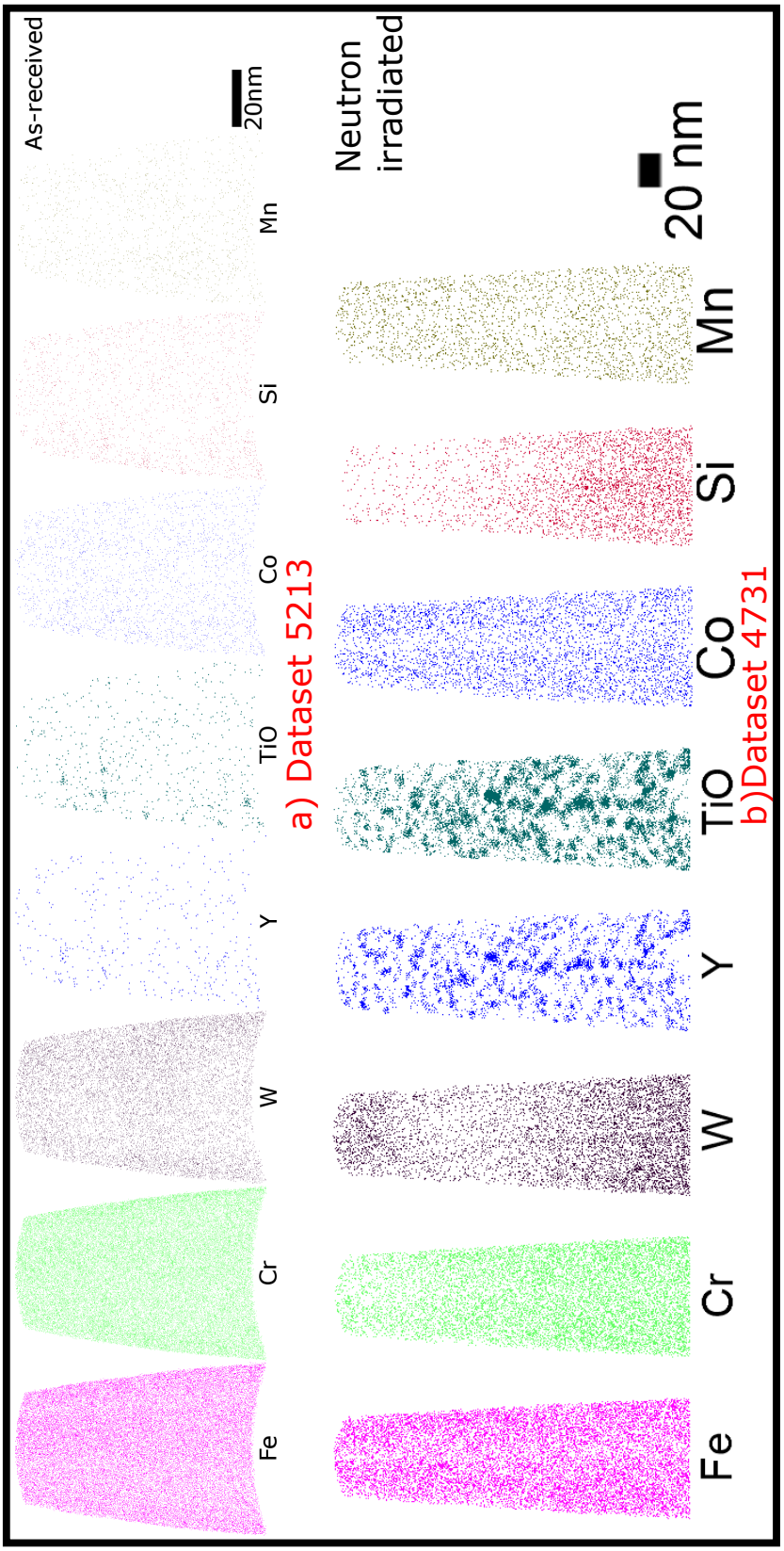


Figure 6.6: Atom map slices of 14YWT3 a) as-received and b) neutron irradiated

6.3.2.1 Distribution of dispersoids in the as-received 14YWT3

The atoms maps of 14YWT3 as-received, shown in figure 6.6a show they contain a reduced number of dispersoids relative to the neutron irradiated datasets.

Using the protocol described in appendix 3.4.5.2, the number of dispersoids within each 14YWT3 as-received, and neutron irradiated dataset is presented in table 6.5.

Dispersoid number densities in the 14YWT3 as-received are significantly lower than the neutron irradiated and vary significantly.

Dataset	Dataset volume $[10^{-23}m^3]$	Number of dispersoids	Number density $[10^{22}m^{-3}]$
	14YWT3 as-received		
5209	4.60	0	0
5210	6.49	1	1.54
5213	17.80	10	5.63
	Neutron irradiated 14YWT3		
4724	192	1207	62.8
4731	249	1565	62.9
4732	293	2084	71.1

Table 6.5: Dispersoids contained in the APT dataset volumes for 14YWT3 as-received and neutron irradiated 14YWT3

APT datasets of 14YWT NFA from the interior of a grain have been reported to contain no dispersoids [170]. Therefore it is not unusual for dispersoids to be absent from regions within 14YWT. Indeed, dispersoid number densities within the various 14YWT APT datasets acquired for the study in chapter 5, which are shown in figure 5.20, show a significant variation in the population too. Therefore the variation in dispersoid number

densities in table 6.5 is expected.

6.3.2.2 Fe and Cr solvent distributions within 14YWT3

Pearson coefficients μ for Fe and Cr concentration distributions within the 14YWT3 as-received and neutron irradiated 14YWT3 samples have been calculated and are presented in table 6.6.

Treatment	Dataset	μ_{Fe}	μ_{Cr}	$\bar{\mu}_{Fe}$	$\bar{\mu}_{Cr}$
As-received	5209	0.35	0.35	0.48 ± 0.07	0.46 ± 0.06
	5210	0.50	0.50		
	5213	0.59	0.54		
Neutron irradiated	4724	0.97	0.76	0.96 ± 0.03	0.79 ± 0.05
	4731	0.99	0.88		
	4732	0.90	0.72		

Table 6.6: Pearson coefficients, μ for the Fe and Cr ions distributions within each 14YWT3 datasets acquired. Averages are calculated from all three experimental repeats for each duration.

μ_{Fe} and μ_{Cr} for the as-received sample are significantly lower than the neutron irradiated sample. From table 6.5, it is apparent that as the number of dispersoids in 14YWT3 as-received APT datasets increase, so does μ_{Fe} and μ_{Cr}.

Magnified atom maps of Fe and Cr and Y+TiO from dataset 5213 (14YWT3 as-received) are shown in figure 6.7a. They show that the Fe and Cr distributions are relatively homogeneous and seem unperturbed by the presence of dispersoids. However concentration profiles, shown in figure 6.7b and 6.7c, through the two dispersoids highlighted in figure 6.7a shows that the dispersoids are enriched with Cr and depleted of Fe.

2D number density plots of Fe and Cr from the same region in figure 6.7, are shown

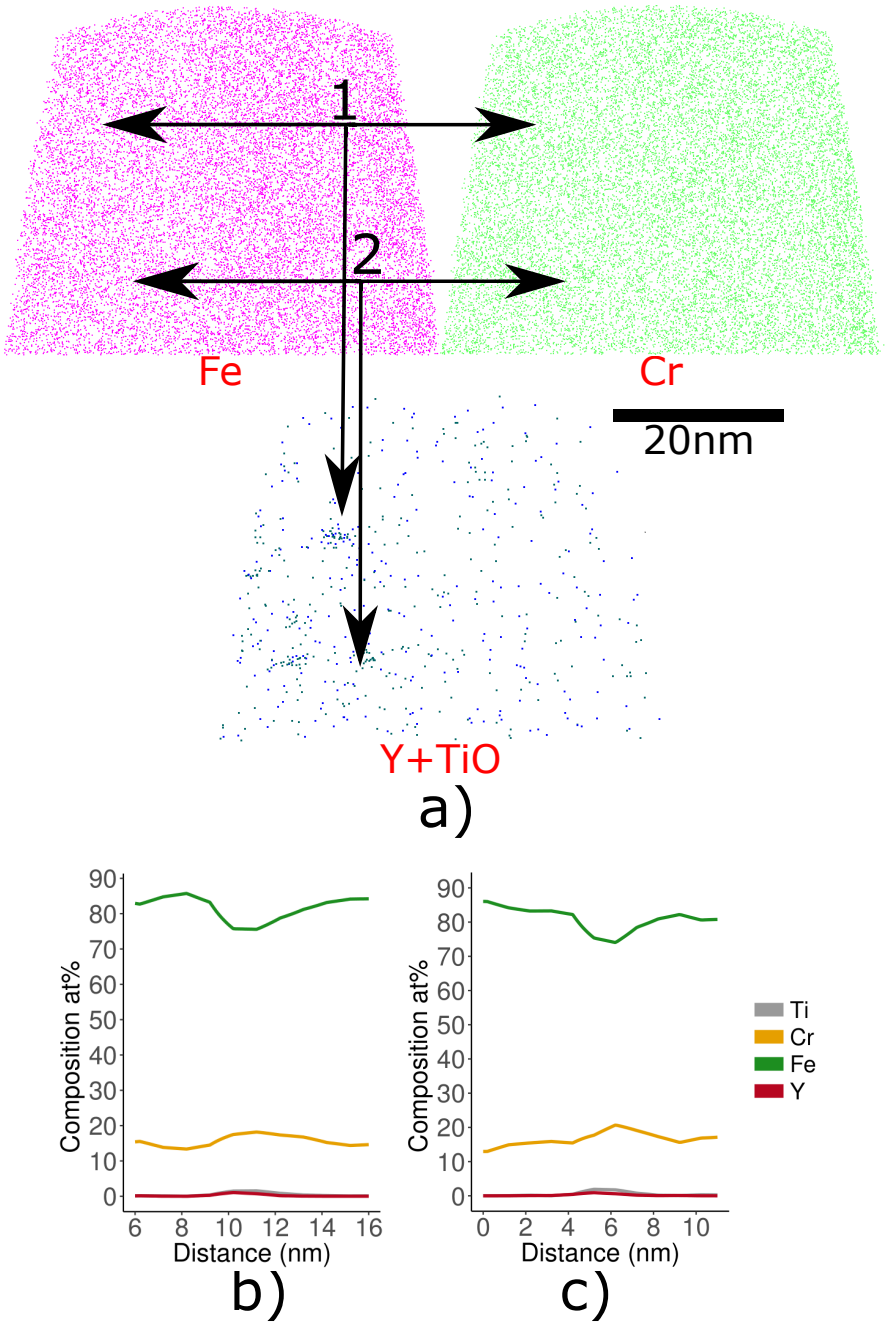


Figure 6.7: a) Zoomed in Fe, Cr, Y+TiO atom maps from the 14YWT3 as-received dataset 5213. b) and c) are concentration profiles through region 1 and 2 in a)

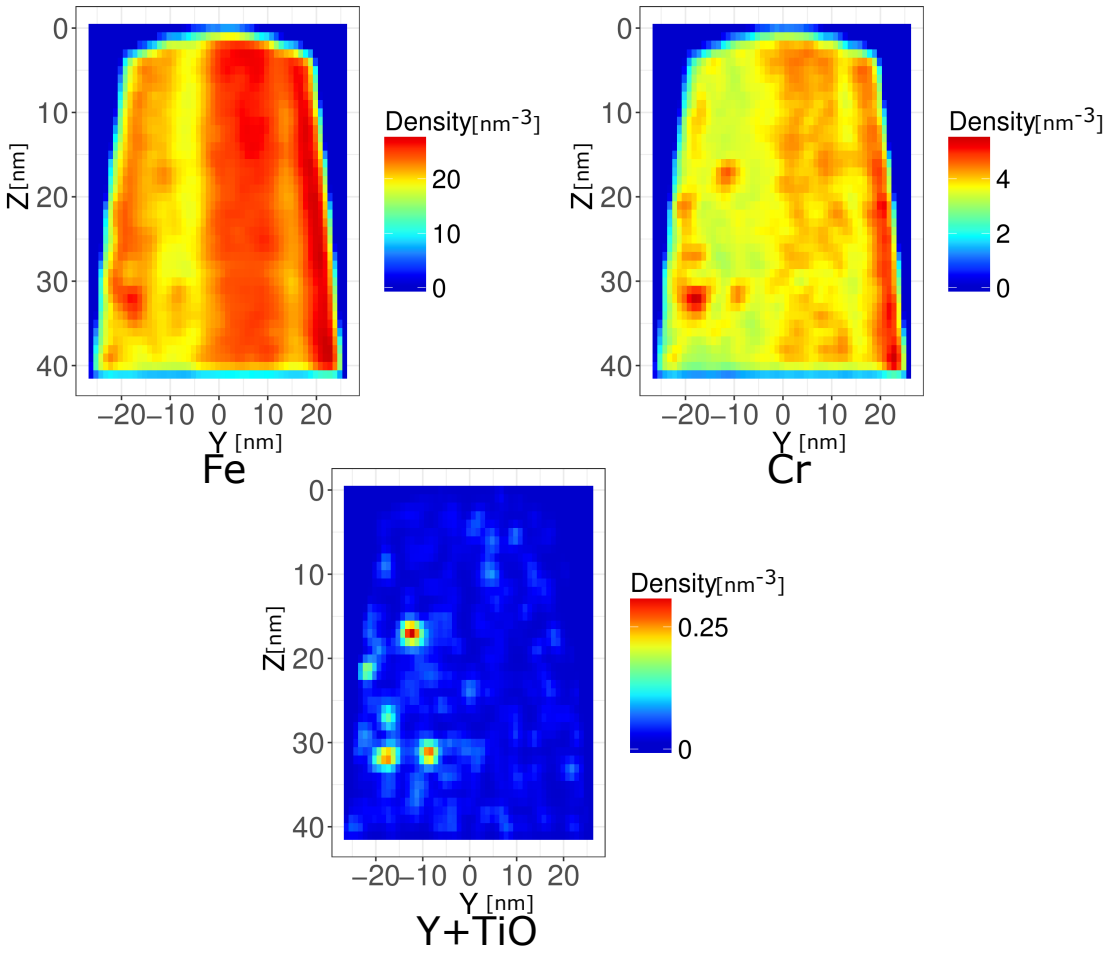


Figure 6.8: Two-dimensional density maps of Fe, Cr, Y+TiO within the same region shown in figure 6.7a. Laser assisted evaporation of atoms did not occur for any 14YWT3 as-received APT datasets.

in figure 6.8. It shows these solvents to be enriched slightly within regions $0 < y < 20$ (right side of the 2D map in figure 6.8) relative to region $-20 < y < 0$ (left side of the 2D map in figure 6.8). The difference in the number density of Fe between the two regions is approximately $6nm^{-3}$. Whereas Cr varies by $< 1nm^{-3}$. These datasets were obtained from experiments conducted under voltage mode. Therefore, the insignificant Fe and Cr density variations observed in figure 6.7 are likely to be due to inherent inhomogeneous distributions of Fe and Cr within the material [27, 279]. Lastly, dispersoid regions, which are represented by a higher density of Y+TiO, show Cr is enriched within these zones.

Magnified Fe, Cr and Y+TiO atom maps from dataset 4731 (neutron irradiated 14YWT3) are shown in figure 6.9a. Regions that are depleted in Fe and enriched in Cr occur and are correlated with the regions that are enriched with Y+TiO. Concentration profiles through two randomly selected dispersoids, shown in figure 6.9b and figure 6.9c, show the depletion of Fe and enrichment of Cr, which is consistent with figure 6.9a.

2D number density plots of the same region shown in figure 6.9, of Fe, Cr and Y+TiO are shown in figure 6.10. Though these datasets were acquired in laser mode, an Fe or Cr lateral number density gradient is not observed. This is probably because APT datasets of the neutron irradiated 14YWT3 were acquired using the LEAP 4000X-HR. This atom probe uses a laser with a wavelength of 355nm and has a laser spot size $< 1\mu m$ [363]. The LEAP 3000X-HR, was used to acquire APT datasets of the 14YWT1 and 14YWT2, and uses a laser with a wavelength of 532nm and has a laser spot size that is $1 - 5\mu m$ [364]. Thus, the reduced wavelength and spot size when using the LEAP 4000X-HR reduces the volume within the APT sample that is heated [337]. As a result, shadow effects, which are explained in section 3.4.8, are less pronounced in this dataset.

Dispersoids within figure 6.9 are represented by the regions with a higher density of

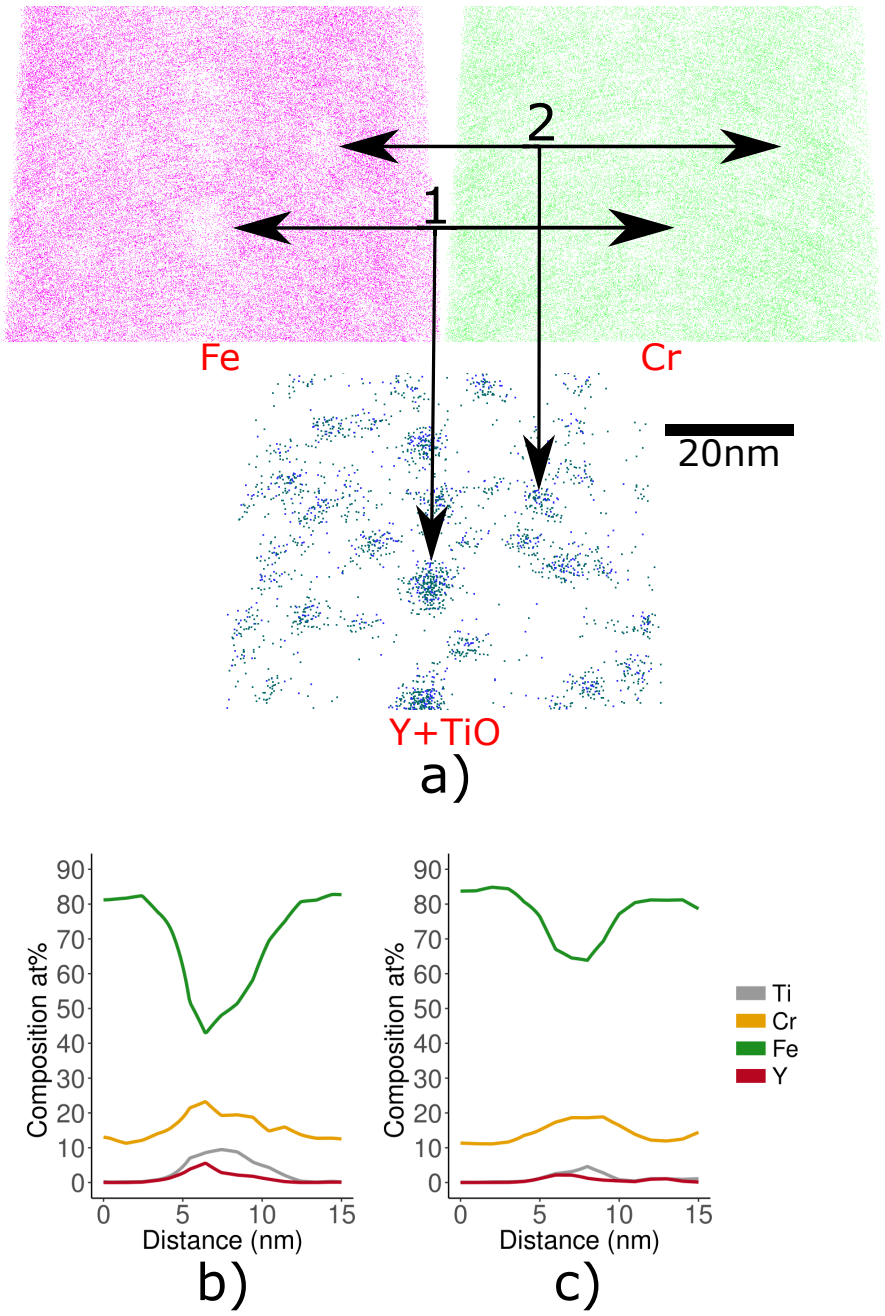


Figure 6.9: a) Zoomed in Fe, Cr, Y+TiO atom maps from the neutron irradiated 14YWT3 dataset 4731. b) and c) are concentration profiles through region 1 and 2 in a)

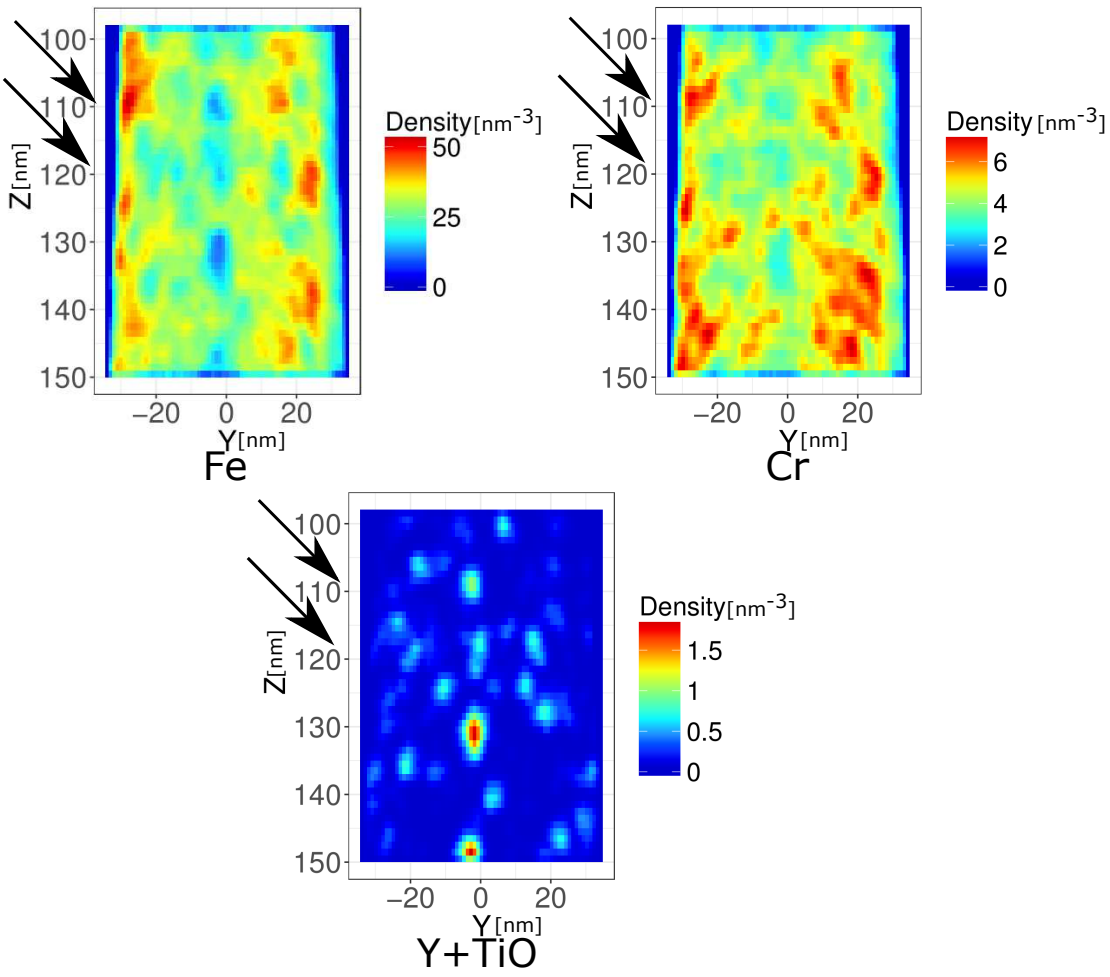


Figure 6.10: Two-dimensional density maps of Fe, Cr, Y+TiO within the same region shown in figure 6.9a. Black arrows represent the approximate direction of the laser pulse

Y and TiO. They show that the distribution of Fe and Cr atoms are highly correlated with the dispersoids. This is consistent with the magnified atom maps and concentration profiles shown in figure 6.9.

This depletion of Fe and enrichment of Cr at the dispersoid regions are indicative of magnification effects, as explained in section 5.3.2.1 and appendix 3.4.7. Therefore, the higher values of μ_{Fe} and μ_{Cr} observed within 14YWT3 as-received and neutron irradiated 14YWT3, are due to magnification effects only, and not due to secondary phase formation such as α'.

6.3.2.3 Grain boundary segregation of alloying elements within 14YWT3

Two neutron irradiated 14YWT3 APT sample volumes contained a GB. This GB was found in datasets 4724 and 4732, and is shown in appendix E figures E.2 and E.3.

GIE values have been calculated for each of these GBs and are seen to vary significantly between three different regions along the GB. Positive GIE values represent an enrichment of the subject element at the GB. The GB in dataset 4724 was seen to contain on average $+7.3\pm1.7 atoms\,nm^{-2}$ of Cr, $+1.1\pm0.4 atoms\,nm^{-2}$ of W, $+0.1\pm0.0 atoms\,nm^{-2}$ of Mn and $+0.2\pm0.2 atoms\,nm^{-2}$ of Si. The GB in dataset 4732 was seen to contain on average $+10.5\pm3.2 atoms\,nm^{-2}$ of Cr, $+1.7\pm0.9 atoms\,nm^{-2}$ of W, $+0.1\pm0.1 atoms\,nm^{-2}$ of Mn and $+0.5\pm0.4 atoms\,nm^{-2}$ of Si.

As a GB has not been captured in the 14YWT3 as-received APT datasets, a comparison cannot be made. Instead, the data is presented in appendix E tables E.2 and E.3 for use in future studies.

6.3.2.4 14YWT3 Minor solute distributions

Atom maps in figure 6.6, showed Co, Si and Mn to be unclustered and unsegregated. This qualitative assessment has been confirmed by calculating Pearson coefficients, μ,

	14YWT3 as-received			
	5209	5210	5213	$\bar{\mu}$
μ_{Mn}	0.13	0.06	0.07	0.09 ($\pm$0.020)
μ_{Si}	0.09	0.10	0.10	0.10 ($\pm$0.003)
μ_{Co}	0.18	0.13	0.11	0.14 ($\pm$0.022)
	Neutron irradiated 14YWT3			
	4724	4731	4732	$\bar{\mu}$
μ_{Mn}	0.01	0.01	0.01	0.01 ($\pm$0.001)
μ_{Si}	0.06	0.06	0.05	0.06 ($\pm$0.003)
μ_{Co}	0.01	0.01	0.02	0.01 ($\pm$0.003)

Table 6.7: Pearson coefficients, μ, calculated for Mn, Si and Co within each of the 14YWT3 APT datasets

for Co, Si and Mn, which are presented in table 6.7. μ for Co, Si and Mn within 14YWT3 as-received is approximately 0, which suggests that these solute distributions are approximately random. After neutron irradiation, they continue to be approximately random as μ for these solutes is still close to 0.

6.4 Discussion

6.4.1 Phase stability of irradiated 14YWT2 and 14YWT3

The average concentration of Cr within the as-received 14YWT2 and 14YWT3 matrix, as measured by APT is $13.34 \pm 0.20\, wt.\%$ and $13.19 \pm 0.14\, wt.\%$ respectively. A binary Fe-Cr alloy with this quantity of Cr, irradiated at the same irradiation temperature here ($288°C$) should lie within the $\alpha + \alpha'$ region in the Fe-Cr phase diagram [32], as

shown in figure 2.11. In the presence of ion and neutron irradiation α' precipitation is enhanced due to enhanced diffusion of Cr and RIS which is discussed in section 2.5.2 [42, 272, 365]. Therefore, current knowledge indicates it is favourable for α' regions to form approximately spherical isolated precipitates within irradiated 14YWT2 and 14YWT3.

MA957 (12.6wt.%Cr) ODS alloys neutron irradiated to 2dpa at $325°C$ have formed α' precipitates [354]. K2 (13.6wt.%Cr) ODS neutron irradiated to 0.79dpa at $300°C$ exhibited mechanical property changes that were indicative of α' formation [151]. No DSAs have been reported to form α' precipitates after ion-irradiation. Only Fe-15Cr irradiated with Fe^{2+} up to 1dpa has formed α' precipitates [272].

Irradiation conditions are unlikely to account for the absence of α' precipitates. 14YWT irradiated to 100dpa at $300°C$ with Ni^{2+}, did not form any α' precipitates in the sampled volume [356]. Therefore increasing the target dose for the ion-irradiated 14YWT2 is unlikely to increase the chances of α' formation. Similarly, increasing the target dose for the neutron irradiated 14YWT3 is also unlikely to promote the formation of α' precipitates, as many neutron irradiated binary Fe-Cr and Fe-Cr-Al alloys have formed α' precipitates at lower peak doses [125, 208].

Hypothetically, increasing the dose rate up to $10^{-3} dpa\, s^{-1}$ at $290°C$ is unlikely to deter α' precipitate formation via ballistic dissolution [261]. But higher dose rates are unlikely to promote α' formation, as recombination events are enhanced significantly [235] and therefore RED is suppressed. The neutron irradiated 14YWT3 has also shown that reducing the dose rate doesn't promote α' precipitate formation either. This may be because long-range diffusion of point defects is favoured, and in 14YWT this would increase the probability of point defects pinned to dispersoids. In this event, the recombination rate would be enhanced, and therefore RED is suppressed

Though α' precipitates did not form at $475°C$ within 14YWT1, as shown in chapter 5,

it is possible that higher temperatures are required in non-equilibrium environments. However, as discussed in section 2.5.3, the phase stability of 14YWT NFAs in non-equilibrium environments is still not understood at this time.

The absence of α' in the ion-irradiated and neutron-irradiated atom maps suggests a possible deviation from the theorised Fe-Cr phase diagram, as well as the experimental trends cited in section 2.5. 14YWT's free energy is unknown both at equilibrium and non-equilibrium. As α' precipitates have not formed within either irradiated 14YWT2 and 14YWT3, the α phase is stable under these irradiation conditions.

6.4.2 Comparison of ion and neutron irradiated 14YWT microstructures

Comparing figure 6.1b with 6.6b, it is evident that these ion-irradiation conditions are a good analogue to fission irradiation, in terms of distributions of alloying elements. This is significantly different to the irradiation comparative study on Fe-12Cr alloys, reported by Pareige et al. [43]. Electron microscopy is required to clarify whether dislocation networks are also reproduced well by ion-irradiation. RIS of alloying elements to GBs may also differ between different irradiation environment and also requires confirmation.

6.5 Conclusion

14YWT2 NFA irradiated with 24MeV $^{56}Fe^{8+}$ to 0.74-1.49dpa, and 14YWT3 were neutron irradiated to 1.82dpa at $288°C$. Post-irradiation analysis via APT showed no changes to the solvent and solute distributions had occured within both alloys after irradiation. α' precipitates and other tertiary intermetallics had not formed after irradiation. Therefore, the α matrix was found to be stable after irradiation.

The effects of neutron irradiation on the distributions of alloying elements within 14YWT3

are similar to that of the $^{56}Fe^{8+}$ irradiated 14YWT2. Indeed, this only provides one perspective as irradiation effects other microstructural features such as dislocation networks and defect clusters. It is unclear whether these features are also replicated. Therefore, future work would be to conduct TEM studies to study these features in the irradiated samples. Mechanical tests would also be advantageous to determine whether irradiation induced mechanical changes are also replicated.

Chapter 7

Summary and conclusions

7.1 Previous work

α' precipitates can form within Fe-Cr based alloys that reside at temperatures $\leq 475℃$ [32] (section 2.3.1.2). This can lead to mechanical property changes such as increases in hardness and embrittlement [36] (section 2.3.1.5). Dispersoid Strengthened Alloys (DSAs) such as PM2000 are also susceptible to this phenomenon [40]. In addition to α', other secondary phases e.g. M_7C_3 precipitates as well as tertiary intermetallics e.g. β' in PM2000 [39, 40], may also form in higher order alloys (section 2.3.1.7).

In the presence of irradiation, secondary phase formation is enhanced [42]. Ion-irradiation and neutron irradiation comparative studies on Fe-12Cr alloys, that achieve similar target doses and irradiation temperatures, have yielded significantly different microstructures [43], as seen in figure 2.41 (section 2.5.2.2). The ion-irradiated alloys were seen to contain clusters rich in Cr, Si, P and Ni. These clusters also formed within the neutron irradiated sample, but contained higher concentrations of Cr, Si and Ni. A second class of clusters were also identified in the neutron irradiated sample as α'. The lower concentrations of Cr, Si and Ni, as well as the absence of α' within the ion-irradiated

sample, was attributed to the excess population of interstitials introduced into the sample following multi-energy ion implantation [272].

7.2 Work completed in this thesis

Two distinct gaps in the literature were identified and outlined in section 2.6. Firstly, it was unknown whether 14YWT Nanostructured Ferritic Alloys (NFAs) are also susceptible to the formation of α', other secondary phases and tertiary intermetallics, as a result of exposure to temperatures $\leq 475℃$. Segregation of alloying elements may also occur at the dispersoid-matrix interface as a result of ageing and is yet to be confirmed. Secondly, it was unknown whether secondary phases, such as α', or tertiary intermetallics form after either multi-energy ion-irradiation or neutron irradiation. It was also unknown whether ion-irradiation and neutron irradiation to similar peak doses and irradiation temperatures yield different microstructures, as was the case for Fe-12Cr [43].

To investigate the two research areas described above, two studies were designed and implemented. The first study, consisted of an isothermal ageing experiment on 14WT non-NFA and 14YWT NFA at $475℃$. The second study was an ion and neutron irradiation comparative study on 14YWT NFA.

7.2.1 Atom probe tomographic parameter determination experiment

Post experimental analysis utilised APT to characterise the distributions of alloying elements within each of the treated alloys. To ensure accurate composition measurements, as well as an superior signal-to-noise ratio and mass resolution; a calibration experiment was conducted. This was done for laser mode only on the LEAP 3000X-HR and is presented in chapter 4. The analysis chamber temperatures ($45K - 55K$) and laser

energies ($0.2nJ - 0.4nJ$) were varied, and the laser pulse repetition rate ($200kHz$) and evaporation rate ($0.005\,ions\,pulse^{-1}$) were kept constant. APT datasets fulfilled the three criteria of accurate composition measurement, superior signal-to-noise ratio and mass resolution when the following combination of parameters were utilised: $T = 55K$, $E_{Laser} = 0.4nJ$, $\nu = 200kHz$ and $\Phi_{evap} = 0.005\,ion\,pulse^{-1}$.

7.2.2 Isothermal ageing experiment

The isothermal ageing study, as presented in chapter 5, showed that 14WT, the control alloy without dispersoids, did form α' precipitates. α' precipitates were only seen in the 14WT samples aged for 3 and 8 months and not in the 14WT aged for 1 month at $475℃$. This indicates that there was an incubation period between 1 and 3 months. However, [33] and [40] observed α' to form after just 50 hours and 10 hours respectively. Therefore the incubation period observed in this thesis is a significantly longer period. Further, as shown in table 5.12, Cr concentrations within the 14WT and number densities were much lower than other studies in the literature e.g. [307]. Table 5.2 shows number densities of α' in the aged 14WT also varied significantly between experimental repeats for a given ageing duration. Overall, the 14WT aged for 8 months hardened by $32 \pm 4kgf\,mm^{-2}$ from $238 \pm 2kgf\,mm^{-2}$.

The longer incubation period is probably due to a decrease in the driving force for α' formation in 14WT, relative to the PM2000 used in [40] and binary alloy in [33] (discussed in section 5.4.1.1). The reduction in driving force may be due to a significant change in 14WT's free energy, relative to that of a simple Fe-Cr binary alloy, as a result of additional alloying elements [41]. The variation in precipitate number density is probably due to the inherent inhomogeneity associated with the distribution of Cr in the 14WT as-received as shown in table 5.13 and the analysis conducted by Gorley [44]. Section 5.4.5 showed that the net hardening observed in 14WT aged for 8 months, was

due to α' precipitates acting as very weak obstacles to dislocation motion.

Section 5.3.2 showed that 14YWT NFA aged at $475℃$ for up to 8 months did not form any α' precipitates, other secondary phases or tertiary intermetallics. As stated in section 5.4.2, it is evident that 14YWT NFA is resistant to α' precipitate formation. This could be due to a significant change in 14YWT's free-energy relative to that belonging to an Fe-Cr binary alloy, as a result of the additional alloying elements.

Under isothermal ageing conditions, alloying elements did not segregate to the dispersoid-matrix interface as a result of ageing. However, the enrichment of Cr and W at the GBs as a function of ageing duration occurred. It was also shown that after 8 months of ageing, 14YWT had softened by $26 \pm 10 kgf\, mm^{-2}$. The reason for this softening is probably due to a reduction in the number density of dislocations and needs to be confirmed by other characterisation techniques.

7.2.3 Ion and neutron irradiation comparative study

This comparative study, presented in chapter 6, also showed that α' precipitates, other secondary phases and intermetallics do not form within 14YWT. There was very little difference in terms of elemental distribution within the as-received and ion-irradiated alloys as well as the as-received and neutron irradiated alloys. Differences in terms of the distribution of elements between the ion-irradiated sample relative to the neutron irradiated were also seen to be negligible.

As stated in section 2.5.3, the temperature and Cr concentration for non-equilibrium phase formation within Fe-Cr alloys is generally unknown. However, MA957 ODS, which contains a lower concentrations of Cr than 14YWT ($Cr_{MA957} = 12.6 wt.\%$, $Cr_{14YWT3} = 13.19 \pm 0.14 wt.\%$), neutron irradiated to 2dpa at $325℃$ formed α' precipitates [354]. No studies on ion-irradiated 14YWT at low-temperatures have been conducted in the literature. Considering this and the observations from the isothermal

ageing experiment conducted here, it is evident that 14YWT's matrix is stable under irradiation conditions (section 6.4.1). Therefore, it is likely that 14YWT's free energy is significantly different relative to other Fe-Cr based alloys.

The similarity in terms of the microstructures between the ion irradiated 14YWT and the neutron irradiated 14YWT is distinctly different to what was observed in the ion and neutron irradiation comparative study on Fe-12Cr (described in section 2.5.2.2). As proposed in section 6.4.1, this is probably because the recombination rate in DSAs is enhanced, due to the pinning of point defects at the dispersoid surface [90]. As the population of point defects reduces, so do the point defect fluxes to RIS sites. Therefore the redistribution of alloying elements effected by point defect fluxes is reduced and hence, the probability of RIP occurring reduces too.

7.3 Limitations

APT characterisation relies on the assumption that the small volumes captured in the APT datasets are representative of the bulk. This assumption in this thesis is stretched somewhat, as 14WT and 14YWT atom maps presented in section chapter 5 and 6, exhibited significant inhomogeneity in terms of elemental distributions and microstructural features. This is consistent with Gorley's observations as he reported fluctuations >10% in the concentrations of Cr, W and Ti over $20\mu m$ of 14WT and 14YWT [44]. It was proposed in section 5.4.1.1, that fluctuations in the matrix concentration of Cr was the reason why significant inhomogeneity in the α' precipitate number density was observed. In 14YWT, dispersoid number densities within the APT densities ranged between $1.11 \times 10^{22} - 6.85 \times 10^{23} m^{-3}$ (shown in figure 5.20). Indeed, some intragranular regions of 14YWT contained no dispersoids, as seen in figure D.3 in appendix D. To reduce the uncertainty associated with key metrics such as α' precipitate and dispersoid

number density in future studies, it is suggested that Small Angle Neutron Scattering (SANS) experiments be conducted in addition to APT. This technique would allow for the characterisation of samples over a larger analysis volume, and would complement APT data.

Secondly, APT induced artefacts such as magnification effects, laser-induced surface migration of Fe and Cr and shadow effects were consistently observed to occur in each of the datasets acquired on the LEAP3000X-HR. APT datasets of the neutron-irradiated 14YWT3 were acquired on the LEAP 4000X-HR, and only induced magnification effects. Nevertheless, both of these artefacts can introduce errors into local composition measurements of Fe, Cr, Y, Ti and O.

The ion-irradiation experiment conducted at the JANNuS facility was not completed to the specifications stated in the original proposal. The secondary emissions that occurred during implantation reduced the peak dose achieved and introduced significant uncertainty to this metric.

7.4 Future work

- TEM studies should be conducted on 14YWT1 as-received and the 14YWT1 aged for 8 months. A comparison of the dislocation densities within these two samples, may provide insight into why 14YWT1 softens after 8 months of ageing at $475℃$.
- TEM Energy Dispersive Spectroscopy (EDS) and SANS studies should be conducted on the 14WT and 14YWT1 aged for 8 months, as well as the ion-irradiated 14YWT2 and neutron irradiated 14YWT3. This would complement the APT data presented in chapters 5 and 6, as it would provide more accurate averaged metrics, such as those described in the preceeding section, over a larger volume
- Thermodynamic calculations should be completed to generate phase diagrams for

14YWT and 14WT. This should provide details to why 14YWT is resistant to α' precipitate formation and why there is such a long incubation period for α' precipitates to form within 14WT

- Ageing durations for 14YWT1 and 14WT should also be extended by at least four months. This may provide insight to whether 14YWT1 develops α' precipitates at longer durations. It would also be useful to determine if α' precipitate Cr concentrations attain equilibrium during this extended ageing period

- Neutron and ion-irradiation experiments at higher temperatures, and to higher doses, should also be conducted. This would show whether solute distributions in the fission neutron irradiated sample continue to be replicated within the ion-irradiated sample

- TEM studies should be conducted on the ion-irradiated and neutron irradiated samples to determine whether the two irradiation regimes produce similar microstructures.

  - Hardness measurements would also provide insight into whether the two irradiation environments induce mechanical property changes differently

Bibliography

[1] British Petroleum. Energy outlook 2016. 0:1–98, 2016.

[2] Ernst and Young. Renewable energy country attractive index. 37:1–44, 2013.

[3] ITER. ITER schematic. `https://www.iter.org`. Accessed: 23/09/2016.

[4] European nuclear Society. Binding energy per nucleon. `https://www.euronuclear.org/info/encyclopedia/bindingenergy.htm`. Accessed: 05/10/2016.

[5] Y. Demirel. *Energy: Production, Conversion, Storage, Conservation, and Coupling*. Springer-Verlag London, 2012.

[6] L. Bengtsson, E. Rachlew, and F. Wagner. Sustainable energy supply and consumption by 2050 and outlook towards the end of the century: Possible scientific breakthroughs. *Ambio*, 45:1–4, 2016.

[7] A. Horvath and E. Rachlew. Nuclear power in the 21st century: Challenges and possibilities. *Ambio*, 45:38–49, 2016.

[8] J. Knaster, A. Moeslang, and T. Muroga. Materials research for fusion energy. *Nature materials*, 12:424–434, 2016.

[9] ITER. The ITER tokamak: magnets. `https://www.iter.org/mach/Magnets`. Accessed: 16/12/2016.

[10] T. Berlincourt and R. Hake. Superconductivity at High Magnetic Fields. *Physical Review*, 131:140–157, 1963.

[11] G.M. Crawley. *Energy from the Nucleus: The science and engineering of fission and fusion*. World scientific, 2016.

[12] S.J. Zinkle and J.T. Busby. Structural materials for fission & fusion energy. *Materials Today*, 12:12–19, 2009.

[13] K. Ehrlich, E.E. Bloom, and T. Kondo. International strategy for fusion materials development. *Journal of Nuclear Materials*, 283-287:79–88, 2000.

[14] Y. Song, W. Wu, and S. Du. *Tokamak engineering mechanics*. Springer-Verlag Berlin Heidelberg, 2014.

[15] T. Ihli, T. K. Basu, L. M. Giancarli, S. Konishi, S. Malang, F. Najmabadi, S. Nishio, A. R. Raffray, C. V S Rao, A. Sagara, and Y. Wu. Review of blanket designs for advanced fusion reactors. *Fusion Engineering and Design*, 83:912–919, 2008.

[16] Materials R&D for a timely DEMO: Key findings and recommendations of the EU Roadmap Materials Assessment Group. *Fusion Engineering and Design*, 89:1586–1594, 2014.

[17] L. M. Giancarli, M. Abdou, D. J. Campbell, V. A. Chuyanov, M. Y. Ahn, M. Enoeda, C. Pan, Y. Poitevin, E. Rajendra Kumar, I. Ricapito, Y. Strebkov, S. Suzuki, P. C. Wong, and M. Zmitko. Overview of the ITER TBM Program. *Fusion Engineering and Design*, 87:395–402, 2012.

[18] G. Rampal, A. Li Puma, Y. Poitevin, E. Rigal, J. Szczepanski, and C. Boudot. HCLL TBM for ITER-design studies. *Fusion Engineering and Design*, 75-79:917–922, 2005.

[19] N. Baluc, K. Abe, J.L. Boutard, V.M. Chernov, E. Diegele, S. Jitsukawa, A. Kimura, R.L. Klueh, A. Kohyama, R.J. Kurtz, R. Lässer, H. Matsui, A. Möslang, T. Muroga, G.R. Odette, M.Q. Tran, B. van der Schaaf, Y. Wu, J. Yu, and S.J. Zinkle. Status of R&D activities on materials for fusion power reactors. *Nuclear Fusion*, 47:696–717, 2007.

[20] H.R. Brager, F.A. Garner, and G.L. Guthrie. The effect of stress on the microstructure of neutron irradiated type 316 stainless steel. *Journal of Nuclear Materials*, 66:301–321, 1977.

[21] F.A. Garner. *Materials Science and Technology*. VCH New york, 10a edition, 1994.

[22] S.J Zinkle and G.E Lucas. Deformation and fracture mechanisms in irradiated FCC and BCC metals. *Report DOE/ER0313/34*, 30:101–125, 2003.

[23] F. Abe and T. Noda. Fusion Reactors : Low-activation structural materials. *Encyclopedia of materials: science and technology*, 0:3418–3422, 1989.

[24] S. Ukai, H. Okada, M. Inoue, T. Nishida, M. Fujiwara, S. Nomura, S. Shikakura, and K. Asabe. Alloying design of oxide dispersion for long life FBRs core materials strengthened ferritic steel. *Journal of Nuclear Materials*, 204:65–73, 1993.

[25] S. Ukai, M. Harada, H. Okada, M. Inoue, S. Nomura, S. Shikakura, T. Nishida, M. Fujiwara, and K. Asabe. Tube manufacturing and mechanical properties of oxide dispersion strengthened ferritic steel. *Journal of Nuclear Materials*, 204:74–80, 1993.

[26] S. Ukai, T. Nishida, T. Okuda, and T. Yoshitake. Development of Oxide Dispersion Strengthened Steels for FBR Core Application, (I). *Journal of Nuclear Science and Technology*, 34:256–263, 1997.

[27] M.J Alinger. *On the Formation and Stability of Nanometer Scale Precipitates in Ferritic Alloys during Processing and High Temperature Service*. Phd thesis, University of California Santa Barbara, 2004.

[28] E. Arzt. High temperature properties of dispersion strengthened materials produced by mechanical alloying : current theoretical understanding and some practical implications. *New Materials by Mechanical Alloying Techniques*, 0:185–200, 1988.

[29] G.R. Odette, M.J. Alinger, and B.D. Wirth. Recent Developments in Irradiation-Resistant Steels. *Annual Review of Materials Research*, 38:471–503, 2008.

[30] H. Oka, M. Watanabe, H. Kinoshita, T. Shibayama, N. Hashimoto, S. Ohnuki, S. Yamashita, and S. Ohtsuka. In situ observation of damage structure in ODS austenitic steel during electron irradiation. *Journal of Nuclear Materials*, 417:279–282, 2011.

[31] M.C. Brandes, L. Kovarik, M.K. Miller, and M.J. Mills. Morphology, structure, and chemistry of nanoclusters in a mechanically alloyed nanostructured ferritic steel. *Journal of Materials Science*, 47:3913–3923, 2012.

[32] G. Bonny, D. Terentyev, and L. Malerba. On the α–α' miscibility gap of Fe–Cr alloys. *Scripta Materialia*, 59:1193–1196, 2008.

[33] S. Novy, P. Pareige, and C. Pareige. Atomic scale analysis and phase separation understanding in a thermally aged Fe–20at.%Cr alloy. *Journal of Nuclear Materials*, 384:96–102, 2009.

[34] R.O. Williams and H.W. Paxton. The nature of aging of binary iron-chromium alloys around 500 C. *The journal of the iron and steel institute*, 185:358–374, 1957.

[35] J. Ribis and S. Lozano-Perez. Orientation relationships and interface structure of α'-Cr nanoclusters embedded in α-Fe matrix after α–α' demixing in neutron irradiated Oxide Dispersion Strengthened material. *Materials Letters*, 74:143–146, 2012.

[36] P.J. Grobner. The 885°F (475°c) embrittlement of ferritic stainless steels. *Metallurgical Transactions*, 4:251–260, 1973.

[37] G. Bonny, D. Terentyev, and L. Malerba. The hardening of iron–chromium alloys under thermal ageing: An atomistic study. *Journal of Nuclear Materials*, 385:278–283, 2009.

[38] C. Capdevila, M. K. Miller, and K. F. Russell. Aluminum partitioning during phase separation in Fe–20%Cr–6%Al ODS alloy. *Journal of Materials Science*, 43:3889–3893, 2008.

[39] The β'-α' interaction: a study of early stages of phase separation in a Fe-20%Cr-6%Al-0.5%Ti alloy. *Solid State Phenomena*, 172-174:315–320, 2011.

[40] C. Capdevila, M.K. Miller, K.F. Russell, J. Chao, and J.L. González-Carrasco. Phase separation in PM 2000 Fe–base ODS alloy: Experimental study at the atomic level. *Materials Science and Engineering: A*, 490:277–288, 2008.

[41] D.A. Porter, K.E. Easterling, and M.Y. Sherif. *Phase transformations in metals and alloys.* Taylor and Francis group, 2009.

[42] M.H Mathon, Y de Carlan, G Geoffroy, X Averty, A Alamo, and C.H de Novion. A SANS investigation of the irradiation-enhanced α–α' phases separation in 7–12 Cr martensitic steels. *Journal of Nuclear Materials*, 312:236–248, 2003.

[43] C. Pareige, V. Kuksenko, and P. Pareige. Behaviour of P, Si, Ni impurities and Cr in self ion irradiated Fe–Cr alloys - Comparison to neutron irradiation. *Journal of Nuclear Materials*, 456:471–476, 2015.

[44] M.J. Gorley. *Powder processing of oxide dispersion strengthened alloys for nuclear applications.* DPhil thesis, University of Oxford, 2014.

[45] C. Burrows. *The Irradiation Resistance of Oxide Dispersion Strengthened Steels.* DPhil thesis, University of Oxford, 2015.

[46] M.A. Auger, T. Leguey, A. Muñoz, M.A Monge, V. de Castro, P. Fernández, G. Garcés, and R. Pareja. Microstructure and mechanical properties of ultrafine-grained Fe-14Cr and ODS Fe-14Cr model alloys. *Journal of Nuclear Materials*, 417:213–216, 2011.

[47] A. Kohyama, A. Hishinuma, and D.S. Gelles. Low-activation ferritic and martensitic steels for fusion application. *Journal of Nuclear Materials*, 233-237:138–147, 1996.

[48] J. Nutting. The long term structural stability of power generation steels -Some basic considerations. *Institute of materials*, 708:12–30, 1998.

[49] F Masuyama. New developments in steels for power generation boilers. *Advanced Heat Resistant Steel for Power Generation*, 708:33–48, 1998.

[50] Y. Wang, K.H. Mayer, A. Scholz, C. Berger, H. Chilukuru, K. Durst, and W. Blum. Development of new 11%Cr heat resistant ferritic steels with enhanced creep resistance for steam power plants with operating steam temperatures up to 650°C. *Materials Science and Engineering A*, 510-511:180–184, 2009.

[51] K.H.S. Mayer. Proceedings of the 29th seminar: Materials & Component Behaviour in Energy & Plant Technology. MPA - Stuttgart - Germany.

[52] M. Matijasevic and A. Almazouzi. Effect of Cr on the mechanical properties and microstructure of Fe–Cr model alloys after n-irradiation. *Journal of Nuclear Materials*, 377:147–154, 2008.

[53] A. Kimura, R. Kasada, N. Iwata, H. Kishimoto, C.H. Zhang, J. Isselin, P. Dou, J.H. Lee, N. Muthukumar, T. Okuda, M. Inoue, S. Ukai, S. Ohnuki, T. Fujisawa, and T.F. Abe. Development of Al added high-Cr ODS steels for fuel cladding of next generation nuclear systems. *Journal of Nuclear Materials*, 417:176–179, 2011.

[54] V.V. Sagaradze, V.I. Shalaev, V.L. Arbuzov, B.N. Goshchitskii, Y. Tian, W. Qun, and S. Jiguang. Radiation resistance and thermal creep of ODS ferritic steels. *Journal of Nuclear Materials*, 295:265–272, 2001.

[55] J.J. Sniegowski and W.G. Wolfer. Proceedings of the AIME conference on ferritic alloys for use in nuclear energy technologies: On the physical basis for the swelling resistance of ferritic steels. Snowbird, Utah.

[56] M.K. Miller and C.M. Parish. Role of alloying elements in nanostructured ferritic steels. *Materials Science and Technology*, 27:729–734, 2011.

[57] J.M. Bonnerot, V. Broudic, and M. Phelip. Transmutation in reactor and aqueous corrosion resistance of technetium metal. *Journal of Nuclear Radiochemical sciences*, 6:287–290, 2005.

[58] J. Hoffmann, M. Rieth, R. Lindau, M. Klimenkov, A. Möslang, and H.R.Z. Sandim. Investigation on different oxides as candidates for nano-sized ODS particles in reduced-activation ferritic (RAF) steels. *Journal of Nuclear Materials*, 442:444–448, 2013.

[59] M. Ratti, D. Leuvrey, M.H. Mathon, and Y. de Carlan. Influence of titanium on nano-cluster (Y, Ti, O) stability in ODS ferritic materials. *Journal of Nuclear Materials*, 386-388:540–543, 2009.

[60] J.H. Schneibel, M. Heilmaier, W. Blum, G. Hasemann, and T. Shanmugasundaram. Temperature dependence of the strength of fine- and ultrafine-grained materials. *Acta Materialia*, 59:1300–1308, 2011.

[61] Y. Wu, E.M. Haney, N.J. Cunningham, and G.R. Odette. Transmission electron microscopy characterization of the nanofeatures in nanostructured ferritic alloy MA957. *Acta Materialia*, 60:3456–3468, 2012.

[62] J. He, F. Wan, K. Sridharan, T.R. Allen, A. Certain, V. Shutthanandan, and Y.Q. Wu. Stability of nanoclusters in 14YWT oxide dispersion strengthened steel under heavy ion-irradiation by atom probe tomography. *Journal of Nuclear Materials*, 455:41–45, 2014.

[63] R.L. Klueh, J.P. Shingledecker, R.W. Swindeman, and D.T. Hoelzer. Oxide dispersion-strengthened steels: A comparison of some commercial and experimental alloys. *Journal of Nuclear Materials*, 341(2-3):103–114, 2005.

[64] Shigeharu Ukai and Masayuki Fujiwara. Perspective of ODS alloys application in nuclear environments. *Journal of Nuclear Materials*, 307–311:749–757, 2002.

[65] K.L. Murty and I. Charit. *An Introduction to Nuclear Materials: Fundamentals and Applications*. Wiley, 2013.

[66] H.W. Hayden, L.G. Moffatt, and J. Wulff. *Structure and Properties of Materials: Mechanical behavior*, volume 3. Wiley, 1965.

[67] W.C. Oliver and W.D. Nix. High temperature deformation of oxide dispersion strengthened al and Al-Mg solid solutions. *Acta Metallurgica*, 30:1335–1347, 1982.

[68] J.S. Benjamin. Dispersion strengthened superalloys by mechanical alloying. *Metallurgical Transactions*, 1:2943–2951, 1970.

[69] S.K. Karak, T. Chudoba, Z. Witczak, W. Lojkowski, and I. Manna. Development of ultra high strength nano-Y2O3 dispersed ferritic steel by mechanical alloying and hot isostatic pressing. *Materials Science and Engineering: A*, 528:7475–7483, 2011.

[70] A. Lasalmonie and J.l. Strudel. Influence of grain size on the mechanical behaviour of some high strength materials. *Journal of Materials Science*, 21:1837–1852, 1986.

[71] A. Baldan. Review progress in Ostwald ripening theories and their applications to nickel-base superalloys Part I: Ostwald ripening theories. *Journal of materials science*, 7:2171–2202, 2002.

[72] J. Ribis and Y. De Carlan. Interfacial strained structure and orientation relationships of the nanosized oxide particles deduced from elasticity-driven morphology in oxide dispersion strengthened materials. *Acta Materialia*, 60:238–252, 2012.

[73] L. Yang, Y. Jiang, G.R. Odette, W. Zhou, Z. Liu, and Y. Liu. Nonstoichiometry and relative stabilities of Y2Ti 2O7 polar surfaces: A density functional theory prediction. *Acta Materialia*, 61:7260–7270, 2013.

[74] D. Bhattacharyya, P. Dickerson, G.R. Odette, S.A. Maloy, A. Misra, and M.A. Nastasi. On the structure and chemistry of complex oxide nanofeatures in nanostructured ferritic alloy U14YWT. *Philosophical Magazine*, 92:2089–2107, 2012.

[75] A. Hirata, T. Fujita, Y.R. Wen, J.H. Schneibel, C.T. Liu, and M.W. Chen. Atomic structure of nanoclusters in oxide-dispersion-strengthened steels. *Nature Materials*, 10:922–926, 2011.

[76] D. Murali, B.K. Panigrahi, M.C. Valsakumar, S. Chandra, C.S. Sundar, and B. Raj. The role of minor alloying elements on the stability and dispersion of yttria nanoclusters in nanostructured ferritic alloys: An ab initio study. *Journal of Nuclear Materials*, 403:113–116, 2010.

[77] V. Badjeck, M.G. Walls, L. Chaffron, J. Malaplate, and K. March. New insights into the chemical structure of $Y_2Ti_2O_{7-\delta}$ nanoparticles in oxide dispersion-strengthened steels designed for sodium fast reactors by electron energy-loss spectroscopy. *Journal of Nuclear Materials*, 456:292–301, 2015.

[78] T. Okuda and M. Fujiwara. Dispersion behaviour of oxide particles in mechanically alloyed ODS steel. *Journal of Materials Science Letters*, 14:1600–1603, 1995.

[79] J.L. Béchade, D. Menut, M.L. Lescoat, B. Sitaud, S. Schlutig, P.L. Solari, I. Llorens, H. Hermange, Y. De Carlan, J. Ribis, and L. Toualbi. Application of synchrotron radiation to analyze the precipitation in ODS materials before irradiation in Fe-9%Cr single grain of powder and consolidated Fe-18%Cr. *Journal of Nuclear Materials*, 428:183–191, 2012.

[80] M. Klimiankou, R. Lindau, and A. Möslang. Energy-filtered TEM imaging and EELS study of ODS particles and Argon-filled cavities in ferritic-martensitic steels. *Micron*, 36:1–8, 2005.

[81] S. Yamashita, S. Ohtsuka, N. Akasaka, S. Ukai, and S. Ohnukiy. Philosophical Magazine Letters Formation of nanoscale complex oxide particles in mechanically alloyed ferritic steel Formation of nanoscale complex oxide particles in mechanically alloyed ferritic steel. *Philosophical Magazine Letters*, 84:525–529, 2004.

[82] H Kishimoto, M.J Alinger, G.R Odette, and T. Yamamoto. TEM examination of microstructural evolution during processing of 14CrYWTi nanostructured ferritic alloys. *Journal of Nuclear Materials*, 329-333:369–371, 2004.

[83] E.A. Marquis. Core/shell structures of oxygen-rich nanofeatures in oxide-dispersion strengthened Fe-Cr alloys. *Applied Physics Letters*, 93:1–3, 2008.

[84] A.J London, S. Lozano-Perez, M.P. Moody, S. Amirthapandian, B.K. Panigrahi, C.S. Sundar, and C.R.M. Grovenor. Quantification of oxide particle composition in model oxide dispersion strengthened steel alloys. *Ultramicroscopy*, 159:360–367, 2015.

[85] C. Zener. Theory of growth of spherical precipitates from solid solution. *Journal of Applied Physics*, 20:950–953, 1949.

[86] D.T. Hoelzer, J. Bentley, M.A. Sokolov, M.K. Miller, G.R. Odette, and M.J. Alinger. Influence of particle dispersions on the high-temperature strength of ferritic alloys. *Journal of Nuclear Materials*, 367-370:166–172, 2007.

[87] V. De Castro, E.A. Marquis, S. Lozano-Perez, R. Pareja, and M.L. Jenkins. Stability of nanoscale secondary phases in an oxide dispersion strengthened Fe-12Cr alloy. *Acta Materialia*, 59:3927–3936, 2011.

[88] N.J. Cunningham, Y. Wu, A. Etienne, E.M. Haney, G.R. Odette, E. Stergar, D.T. Hoelzer, Y.D. Kim, B.D. Wirth, and S.A. Maloy. Effect of bulk oxygen on 14YWT nanostructured ferritic alloys. *Journal of Nuclear Materials*, 444:35–38, 2014.

[89] Private communication: Dr A.J. London, Postdoctoral researcher at the department of Materials, University of Oxford, 2016.

[90] T. Lazauskas, S.D. Kenny, R. Smith, G. Nagra, M. Dholakia, and M.C. Valsakumar. Simulating radiation damage in a bcc Fe system with embedded yttria nanoparticles. *Journal of Nuclear Materials*, 437:317–325, 2013.

[91] M.K. Miller, K.F. Russell, and D.T. Hoelzer. Characterization of precipitates in MA/ODS ferritic alloys. *Journal of Nuclear Materials*, 351:261–268, 2006.

[92] P.P. Liu, R. Yu, Y.M. Zhu, M.Z. Zhao, J.W. Bai, F.R. Wan, and Q. Zhan. Deuterium ion irradiation induced precipitation in Fe–Cr alloy: Characterization and effects on irradiation behavior. *Journal of Nuclear Materials*, 459:81–89, 2015.

[93] L. Yang, Y. Jiang, Y. Wu, G.R. Odette, Z. Zhou, and Z. Lu. The ferrite/oxide interface and helium management in nano-structured ferritic alloys from the first principles. *Acta Materialia*, 103:474–482, 2016.

[94] G.R. Odette and D.T. Hoelzer. Irradiation-tolerant nanostructures ferritic alloys–transforming helium from a liability to an asset. *Journal of the Minerals, Metals and Materials Society (TMS)*, 62:84–92, 2010.

[95] G.R. Odette, P. Miao, D.J. Edwards, T. Yamamoto, R.J. Kurtz, and H. Tanigawa. Helium transport, fate and management in nanostructured ferritic alloys: In situ helium implanter studies. *Journal of Nuclear Materials*, 417:1001–1004, 2011.

[96] G.R. Odette, P.J. Maziasz, and J.A. Spitznagel. Fission-fusion correlations for swelling and microstructure in stainless steels: Effect of the helium to displacement per atom ratio. *Journal of Nuclear Materials*, 104:1289–1303, 1981.

[97] H. Ullmaier. The influence of helium on the bulk properties of fusion reactor structural materials. *Nuclear Fusion*, 24:1039–1083, 1984.

[98] R.J. Kurtz, G.R. Odette, T. Yamamoto, D.S. Gelles, P. Miao, and B.M. Oliver. The transport and fate of helium in martensitic steels at fusion relevant He/dpa ratios and dpa rates. *Journal of Nuclear Materials*, 367-370:417–422, 2007.

[99] J.O. Andersson and B. Sundman. Thermodynamic properties of the Cr– Fe system. *CALPHAD*, 11:83–92, 1987.

[100] N. Saunders and A.P. Miodownik. *CALPHAD (Calculation of Phase Diagrams): A Comprehensive Guide*, volume 1. Pergamon, 1998.

[101] W.A. Dench. Adiabatic high-temperature calorimeter for the measurement of heats of alloying. *Transactions of the Faraday Society*, 59:1279–1292, 1963.

[102] G. Ackland. Magnetically Induced Immiscibility in the Ising Model of FeCr Stainless Steel. *Physical Review Letters*, 97:1–4, 2006.

[103] D. Nguyen-Manh, M.Yu. Lavrentiev, and S.L. Dudarev. Ab initio and Monte Carlo modeling in Fe–Cr system: Magnetic origin of anomalous thermodynamic and kinetic properties. *Computational Materials Science*, 44:1–8, 2008.

[104] D. Nguyen-Manh, M.Y. Lavrentiev, and S.L. Dudarev. The Fe–Cr system: atomistic modelling of thermodynamics and kinetics of phase transformations. *Comptes Rendus Physique*, 9:379–388, 2008.

[105] M.Yu. Lavrentiev, D. Nguyen-Manh, and S.L. Dudarev. Cluster expansion models for Fe–Cr alloys, the prototype materials for a fusion power plant. *Computational Materials Science*, 49:S199–S203, 2010.

[106] M.Y. Lavrentiev, S.L. Dudarev, and D. Nguyen-Manh. Magnetic cluster expansion model for high-temperature magnetic properties of iron and iron–chromium alloys. *Journal of Applied Physics*, 109:1–3, 2011.

[107] M.Y. Lavrentiev, R. Soulairol, C.C. Fu, D. Nguyen-Manh, and S.L. Dudarev. Noncollinear magnetism at interfaces in iron-chromium alloys: The ground states and finite-temperature configurations. *Physical Review B*, 84:1–13, 2011.

[108] M.Y. Lavrentiev, K. Mergia, M. Gjoka, D. Nguyen-Manh, G. Apostolopoulos, and S.L. Dudarev. Magnetic cluster expansion simulation and experimental study of high temperature magnetic properties of Fe-Cr alloys. *Journal of physics: Condensed matter*, 24:1–5, 2012.

[109] Y. Ustinovshikov. "Chemical" phase transition in alloys: Ordering-phase separation. *Current Opinion in Solid State and Materials Science*, 14:7–20, 2010.

[110] T. Klaver, R. Drautz, and M. Finnis. Magnetism and thermodynamics of defect-free Fe-Cr alloys. *Physical Review B*, 74:1–11, 2006.

[111] M.Y. Lavrentiev, D. Nguyen Manh, and S.L. Dudarev. Magnetic Cluster Expansion Study of Chromium Precipitates in Fe-Cr Alloys. *Solid State Phenomena*, 172-174:1002–1007, 2011.

[112] D. Nguyen-Manh, M.Y. Lavrentiev, and S.L. Dudarev. Magnetic origin of nano-clustering and point defect interaction in Fe–Cr alloys: an ab-initio study. *Journal of Computer-Aided Materials Design*, 14:159–169, 2008.

[113] G. Bonny, D. Terentyev, and L. Malerba. New Contribution to the Thermodynamics of Fe-Cr Alloys as Base for Ferritic Steels. *Journal of Phase Equilibria and Diffusion*, 31:439–444, 2010.

[114] P. Olsson, I.A. Abrikosov, L. Vitos, and J. Wallenius. Ab initio formation energies of Fe–Cr alloys. *Journal of Nuclear Materials*, 321:84–90, 2003.

[115] J. Wallenius, P. Olsson, L. Malerba, and D. Terentyev. Simulation of thermal ageing and radiation damage in Fe–Cr. *Nuclear Instruments and Methods in Physics Research B*, 255:68–74, 2007.

[116] F. Bergner, A. Ulbricht, and C. Heintze. Estimation of the solubility limit of Cr in Fe at $300°C$ from small-angle neutron scattering in neutron-irradiated Fe–Cr alloys. *Scripta Materialia*, 61:1060–1063, 2009.

[117] A. Tissot. Kinetics of α' precipitation in an electron–irradiated Fe15Cr alloy. *Scripta Materialia*, 122:31–35, 2016.

[118] M.K. Miller, J.M. Hyde, and M.G. Hetherington. Spinodal decomposition in Fe-Cr alloys: Experimental study at the atomic level and comparison with computer models–I. Introduction and methodology. *Acta Metallurgica et Materialia*, 43:3385–3401, 1995.

[119] W. Xiong, M. Selleby, Q. Chen, J. Odqvist, and Y. Du. Phase Equilibria and Thermodynamic Properties in the Fe-Cr System. *Critical Reviews in Solid State and Materials Sciences*, 35:125–152, 2010.

[120] SS Brenner, MK Miller, and WA Soffa. Spinodal decomposition of iron-32 at.% chromium at $470°C$. *Scripta Metallurgica*, 16:831–836, 1982.

[121] S. Lu, Q.M. Hu, R. Yang, B. Johansson, and L. Vitos. First-principles determination of the α-α' interfacial energy in Fe-Cr alloys. *Physical Review B*, 82:1–7, 2010.

[122] W. Li, S. Lu, Q.M. Hu, H. Mao, B. Johansson, and L. Vitos. The effect of Al on the $475°C$ embrittlement of Fe–Cr alloys. *Computational Materials Science*, 74:101–106, 2013.

[123] S. Karthika, T.K. Radhakrishnan, and P. Kalaichelvi. A Review of Classical and Nonclassical Nucleation Theories. *Crystal Growth and Design*, 16:6663–6681, 2016.

[124] P. Jacobsson, Y. Bergström, and B. Aronsson. Kinetics and hardening mechanism of the $475°C$ embrittlement in 18Cr-2Mo ferritic steels. *Metallurgical Transactions A*, 6A:1577–1580, 1975.

[125] M. Bachhav, G.R. Odette, and E.A. Marquis. α' precipitation in neutron-irradiated Fe–Cr alloys. *Scripta Materialia*, 74:48–51, 2014.

[126] G.S. Was. *Fundamentals of Radiation Materials Science: Metals and Alloys*. Springer Berlin Heidelberg, 1^{st} edition, 2007.

[127] D.A. Terentyev, G. Bonny, and L. Malerba. Strengthening due to coherent Cr precipitates in Fe-Cr alloys: Atomistic simulations and theoretical models. *Acta Materialia*, 56:3229–3235, 2008.

[128] H. Kuwano. Mössbauer Effect Study on the Miscibility Gap of the Iron-Chromium Binary System. *Transactions of the Japan Institute of Metals*, 26:473–481, 1985.

[129] H.G. Read, H. Murakami, and K. Hono. Al partioning in MA 956, An ODS ferritic stainless steel. *Scripta Materialia*, 36:355–361, 1997.

[130] J.S. Lee, C.H. Jang, I.S. Kim, and A. Kimura. Embrittlement and hardening during thermal aging of high Cr oxide dispersion strengthened alloys. *Journal of Nuclear Materials*, 367-370:229–233, 2007.

[131] T.J. Nichol, A. Datta, and G. Aggen. Embrittlement of ferritic stainless steels. *Metallurgical Transactions A*, 11:573–585, 1980.

[132] P. Hedström, F. Huyan, J. Zhou, S. Wessman, M. Thuvander, and J. Odqvist. The $475°C$ embrittlement in Fe-20Cr and Fe-20Cr-X (X=Ni, Cu, Mn) alloys studied by mechanical testing and atom probe tomography. *Materials Science and Engineering A*, 574:123–129, 2013.

[133] K.L. Weng, H.R. Chen, and J.R. Yang. The low-temperature aging embrittlement in a 2205 duplex stainless steel. *Materials Science and Engineering A*, 379:119–132, 2004.

[134] W. Han, K. Yabuuchi, A. Kimura, S. Ukai, N. Oono, T. Kaito, T. Torimaru, and S. Hayashi. Effect of Cr/Al contents on the 475^{o}C age-hardening in oxide dispersion strengthened ferritic steels. *Nuclear Materials and Energy*, 0:1–6, 2016.

[135] D. Chen, A. Kimura, W. Han, and H. Je. Age-hardening susceptibility of high-Cr ODS ferritic steels and SUS430 ferritic steel. *Fusion Engineering and Design*, 98-99:1945–1949, 2015.

[136] J. Chao, C. Capdevila, M. Serrano, A. Garcia-Junceda, J.A. Jimenez, and M.K. Miller. Effect of α–α' phase separation on notch impact behavior of oxide dispersion strengthened (ODS) Fe20Cr5Al alloy. *Materials & Design*, 53:1037–1046, 2014.

[137] K. Turba, R.C. Hurst, and P. Hähner. Anisotropic mechanical properties of the MA956 ODS steel characterized by the small punch testing technique. *Journal of Nuclear Materials*, 428:76–81, 2012.

[138] A.L. Rouffié, J. Crépin, M. Sennour, B. Tanguy, A. Pineau, D. Hamon, P. Wident, S. Vincent, V. Garat, and B. Fournier. Effect of the thermal ageing on the tensile and impact properties of a 18%Cr ODS ferritic steel. *Journal of Nuclear Materials*, 445:37–42, 2014.

[139] J. Ejenstam, M. Thuvander, P. Olsson, F. Rave, and P. Szakalos. Microstructural stability of Fe-Cr-Al alloys at 450-550 $°C$. *Journal of Nuclear Materials*, 457:291–297, 2015.

[140] K. Suganuma and H. Kayano. Irradiation hardening of Fe-Cr alloys. *Journal of Nuclear Materials*, 118:234–241, 1983.

[141] D. Terentyev, G. Bonny, C. Domain, G. Monnet, and L. Malerba. Mechanisms of radiation strengthening in Fe-Cr alloys as revealed by atomistic studies. *Journal of Nuclear Materials*, 442:470–485, 2013.

[142] D. Terentyev, G. Bonny, and L. Malerba. Interplay of strengthening mechanisms in the interaction of a 1/2<111> screw dislocation with Cr precipitates in bcc Fe: An atomistic study. *Nuclear Instruments and Methods in Physics Research, Section B*, 267:3155–3158, 2009.

[143] D. Terentyev, P. Olsson, L. Malerba, and A.V. Barashev. Characterization of dislocation loops and chromium-rich precipitates in ferritic iron–chromium alloys as means of void swelling suppression. *Journal of Nuclear Materials*, 362:167–173, 2007.

[144] D. Terentyev, G. Bonny, C. Domain, and R.C. Pasianot. Interaction of a 1/2 <111> screw dislocation with Cr precipitates in bcc Fe studied by molecular dynamics. *Physical Review B*, 81:1–12, 2010.

[145] D. Terentyev, S.M. Hafez-Haghighat, and R. Schaublin. Strengthening due to Cr-rich precipitates in Fe–Cr alloys: Effect of temperature and precipitate composition. *Journal of Applied Physics*, 107:061806, 2010.

[146] J. Weertman and J Weertman. *Elementary Dislocation Theory*. Macmillan, 1^{st} edition, 1992.

[147] D. Hull and D.J. Bacon. *Introduction to Dislocations*. Elsevier, 5^{th} edition, 2001.

[148] F. Bergner, C. Pareige, M. Hernández-Mayoral, L. Malerba, and C. Heintze. Application of a three-feature dispersed-barrier hardening model to neutron-irradiated Fe-Cr model alloys. *Journal of Nuclear Materials*, 448:96–102, 2014.

[149] X. Xiao, D. Terentyev, L. Yu, A. Bakaev, Z. Jin, and H. Duan. Investigation of the thermo-mechanical behavior of neutron-irradiated Fe-Cr alloys by self-consistent plasticity theory. *Journal of Nuclear Materials*, 477:123–133, 2016.

[150] P. Olsson, J. Wallenius, C. Domain, K. Nordlund, and L. Malerba. Two-band modeling of α-prime phase formation in Fe-Cr. *Physical Review B*, 72:1–6, 2005.

[151] S. Oh, J.S. Lee, C. Jang, and A. Kimura. Irradiation hardening and embrittlement in high-Cr oxide dispersion strengthened steels. *Journal of Nuclear Materials*, 386-388:503–506, 2009.

[152] B.W. Baker, T.R. McNelley, and L.N. Brewer. Grain size and particle dispersion effects on the tensile behavior of friction stir welded MA956 oxide dispersion strengthened steel from low to elevated temperatures. *Materials Science and Engineering A*, 589:217–227, 2014.

[153] M.B. Toloczko, D.S. Gelles, F.A. Garner, R.J. Kurtz, and K. Abe. Irradiation creep and swelling from 400 to 600 $^{\circ}C$ of the oxide dispersion strengthened ferritic alloy MA957. *Journal of Nuclear Materials*, 329-333:352–355, 2004.

[154] P.H. Pumphrey and K.N. Akhurst. Aging kinetics of CF3 cast stainless steel in temperature range 300–400°C. *Materials Science and Technology*, 6:211–220, 1990.

[155] S. Bonnet, J. Bourgoin, J. Champredonde, D. Guttmann, and M. Guttmann. Relationship between evolution of mechanical properties of various cast duplex stainless steels and metallurgical and aging parameters: outline of current EDF programmes. *Materials Science and Technology*, 6:221–229, 1990.

[156] J.J. Heger. 885F embrittlement of the ferritic chromium-iron alloys. *Metal Progress*, 60:55–61, 1951.

[157] H.M. Chung, O.K. Chopra, and M. Prager. Properties of stainless steels in elevated temperature service. *Pressure Vessels Piping Div Publ PVP*, 132:17, 1987.

[158] H. Brandis, H. Kiesheyer, and G. Lennartz. Mechanical properties and precipitation characteristics of high-purity ferritic steels containing Cr 20-28 and Mo up to 5 per cent. *Arch Eisenhuttenwes*, 46:799–804, 1975.

[159] M. Courtnall and F.B. Pickering. The effect of alloying on 485C embrittlement. *Metal Science*, 10:273–276, 1976.

[160] F. Zhu, H. Wendt, and P. Haasen. Atom probe field ion microscopy of a Fe–Cr–Co permanent magnet alloy. *Scripta Metallurgica*, 16:1175–1180, 1982.

[161] H. Kuwano. Mossbauer Effect Study on the Mechanism of the Phase Decomposition in Iron-Chromium Alloys. *Transactions of the Japan institute of metals*, 26:482–491, 1985.

[162] W.S. Spear and D.H. Polonis. Interstitial precipitation in Fe-Cr-Al alloys. *Metallurgical and Materials Transactions A*, 25:1135–1146, 1994.

[163] S. Kobayashi and T. Takasugi. Mapping of 475°C embrittlement in ferritic Fe–Cr–Al alloys. *Scripta Materialia*, 63:1104–1107, 2010.

[164] I. Shuro, H.H. Kuo, T. Sasaki, K. Hono, Y. Todaka, and M. Umemoto. G-phase precipitation in austenitic stainless steel deformed by high pressure torsion. *Materials Science and Engineering A*, 552:194–198, 2012.

[165] H.U. Hong and S.W. Nam. The occurrence of grain boundary serration and its effect on the M23C6 carbide characteristics in an AISI 316 stainless steel. *Materials Science and Engineering A*, 332:255–261, 2002.

[166] G. Restrepo Garcés, J. Le Coze, J.L. Garin, and R.L. Mannheim. Sigma phase precipitation in two heat-resistant steels - Influence of carbides and microstructure. *Scripta Materialia*, 50:651–654, 2004.

[167] C. Capdevila, M.K. Miller, I. Toda, and J. Chao. Influence of the alpha–alpha prime phase separation on the tensile properties of Fe-base ODS PM 2000 alloy. *Materials Science and Engineering A*, 527:7931–7938, 2010.

[168] H.G Read and H. Murakami. Microstructural influences on the decomposition of an Al-containing ferritic stainless steel. 95:334–342, 1996.

[169] T.P. Battle and R.D. Pehlke. Equilibrium partition coefficients in iron-based alloys. *Metallurgical and Materials Transactions B*, 20:149–160, 1989.

[170] M.K. Miller, D.T. Hoelzer, E.A. Kenik, and K.F. Russell. Stability of ferritic MA/ODS alloys at high temperatures. *Intermetallics*, 13:387–392, 2005.

[171] M.K. Miller, E.A. Kenik, K.F. Russell, L. Heatherly, D.T. Hoelzer, and P.J. Maziasz. Atom probe tomography of nanoscale particles in ODS ferritic alloys. *Materials Science and Engineering: A*, 353:140–145, 2003.

[172] D. Isheim, M.S. Gagliano, M.E. Fine, and D.N. Seidman. Interfacial segregation at Cu-rich precipitates in a high-strength low-carbon steel studied on a sub-nanometer scale. *Acta Materialia*, 54:841–849, 2006.

[173] D.S. Gelles. Effects of Radiation on Materials: 17th International Symposium. *ASTM committee E-10 on nuclear technology and applications*, pages 1–1164, 1996.

[174] P.E. L'vov and V.V. Svetukhin. Influence of composition fluctuations on the formation and growth of clusters in alloys based on the iron-chromium system. *Physics of the Solid State*, 54:2285–2290, 2012.

[175] J. Ribis, M.A. Thual, T. Guilbert, Y. de Carlan, and A. Legris. Relaxation path of metastable nanoclusters in Oxide Dispersion Strengthened materials. *Journal of Nuclear Materials*, 484:183–192, 2016.

[176] C. Fu, M. Krčmar, G. Painter, and X.Q. Chen. Vacancy Mechanism of High Oxygen Solubility and Nucleation of Stable Oxygen-Enriched Clusters in Fe. *Physical Review Letters*, 99:1–4, 2007.

[177] F. Matteucci, G. Cruciani, M. Dondi, G. Baldi, and A. Barzanti. Crystal structural and optical properties of Cr-doped Y2Ti2O7 and Y2Sn2O7 pyrochlores. *Acta Materialia*, 55:2229–2238, 2007.

[178] Z. Oksiuta, M. Lewandowska, and K.J. Kurzydłowski. Mechanical properties and thermal stability of nanostructured ODS RAF steels. *Mechanics of Materials*, 67:15–24, 2013.

[179] E.M. Grieveson. *Irradiation Effects on the Deformation of Oxide Dispersion Strengthened Steels*. DPhil thesis, University of Oxford, 2015.

[180] P. He, M. Klimenkov, R. Lindau, and A. Möslang. Characterization of precipitates in nano structured 14% Cr ODS alloys for fusion application. *Journal of Nuclear Materials*, 428:131–138, 2012.

[181] H.S Cho, A. Kimura, S. Ukai, and M. Fujiwara. Corrosion properties of oxide dispersion strengthened steels in super-critical water environment. *Journal of Nuclear Materials*, 329-333:387–391, 2004.

[182] P. Krautwasser, A. Czyrska-Filemonowicz, M. Widera, and F. Carsughi. Thermal stability of dispersoids in ferritic oxide-dispersion-strengthened alloys. *Materials Science and Engineering: A*, 177:199–208, 1994.

[183] S.Y. Zhong, J. Ribis, V. Klosek, Y. De Carlan, N. Lochet, V. Ji, and M.H. Mathon. Study of the thermal stability of nanoparticle distributions in an oxide dispersion strengthened (ODS) ferritic alloys. *Journal of Nuclear Materials*, 428:154–159, 2012.

[184] M. Tikhonchev, V. Svetukhin, A. Kadochkin, and E. Gaganidze. MD simulation of atomic displacement cascades in Fe-10 at.%Cr binary alloy. *Journal of Nuclear Materials*, 395:50–57, 2009.

[185] P. Vladimirov and A. Möslang. Comparison of material irradiation conditions for fusion, spallation, stripping and fission neutron sources. *Journal of Nuclear Materials*, 329-333:233–237, 2004.

[186] G.R. Odette, T. Yamamoto, B. Sams, D. Klingesmith, N. Cunningham, G. Waches, J.I. Cole, and P.E. Murrey. Summary of the USCB Advanced Test Reactor National Scientific. Experimental report, University of California Santa Barbara, 2010.

[187] R.E. Stoller and L.R. Greenwood. Subcascade formation in displacement cascade simulations: implications for fusion reactor materials. *Journal of Nuclear Materials*, 271-272:57–62, 1999.

[188] C.A. English. Recoil effects in radiation damage. *Radiation Effects and Defects in Solids*, 113:15–28, 1990.

[189] S.J. Zinkle. Overview of the US fusion materials sciences program. Research programme report, Oak Ridge National Laboratory, 2005.

[190] M.W. Guinan and J.H. Kinney. Molecular dynamic calculations of energetic displacement cascades. *Journal of Nuclear Materials*, 104:1319–1323, 1981.

[191] M.J. Norgett, M.T. Robinson, and I.M. Torrens. A proposed method of calculating displacement dose rates. *Nuclear Engineering and Design*, 33:50–54, 1975.

[192] J.A. Brinkman. Production of Atomic Displacements by High-Energy Particles. *American Journal of Physics*, 24:246–267, 1956.

[193] L.R. Greenwood. Neutron interactions and atomic recoil spectra. *Journal of Nuclear Materials*, 216:29–44, 1994.

[194] M.R. Gilbert, S.L. Dudarev, S. Zheng, L.W. Packer, and J.Ch. Sublet. An integrated model for materials in a fusion power plant: transmutation, gas production, and helium embrittlement under neutron irradiation. *Nuclear Fusion*, 52:1–12, 2012.

[195] C.D. Hardie, C.A. Williams, S. Xu, and S.G. Roberts. Effects of Irradiation Temperature and Dose Rate on the Mechanical Properties of Self-Ion Implanted Fe and Fe-Cr Alloys. *Journal of Nuclear Materials*, 439:33–40, 2013.

[196] P. Spätig, R. Schäublin, N. Baluc, J. Kohlbrecher, and M. Victoria. SANS investigation of proton-irradiated EUROFER97. *Journal of Nuclear Materials*, 329-333:289–293, 2004.

[197] L.L. Hsiung, M.J. Fluss, S.J. Tumey, B.W. Choi, Y. Serruys, F. Willaime, and A. Kimura. Formation mechanism and the role of nanoparticles in Fe-Cr ODS steels developed for radiation tolerance. *Physical Review B*, 82:1–13, 2010.

[198] J. Chen, P. Jung, W. Hoffelner, and H. Ullmaier. Dislocation loops and bubbles in oxide dispersion strengthened ferritic steel after helium implantation under stress. *Acta Materialia*, 56:250–258, 2008.

[199] P.D. Edmondson, C.M. Parish, Y. Zhang, A. Hallén, and M.K. Miller. Helium entrapment in a nanostructured ferritic alloy. *Scripta Materialia*, 65:731–734, 2011.

[200] N. Yoshida, H. Iwakiri, K. Tokunaga, and T. Baba. Impact of low energy helium irradiation on plasma facing metals. *Journal of Nuclear Materials*, 337-339:946–950, 2005.

[201] A.E. Pontau, M.I. Baskes, K.L. Wilson, L.G. Haggmark, J. Bohdansky, B.M.U. Scherzer, and J. Roth. Deuterium retention in helium-damaged stainless steel: Detrapping energy. *Journal of Nuclear Materials*, 111-112:651–653, 1982.

[202] G Dearnaley. *Ion Implantation*. North-Holland publishing company, 8^{th} edition, 1973.

[203] G.H. Kinchin and R.S. Pease. the Displacement of Atoms in Solids By Radiation. *Reports on Progress in Physics*, 18:1–51, 1955.

[204] J.F. Ziegler, M.D. Ziegler, and J.P. Biersack. SRIM – The stopping and range of ions in matter (2010). *Nuclear Instruments and Methods in Physics Research Section B: Beam Interactions with Materials and Atoms*, 268:1818–1823, 2010.

[205] Kay Online and Laby. Tables of Physical and Chemical Constants 16th edition, 1995.

[206] A.M. Rutherford and D.M. Duffy. The effect of electron–ion interactions on radiation damage simulations. *Journal of Physics: Condensed Matter*, 19:1–11, 2007.

[207] K. Ehrlich and A. Möslang. IFMIF – An international fusion materials irradiation facility. *Nuclear Instruments and Methods in Physics Research Section B: Beam Interactions with Materials and Atoms*, 139:72–81, 1998.

[208] P.D. Edmondson, S.A. Briggs, Y. Yamamoto, R.H. Howard, K. Sridharan, K.A. Terrani, and K.G. Field. Irradiation-Enhanced α' Precipitation in Model FeCrAl Alloys. *Scripta Materialia*, 116:112–116, 2016.

[209] D.S. Gelles, S. Ohnuki, H. Takahashi, H. Matsui, and Y. Kohno. Electron irradiation experiments in support of fusion materials development. *Journal of Nuclear Materials*, 191-194:1336–1341, 1992.

[210] G. Dearnaley and N.E.W. Hartley. Ion implantation into metals and cabrides. *Thin Solid Films*, 54:215–232, 1978.

[211] C. Abromeit. Aspects of simulation of neutron damage by ion irradiation. *Journal of Nuclear Materials*, 216:78–96, 1994.

[212] C.D. Hardie. *Micro-Mechanics of Irradiated Fe-Cr Alloys for Fusion Reactors*. DPhil thesis, University of Oxford, 2014.

[213] N.H. Packan, K. Farrell, and J.O. Stiegler. Correlation of neutron and heavy-ion damage: I. The influence of dose rate and injected helium on swelling in pure nickel. *Journal of Nuclear Materials*, 78:143–155, 1978.

[214] T. Yamamoto, G.R. Odette, P. Miao, D.T. Hoelzer, J. Bentley, N. Hashimoto, H. Tanigawa, and R.J. Kurtz. The transport and fate of helium in nanostructured ferritic alloys at fusion relevant He/dpa ratios and dpa rates. *Journal of Nuclear Materials*, 367-370:399–410, 2007.

[215] A.D. Marwick. The primary recoil spectrum in the simulation of fast-reactor radiation damage by charged-particle bombardment. *Journal of Nuclear Materials*, 55:259–266, 1975.

[216] H. Wiedersich. Effects of the primary recoil spectrum on microstructural evolution. *Journal of Nuclear Materials*, 179-181:70–75, 1991.

[217] M. Kiritani. Point defect processes in the defect structure development from cascade damage. *Materials Science Forum*, 15-18:1023–1046, 1987.

[218] C.A. English and M.L. Jenkins. Insight into Cascade Processes Arising from Studies of Cascade Collapse. *Materials Science Forum*, 15-18:1003–1022, 1987.

[219] R.E. Stoller. Point defect survival and clustering fractions obtained from molecular dynamics simulations of high energy cascades. *Journal of Nuclear Materials*, 233-237:999–1003, 1996.

[220] OECD (Organisation for Economic Co-operation and Development) Nuclear energy agency. State-of-the-art report on structural materials modelling. Review, 2017.

[221] D.A. Terentyev, L. Malerba, R. Chakarova, K. Nordlund, P. Olsson, M. Rieth, and J. Wallenius. Displacement cascades in Fe–Cr: A molecular dynamics study. *Journal of Nuclear Materials*, 349:119–132, 2006.

[222] J.H. Shim, H.J. Lee, and B.D. Wirth. Molecular dynamics simulation of primary irradiation defect formation in Fe-10%Cr alloy. *Journal of Nuclear Materials*, 351:56–64, 2006.

[223] C. Björkas, K. Nordlund, L. Malerba, D. Terentyev, and P. Olsson. Simulation of displacement cascades in Fe90Cr10 using a two band model potential. *Journal of Nuclear Materials*, 372:312–317, 2008.

[224] R.S. Averback, R. Benedek, and K.L. Merkle. Correlations between ion and neutron irradiations: Defect production and stage I recovery. *Journal of Nuclear Materials*, 75:162–166, 1978.

[225] R.S. Averback, R. Benedek, and K.L. Merkle. Ion-irradiation studies of the damage function of copper and silver. *Physical Review B*, 18:4156–4171, 1978.

[226] D.J. Bacon and T. Diaz de la Rubia. Molecular dynamics computer simulations of displacement cascades in metals. *Journal of Nuclear Materials*, 216:275–290, 1994.

[227] T. Muroga. Pka spectral effects on subcascade structures and free defect survival ratio as estimated by cascade- annealing computer simulation. 113:119–134, 1990.

[228] F. Gao, D.J. Bacon, Y.N. Osetsky, P.E.J. Flewitt, and T.A. Lewis. Properties and evolution of sessile interstitial clusters produced by displacement cascades in alpha-iron. *Journal of Nuclear Materials*, 276:213–220, 2000.

[229] W.J. Phythian, R.E. Stoller, A.J.E. Foreman, A.F. Calder, and D.J. Bacon. A comparison of displacement cascades in copper and iron by molecular dynamics and its application to microstructural evolution. *Journal of Nuclear Materials*, 223:245–261, 1995.

[230] L. Malerba. Molecular dynamics simulation of displacement cascades in α-Fe: A critical review. *Journal of Nuclear Materials*, 351:28–38, 2006.

[231] F.A. Garner and W.G. Wolfer. Factors which determine the swelling behavior of austenitic stainless steels. *Journal of Nuclear Materials*, 122:201–206, 1984.

[232] J. Nord, K. Nordlund, and J. Keinonen. Amorphization mechanism and defect structures in ion-beam-amorphized Si, Ge, and GaAs. *Physical Review B*, 65:1–14, 2002.

[233] R.A. Johnson. Interstitials and vacancies in iron. *Physical Review*, 134:A1329–A1336, 1964.

[234] T. Okita, T. Sato, N. Sekimura, F. A. Garner, and L.R. Greenwood. The primary origin of dose rate effects on microstructural evolution of austenitic alloys during neutron irradiation. *Journal of Nuclear Materials*, 307-311:322–326, 2002.

[235] L.K. Mansur. Correlation of neutron and heavy-ion damage. II. The predicted temperature shift if swelling with changes in radiation dose rate. *Journal of Nuclear Materials*, 78:156–160, 1978.

[236] L.K. Mansur. Void swelling in metals and alloys under irradiation: An assessment of the theory. *Nuclear Technology*, 40:5–34, 1978.

[237] D.A. McClintock, M.A. Sokolov, D.T. Hoelzer, and R.K. Nanstad. Mechanical properties of irradiated ODS-EUROFER and nanocluster strengthened 14YWT. *Journal of Nuclear Materials*, 392:353–359, 2009.

[238] D.J. Bacon and Y.N. Osetsky. Modelling dislocation-obstacle interactions in metals exposed to an irradiation environment. *Materials Science and Engineering A*, 400-401:353–361, 2005.

[239] S.I. Porollo and A.M. Dvoriashin. The microstructure and tensile properties of Fe–Cr alloys after neutron irradiation at $400^{\circ}C$ to 5.5–7.1 dpa. *Journal of Nuclear Materials*, 256:1–7, 1998.

[240] Y.V. Konobeev, A.M. Dvoriashin, S.I. Porollo, and F.A. Garner. Swelling and microstructure of pure Fe and Fe–Cr alloys after neutron irradiation to ∼26dpa at $400^{\circ}C$. *Journal of Nuclear Materials*, 355:124–130, 2006.

[241] C.M. Parish, K.G. Field, A.G. Certain, and J.P. Wharry. Application of STEM characterization for investigating radiation effects in BCC Fe-based alloys. *Journal of Materials Research*, 30:1275–1289, 2015.

[242] H.S. Cho, R. Kasada, and A. Kimura. Effects of neutron irradiation on the tensile properties of high-Cr oxide dispersion strengthened ferritic steels. *Journal of Nuclear Materials*, 367-370:239–243, 2007.

[243] G.J. Dienes and A.C. Damask. Radiation enhanced diffusion in solids. *Journal of Applied Physics*, 29:1713–1721, 1958.

[244] A.J. Ardell and P. Bellon. Radiation-induced solute segregation in metallic alloys. *Current Opinion in Solid State and Materials Science*, 20:115–139, 2016.

[245] J.P. Wharry and G.S. Was. A systematic study of radiation-induced segregation in ferritic-martensitic alloys. *Journal of Nuclear Materials*, 442:7–16, 2013.

[246] P.R. Okamoto, S.D. Harkness, and J.J. Laidler. Solute segregation to voids during electron irradiation. *Transactions of the American Nuclear Society*, 16:70, 1973.

[247] A.J. Ardell. Radiation-induced solute segregation in alloys. *Materials Issues for Generation IV Systems*, 0:285–310, 2008.

[248] J.T. Busby, G.S. Was, and E.A. Kenik. Isolating the effect of radiation-induced segregation in irradiation-assisted stress corrosion cracking of austenitic stainless steels. *Journal of Nuclear Materials*, 302:20–40, 2002.

[249] V. Kuksenko, C. Pareige, and P. Pareige. Cr precipitation in neutron irradiated industrial purity Fe–Cr model alloys. *Journal of Nuclear Materials*, 432:160–165, 2013.

[250] Y. Nishiyama, K. Onizawa, M. Suzuki, J.W. Anderegg, Y. Nagai, T. Toyama, M. Hasegawa, and J. Kameda. Effects of neutron-irradiation-induced intergranular phosphorus segregation and hardening on embrittlement in reactor pressure vessel steels. *Acta Materialia*, 56:4510–4521, 2008.

[251] S. Watanabe, N. Sakaguchi, K. Kurome, M. Nakamura, and H. Takahashi. On the mechanism of radiation-induced segregation. *Journal of Nuclear Materials*, 240:251–253, 1997.

[252] R.E Stoller, A.S. Kumar, and D.S. Gelles. Effects of radiation on materials: 15th international symposium. ASTM, 1992.

[253] S. Watanabe, H. Kinoshita, N. Sakaguchi, and H. Takahashi. Concentration dependence of radiation-induced segregation in Fe-Cr-Ni alloy. *Journal of Nuclear Materials*, 226:330–331, 1995.

[254] C.C. Wei, A. Aitkaliyeva, M.S. Martin, D. Chen, and L. Shao. Microstructural changes of T-91 alloy irradiated by Fe self ions to ultrahigh displacement ratios. *Nuclear Instruments and Methods in Physics Research, Section B*, 307:181–184, 2013.

[255] Z. Lu, R.G. Faulkner, G. Was, and B.D. Wirth. Irradiation-induced grain boundary chromium microchemistry in high alloy ferritic steels. *Scripta Materialia*, 58:878–881, 2008.

[256] J.P. Wharry, Z. Jiao, and G.S. Was. Application of the inverse Kirkendall model of radiation-induced segregation to ferritic–martensitic alloys. *Journal of Nuclear Materials*, 425:117–124, 2012.

[257] K.L. Wong, H.J. Lee, J.H. Shim, B. Sadigh, and B.D. Wirth. Multiscale modeling of point defect interactions in Fe-Cr alloys. *Journal of Nuclear Materials*, 386-388:227–230, 2009.

[258] G.S. Was, J.P. Wharry, B. Frisbie, B.D. Wirth, D. Morgan, J.D. Tucker, and T.R. Allen. Assessment of radiation-induced segregation mechanisms in austenitic and ferritic-martensitic alloys. *Journal of Nuclear Materials*, 411:41–50, 2011.

[259] Janelle P. Wharry and Gary S. Was. The mechanism of radiation-induced segregation in ferritic–martensitic alloys. *Acta Materialia*, 65:42–55, 2014.

[260] O. Senninger, F. Soisson, E. Martínez, M. Nastar, C.C. Fu, and Y. Bréchet. Modeling radiation induced segregation in iron-chromium alloys. *Acta Materialia*, 103:1–11, 2016.

[261] F. Soisson and T. Jourdan. Radiation-accelerated precipitation in Fe-Cr alloys. *Acta Materialia*, 103:870–881, 2016.

[262] K.G. Field, B.D. Miller, H.J.M Chichester, K. Sridharan, and T.R. Allen. Relationship between lath boundary structure and radiation induced segregation in a neutron irradiated 9 wt.% Cr model ferritic-martensitic steel. *Journal of Nuclear Materials*, 445:143–148, 2014.

[263] K.G. Field, Y. Yang, T.R. Allen, and J.T Busby. Defect sink characteristics of specific grain boundary types in 304 stainless steels under high dose neutron environments. *Acta Materialia*, 89:438–449, 2015.

[264] M. Bachhav, G.R. Odette, and E.A. Marquis. Microstructural changes in a neutron-irradiated Fe-6 at.%Cr alloy. *Journal of Nuclear Materials*, 454:381–386, 2014.

[265] K.G. Field, L.M. Barnard, C.M. Parish, J.T. Busby, D. Morgan, and T.R. Allen. Dependence on grain boundary structure of radiation induced segregation in a 9wt.% Cr model ferritic-martensitic steel. *Journal of Nuclear Materials*, 435:172–180, 2013.

[266] J.H. Kim, T.S. Byun, D.T. Hoelzer, S.W. Kim, and B.H. Lee. Temperature dependence of strengthening mechanisms in the nanostructured ferritic alloy 14YWT: Part I-Mechanical and microstructural observations. *Materials Science and Engineering A*, 559:101–110, 2013.

[267] H.W. King. Quantitative size-factors for metallic solid solutions. *Journal of Materials Science*, 1:79–90, 1966.

[268] Z. Jiao, V. Shankar, and G.S. Was. Phase stability in proton and heavy ion irradiated ferritic-martensitic alloys. *Journal of Nuclear Materials*, 419:52–62, 2011.

[269] J. He, F. Wan, K. Sridharan, T.R. Allen, A. Certain, and Y.Q. Wu. Response of 9Cr-ODS steel to proton irradiation at $400^{\circ}C$. *Journal of Nuclear Materials*, 452:87–94, 2014.

[270] C.A. Williams, J.M. Hyde, G.D.W. Smith, and E.A. Marquis. Effects of heavy-ion irradiation on solute segregation to dislocations in oxide-dispersion-strengthened Eurofer 97 steel. *Journal of Nuclear Materials*, 412:100–105, 2011.

[271] V. Kuksenko, C. Pareige, C. Genevois, F. Cuvilly, M. Roussel, and P. Pareige. Effect of neutron-irradiation on the microstructure of a Fe–12at.%Cr alloy. *Journal of Nuclear Materials*, 415:61–66, 2011.

[272] O. Tissot, C. Pareige, E. Meslin, B. Décamps, and J. Henry. Influence of injected interstitials on α' precipitation in Fe–Cr alloys under self-ion irradiation. *Materials Research Letters*, 3831:1–7, 2017.

[273] R.S. Nelson, J.A. Hudson, and D.J. Mazey. The stability of precipitates in an irradiation environment. *Journal of Nuclear Materials*, 44:318–330, 1972.

[274] R.A. Enrique and P. Bellon. Compositional patterning in immiscible alloys driven by irradiation. *Physical Review B*, 63:13–15, 2001.

[275] M. Nastasi and J.W. Mayer. Thermodynamics and kinetics of phase transformations induced by ion irradiation. *Materials Science Reports*, 6:1–51, 1991.

[276] H. Kuwano and Y. Hamaguchi. Mossbauer study of iron-chromium alloys irradiated by energetic protons. *Journal of Nuclear Materials*, 155-157:1071–1074, 1988.

[277] E Wakai, A Hishinuma, and K Usami. Damage structures and mechanical properties of high-purity Fe-9Cr alloys irradiated by neutrons. *Materials Transactions, JIM*, 41:1180–1183, 2000.

[278] H. Lukas, S.G. Fries, and B. Sundman. *Computational Thermodynamics: the Calphad Method*. Cambridge University Press, 1^{st} edition, 2007.

[279] P. Miao, G.R. Odette, T. Yamamoto, M. Alinger, D. Hoelzer, and D. Gragg. Effects of consolidation temperature, strength and microstructure on fracture toughness of nanostructured ferritic alloys. *Journal of Nuclear Materials*, 367-370:208–212, 2007.

[280] S. Pellegrino, P. Trocellier, S. Miro, Y. Serruys, É. Bordas, H. Martin, N. Chaâbane, S. Vaubaillon, J.P. Gallien, and L. Beck. The JANNuS Saclay facility: A new platform for materials irradiation, implantation and ion beam analysis. *Nuclear Instruments and Methods in Physics Research Section B*, 273:213–217, 2012.

[281] JANNuS irradiation base plate photo - Courtesy of L. Hewitt, University of Oxford, 2014.

[282] R.E. Stoller. Evaluation of neutron energy spectrum effects and RPV thru-wall attenuation based on molecular dynamics cascade simulations. *Nuclear Engineering and Design*, 195:129–136, 2000.

[283] R.E. Stoller, M.B. Toloczko, G.S. Was, A.G. Certain, S. Dwaraknath, and F.A. Garner. On the use of SRIM for computing radiation damage exposure. *Nuclear Instruments and Methods in Physics Research, Section B*, 310:75–80, 2013.

[284] M.T. Robinson. Basic physics of radiation damage production. *Journal of Nuclear Materials*, 216:1–28, 1994.

[285] J.W. Nielsen. As-Run Physics Analysis for the UCSB–1 Experiment in the Advanced Test Reactor. Summary of neutron irradiation experiment, Idaho National Laboratory, 2015.

[286] J.F Briesmeister. *MCNP–A general Monte Carlo code for neutron and photon transport*. Los Alamos National Laboratory, 1986.

[287] M.K. Miller. *Atom probe tomography: analysis at the atomic level*. Springer-US, 2000.

[288] G.L. Kellogg and T.T. Tsong. Pulsed laser-induced atom-probe mass-spectroscopy. *Ultramicroscopy*, 5:259–260, 1980.

[289] B. Gault, M.P. Moody, J.M. Cairney, and S.P. Ringer. *Atom Probe Microscopy*. Springer, 1^{st} edition, 2012.

[290] M.K. Miller and R.G. Forbes. Atom probe tomography. *Materials Characterization*, 60:461–469, 2009.

[291] H. Keller, G. Klingelhofer, and E. Kankeleit. A position sensitive microchannelplate detector using a delay line readout anode. *Nuclear Inst. and Methods in Physics Research, A*, 258:221–224, 1987.

[292] G. Da Costa, F. Vurpillot, A. Bostel, M. Bouet, and B. Deconihout. Design of a Delay-Line Position-Sensitive Detector with Improved Performance. *Review of Scientific Instruments*, 76:1–8, 2005.

[293] M.K. Miller and R.G. Forbes. *Atom-probe tomography: The local electrode atom probe*. Springer, 1^{st} edition, 2014.

[294] R. Gomer and L.W. Swanson. Theory of Field Desorption. *The Journal of Chemical Physics*, 38:1613–1629, 1963.

[295] E.W. Müller. Field desorption. *Physical Review*, 102:618–624, 1956.

[296] Robert Gomer. Field Desorption. *The Journal of Chemical Physics*, 31:341–345, 1959.

[297] D. Santhanagopalan, D.K. Schreiber, D.E. Perea, R.L. Martens, Y. Janssen, P. Khalifah, and Y.S. Meng. Effects of laser energy and wavelength on the analysis of LiFePO4 using laser assisted atom probe tomography. *Ultramicroscopy*, 148:57–66, 2015.

[298] A. R. Sakulich and V.C. Li. Microscopic Characterization of Autogenous Healing Products in Engineered Cementitious Composites (ECC). 33^{rd} *International Conference on Cement Microscopy, USA*, 13:1–10, 2011.

[299] J.M. Hyde, E.A. Marquis, K.B. Wilford, and T.J. Williams. A sensitivity analysis of the maximum separation method for the characterisation of solute clusters. *Ultramicroscopy*, 111:440–7, 2011.

[300] J.M. Hyde and C.A. English. An Analysis of the Structure of Irradiation Induced Cu-Enriched Clusters in Low and High Nickel Welds. *Materials Research Society Symposium Proceedings*, 650:1–12, 2001.

[301] L.T. Stephenson, M.P. Moody, P.V. Liddicoat, and S.P. Ringer. New techniques for the analysis of fine-scaled clustering phenomena within atom probe tomography (APT) data. *Microscopy and microanalysis*, 13:448–463, 2007.

[302] M.P. Moody, L.T. Stephenson, A.V. Ceguerra, and S.P. Ringer. Quantitative binomial distribution analyses of nanoscale like-solute atom clustering and segregation in atom probe tomography data. *Microscopy Research and Technique*, 71:542–550, 2008.

[303] C.A. Williams, D. Haley, E.A. Marquis, G.D.W Smith, and M.P. Moody. Defining clusters in APT reconstructions of ODS steels. *Ultramicroscopy*, 132:271–278, 2013.

[304] P.R. Kolli and D.N. Seidman. Comparison of Compositional and Morphological Atom-Probe Tomography Analyses for a Multicomponent Fe-Cu-Steel. *Microscopy and Microanalysis*, 13:272–284, 2007.

[305] C. Williams. *Atomic Scale Characterisation of Oxide Dispersion Strengthened Steels for Fusion Applications*. DPhil thesis, University of Oxford, 2011.

[306] A.J. London. *Irradiation Damage of Oxide Dispersion Strengthened Steels*. DPhil thesis, University of Oxford, 2015.

[307] C. Capdevila, M.K. Miller, and J. Chao. Phase separation kinetics in a Fe–Cr–Al alloy. *Acta Materialia*, 60:4673–4684, 2012.

[308] J.M. Hyde, G. DaCosta, C. Hatzoglou, H. Weekes, B. Radiguet, P.D. Styman, F. Vurpillot, C. Pareige, A. Etienne, G. Bonny, N. Castin, L. Malerba, and P. Pareige. Analysis of Radiation Damage in Light Water Reactors: Comparison of Cluster Analysis Methods for the Analysis of Atom Probe Data. *Microscopy and Microanalysis*, 23:366–375, 2017.

[309] F. Vurpillot, A. Bostel, and D. Blavette. Trajectory overlaps and local magnification in three-dimensional atom probe. *Applied Physics Letters*, 76:3127–3129, 2000.

[310] D.J. Larson, T.J. Prosa, R.M. Ulfig, B.P. Geiser, and Th.F. Kelly. *Local Electrode Atom Probe Tomography*. Springer, 1^{st} edition, 2013.

[311] C. Oberdorfer and G. Schmitz. On the Field Evaporation Behavior of Dielectric Materials in Three-Dimensional Atom Probe: A Numeric Simulation. *Microscopy and Microanalysis*, 17:15–25, 2010.

[312] D. Blavette, F. Vurpillot, P. Pareige, and A. Menand. A model accounting for spatial overlaps in 3D atom-probe microscopy. *Ultramicroscopy*, 89:145–53, 2001.

[313] C.A. Williams, G.D.W Smith, and E.A. Marquis. Quantifying the composition of yttrium and oxygen rich nanoparticles in oxide dispersion strengthened steels. *Ultramicroscopy*, 125:10–17, 2013.

[314] C.A. Williams, P. Unifantowicz, Z. Oksiuta, N. Baluc, G.D.W. Smith, and E.A. Marquis. Atom probe tomography analysis of Ti-Y-O clustering during processing of nanoscale oxide particles in 14%Cr ODS ferritic steels. *Materials Research Society Symposium Proceedings*, 1298:15–20, 2011.

[315] Y.T. Kwak, C.M.and Kim, C.G. Park, and J.B. Seol. Understanding of capping effects on the tip shape evolution and on the atom probe data of bulk $LaAlO_3$ using transmission electron microscopy. *Microscopy and Microanalysis*, 23:1–7, 2017.

[316] G. Sha, A. Cerezo, and G.D.W Smith. Field evaporation behavior during irradiation with picosecond laser pulses. *Applied Physics Letters*, 92:1–3, 2008.

[317] B. Gault, M.P. Moody, F. De Geuser, G. Tsafnat, A. La Fontaine, L.T. Stephenson, D. Haley, and S.P. Ringer. Advances in the calibration of atom probe tomographic reconstruction. *Journal of Applied Physics*, 105:1–9, 2009.

[318] S. Koelling, N. Innocenti, A. Schulze, M. Gilbert, A.K. Kambham, and W. Vandervorst. In-situ observation of non-hemispherical tip shape formation during laser-assisted atom probe tomography. *Journal of Applied Physics*, 109:1–6, 2011.

[319] D. Tabor. The hardness of solids. *Review of physics in technology*, 1:145, 1970.

[320] D. Tabor. *The Hardness of Metals*. Oxford university press, 1^{st} edition, 1951.

[321] S. Ukai, S. Ohtsuka, T. Kaito, H. Sakasegawa, N. Chikata, S. Hayashi, and S. Ohnuki. High-temperature strength characterization of advanced 9Cr-ODS ferritic steels. *Materials Science and Engineering A*, 510-511:115–120, 2009.

[322] S. Ukai. Microstructure and High-Temperature Strength of 9CrODS Ferritic Steel. In *Metal, Ceramic and Polymeric Composites for Various Uses*. InTech, 1^{st} edition, 2011.

[323] L Yao, J.M. Cairney, C. Zhu, and S.P. Ringer. Optimisation of specimen temperature and pulse fraction in atom probe microscopy experiments on a microalloyed steel. *Ultramicroscopy*, 111:648–51, 2011.

[324] F. Danoix, M.K. Miller, and A. Bigot. Analysis conditions of an industrial Al-Mg-Si alloy by conventional and 3D atom probes. *Ultramicroscopy*, 89:177–188, 2001.

[325] R. Hu. *Irradiation Effects on Fe Cr Alloys.* DPhil thesis, University of Oxford, 2012.

[326] Y. Yamaguchi, J. Takahashi, and K. Kawakami. The study of quantitativeness in atom probe analysis of alloying elements in steel. *Ultramicroscopy*, 109:541–544, 2009.

[327] M.K. Miller and R. Jayaram. Some factors affecting analysis in the atom probe. *Surface Science*, 266:458–462, 1992.

[328] F. Vurpillot, A. Bostel, A. Menand, and D. Blavette. Trajectories of field emitted ions in 3D atom-probe. *The European Physical Journal Applied Physics*, 6:217–221, 1999.

[329] F. Vurpillot, A. Bostel, and D. Blavette. A new approach to the interpretation of atom probe field-ion microscopy images. *Ultramicroscopy*, 89:137–144, 2001.

[330] P.J. Naish and S. Hartwell. Exponentially Modified Gaussian functions-A good model for chromatographic peaks in isocratic HPLC? *Chromatographia*, 26:285–296, 1988.

[331] T.T. Tsong. Field ion image formation. *Surface Science*, 70:211–233, 1978.

[332] G. Sha and S.P. Ringer. Effect of laser pulsing on the composition measurement of an Al-Mg-Si-Cu alloy using three-dimensional atom probe. *Ultramicroscopy*, 109:580–584, 2009.

[333] P. Bas, A. Bostel, B. Deconihout, and D. Blavette. A general protocol for the reconstruction of 3D atom probe data. *Applied Surface Science*, 87-88:298–304, 1995.

[334] V. Migunov, A. London, M. Farle, and R.E. Dunin-Borkowski. Model-independent measurement of the charge density distribution along an Fe atom probe needle using off-axis electron holography without mean inner potential effects. *Journal of Applied Physics*, 117:1–8, 2015.

[335] B. Gault, M.P. Moody, F. De Geuser, D. Haley, L.T. Stephenson, and S.P. Ringer. Origin of the spatial resolution in atom probe microscopy. *Applied Physics Letters*, 95:10–13, 2009.

[336] B. Gault, M.P. Moody, F. De Geuser, A. La Fontaine, L.T. Stephenson, D. Haley, and S.P. Ringer. Spatial Resolution in Atom Probe Tomography. *Microscopy and Microanalysis*, 16:99–110, 2010.

[337] B. Gault, M. Muller, A. La Fontaine, M.P. Moody, A. Shariq, A. Cerezo, S.P. Ringer, and G.D.W Smith. Influence of surface migration on the spatial resolution of pulsed laser atom probe tomography. *Journal of Applied Physics*, 108:1–6, 2010.

[338] J. Neugebauer and M. Scheffler. Theory of adsorption and desorption in high electric fields. *Surface Science*, 287-288:572–576, 1993.

[339] C. G. Sánchez, A. Y. Lozovoi, and A. Alavi. Field-evaporation from first-principles. *Molecular Physics*, 102:1045–1055, 2004.

[340] L. Yao, B. Gault, J.M. Cairney, and S.P. Ringer. On the multiplicity of field evaporation events in atom probe: A new dimension to the analysis of mass spectra. *Philosophical Magazine Letters*, 90:121–129, 2010.

[341] D.W. Bassett. The thermal stability and rearrangment of field-evaporated tungsten surfaces. *Proceedings of the royal society*, 286:191–203, 1965.

[342] B. Gault, F. Danoix, K. Hoummada, D. Mangelinck, and H. Leitner. Impact of directional walk on atom probe microanalysis. *Ultramicroscopy*, 113:182–191, 2012.

[343] G. Ehrlich and K. Stolt. Surface Diffusion. *Annual review of physical chemistry*, 31:603–637, 1980.

[344] Private communication: Dr C. Burrows and Dr M Gorley, former DPhil students at the department of Materials , University of Oxford: private communication 2014.

[345] O. Kubaschewski. *Iron-binary phase diagrams*. Springer Berlin Heidelberg, 1^{st} edition, 1982.

[346] C.A. Williams, E.A. Marquis, A. Cerezo, and G.D.W. Smith. Nanoscale characterisation of ODS–Eurofer 97 steel: An atom–probe tomography study. *Journal of Nuclear Materials*, 400:37–45, 2010.

[347] C.A. Williams, P. Unifantowicz, N. Baluc, G.D.W Smith, and E.A. Marquis. The formation and evolution of oxide particles in oxide-dispersion-strengthened ferritic steels during processing. *Acta Materialia*, 61:2219–2235, 2013.

[348] C. Lu, Z. Lu, R. Xie, C. Liu, and L. Wang. Microstructure of a 14Cr-ODS ferritic steel before and after helium ion implantation. *Journal of Nuclear Materials*, 455:366–370, 2014.

[349] A. Hirata, T. Fujita, C.T. Liu, and M.W. Chen. Characterization of oxide nanoprecipitates in an oxide dispersion strengthened 14YWT steel using aberration-corrected STEM. *Acta Materialia*, 60:5686–5696, 2012.

[350] D.J. Larson, P.J. Maziasz, I-S. Kim, and K. Miyahara. Three-dimensional atom probe observation of nanoscale titanium-oxygen clustering in an oxide-dispersion-strengthened Fe-12Cr-3W-0.4Ti + Y_2O_3. *Scripta materialia*, 44:359–364, 2001.

[351] J.H. Kim, T.S. Byun, J.H. Lee, J. Y. Min, S. W. Kim, C. H. Park, and B.H. Lee. Effects of processing condition on the microstructural and tensile properties of 14Cr-based oxide dispersion strengthened alloys. *Journal of Nuclear Materials*, 449:300–307, 2014.

[352] P. Pareige, M.K. Miller, and R.E. Stoller. Stability of nanometer-sized oxide clusters in mechanically-alloyed steel under ion-induced displacement cascade damage conditions. *Journal of Nuclear Materials*, 360:136–142, 2007.

[353] D. Schwen, E. Martinez, and A. Caro. On the analytic calculation of critical size for alpha prime precipitation in FeCr. *Journal of Nuclear Materials*, 439:180–184, 2013.

[354] M.H. Mathon, Y.D. Carlan, X. Averty, and A. Alamo. Small Angle Neutron Scattering Study of Irradiated Martensitic Steels: relation Between Microstructural Evolution and Hardening. *ASTM international*, 2:1–15, 2005.

[355] M.J. Alinger, G.R. Odette, and D.T. Hoelzer. The development and stability of Y-Ti-O nanoclusters in mechanically alloyed Fe-Cr based ferritic alloys. *Journal of Nuclear Materials*, 329-333:382–386, 2004.

[356] A. Certain, S. Kuchibhatla, V. Shutthanandan, D.T. Hoelzer, and T.R. Allen. Radiation stability of nanoclusters in nano-structured oxide dispersion strengthened (ODS) steels. *Journal of Nuclear Materials*, 434:311–321, 2013.

[357] C.M. Parish, P.D. Edmondson, Y. Zhang, and M.K. Miller. Direct observation of ion-irradiation-induced chemical mixing. *Journal of Nuclear Materials*, 418:106–109, 2011.

[358] J.J Shiao, C.H. Tsai, J.J. Kai, and J.H. Huang. Aging embrittlement and lattic image analysis in a Fe-Cr-Ni duplex stainless steel aged at 400^{o}C. *Journal of Nuclear Materials*, 217:269–278, 1994.

[359] J. Souza, H. Abreu, A. Nascimento, J. de Paiva, P. de Lima-Neto, and S. Tavares. Effects of low-temperature aging on AISI 444 steel. *Journal of Materials Engineering and Performance*, 14:367–372, 2005.

[360] P.J. Grobner and R.F. Steigerwald. Effect of cold work on the 885°F (475°C) embrittlement of 18Cr-2Mo ferritic stainless steels. *The Journal of The Minerals, Metals & Materials Society*, 29:17–23, 1977.

[361] M. Terada, M.F. Hupalo, I. Costa, and A.F. Padilha. Effect of alpha prime due to 475c aging on fracture behavior and corrosion resistance of DIN 1.4575 and MA 956 high performance ferritic stainless steels. *Journal of Materials Science*, 43:425–433, 2008.

[362] R.B. Scarlin and J.W. Edington. On the "Friedel relation" in precipitation hardening. *Scripta Metallurgica*, 9:587–589, 1975.

[363] R. Kirchhofer, M.C. Teague, and B.P. Gorman. Thermal effects on mass and spatial resolution during laser pulse atom probe tomography of cerium oxide. *Journal of Nuclear Materials*, 436:23–28, 2013.

[364] University of North Texas Materials research facility. LEAP 3000 specifications. `https://cart.research.unt.edu/node/25`. Accessed: 09/08/2017.

[365] M.K. Miller, R.E. Stoller, and K.F. Russell. Effect of neutron-irradiation on the spinodal decomposition of Fe–32% Cr model alloy. *Journal of Nuclear Materials*, 230:219–225, 1996.

[366] A. Shariq, S. Mutas, K. Wedderhoff, C. Klein, H. Hortenbach, S. Teichert, P. Kucher, and S.S.A. Gerstl. Investigations of field-evaporated end forms in voltage- and laser-pulsed atom probe tomography. *Ultramicroscopy*, 109:472–479, 2009.

[367] A.J.W Moore and J.A. Spink. Field evaporation from tungsten and the bonding of surface atoms. *Surface Science*, 12:479–496, 1968.

[368] K. Stiller and H.O. Andren. Faulty field evaporation at di-vacancies in {222} tungsten. *Surface Science*, 114:57–61, 1982.

[369] A. Cerezo, P.H. Clifton, A. Gomberg, and G.D.W. Smith. Aspects of the performance of a femtosecond laser-pulsed 3-dimensional atom probe. *Ultramicroscopy*, 107:720–725, 2007.

[370] P.R. Kolli and F. Meisenkothen. Optimization of Experimental Parameters and Specimen Geometry for PulsedLaser Atom-Probe Tomography of Copper. *Microscopy and Microanalysis*, 20:768–769, 2014.

[371] K. Thompson, D. Lawrence, D.J. Larson, J.D. Olson, T.F. Kelly, and B. Gorman. In situ site-specific specimen preparation for atom probe tomography. *Ultramicroscopy*, 107:131–9, 2007.

[372] K. Thompson, B. Gorman, D. Larson, B. V. Leer, and L. Hong. Minimization of Ga Induced FIB Damage Using Low Energy Clean-up. *Microscopy and Microanalysis*, 12:1736–1737, 2006.

[373] D Haley. Weights program. User manual guide, University of Oxford, 2014.

[374] R. Haydock and D.R. Kingham. Post-Ionization of Field-Evaporated Ions. *Physical Review Letters*, 44:1520–1523, 1980.

[375] O.C. Hellman and D.N. Seidman. Measurement of the Gibbsian interfacial excess of solute at an interface of arbitrary geometry using three-dimensional atom probe microscopy. *Materials Science and Engineering A*, 327:24–28, 2002.

[376] E.A. Marquis, S. Lozano-Perez, and V.D. Castro. Effects of heavy-ion irradiation on the grain boundary chemistry of an oxide-dispersion strengthened Fe-12 wt.% Cr alloy. *Journal of Nuclear Materials*, 417:257–261, 2011.

[377] B.W. Krakauer and D.N. Seidman. Absolute atomic-scale measurements of the Gibbsian interfacial excess of solute at internal interfaces. *Physical Review B*, 48:6724–6727, 1993.

[378] R. Hu, G.D.W Smith, and E.A. Marquis. Atom probe study of radiation induced grain boundary segregation/depletion in a Fe-12%Cr alloy. *Progress in Nuclear Energy*, 57:14–19, 2012.

Appendix A

Atom probe tomographic procedures

Protocols to fabricate APT samples, reconstruct APT datasets, identify mass spectrum peaks and conduct GB analysis within APT datasets are described here

A.1 Sample fabrication

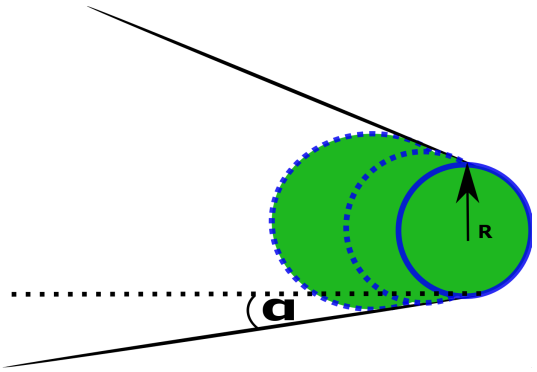


Figure A.1: Assumed evolution of the tip curvature radius during an APT experiment. α is the shank angle and R is the tip's curvature of radius.

Sample fabrication for atom probe experiments is challenging given the number of criteria the sample should fulfill. During the reconstruction of the APT dataset, the IVAS software package assumes a tip that maintains a perfect hemispherical sphere that increases in radius which is a function of a constant shank angle α. This assumption is illustrated in figure A.1 and shows successive hemispherical spheres increasing in radius. In reality, this is unlikely to be the case especially for multicomponent alloys. Multiphase materials, such as 14YWT, will have different evaporation fields and will

not evaporate uniformly along the surface [335, 366]. This could give rise to preferential retention and evaporation taking place. Secondly, a sample must have a tip curvature of radius that is $\sim 50nm - 150nm$. The base of the sample has to be cleared of protruding sections at least $10\mu m$ from the tip. This is to reduce the likelihood of secondary evaporation events taking place away from the tip [367, 368]. Such events can introduce uncertainty into calculated metrics such as M (mass-to-charge ratio) and will likely contribute to spectrum background noise. Shank angles have also been observed to affect the mass resolving power as they impact the rate at which the tip cools down, especially in laser mode experiments [369]. Generally the data acquired from APT experiments is influenced greatly by the sample geometry and dimensions [366, 369, 370]. There remains no general ideal shape as varying materials will respond to the electrostatic environment within the APT analysis chamber differently.
Electropolishing [289] and the FIB lift out technique [371] are the most common methods of fabricating APT samples. Electropolishing tends to utilise the double layer method which consists of a rough initial polish, to shape the initial material specimen, and then a fine polish to sharpen the tip [289]. The FIB lift out procedure uses a Ga beam to sputter atoms from the sample in a predefined pattern.
Manufacturing samples using the FIB offers site specificity and is advantageous when working on radioactive samples. However it can also introduce Ga beam induced damage and artefacts [372]. Electropolishing produces samples that are cleaner and more uniform when produced by a skilled operator, but uses more material in the process [289, 293]. As specimens used in this thesis are of a limited supply, all APT samples were manufactured via the FIB lift out technique [371].

A.1.0.1 Fabricating APT samples via the FIB lift out technique

This method is based on the technique "bar extraction method" described in [371] and has been adapted for the use within 14WT and 14YWT NFAs. The first part of the procedure involves producing a bar in the material using the ion beam. As it is necessary to preserve the microstructure and ensure it is not sputtered by the Ga beam, a protective layer of Pt is deposited first via a 5kV, 200nA electron beam for 5 minutes. This lays a thin layer of Pt and protects the microstructure underneath from the following Ga beam deposition of Pt using a 30kV and 20pA beam for 5 minutes. The deposition of Pt by both beams usually provides a Pt layer $0.5\mu m$ thick as shown in figure A.2a. The next step is to prepare a bar-like cantilever ensuring the protective layer remains intact as shown in figure A.2b. This step is carefully controlled and monitored in order to preserve the Pt layer from damage and erosion from the Ga beam tails. Once the cantilever is under-cut and freed on one side, as it is in figure A.2b, the micro-manipulator can be brought in. It is then welded to the to the freed end of the cantilever using a Ga beam deposited Pt-strap at 30kV and 20pA. Once attached securely, the opposite side of the cantilever can be cut and the micro-manipulator and the sample can be lifted out as shown in figure A.2c. The next step requires the user

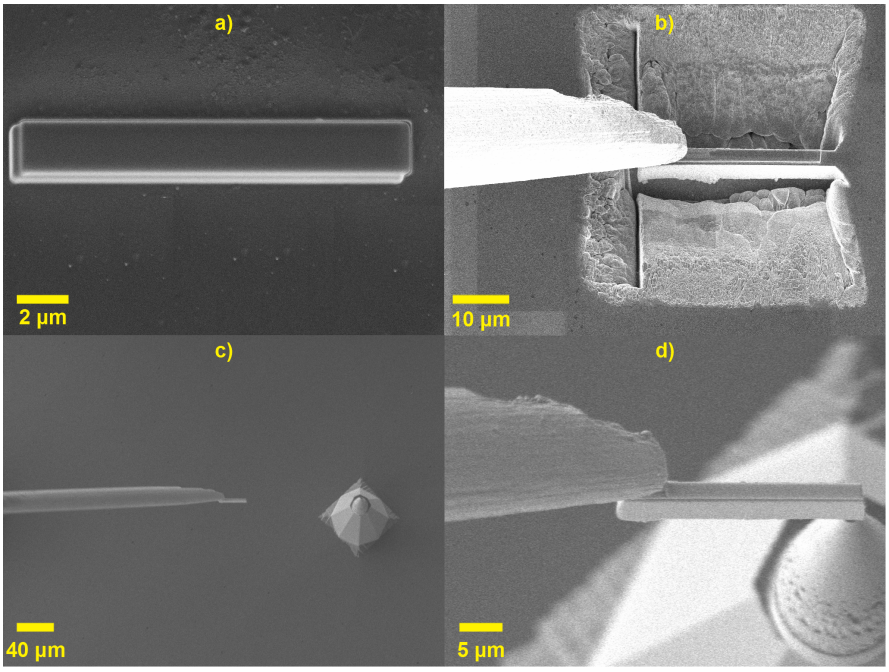


Figure A.2: SEM images of the main stages in the construction of a cantilever, its subsequent lift out and welding on a Si post

to position the manipulator over a Si post on a microcoupon as shown in figure A.2d. Once the end of the cantilever is aligned with the top of the post it can be attached using a Ga beam deposited Pt-strap again at 30kV and 20pA for 2.5 minutes. Once attached securely the rest of the cantilever can be cut from the portion attached to the post. This process of attaching sections of the cantilever onto the Si posts is repeated until no more sections of the cantilever can be attached to posts. The coupon is then rotated 180° so that the other side can be welded using the same Pt beam conditions, thus securing the specimen further.

A single Si post with an attached section of the sample should look like that shown in figure A.3a in the SEM view. Using the Nano-Patterning Engine (NPE) software the annulus milling tool should be selected and its centre should be placed at approximately the centre of the Si post. Using the steps listed in table A.1, the specimen is sharpened until the desired tip shape and size is achieved as shown in figure A.3b-d. When the beams are changed, the FIB image must be re-focussed to ensure milling accuracy.

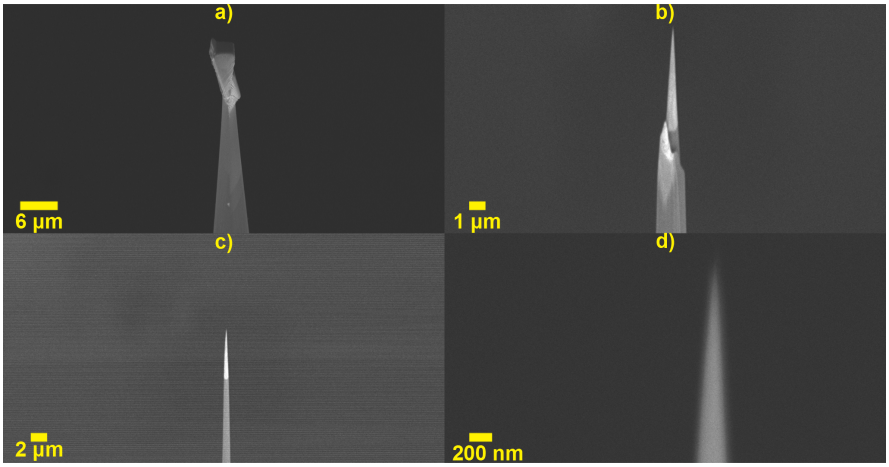


Figure A.3: SEM images that depict the formation of a 14YWT as received APT tip, from the original cantilever section

Step	Diameter $[\mu m]$	Outline thickness $[\mu m]$	Beam accelerating voltage $[kV]$	Beam current
1	6.00	1.000	30	2nA
2	4.50	1.250	30	1nA
3	4.00	1.250	30	240pA
4	2.50	0.750	30	120pA
5	2.50	0.895	30	120pA
6	2.00	0.750	30	50pA
7	1.50	0.600	30	20pA
8	1.00	0.350	30	20pA
9	1.00	0.350	5	20pA

Table A.1: 14WT and 14YWT annular milling protocol for use on the nano-patterning engine on the Zeiss Auriga FIB system at the University of Oxford

A.2 Post-experimental analysis

A.2.1 Reconstructing datasets

IVAS 3.6.8 is the commercial software used to process the raw detector data by implementing the point projection model [333]. This estimates the ion positions within the original sample, by back-projecting the coordinates at which the ion impacted the detector. The main assumptions for this model are:

1. Electric field penetration into the surface of the sample is shallow such that only the surface atoms may evaporate
2. Ions travel from the tip with a radial trajectory
3. The tip is always hemispherical as shown in figure A.4
4. The tip's shank angle is small
5. Surface atoms are field evaporated homogeneously across the area that is imaged

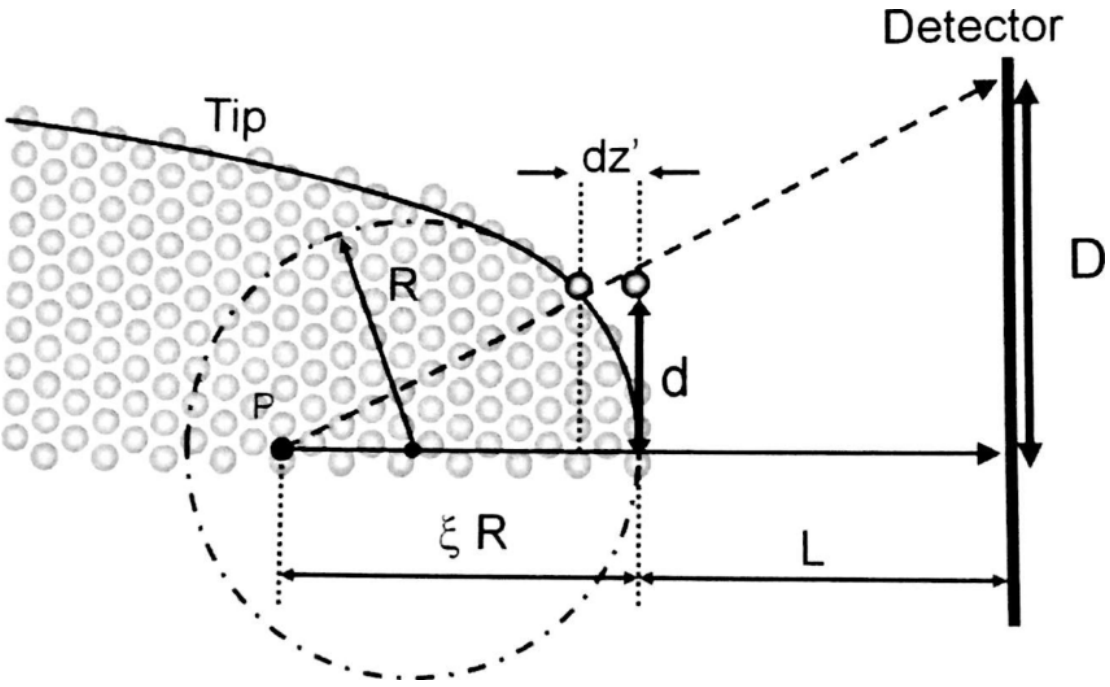


Figure A.4: Schematic of the pont projection model with the Bas proposed depth correction incorporated [333], originally published in [289]

The equations to calculate the atomic positions in space will only be presented here and the reader is referred to [289, 333] for more comprehensive derivations. The reconstruction process commences by calculating the planar coordinates $(x^{(i)}, y^{(i)})$ for the i^{th} ion detected using equations A.1 and A.2.

$$x^{(i)} = \frac{x_d^{(i)}}{M} \tag{A.1}$$

$$y^{(i)} = \frac{y_d^{(i)}}{M} \tag{A.2}$$

where

$$M = \frac{D}{d} = \frac{L + \xi R}{\xi R} \sim \frac{L}{\xi R} \tag{A.3}$$

x_d and y_d refer to the ion hit coordinates on the detector, ξ is the image compression factor which takes into account the compression of the field lines due to the electrostatic field around the tip; and L is the flight length to the detector shown in figure A.4.

The depth coordinate $z^{(i)}$ is deduced under the assumption that evaporated ions are originally situated from the sample surface and that ions are evaporated layer by layer in increments of dz. The caculation of the depth component is given by equation A.4. The $\left(\sum_1^i dz\right)$ term generates values for z that are within the plane tangent to the sample apex, as shown in figure A.4. Therefore a corrective term, dz', is applied to take into account the curvature of the sample. This has the effect of bringing the atom closer towards the centre of the assumed spherical tip.

$$z^{(i)} = \left(\sum_1^i dz\right) + dz'^{(i)} = \frac{\Omega^{(i)} L^2 k_f^2 F^2}{\eta S_D \xi^2 V^{(i)2}} + R_i \left(1 - \sqrt{1 - \frac{x^{(i)2} + y^{(i)2}}{R^{(i)2}}}\right) \tag{A.4}$$

where S_D is the detector surface area, η is the detection efficiency, Ω is the atomic volume, F is the electric field and $V^{(i)}$ is the potential difference for the i^{th} detected atom.

The calculation of z from equation A.4 requires knowledge of ξ, shank angle and the initial tip radius. While methods to determine these variables are available in the literature [289], most require a crystallographic pole to be sampled in the dataset. Such features were not observed in the majority of APT experiments here and therefore could not be used to determine ξ, shank angle and the initial tip radius. To overcome this, reconstructions were conducted whereby the shank angle, initial tip radius and image compression factor were varied to observe in real time their influence on the tip shape. These three variables were adjusted appropriately to ensure the NFA particles in the 14YWT dataset remained spherical as they are observed in the TEM [84]. This method was originally employed by Burrows [45] for the 14YWT1 system too and were guided by NFA particle images acquired from TEM experiments.

Whilst this method of reconstruction may not be as reproduceable as the methods outlined in [289] that utilise crystallographic features, the total number of ions within the dataset is not affected. Therefore NFA particle characteristics such as composition and particle density remains invariant to the reconstruction protocol here and those that use crystallographic features [289].

For the case of 14WT, a voltage profile based tip reconstruction was seen to be adequate as features such as Ti rich precipitates, which were often captured in the APT sample volume, remained spherical.

A.2.2 Peak identification

In order to determine elemental compositions within the APT datasets, peaks within the mass spectrum must be identified. Peaks belonging to Fe and Cr can be easily identified relative to those belonging to minor elements, due to their large peak heights. For minor solutes, a list of possible ionic candidates generated by the 'Weights' program [373] was utilised. Isotopic ratios of unidentified peaks and their satellites are usually preserved in APT datasets. Therefore they can be used to determine whether they belong to any of the ionic candidates in the list compiled from the previous step. Candidates that do not satisfy the relative abundancies are continually discarded until a suitable candidate is found.

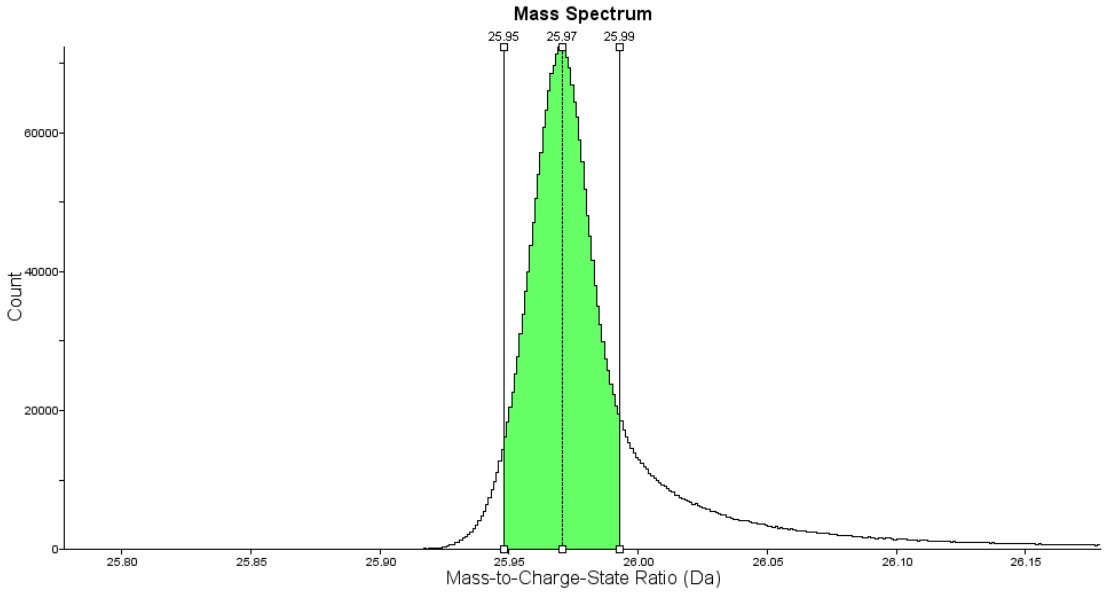


Figure A.5: An example of the ranging technique employed for each peak in each APT dataset acquired in this thesis. The peak shown is identified as Cr^{2+} and is extracted from a dataset belonging to 14YWT 2 NFA.

Once peaks were identified, they were ranged in IVAS 3.6.8 by ensuring the middle of the ranging tool was aligned with the peaks apex, as shown in figure A.5. The minimum and maximum range values were adjusted appropriately to accomodate this. The broadening often observed in the peaks, such as that seen in figure A.5, often stem from evaporation events taking places between pulses. As a result, uncertainty in the ion's ToF is introduced. This broadening effect also varies between peaks and so no general rule was applied. Contributions from ions in these peak tails were minimised as best as possible and were determined by sight. Dataset bulk compositions were consistent with those measured using EPMA and therefore this ranging method was

deemed appropriate.

A.2.3 Peak overlap

Instances where the same value of M for two or more ions may occur and result in peak overlaps on a mass spectrum. An example of this, within Fe-Cr based alloys in particular, is that for Fe and Cr. In atom probe experiments the peak belonging to ^{54}Fe will overlap with that from ^{54}Cr for each of the ionisation states. $(^{48}Ti^{16}O)^{2+}$ and the $^{16}O_2^+$ peaks may also overlap. Both examples given will impact the compositional measurements for the matrix and NFA particles respectively, and therefore need to be considered. Protocols such as 'decomposition of peaks' in Cameca's IVAS software can be applied which attempts to deconvolute the overlapping peaks. It does this by determining the total number of ions that make up the peak, i.e. the integral under the curve. Once this total is known, the proportion of ions each of the shortlisted ions that are likely to contribute are then determined. The shortlisted ions are comprised of the elements that are detected in the dataset.
Whether a certain combination of ions overlaps, is dependant on the analysis parameters used during the APT experiments. This is because post evaporation ionisation processes may occur which will influence the abundance of certain ionisation states for a specific ion [374]. As the analysis parameters are determined in chapter 4, peak overlaps that occur in the mass spectrum are described there.

A.2.4 Grain boundary analysis

Some of the APT datasets acquired in this thesis contained a GB. These datasets are summarised in tables A.2 and A.3. Quantities of particular elemental species at the GB were also measured.

Ageing duration $[Months]$	14WT datasets	14YWT1 datasets
0	-	23146, 23181
1	-	20713, 21112
3	22361	23065
8	-	22826, 22920

Table A.2: Summary of 14WT and 14YWT1 APT datasets containing a GB

The standard method to quantify the number of atoms belonging to a certain element, within a GB, is to calculate the GIE. This simple method also allows for the direct comparison of solute segregation between different APT datasets [375, 376, 377, 378].

Alloy state	Datasets number
14YWT2 as-received	24154
Neutron irradiated 14YWT3	4724, 4732

Table A.3: Summary of 14YWT2 and 14YWT3 APT datasets containing a GB

$$\Gamma = \frac{n_i}{A} \tag{A.5}$$

The GIE is calculated via equation A.5. n_i is the number of excess solute atoms and can be calculated by numerically integrating the 1D concentration profile of element i across the GB feature. A can be assumed to be equivelent to the cross sectional area of the cylindrical shaped Region Of Interest (ROI) which is used to generate the concentration profile. This is depicted in figure A.6.
This method assumes that the GB shows minimal curvature inside the ROI and that the integration step size is much greater than the voxel size. Three different regions within the same GB was studied from each APT dataset containing a GB and the full width of the peak was used to set the integration limits.

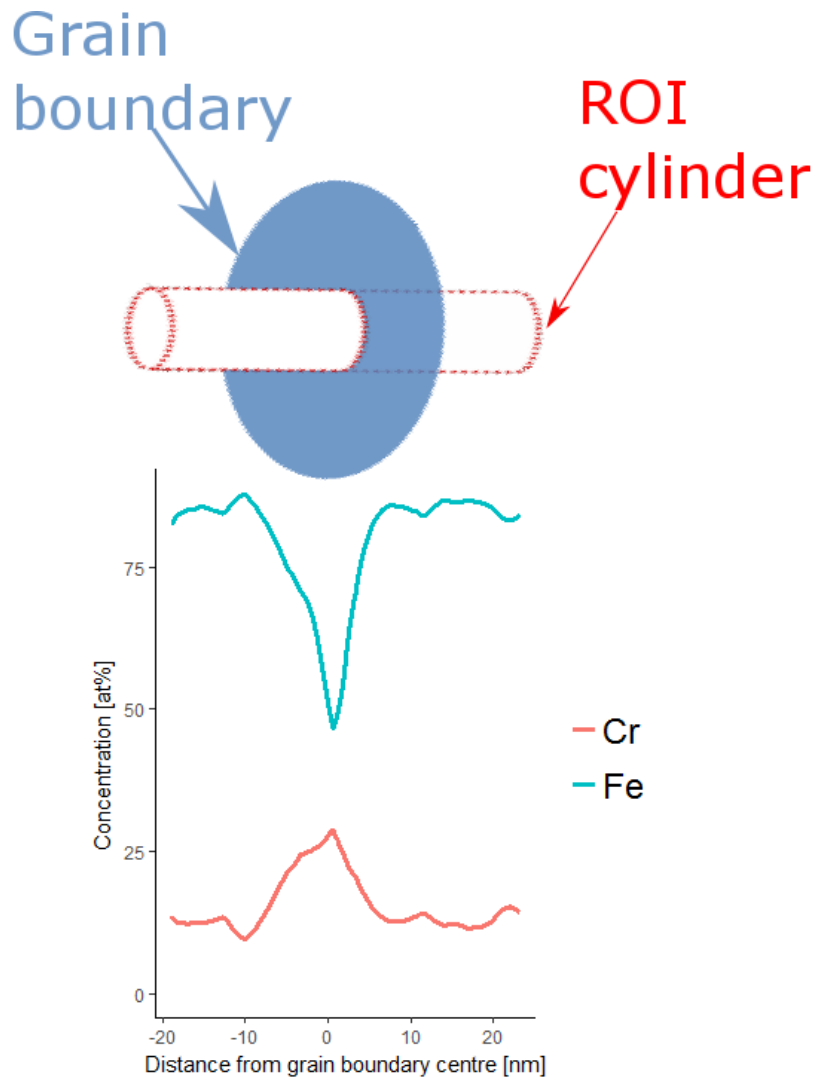


Figure A.6: Concentration profile is from the GB captured in 14YWT1 aged for 8 months - dataset 22920

Appendix B

Isothermal ageing experiment: 14YWT1 experimental repeats

Ageing duration	14YWT1 dataset	APT maps presented in
As-received	23181	Chapter 5 figure 5.12a
	23070	Appendix A figure B.1a
	23146	Appendix A figure B.1b
1 month	20713	Chapter 5 figure 5.12b
	21112	Appendix A figure B.2a
	21240	Appendix A figure B.2b
3 months	23065	Chapter 5 figure 5.12c
	20823	Appendix A figure B.3a
	20901	Appendix A figure B.3b
8 months	22826	Chapter 5 figure 5.12d
	22894	Appendix A figure B.4a
	22920	Appendix A figure B.4b

Table B.1: Summary of all the 14YWT1 APT datasets acquired in the isothermal ageing study conducted in this thesis

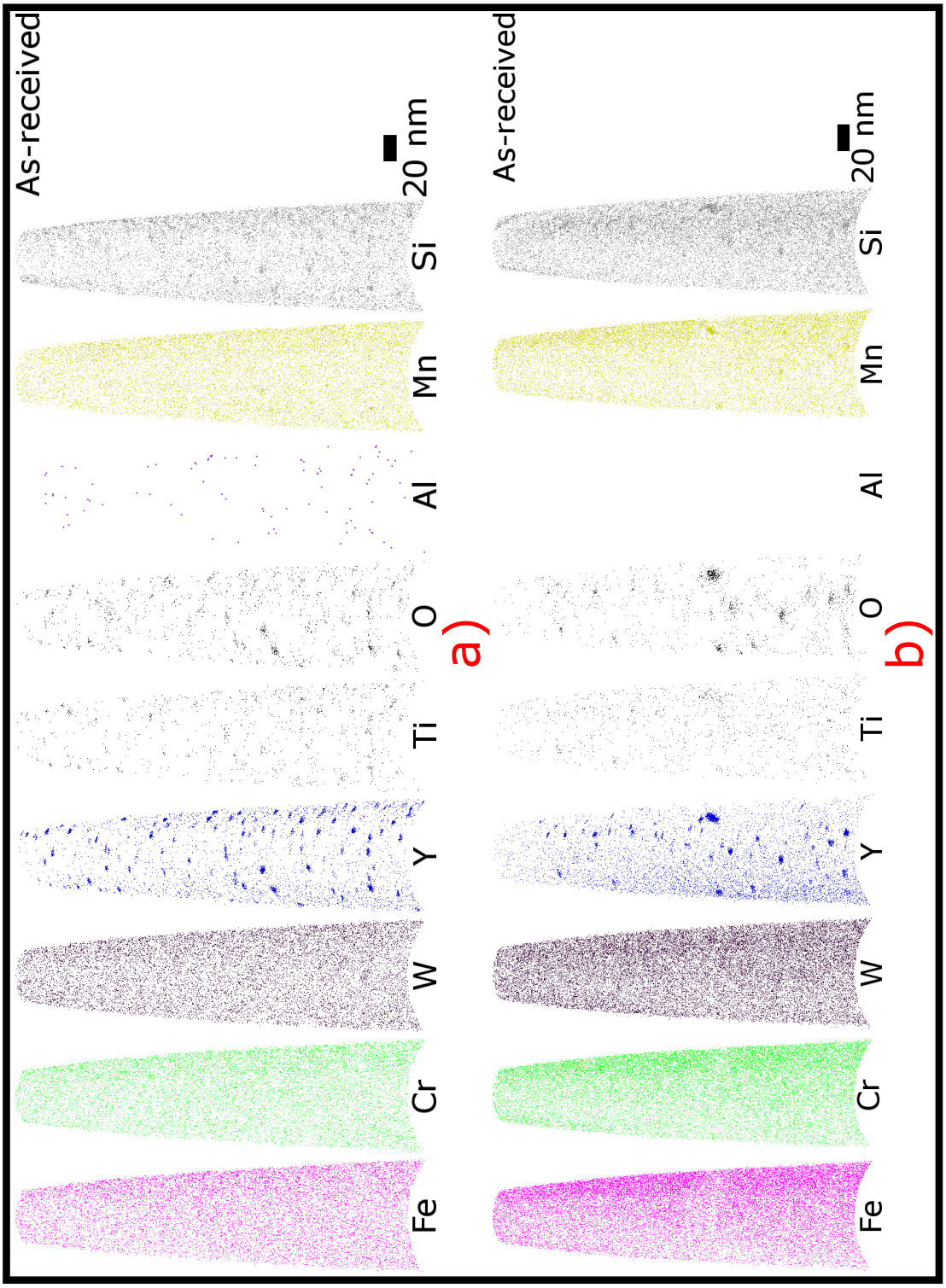


Figure B.1: Atom map slices of as-received 14YWT1: dataset a) 23070 and b) 23146

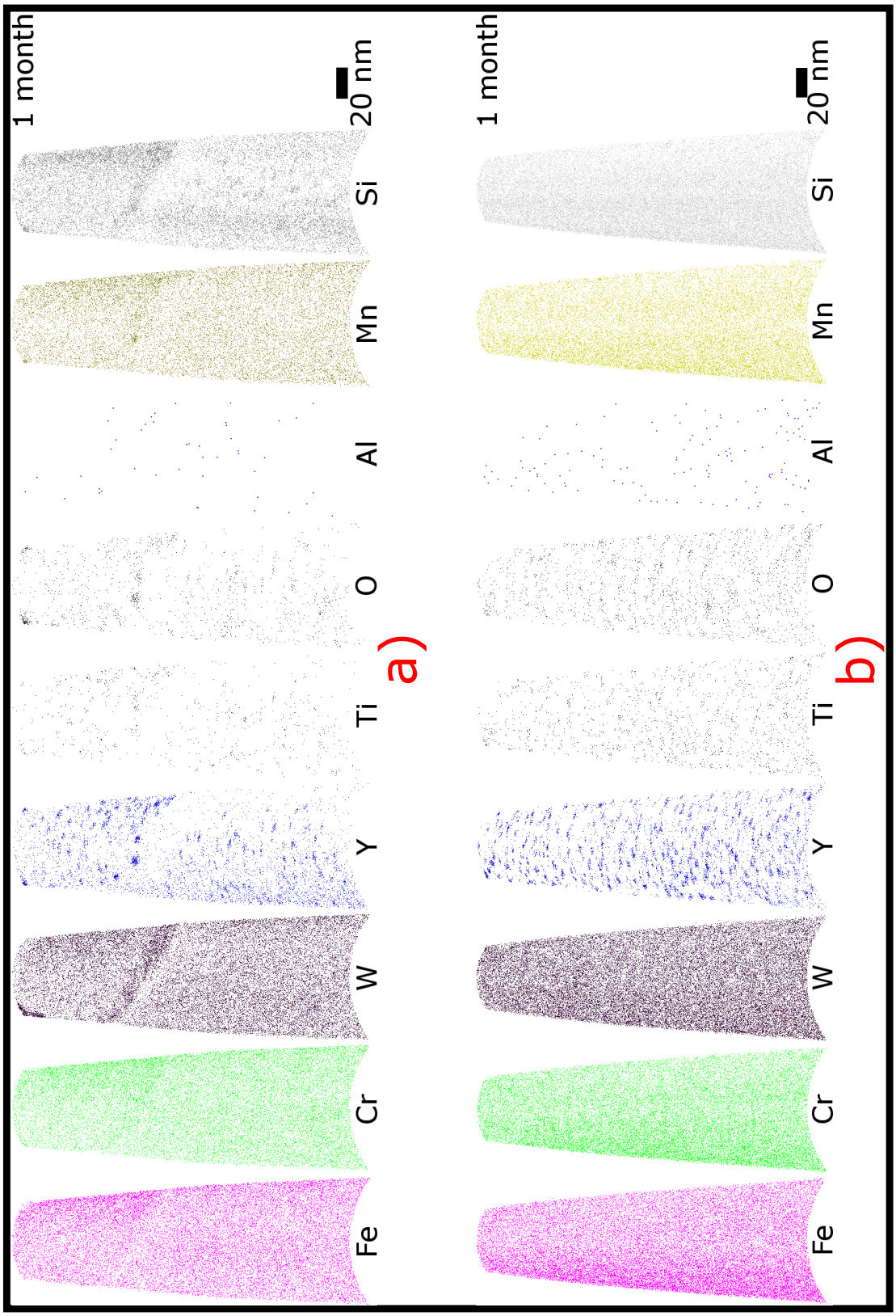


Figure B.2: Atom map slices of 14YWT1 aged at 475℃ for 1 month: dataset a) 21112 and b) 21240

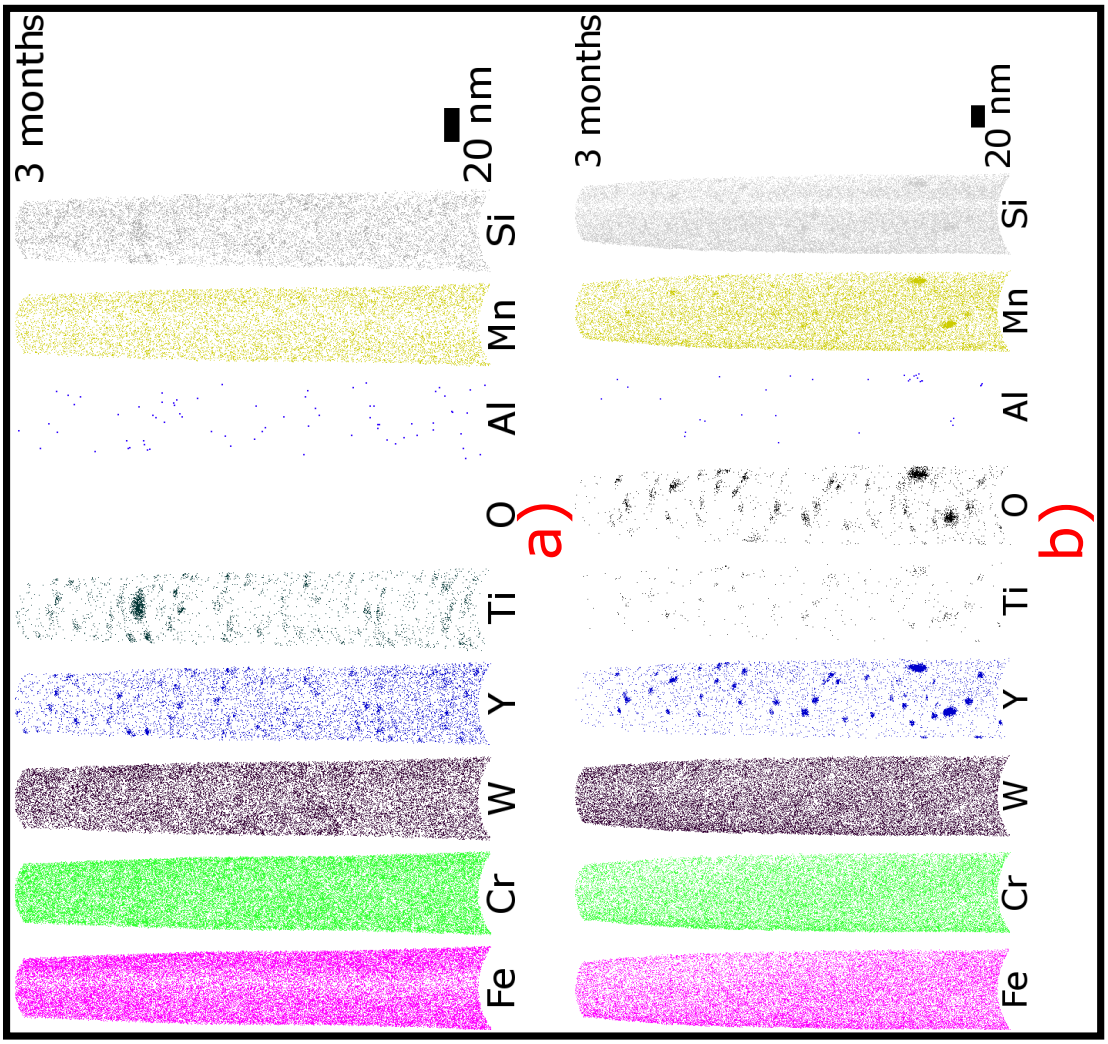


Figure B.3: Atom map slices of 14YWT1 aged at 475℃ for 3 months: dataset a) 20823 and b) 20901

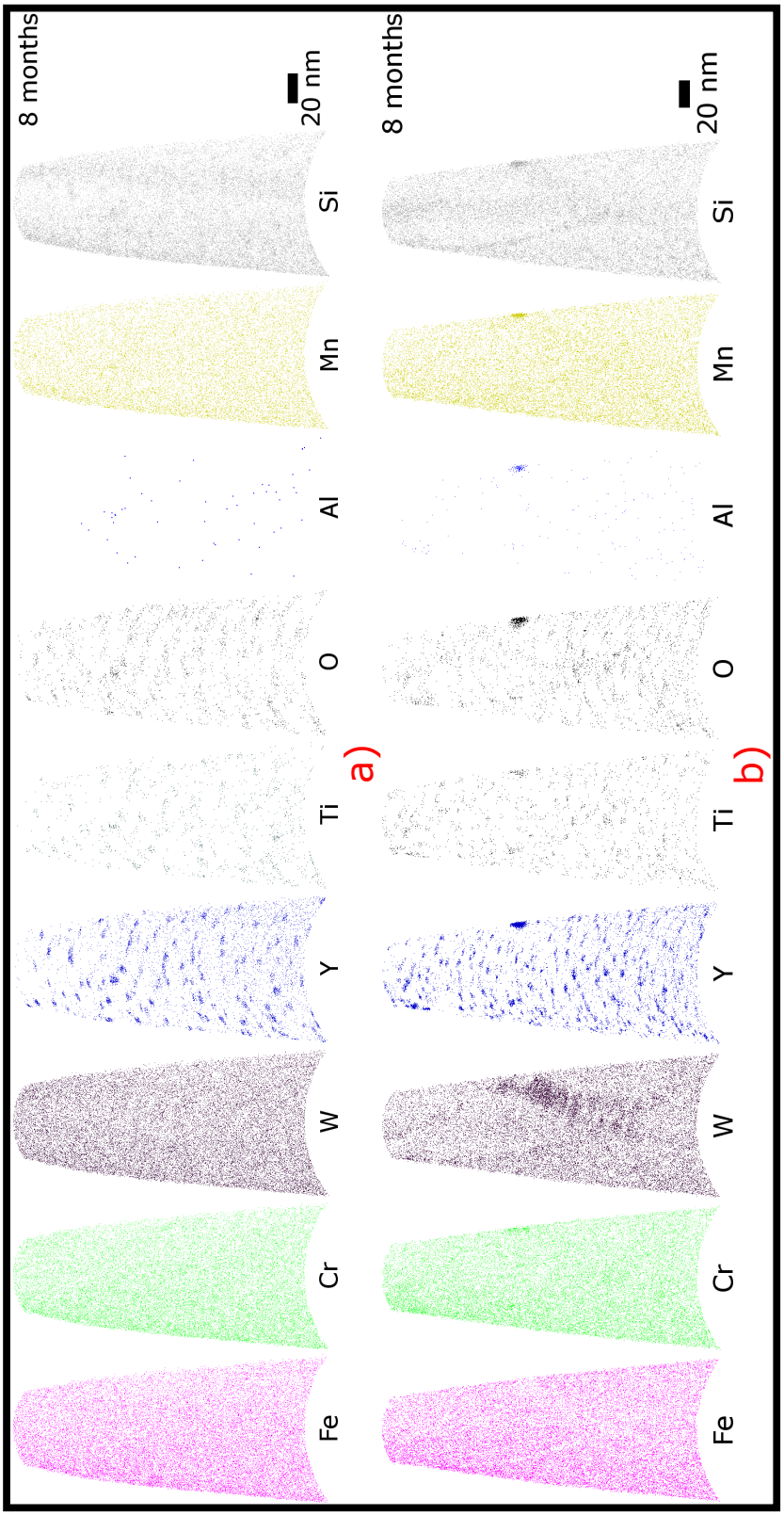


Figure B.4: Atom map slices of 14YWT1 aged at 475℃ for 3 months: dataset 22894 and 22920

Appendix C

Aged 14WT grain boundary Gibbsian excess data

Out of the 12 14WT APT datasets acquired in the isothermal ageing experiment, only dataset 22361 contained a GB. Figure C.1 shows a slice of a C atom map. C is usually seen to segregate to GBs and therefore is a good indicator to where the GB lies.

Table C.1 presents the Gibbsian excess values for Cr, W, Mn, Si and Ti for the GB shown in figure C.1. The magnified image of the GB also shows where the three ROIs where the Gibbsian excess values were calculated from.

	Gibbsian excess $[atoms\,nm^{-2}]$				
	Cr	W	Mn	Si	Ti
ROI0	13.84	23.19	0.35	8.06	-0.92
ROI1	38.73	28.40	0.53	7.05	-0.07
ROI2	54.31	15.85	0.28	3.07	-0.63
Average	35.62 ± 11.78	22.48 ± 3.64	0.38 ± 0.07	6.06 ± 1.52	-0.54 ± 0.25

Table C.1: Gibbsian interfacial excess values for the GB found in one of the three APT datasets belonging to 14WT aged for 3 months [dataset 22361].

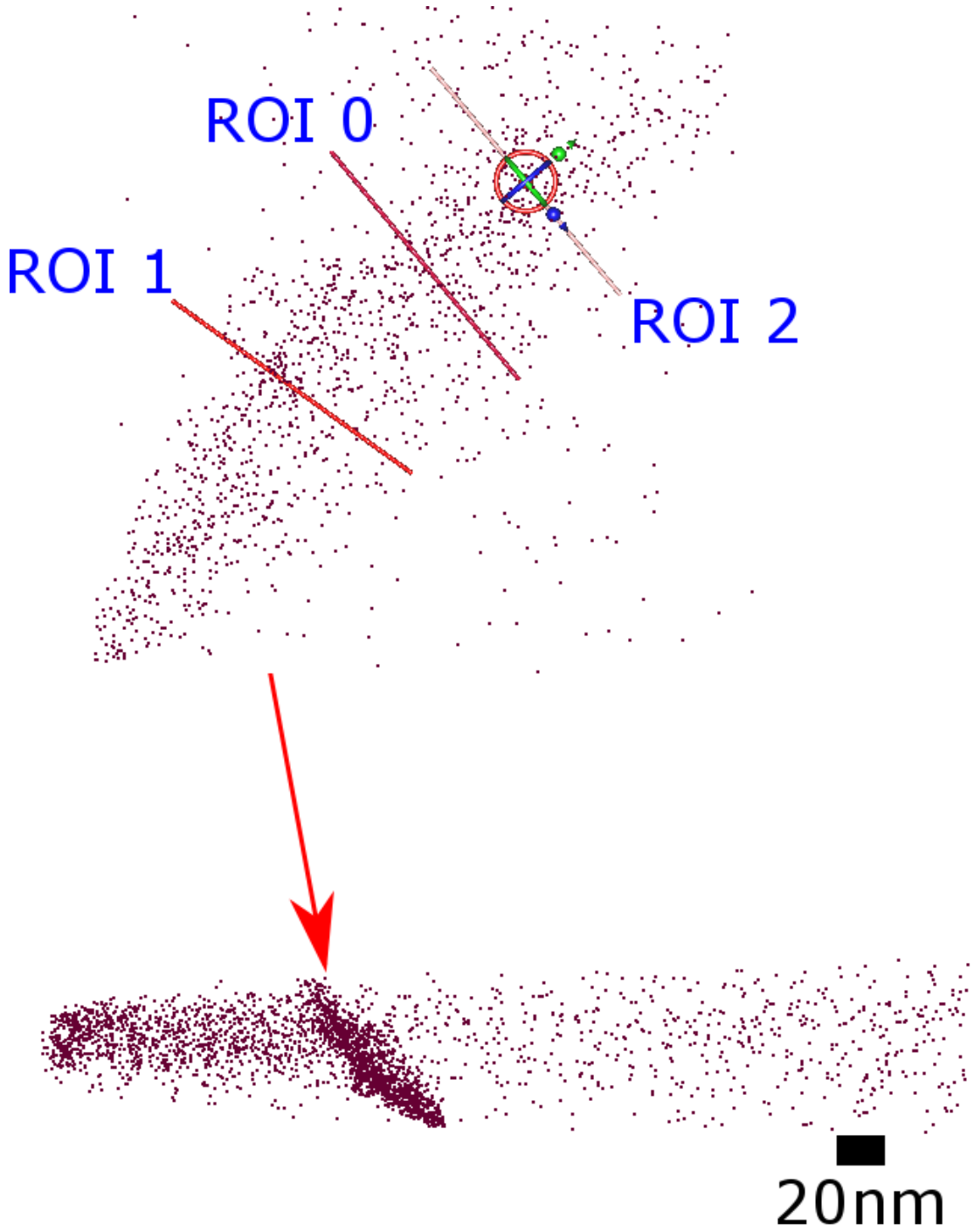


Figure C.1: C atom map slice from dataset 22361 (14WT aged for 3 months). The C dense zone represents the GB. The magnified image of the GB shows three ROIs where the Gibbsian excess values were calculated.

Appendix D

Irradiated 14YWT2 and 14YWT3 experimental repeats

Sample	Dataset	Presented in
14YWT2 As-received	21454	figure D.1a
	24344	figure D.1b
14YWT2 ion irradiated	24492	figure D.2a
	24493	figure D.2b
14YWT3 As-received	5209	figure D.3a
	5210	figure D.3b
14YWT3 neutron irradiated	4724	figure D.4a
	4732	figure D.4b

Table D.1: Summary of the additional APT experimental repeats used in the ion and neutron irradiation comparitive study

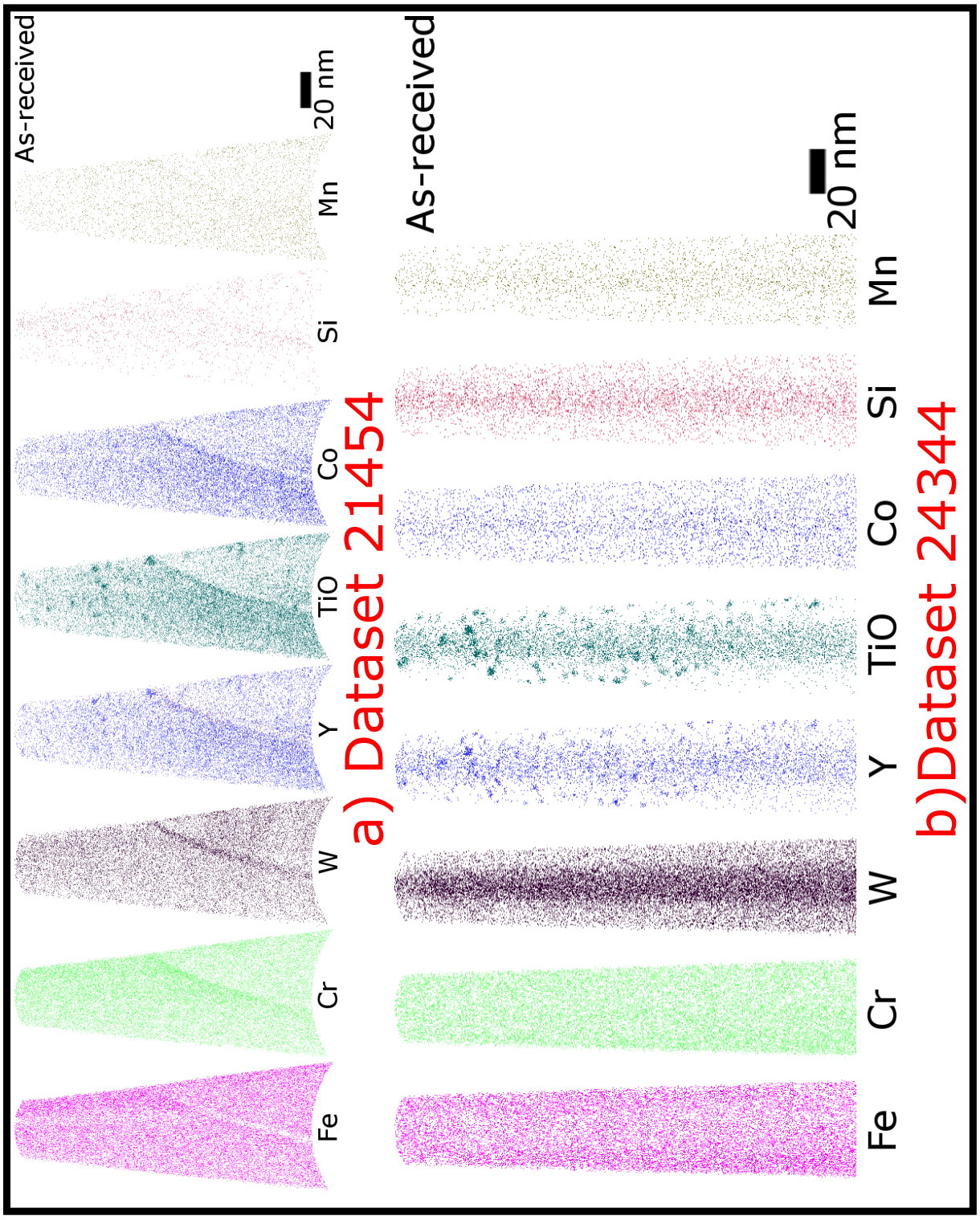


Figure D.1: As-received 14YWT2: a) dataset 21454 b) dataset 24344

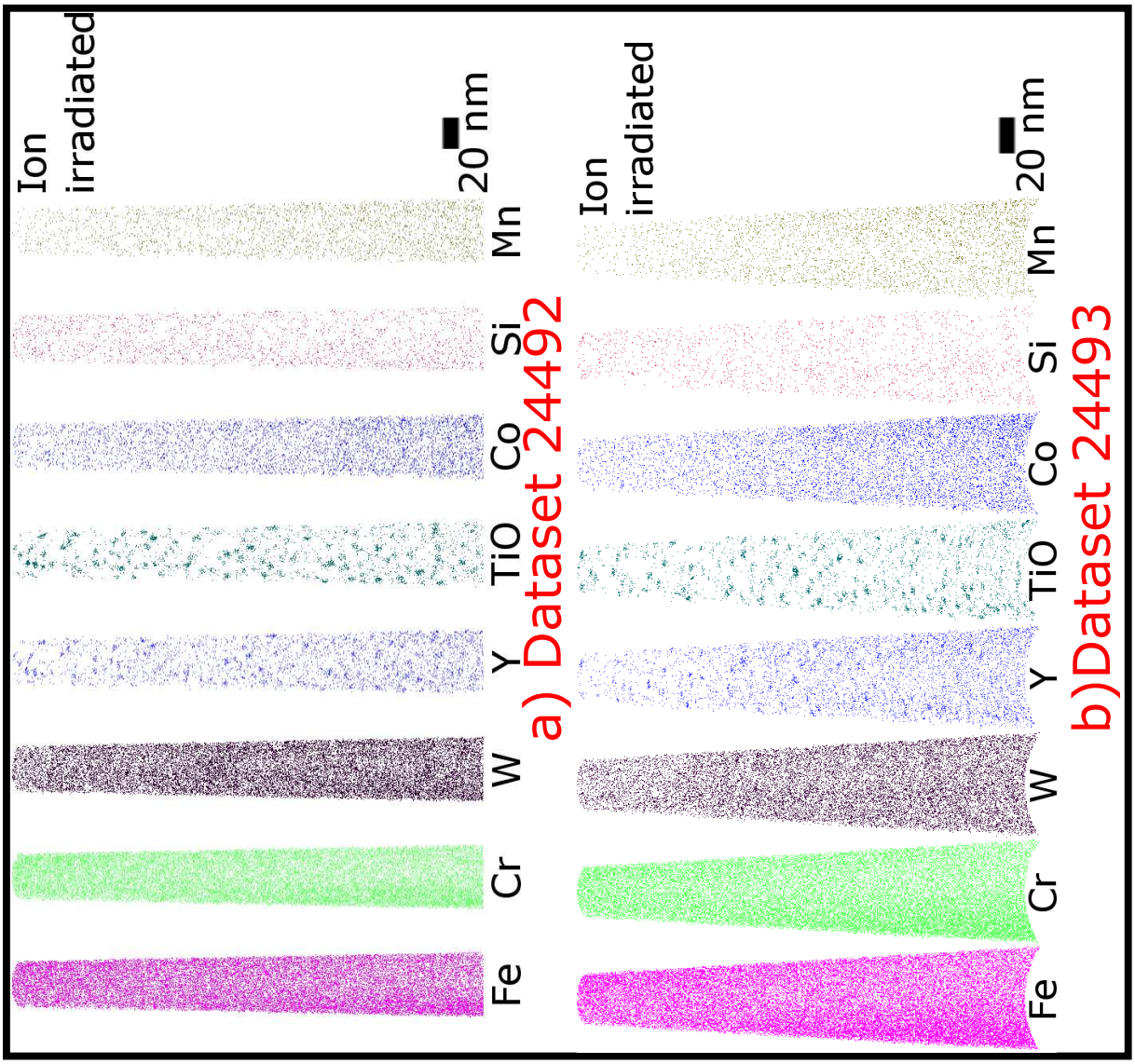


Figure D.2: Ion irradiated 14YWT2: a) dataset 24492 b) dataset 24493

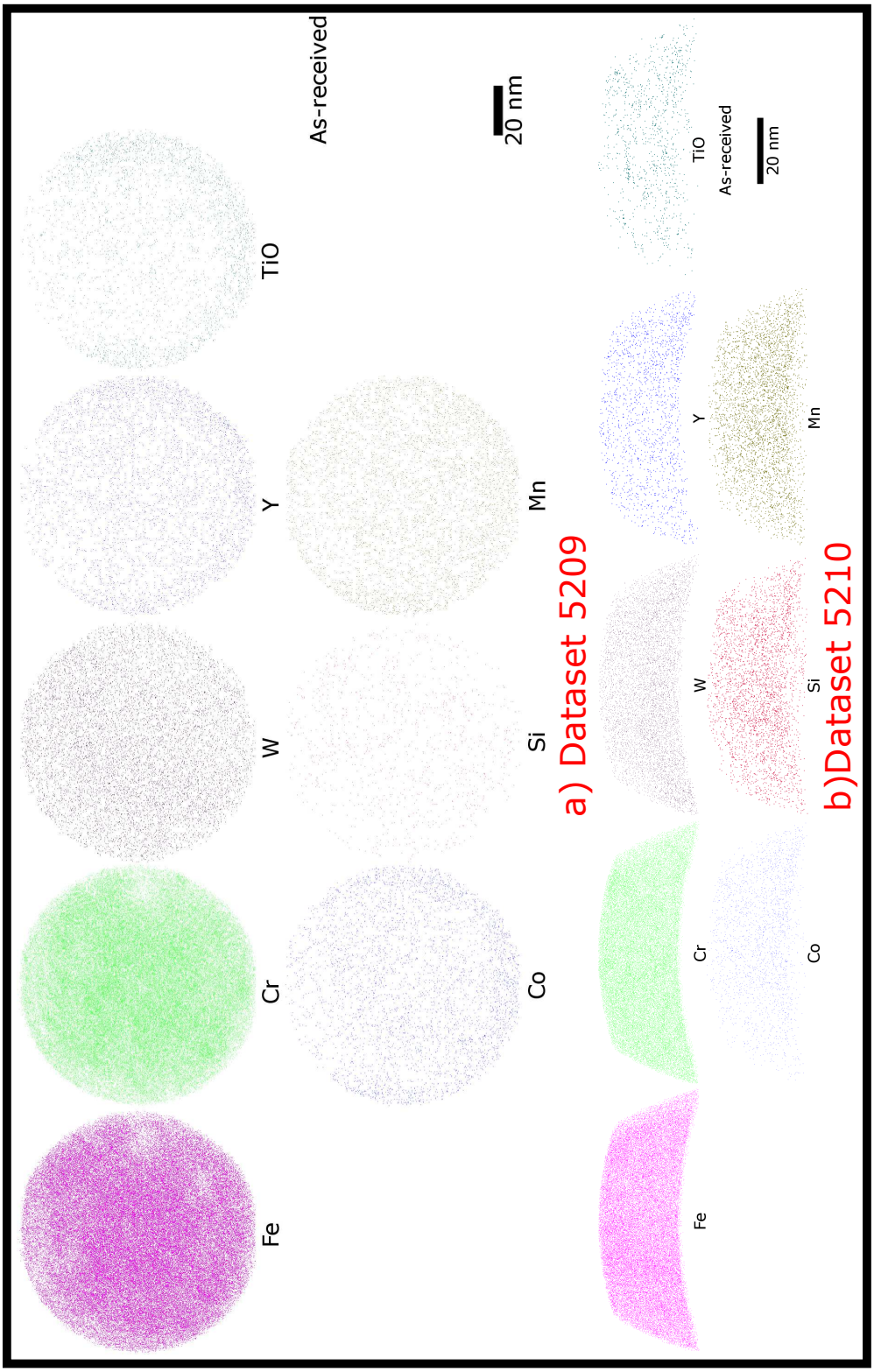


Figure D.3: As-received 14YWT3: a) dataset 5209 b) dataset 5210

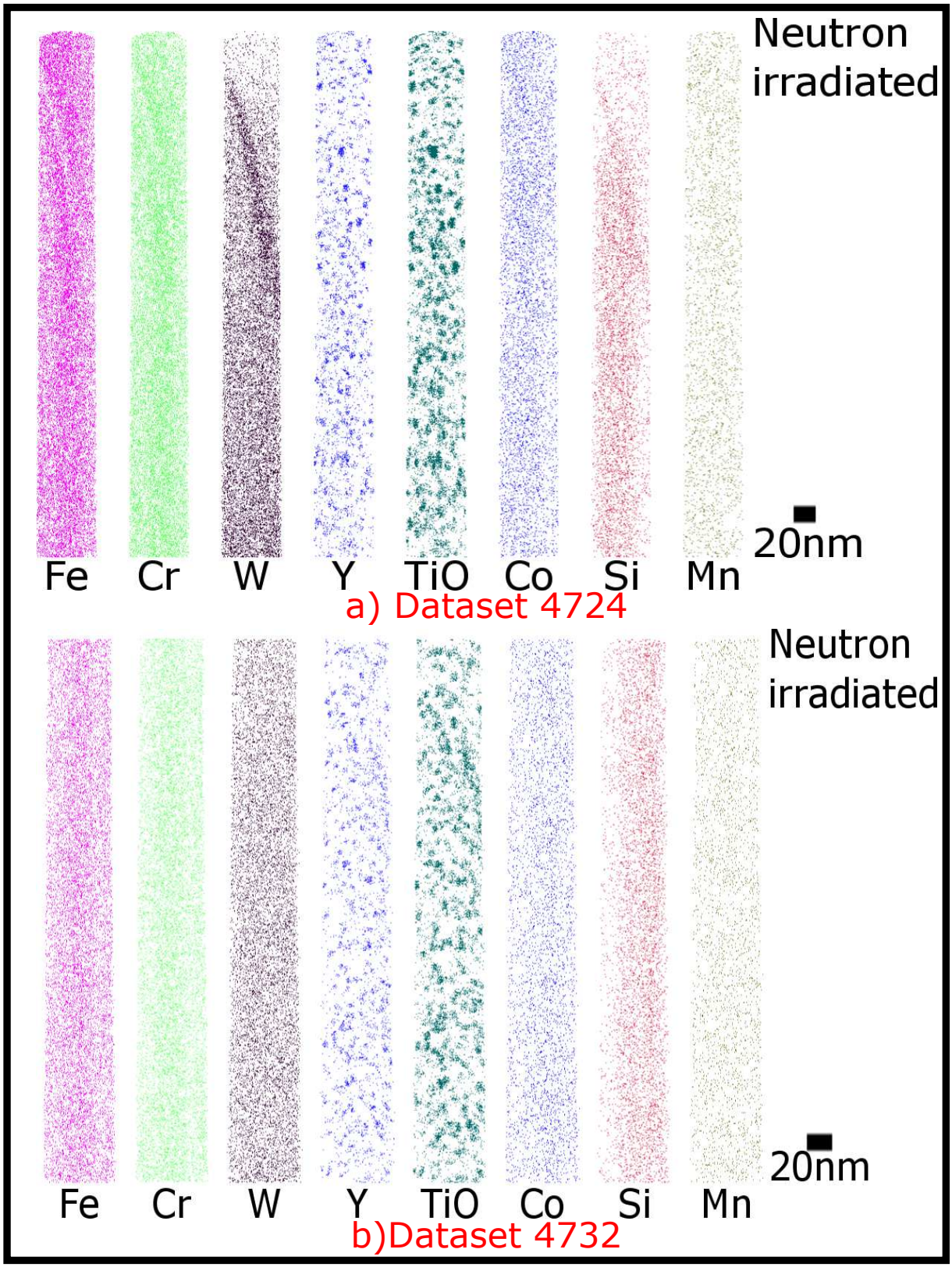


Figure D.4: Neutron irradiated 14YWT3: a) dataset 4724 b) dataset 4732

Appendix E

Gibbsian excess data from GBs in 14YWT2 and 14YWT3

Three GBs were captured in the APT datasets acquired for the study described in chapter 6. C atom maps showing each of these GBs are presented here. GIE data for Cr, W, Mn and Si at each of these GBs are also given.

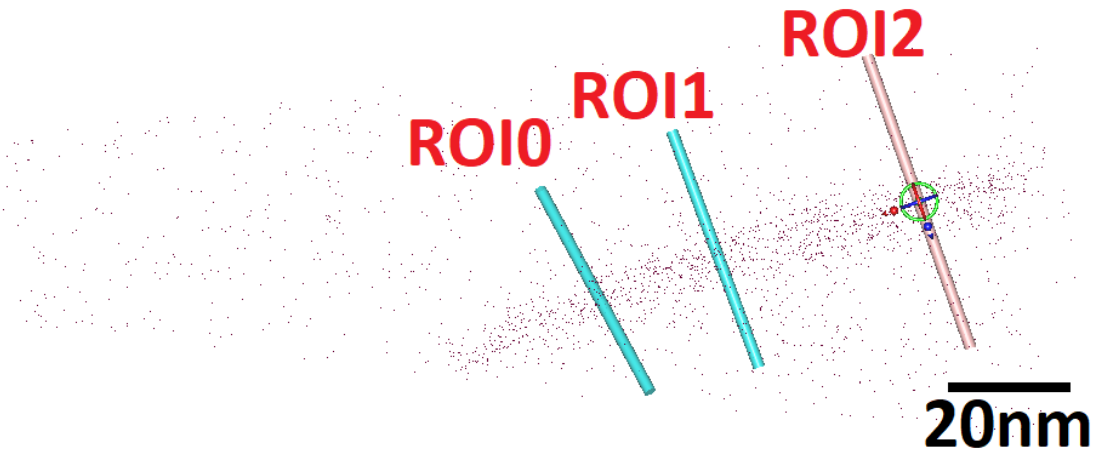


Figure E.1: C atom map slice from dataset 24154, the as-received 14YWT2. The dense regions of C represents a GB. The three cylinders show where a concentration profile has been obtained.

	Gibbsian excess $[atoms\,nm^{-2}]$			
	Cr	W	Mn	Si
ROI0	10.3	3.0	-0.5	0.2
ROI1	15.2	1.7	0	0.1
ROI2	14.7	2.1	0.4	0.3
Average	13.4±1.6	2.3± 0.4	0.0 ±0.3	0.2 ± 0.1

Table E.1: GIE values for the GB found in dataset 24154, the as-received 14YWT2

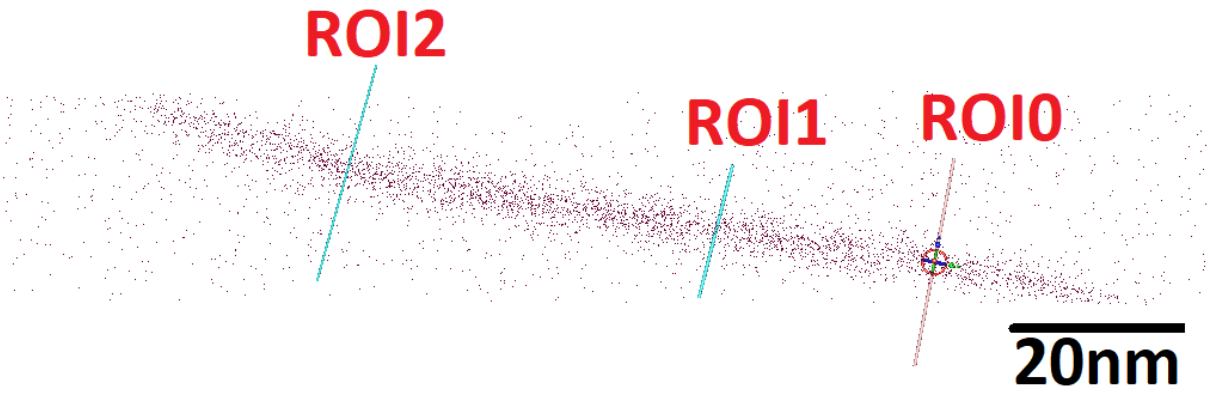


Figure E.2: C atom map slice from dataset 4724, the neutron irradiated 14YWT3. The dense regions of C represents a GB. The three cylinders show where a concentration profile has been obtained.

	Gibbsian excess $[atoms\,nm^{-2}]$			
	Cr	W	Mn	Si
ROI0	9.2	1.7	0.1	0.3
ROI1	8.7	0.4	0.2	0.5
ROI2	3.9	1.1	0.1	-0.2
Average	7.3 ± 1.7	1.1 ± 0.4	0.1 ± 0	0.2 ± 0.2

Table E.2: GIE values for the GB found in dataset 4724, the neutron irradiated 14YWT3

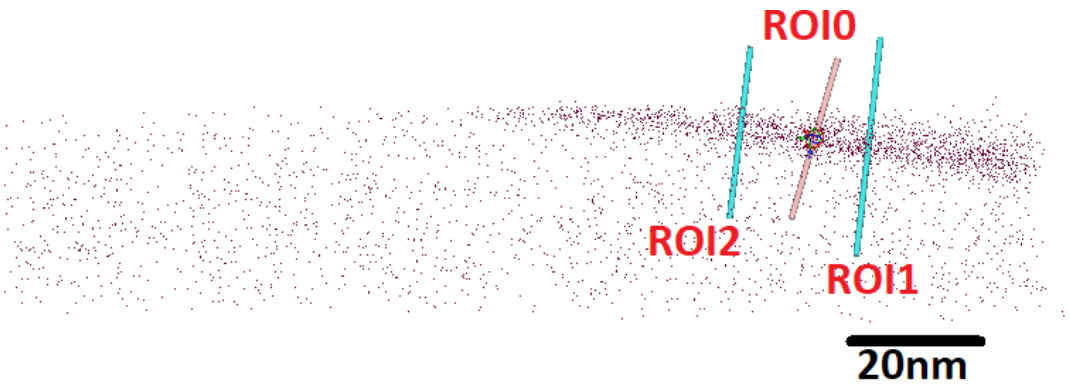


Figure E.3: C atom map slice from dataset 4732, the neutron irradiated 14YWT3. The dense regions of C represents a GB. The three cylinders show where a concentration profile has been obtained.

	Gibbsian excess $[atoms\,nm^{-2}]$			
	Cr	W	Mn	Si
ROI0	16.9	0.9	0.2	1.2
ROI1	6.5	3.6	0.0	0.2
ROI2	8.1	0.7	0.0	0.1
Average	10.5 ± 3.2	1.7 ± 0.9	0.1 ± 0.1	0.5 ± 0.4

Table E.3: GIE values for the GB found in dataset 4732, the neutron irradiated 14YWT3